Study of the relations between the performances of PEM fuel cell components and their behaviors in stacks operated in the complete system. : Development of electrical and mechanical characterization techniques

Khadidja Bouziane

▶ **To cite this version:**

Khadidja Bouziane. Study of the relations between the performances of PEM fuel cell components and their behaviors in stacks operated in the complete system. : Development of electrical and mechanical characterization techniques. Other. Université Paris-Saclay, 2021. English. NNT : 2021UPAST066 . tel-04190527

HAL Id: tel-04190527
https://theses.hal.science/tel-04190527v1

Submitted on 29 Aug 2023

HAL is a multi-disciplinary open access archive for the deposit and dissemination of scientific research documents, whether they are published or not. The documents may come from teaching and research institutions in France or abroad, or from public or private research centers.

L'archive ouverte pluridisciplinaire **HAL**, est destinée au dépôt et à la diffusion de documents scientifiques de niveau recherche, publiés ou non, émanant des établissements d'enseignement et de recherche français ou étrangers, des laboratoires publics ou privés.

Thèse de doctorat

NNT 2021UPAST066

université PARIS-SACLAY

Study of the relationship between the performance of PEM fuel cell components and their behaviours in stacks operated in the complete system. Development of electrical and mechanical characterization techniques.

Etude des liens entre les performances de composants de pile à combustible PEM et leurs comportements à l'intérieur de la pile observés en fonctionnement. Développement de caractérisations électriques et mécaniques in-situ et ex-situ.

Thèse de doctorat de l'Université Paris-Saclay

École doctorale n°575 : electrical, optical, bio : physics and engineering (EOBE)
Spécialité de doctorat : Génie Electrique
Unité de recherche : SATIE UMR CNRS 8029
Référent : ENS Paris-Saclay

Thèse présentée et soutenue à Paris-Saclay le 20 juillet 2021

Khadidja BOUZIANE

Composition du Jury

Patrice MÉLÉ Professeur, Université de Savoie	Président
Jean-Claude GRANDIDIER Professeur, ISAE-ENSMA	Rapporteur
François LAPICQUE Directeur de recherche, Université de Lorraine	Rapporteur
Nada ZAMEL Docteure, Fraunhofer Institute for Solar Energy Systems ISE (Allemagne)	Examinatrice
Najla FOURATI Maitresse de conférences, CNAM Paris	Examinatrice
Dominique CHAMORET Maîtresse de conférences, Université de Technologie de Belfort-Montbéliard	Examinatrice

Direction de la thèse

Denis CANDUSSO Directeur de recherche, Université Gustave Eiffel	Directeur de thèse
Yann MEYER Professeur, Université Savoie Mont Blanc	Co-Directeur
Rémy LACHAT Maître de conférences, Université de Technologie de Belfort-Montbéliard	Co-Encadrant

Summary

Low Temperature Polymer Electrolyte Membrane Fuel cell (PEMFC) is the most mature fuel cell technology, and it can be used in a variety of applications, (transport, space, stationary and portable applications). This electrochemical generator converts Hydrogen and Oxygen into electricity, heat and water through oxidoreduction reaction. PEMFC power production and overpotentials are related to the operating conditions and physical properties of cell components. Increasing cell efficiency can be achieved by reducing the overpotential losses, such as the Ohmic losses. This requires a better understanding of the relationship between the physical properties of the materials, their variation with regards to the operating conditions, and the influence of this variation on the Ohmic losses.

A PEMFC is made of an electrolyte membrane covered with two catalyst layers, that are hold between two gas diffusion layers - GDLs and compressed by two Bipolar plates - BPPs. Ohmic overpotential losses are due to the protonic resistance of the membrane, to the electronic bulk resistance of the other components and to the contact resistance of interfaces between components. These resistances are function of the material nature , the structure of the components and the operating conditions such as humidity, temperature, and especially mechanical compression. This study contributes in understanding the origin of the electronic Ohmic losses, particularly those due to the GDL and its interfaces.

The GDL plays several transport roles in the PEMFC by providing/evacuating reactant gases from/to BPP, conducting electrons and heat. It also contributes to water management and mechanically support the catalyst coated membrane so that it remains functional. The most common structure used to allow these various functions is a composite porous carbon fibres structure that can be paper or cloth. This porous structure is very sensitive to mechanical excitation which comes from variable external and internal sources generating an unsteady state of stresses.. In addition, the structure of the GDL exhibits a nonlinear compression stress-strain curve, with a strain hysteresis along the loading-unloading cycles. The physical properties of the GDL are affected by this behavior and need to be studied under cyclic compression in order to better approach the use conditions inside the FC and get a clearer idea about the contribution of the GDL to the global Ohmic losses. The optimal levels of mechanical compression must in particular be selected in order to make a trade-off between low Ohmic losses and high reactant diffusion rates.

In this thesis, experimental investigations and analyses of electrical properties have been conducted on several types of commercial carbon paper GDLs:

- Ex-situ characterization techniques have been used to measure the in-plane resistance according to two perpendicular directions. The impact of cyclic mechanical compression, the effects of temperature and humidity were investigated on the GDL through-plane resistance as well.
- The electrical contact resistance between GDL and BPP was measured using the Transmission Line Method.

It has been observed that all resistances decreased non-linearly with compression, meaning that optimal levels of compression can be obtained for PEMFC operation regarding the GDL porosity and diffusion properties. These resistances are more or less sensitive to the cycles of compression, according to the structure of the GDLs (the felt structure being the least sensitive towards cycles). The hysteresis of electrical resistance decreases with the rise of compression levels and with the number of compression cycles. Despite the GDL anisotropy observed for the in-plane resistance, some properties were unchanged with the measurement direction, such as the rate of resistance decrease with compression and the hysteretic behaviour versus the cycles of compression. Finally, in most cases, humidity was found to decrease the through-plane resistance of GDLs.

Keywords: Cyclic mechanical compression, PEM fuel cell, GDL, electrical contact resistance, resistivity

Résumé

L'amélioration du rendement des piles à combustible à membrane polymère basse température (PEMFC) passe par une diminution des pertes liées aux surtensions, telles que les pertes ohmiques, qui dépendent des conditions de fonctionnement et des propriétés des composants. Cela implique une meilleure compréhension de la relation entre propriétés physiques des matériaux, leur variation avec les conditions de fonctionnement et son influence sur les pertes ohmiques. Cette pile à hydrogène est constituée d'une membrane électrolyte en polymère, échangeuse de protons, couverte de deux couches catalytiques, placées entre deux couches de diffusion de gaz (GDLs), maintenues par deux plaques bipolaires (BPPs). Les pertes ohmiques sont en bonne partie dues à la résistance protonique de la membrane, mais également liées à des résistances électroniques volumiques dans les composants de cellule et à des résistances de contact entre ces éléments. Ces résistances sont fonction de la nature du matériau, de la structure des composants et des conditions de fonctionnement telles que l'humidité, la température et la compression mécanique exercée sur l'assemblage. Les travaux menés contribuent à la compréhension de l'origine des pertes ohmiques électroniques, en particulier celles liées à la GDL.

La GDL diffuse/évacue les gaz réactifs de/vers la BPP, conduit les électrons et la chaleur, contribue à la gestion de l'eau à l'intérieur de la pile et maintient mécaniquement l'ensemble membrane-couche catalytique. Les structures permettant ces fonctions sont des structures composites poreuses en fibres de carbone sous forme de papier ou de « tissu ». Cette structure est très sensible à la sollicitation mécanique d'origines diverses générant un état de contrainte variable. De plus, le comportement mécanique de la GDL est non-linéaire et laisse apparaitre une hystérésis de déformation avec les cycles de charge-décharge en compression. Les propriétés physiques de la GDL, à l'instar de sa résistance électrique, sont affectées par ce comportement de structure. Cela nécessite l'utilisation de compressions cycliques pour étudier l'influence de la charge mécanique afin de s'approcher au mieux les conditions de fonctionnement réelles de la pile et in fine mieux appréhender le rôle de la GDL dans les pertes ohmiques globales. Les niveaux optimaux de compression mécanique font l'objet d'un compromis entre de faibles pertes ohmiques et des performances en diffusion élevées.

Dans cette thèse, une investigation des propriétés électriques a été menée sur plusieurs types de GDL papier carbone disponibles dans le commerce :

- Des techniques de caractérisation ex-situ ont été utilisées pour mesurer, d'une part, la résistance dans le plan suivant deux directions perpendiculaires et, d'autre part, la résistance à travers le plan sous une contrainte mécanique cyclique. Les effets des variations de température et d'humidité ont également été analysés.
- La résistance de contact entre la GDL et la plaque bipolaire a été mesurée en utilisant la méthode de transmission de ligne (TLM).

Une diminution non-linéaire de toutes les résistances avec l'augmentation de la compression a été observée, ce qui implique l'existence d'un niveau optimal de compression à utiliser pour la pile, compte tenu de la porosité de la GDL et de ses propriétés de diffusion. Ces résistances sont plus ou moins sensibles aux cycles de compression, selon la structure des GDLs (la structure en feutre étant la moins sensible aux cycles). L'hystérésis de la résistance électrique décroît avec le niveau de compression et le nombre de cycles. Malgré l'anisotropie de la GDL observée pour la résistance dans le plan, quelques propriétés restent invariantes avec la direction de mesure, comme le taux de décroissance de la résistance avec la compression mécanique ou l'hystérésis. Enfin, l'humidité a tendance à faire décroitre la résistance à travers le plan de la GDL.

Mots clés : Compression mécanique cyclique, GDL, pile PEM, résistance de contact, résistivité.

Acknowledgement

First, I would like to gratefully thank Dr. Denis Candusso and Pr. Yann Meyer, my PhD thesis supervisors, for allowing me to conduct this research work. I would like to especially thank them for all the knowledge I have learned from them in fuel cells, electrical and mechanical engineering, for the numerous discussions we had, for their support through all conferences and research stays I had the occasion to do in this thesis, for their technical support through all my thesis steps, for their availability, their encouragement and their kindness.

I would also like to thank Dr Rémy Lachat, my thesis advisor for supervising my research, especially my experimental work. I would like to thank him for his help and supervision of the experiments, for the numerous and enriching discussions we had.

I would like to thank Pr. Patrice Mélé, the President of my PhD committee, for accepting to supervise my thesis defence, and for his pertinent remarks.

I would like to address a special thank to Pr. Jean-Claude Grandidier, for accepting to report this thesis, for the time he spent in analysing my manuscript, and for his highly interesting comments that helped improving this manuscript.

I also address a special thank to Dr. François Lapicque for reporting this thesis and for the time he spent on the manuscript, and for revealing interesting comments that help enhance this work.

I also address my special thanks to all my committee members, Dr. Najla Fourati, that I thank for the interesting discussion. I would like to thank Dr. Dominque Chamoret for her revealing questions and for her supervising of the numerical model.

I would also like to thank Dr. Nada Zamel for taking part in my thesis committee, for her comments on the manuscript, for her warm welcome in the Fraunhofer ISE, Freiburg-im-Breisgau, during my research stays, and for her supervision of my experimental work.

I would also like to thank Chloé Charbonné and Maria-Lisa Dhuitte for their contribution to this research work through numerical modelling. Special thanks are also addressed to Xavier François, for his welcome and help in the Plateforme Hydrogène Energie and also for the numerous discussions we had. I also address a special thank to Dr. Khetabi El Mahdi for sharing his research knowledge and for the numerous discussions.

I am also grateful to my FCLAB and UTBM colleagues, starting by Laurence for her warm welcome and all other PhD students and researchers: Elodie, Rania, Frédéric, Julie, Xianlong, Haider, Dan, Fouad, Meiling, Sondos, Djaffar, Amal, Bruno, Violaine, Jérome, and Sarah. I would also like to thank my colleagues of Franhofer ISE who helped me with the experiments: Rajah, Anne-Christine, Robert, Peter, Sebastien, Kläre, Leo, Mohamed Alisha, Annike. I would also like to thank my CARaDOC friends - that was a nice adventure - as well as all people that helped me during my PhD.

The University Paris-Saclay and French Minister of education are acknowledged for financing my PhD, as well as the UTBM and the University Gustave Eiffel for their support to this work. The DAAD (Deutsch Academic Exchange service) is also gratefully acknowledged for funding my research stay at the Fraunhofer ISE Institute.

I first dedicate this thesis to my dear parents
Saida & Abdelkader for their love & support.

To my parents-in-law Leila & Madjid.
To Abdou & Amira,
To Bouchra, Faten, Sarah & Amine,
To Idir & Samy,
To all my family and friends,
thank you for your support.

To my dear fiancé Ali, for your love,
for your support & for your patience.

Abbreviations

2D/3D: Two dimensions / Three Dimensions.
BPP: BiPolar Plate.
CL: Catalyst Layer.
CCM: Catalyst Coated Membrane.
CPRESS: Contact Pressure.
CR: Electrical Contact Resistance.
DoE: Design of Experiment.
DMA: Dynamic Mechanical Analysis machine.
GDL: Gas Diffusion Layer.
FC: Fuel Cell.
FEP: Tetrafluoroethylene-hexafluoropropylene.
FE: Finite Element.
FEM: Finite Element Method.
HOR: Hydrogen Oxidation Reaction.
MEA: Membrane Electrode Assembly (Anode Catalyst layer-Membrane-Cathode Catalyst layer).
MPL: Microporous Layer.
PEMFC: Polymer Electrolyte Membrane Fuel Cell (also called Proton Exchange Membrane Fuel Cell).
OCV: Open Circuit Voltage.
ORR: Oxygen Reduction Reaction.
PAN: Polyacrylonitrile
PEM: Polymer Electrolyte Membrane (also called Proton Exchange Membrane)
PTFE: Polytetrafluorethylene.
PTL: Porous Transport Layer (Fibrous substrate of a GDL).
SEM: Scanning Electron Microscope.
SGL: Commercial Sigracet carbon Paper GDL series.
TGP: Commercial Toray carbon Paper GDL series.
TLM: Transfer Length Method also called Transmission Line Measurement.

Table of contents

Introduction

Environmental problems related to the use of fossil fuels and the unsustainability of this source along with the continuous increase of global energy demand each year had led to a remarkable growth in the use and the development of renewable and alternative energy technologies. Renewable sources of energy are often intermittent and need a suitable storage solution. Green Hydrogen, produced by electrolysis using extra-electricity from these renewable sources, can be used as an efficient, long-lasting and easily transportable storage solution. Biomass can also be used to produce hydrogen sustainably. Further, the newly discovered natural hydrogen from geological sources, can be considered as a renewable primary source of energy [1][2]. Fuel Cell (FC) can revert the energy stored by hydrogen into electricity and heat. It is also an interesting solution to produce electricity in isolated areas and for powering high range electrical vehicles, high-use vehicles (such as taxis, buses, and fleet cars), and especially heavy vehicles such as trucks and trains. The Low Temperature Polymer Electrolyte Membrane Fuel cell (PEMFC) is the most mature fuel cell technology especially for the automotive industry.

PEMFC power production and overpotentials are related to the operating conditions and physical properties of cell components. Increasing cell efficiency can be achieved by reducing the overpotential losses, such as the ohmic losses. This requires a better understanding of the relationship between the physical properties of the materials, their variation with regards to the operating conditions, and the influence of this variation on the ohmic losses, which is the scope of this thesis.

Mechanical constraints are among the main parameters affecting the ohmic losses in a PEMFC. These are caused by variable internal and external sources, which create an unsteady state of stress inside the cell. On the other hand, the Gas Diffusion Layer (GDL), the component most impacted by compression, exhibits a non-linear behaviour with a strain hysteresis. Hence, studying the impact of compression on the electrical parameters of GDLs depends on the GDLs structure and requires the use of cyclic loads to take into account part of the actual operating conditions of a PEMFC.

In this thesis, the effect of compression on the electrical properties of several structures of carbon paper GDLs and the impact of FC operating conditions

(temperature, humidity, cyclic compression) have been examined experimentally and numerically.

In the first chapter, PEMFC and its components properties are introduced. Then, in the next chapter, a state-of -art concerning the effect of mechanical pressure on the GDL's physical properties in FC, and a theoretical background on the experimental methods to measure different electrical resistances are exposed. In the third chapter, the physical properties of GDL experimentally measured are analysed. In the fourth chapter, a numerical analysis is used to relate these local physical properties of GDL to the global performance of the FC. Finally, a conclusion is given to the different analyses and findings.

Chapter 1: The PEMFC and its electrical properties

1.1 Fuel cell types

A Fuel Cell (FC) is an electrochemical generator that converts the chemical energy of a fuel directly into electrical energy, through an oxidation - reduction reaction, as long as it is supplied with the fuel (generally hydrogen). The process needs three principal elements: an anode (oxidation reaction), an electrolyte, and a cathode (reduction reaction). There are various types of FCs, generally classified according to the nature of their electrolyte and temperature [3]. Table 1.1 summarizes the most important FC types with their operating temperatures and their applications [4].

In this thesis, we investigate the Low-Temperature Polymer Electrolyte Membrane Fuel Cells, also called Proton Exchange Membrane fuel cells (PEMFCs). These FCs are suitable for most applications, thanks to their quick start capabilities at room temperature, their high efficiency, and the possibility of energy conversion with zero-emission.

1.2 Polymer Electrolyte Membrane Fuel Cell (PEMFC)

As shown in fig. 1.1 a single PEMFC cell is composed of a Polymer Electrolyte Membrane, which is generally made of Nafion® (See more on 1.2.1) and can exchange protons. The membrane is coated with two Catalyst Layers (CLs) made of a mix of ionomer, carbon support, and platinum at each side, forming the anode and the cathode. This Membrane Electrode Assembly (MEA) or Catalyst Coated Membrane (CCM) is supported by two Gas Diffusion Layers (GDLs), one at the anode, and the other at the cathode. These GDLs are maintained by two reactant distribution plates, usually referred to as Bipolar Plates (BPPs), that contain flow channels for the reactants and products, and possibly also the sealing gaskets.

FC type	Electrolyte material	Operating temperature (◦C)	Major poison	Advantages	Disadvantages	Most promising applications
Alkaline fuel cell	Solution of potassium hydroxide in water	60 - 250[a]	CO_2	High efficiency, low ORR losses	Must run on pure oxygen without CO_2 contaminant	Space applications with pure O_2/H_2 available
Phosphoric Acid Fuel Cell	Solution of phosphoric acid in porous silicon carbide matrix	160 - 220	Sulfur high levels of CO: 1 - 2%	CO tolerant, good-quality waste heat, demonstrated durability	Low power density, expensive, platinum catalyst used, slow start-up, loss of electrolyte	Premium stationary power
Solid oxide Fuel Cell	Yttria (Y_2O_2) stabilized zirconia (ZrO_2)	600 - 1000	Sulfur	CO tolerant, fuel flexible, high-quality waste heat, inexpensive catalyst	Long start-up time, durability under thermal cycling, inactivity of electrolyte below ~600°C	Stationary power with cogeneration, continuous-power applications.
Molten Carbonate Fuel Cell	Molten alkali metal (Li/K or Li/Na) carbonates in porous matrix	600 - 800	Sulfur	CO tolerant, fuel flexible, high-quality waste heat, inexpensive catalyst	Electrolyte dissolves cathode catalyst, extremely long start-up time, carbon dioxide must be injected to cathode, electrolyte maintenance.	Stationary power with cogeneration, continuous-power applications.
Polymer Electrolyte Fuel Cell[b]	Flexible solid perfluorosulfonic acid polymer	30 - 100	CO, sulfur, metal ions, peroxide	Low-temperature operation, high efficiency, high H_2 power density, relatively rapid start-up	Expensive catalyst, durability of components not yet sufficient, poor-quality waste heat, intolerance to CO, thermal and water management	Portable, transport, and stationary applications

Table 1. 1: Most common FC types [4]

[a] Modern AFCs < 100◦C.

[b] Includes direct methanol fuel cell and direct alcohol fuel cells.

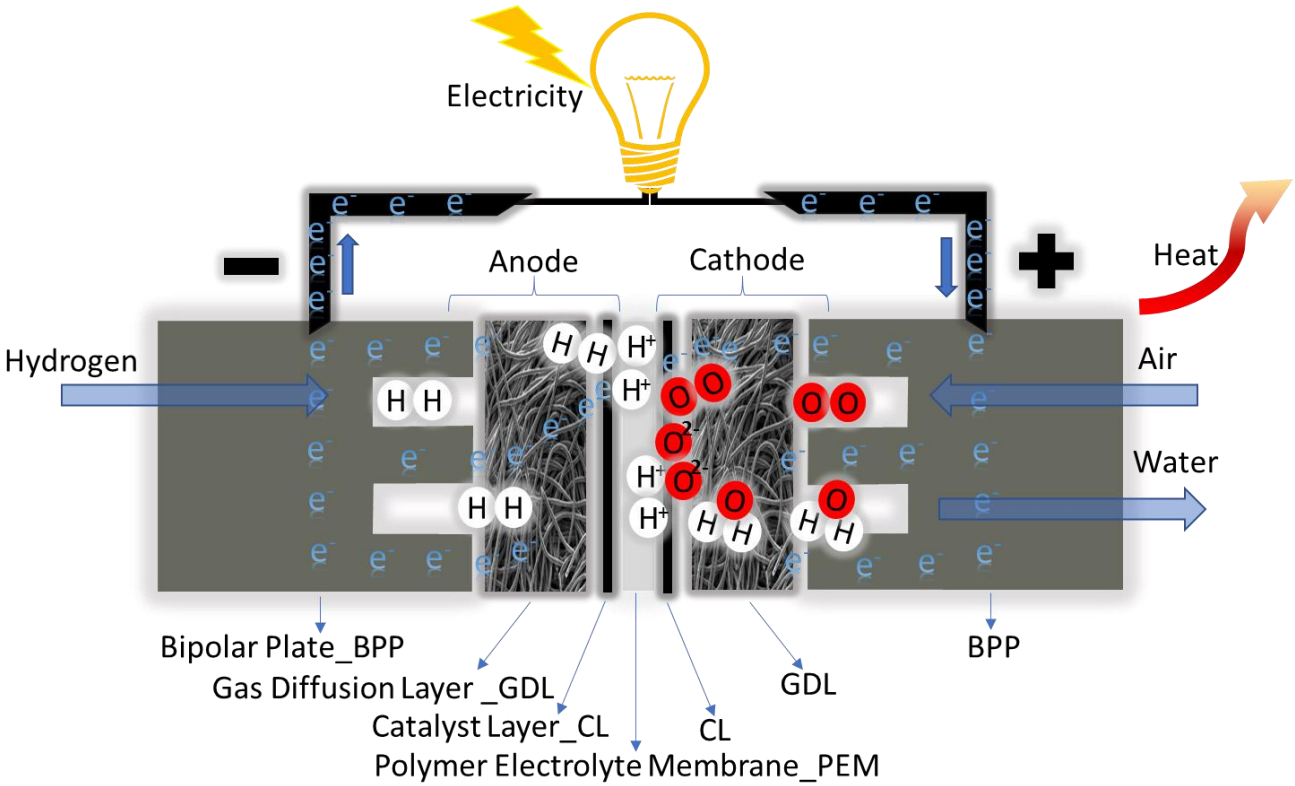

Fig 1. 1: Schematic diagram of a PEMFC

The channels of the BPP at the anode side supply hydrogen to the GDLs. The GDLs allow the hydrogen to diffuse homogenously on the active area of the CL. The CL is a porous layer that is directly in contact with the PEM. The Hydrogen Oxidation Reaction-(HOR) splits the hydrogen molecules into protons and electrons (Equation 1.1) and occurs at the PEM-CL interface, where three phases are in contact together: with the electrode, the electrolyte, and the gas.

$$\boldsymbol{H_2 \rightarrow 2H^+ + 2e^-} \qquad (1.1)$$

The protons cross the membrane to the cathode, whereas the electrons return to the GDLs, to the BPPs, to the current collector, and then travel to the external circuit creating a current before entering the cathode. At the cathode, the oxygen reduction reaction occurs, and water is produced (Equation 1.2).

$$\frac{1}{2}O_2 + 2H^+ + 2e^- \rightarrow H_2O \qquad (1.2)$$

The reaction produces water and heat that are removed first by the GDLs and then by the BPPs. The global oxidation - reduction reaction is described in (Equation 1.3).

$$H_2 + \frac{1}{2}O_2 \rightarrow H_2O \qquad (1.3)$$

In nominal conditions, this reaction usually produces a potential close to 0.7 V [3] because of multiple losses that are detailed in the next paragraph. This voltage is too low for most applications. A FC stack is thus made up of individual cells connected together in series from an electrical point of view (and in parallel from a fluidic point of view) in order to produce more power. Both edges of the stack are equipped with current collectors that are connected to the last and first reactant distribution plates. An end-plate compresses each current collector.

1.3 PEMFC components

1.3.1. Polymer Electrolyte Membrane:

The electrolyte, in PEMFCs, is generally made of sulphonated fluoropolymer [5], such as sulphonated fluroethylene (Nafion®). The structure of the sulphonated fluoroethylene is made of polytetrafluorethylene (PTFE) with side chains ending with a sulphonic acid (HSO_3). This acid is ionically bounded (SO_3^-, H^+). This is why the polymer is called ionomer. PTFE is a polymer of tetrafluoroethylene, which is ethylene with its four hydrogen atoms "H" replaced by four fluorine atoms [5]. The structure is presented in fig 1.2.

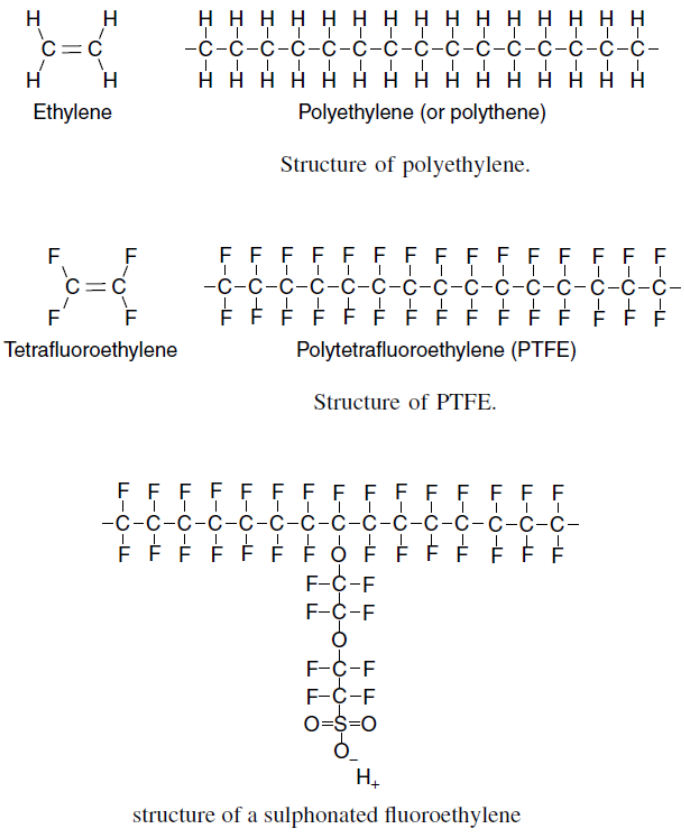

Fig 1. 2: Structure of sulphonated fluoroethylene [5]

The PTFE is hydrophobic while the sulphonic acid is hydrophilic. The absorption of water molecules by the hydrophilic phase of the Nafion makes the ionic bound between SO_3^- and H+ weak, which makes it easier for H^+ transport [5]. The more the membrane is hydrated, the higher is its proton conductivity. Membranes are sensitive to the hygro-thermal cycles that occur during FC operation; they are hardened by these cycles [6,7]. Practical pressure that is transmitted to the membrane through stack compression is estimated to be 0.6 - 4 MPa [8].

1.3.2. Catalyst Layers

The catalyst layer is made of platinum that is supported on carbon. Sometimes PTFE is added too as binder [5], but recently the ionomer (Nafion) was used as a binder [9], this reduced the amount of platinum needed by increasing the three phase surface (electrolyte-catalyst-reactant). Typical loadings are today ranging from 0.2 to 0.4 mg/cm^2. The final structure is a porous, thin layer that is shown in fig 1.3 [10] .

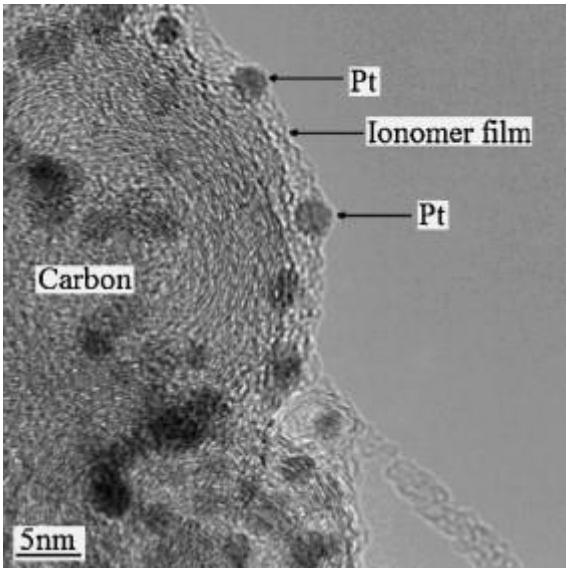

Fig 1. 3: Structure of Catalyst Layer

1.3.3. Bipolar Plates

Bipolar plates in PEMFC provide reactant gases, remove water and heat, conduct electrons, and hold the MEA. The plate is also the separation and connection between two adjacent cells. Classical BPPs are made of graphite, that is known for its high electrical and thermal conductivity and its chemical stability. However, two main drawbacks are the expensive machining of graphite [11] and its brittleness, which means that the thickness cannot be reduced much. Metal BPPs, as depicted in fig 1.4, are a good alternative in that they are easily stamped, thus reducing the price, as well as they have good mechanical properties allowing for the use of very thin layers. However, the high contact resistance and the low corrosion resistance need to be improved [12].

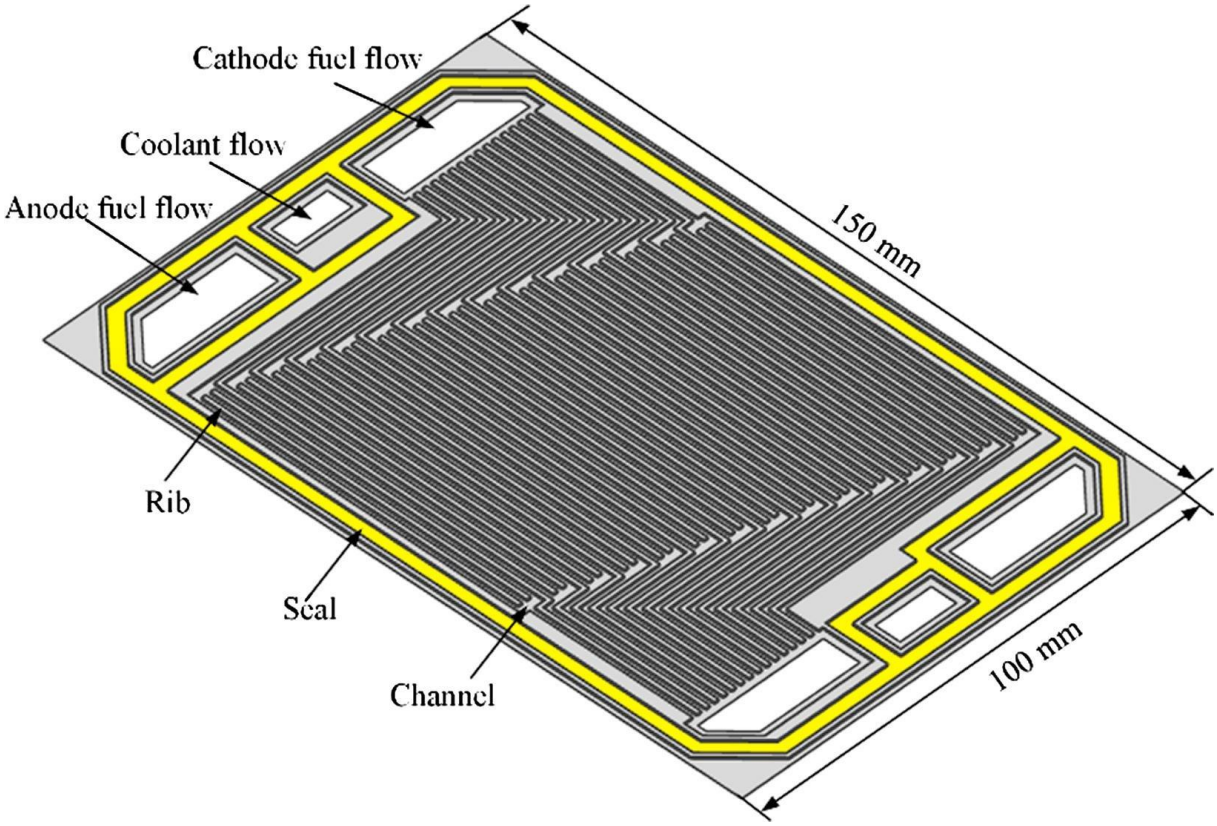

Fig 1. 4: Schematic of a metallic BPP design [13]

1.4 GDL in more details

1.4.1. Function and properties

The Gas Diffusion Layer is a porous composite media, 100-500 µm thick [13], placed between the BPP and the CL. The structure of this important cell component should be adequate to ensure several functions. First, the material must have a high porosity to provide a homogenous reactant gas flow (H_2 in the anode and O_2 in the cathode) to the CL for an optimal use of the electroactive surface area. Besides, it needs a high electrical and thermal conductivity to conduct electrons and heat to/from the BPP. The GDL has also a crucial role for the water management inside the cell (See section 1.3.3.4). In addition, one of its most important functions is to undergo the mechanical support of the MEA, so that the latter does not change its shape and remains functional. In addition to these functions, GDLs must be corrosion resistant as they are in contact with different active substances (BPP materials, water, oxygen, hydrogen).

1.4.2. Composition and structure

To ensure these different functions, the structure of the GDL is usually made of a carbon composite, formed with carbon fibres that are either woven (cloth) or non-woven (paper) [14]. Carbon cloth can have a plain or a knitted weave structure [15]. Carbon paper is constituted of either in-plane random distributed straight fibres (a 2D-structure) or of "spaghetti" shape fibres (a 3D-structure). The former is generally referred to as carbon paper and the latter as felt. The properties of carbon cloth and carbon paper have been compared in some studies [13,15,16]. Fig 1.5 shows the three different carbon structures.

1.4.3. Structure

1.4.1.1 Initialisation step

For all these carbon GDL types, the fabrication process starts by the polymerisation of the acrylonitrile (PAN) and fibre formation. Fig 1.5 shows the different paths of fabrication for the different structures (straight carbon fibre paper, felt paper, and cloth) [17].

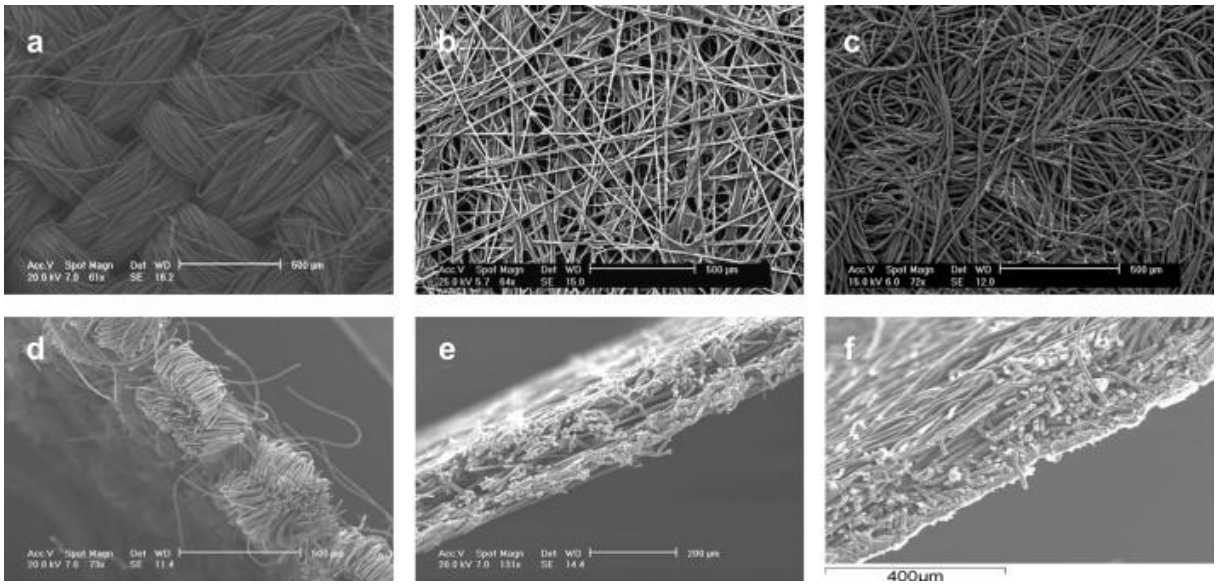

Fig 1. 5: SEM images of GDL fibres configuration; surface and edge views of (a) & (d) woven fibres in carbon cloth - Ballard 1071HCB, (b) and (e) straight stretched fibres in carbon paper - Toray H-060, (c)& (f) felt/spaghetti fibres in carbon paper-Freudenberg.

In felt paper, just after the filament of PAN into fibres, the 3D structure is created using water jets, that moves some fibres in the through-plane direction [18]. Then, the same steps are followed (stabilisation, carbonisation, impregnation,

graphitisation) as shown in the last column of fig 1.6 (on the right). The felt structure is depicted in fig 1.5 c).

In carbon cloth fabrication, spun PAN yarns are woven, which mechanically bounds the fibres together without the need of a resin [18], then the structure is carbonised. Further details on the fabrication process can be found in [18]. The structure of a cloth GDL is exhibited in fig 1.5 a).

Straight-carbon paper fibre is fabricated in two main steps: first paper making, then GDL making.

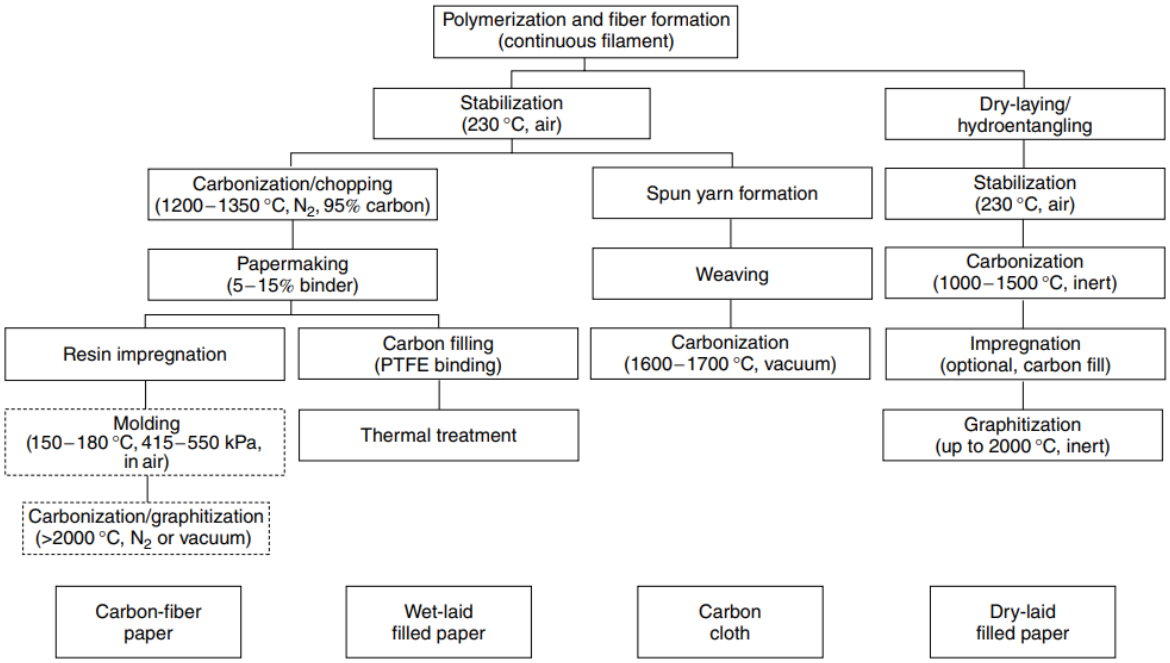

Fig 1. 6: Various routers of GLD processing [18]

1.4.1.2 Paper making step

After fibre formation, a stabilization step where the fibres are heated at 230°C is made in order to transform the thermoplastic fibres to thermoset (to avoid the spun fibres from melting together) [18]. Following this step, a carbonization step by heating the fibre to 1200 - 1350°C in a nitrogen environment is carried out to get a 95% carbon content in fibres. Here, fibres are chopped to the desired length (3 - 12 mm) [18]. Then comes the step of the papermaking where fibres are dispersed in water with a binder. At that point, the web of fibres is dried and rolled up. This procedure affects the anisotropy of the material as the fibres are preferentially following the machine direction [18].

1.4.1.3 GDL making step

The carbon fibre paper is impregnated with a carbonizable thermoset resin (such as phenolic resins) that will help moulding the paper to a desired thickness / density. Then, the carbon paper is heated, and compression moulded to the desired thickness. The last step is a heat treatment of the paper, either carbonization at 1200 - 1300°C (such as SGL GDL series [19]) or graphitization at 2200 - 2400°C where amorphous carbon is transformed to graphite, which enhances physical properties of the fibres (electrical and thermal conductivity, tensile modulus, higher oxidation resistance, density… etc.) (such as Toray [20]).

1.4.1.4 Hydrophobic treatment and MicroPorous Layer

One of the important roles of the GDL consists of ensuring water management inside the cell. The GDL should properly remove the produced water to avoid flooding and keep the pores open to reactant gas diffusion, without drying the membrane (whose ionic conductivity is directly related to water content [3]). In this aim, GDLs are treated with a hydrophobic agent, namely PTFE or FEP [21], or by direct fluorination [16]). Sometimes, a Microporous Layer (MPL) [22], a smooth porous structure made of black carbon–mixed with PTFE, is added to the GDL substrate, on the CL side. This sublayer improves the contact with the Catalyst Coated Membrane (CCM) and blocks the water inside it, which mitigates membrane drying. MPL also protects MEA from fibre penetration (SGL White Paper).

Researchers are developing new methods to improve water management inside the GDLs by promoting preferable water patterns [23–25], by the use of porosity graded MPLs [26], the use of double gas diffusion baking layers [27,28] in self-humidified PEMFCs or by applying hydrophobic treatment on BPP [29].

1.5 Fuel cell function properties

Theoretical (reversible) PEMFC voltage is related to the change of "Gibbs free Energy" along the reaction. The "Gibbs free energy" is defined as the available energy (considering reversible process) that can be transformed to external work (electrical work in case of FCs) excluding work due to changes in pressure / volume [5]. This change is calculated between the "Gibbs free energy" of formation of products and reactants in the global reaction (Equation 1.4).

$$\Delta\bar{g}_f = (\bar{g}_f)_{H_2O} - (\bar{g}_f)_{H_2} - \frac{1}{2}(\overline{g_f})_{O_2} \qquad (1.4)$$

With $(\overline{g_f})_i$: "Gibbs Free Energy" of formation for one mole of "i" (J.mol^{-1}).

This change in the "Gibbs free energy" is equal to the electrical work produced by the PEMFC, which is defined as:

$$\text{Electrical work} = \text{Charge}*\text{Voltage} = Q(C).E(V) \qquad (1.5)$$

In the case of PEMFC, 2 moles of electron are exchanged for one mole of produced water. The corresponding charge is:

$$Q = -2F \qquad (1.6)$$

Where F is the Faraday constant (charge of one mole of electrons, 96485 C).

This means:

$$\boldsymbol{\Delta \bar{g}_f = -2.F.E} \qquad (1.7)$$

Theoretical Open Circuit Voltage (OCV) considering a reversible process is thus deduced:

$$E = \frac{-\Delta \bar{g}_f}{2.F} \qquad (1.8)$$

g_f depends on the temperature and the state of the molecule, and so will the $\Delta \overline{g_f}$.
- For a reaction at 25°C with liquid water, $\Delta \overline{g_f} = -237.2$ kJ mol^{-1}. So: E= 1.23 V.
- For a reaction at 80°C with water vapor, $\Delta \overline{g_f} = -225.2$ kJ mol^{-1}. So: E= 1.17 V.

Δg_f also depends on partial pressure and concentration of the reactants and products. E can be determined by the Nernst equation given these dependencies:

$$E = E_T^0 + \frac{RT}{2F} \ln \left(\frac{a_{H_2} a_{0_2}^{\frac{1}{2}}}{a_{H_2O}}\right) \qquad (1.9)$$

With:
E_T^o: reversible OCV (V)at standard pressure and at temperature T.
a: activity of molecule. It equals 1 for liquid water, and equals (partial pressure) / (reference pressure) for ideal gases.
R: Ideal Gas constant (8,314 J·K^{-1}·mol^{-1})

T: Temperature (K)
This gives the reversible voltage E at given temperature and pressure.

However, in real operating conditions, processes are not reversible and real OCV is lower and around: 0.9 – 1 V. Some of the losses that decrease this real OCV are due to internal currents (electrons crossing the membrane) and H_2 crossover (hydrogen gas crossing the membrane).

Besides, when a PEMFC starts operating and current is delivered, other losses occur. In fact, three types of losses [12] mainly affect the electrical voltage produced by the operating cell:

- *Activation losses:* they are predominant at low current production. Those losses are due to the time and energy necessary for the reaction (kinetics constant times linked with the oxidation - reduction chemical reactions at anode and cathode).

- *Ohmic losses:* the Ohmic losses are due to the different electrical (electronic and protonic) resistances of the components of the cell (bulk electrical resistance of the GDL, the BPP, the CL, proton resistance of the membrane, and the electrical contact resistance between the CL- GDL and between GDL-BPP).

- *Mass transport losses:* they mostly arise at high current production. They are due to the water accumulation in the electrode ("triple points") and/or in the GDLs hindering or even stopping the flow (problem of reactant gas diffusions and starvation in worst cases).

So, the global cell voltage equation is:

$$V = E_r - \Delta V_{act} - \Delta V_{ohm} - \Delta V_{conc} \qquad (1.10)$$

With:
V: cell voltage output (V)
Er : real Open Circuit Voltage (OCV) (V)
$\Delta \mathbf{V_{act}}$: activation losses (V)
$\Delta \mathbf{V_{ohm}}$: Ohmic losses (V)
ΔV_{conc} : Mass transport losses (V)

The polarisation curve depicted in fig. 1.7 (from [30]), summarizes the different losses in a PEMFC.

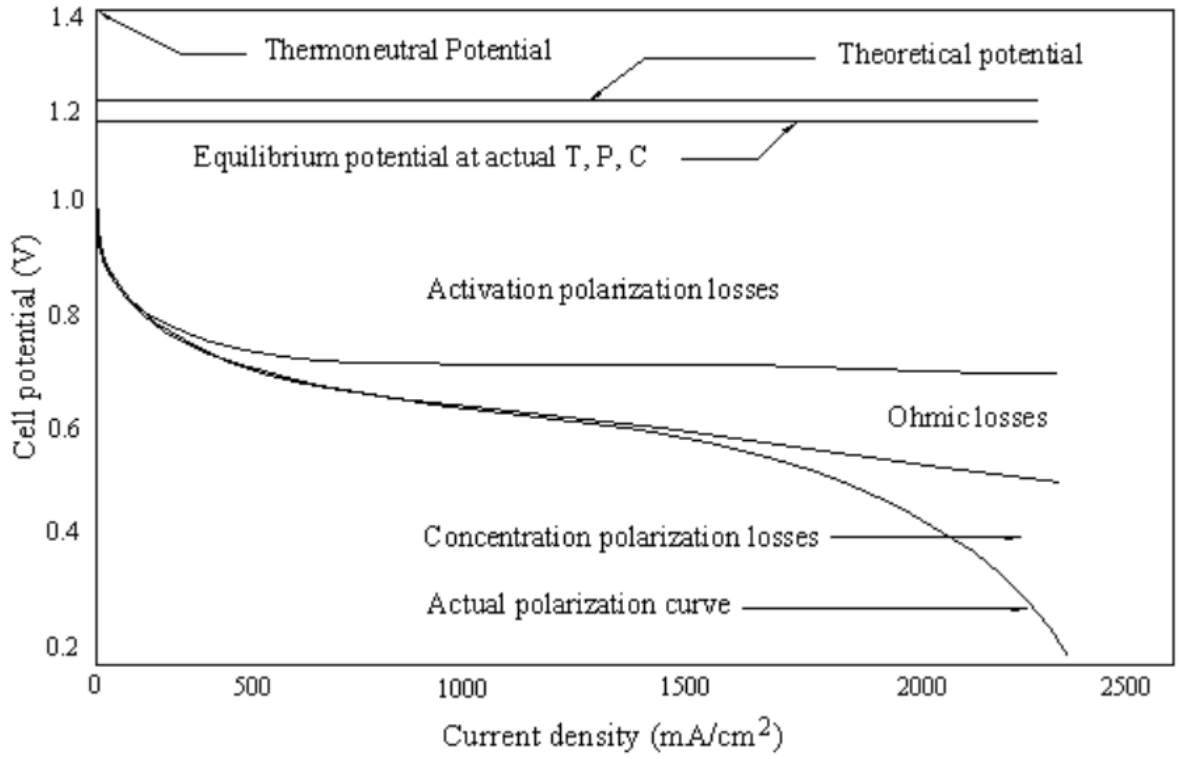

Fig 1. 7: Fuel cell voltage as function of current density showing the different voltage losses.

1.6 Link between cell component properties and cell performance

It is clear that there is a strong dependency between the component properties and the performance of the FC system. To optimize the operation of the FC system, the dialogue between these properties and the FC performance needs to be understood and established more clearly. Due to the PEMFC mechanical architecture (a stack), the cell seems to be the right level to study.

The last equation of losses (Equation 1.11) is strongly related to the working conditions and the physical properties of the FC components. The OCV and the activation overpotential are influenced by the temperature, the gas pressures, the membrane thickness (which influences the H_2 crossover), and the catalyst distribution.

The origin of the Ohmic losses are the protonic resistance of the membrane as well as the electronic bulk and contact resistance between the different components. The Ohmic losses can be expressed as:

$$\Delta V_{ohm} = R_{ohmic} i = (R_{ionic} + R_{electronic}) i = (R_{ionic} + R_{bulk} + R_c) i \qquad (1.11)$$

With:

R_{Ohmic}: global internal electric resistance (Ohm)

i: electrical current of the cell (A)

$R_{electronic}$: electronic bulk and contact resistance of components (Ohm)

R_c: contact resistance between components (Ohm)

R_{bulk}: bulk resistance (Ohm)

R_{ionic}: protonic resistance of the membrane (Ohm)

The ionic resistance of the membrane decreases with its thickness and its humidity rate. The electronic resistance is strongly dependent on the materials used, their structure (porosity rate, fibres type and distribution), their compression behaviour and the influence of this compression on the bulk and contact resistances. Contact resistances are decreased by a better contact that can be assured with an adequate compression level and a smoother surface. The contact resistance is responsible of an important amount of the Ohmic losses. The electrical contact resistance can represent more than 50% of the total electronic losses [31,32]. In some cases, the Rc between GDL and BPP represents 8 - 10% of the total Ohmic losses and is the major cause of electronic losses [32]. The mechanical compression also affects the concentration losses by decreasing the porosity of the GDL.

Understanding the relationship between the applied stress and the resulting change in the physical properties of the PEMFC components, and relating this physical property change to FC performance, will help to achieve a better design for PEMFCs, as fuel cells are exposed to several mechanical excitations. Especially the GDL, which is the most sensitive element to compression because of its high porosity, needs to be considered in these studies.[33]

1.7 Conclusion

The structure of the GDL described is responsible of its physical properties that influences the PEMFC properties. This structure is particularly influenced by compression. The GDL physical properties are also modified by mechanical compression. leading to a change of the cell performance. In the next chapter, we

will review how these physical properties are impacted by compression as depicted in fig 1.8.

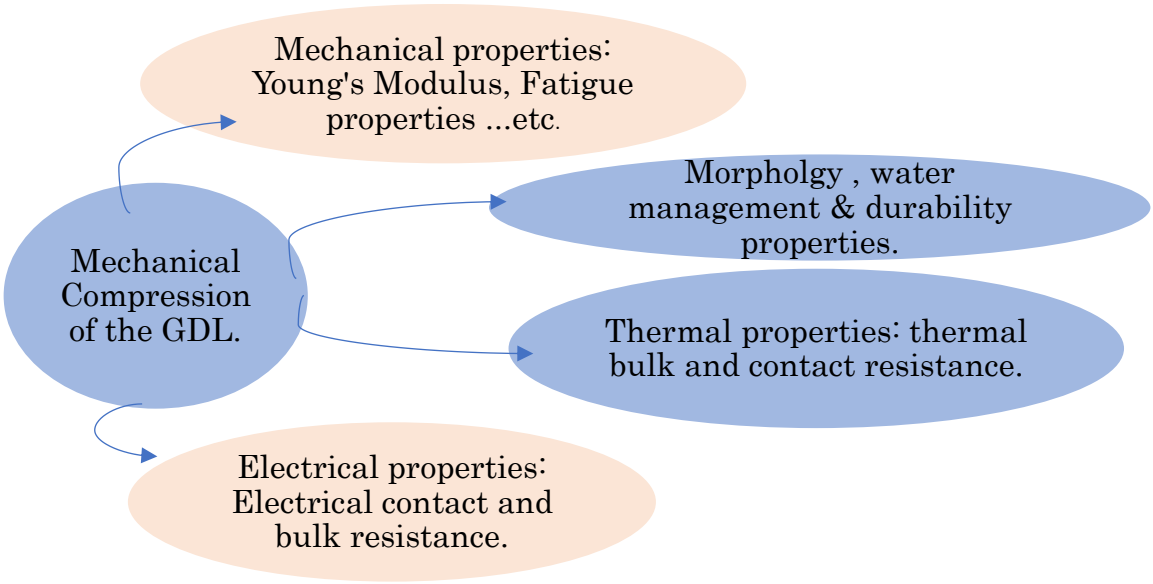

Fig 1. 8: Effect of mechanical compression on GDL Physical properties.

1.8 References

[1] Truche L, Bazarkina EF. Natural hydrogen the fuel of the 21 st century. E3S Web Conf. 2019;98:3006. https://doi.org/10.1051/e3sconf/20199803006.

[2] Zgonnik V. The occurrence and geoscience of natural hydrogen: A comprehensive review. Earth-Science Reviews 2020;203:103140. https://doi.org/10.1016/j.earscirev.2020.103140.

[3] Blunier B, Miraoui A. Piles à combustible: Principes, modélisation, applications avec exercices et problèmes corrigés. Paris: Ellipses; 2007.

[4] Mench MM. Fuel Cell Engines. Hoboken, NJ, USA: John Wiley & Sons, Inc; 2008.

[5] Larminie J, Dicks A. Fuel Cell Systems Explained. West Sussex, England: John Wiley & Sons, Ltd; 2003.

[6] Kusoglu A, Karlsson AM, Santare MH, Cleghorn S, Johnson WB. Mechanical behavior of fuel cell membranes under humidity cycles and effect of swelling anisotropy on the fatigue stresses. Journal of Power Sources 2007;170(2):345–58. https://doi.org/10.1016/j.jpowsour.2007.03.063.

[7] Kusoglu A, Karlsson AM, Santare MH, Cleghorn S, Johnson WB. Mechanical response of fuel cell membranes subjected to a hygro-thermal cycle. Journal of Power Sources 2006;161(2):987–96. https://doi.org/10.1016/j.jpowsour.2006.05.020.

[8] Yun S-H, Shin S-H, Lee J-Y, Seo S-J, Oh S-H, Choi Y-W et al. Effect of pressure on through-plane proton conductivity of polymer electrolyte membranes. Journal of Membrane Science 2012;417-418:210–6. https://doi.org/10.1016/j.memsci.2012.06.041.

[9] Zamel N. The catalyst layer and its dimensionality – A look into its ingredients and how to characterize their effects. Journal of Power Sources 2016;309:141–59. https://doi.org/10.1016/j.jpowsour.2016.01.091.

[10] Scopus preview - Scopus - Document details. [August 27, 2020]; Available from: https://www.scopus.com/record/display.uri?eid=2-s2.0-33846981457&origin=inward&txGid=6a480f55cc6dc38a0f378b4e480ec393.

[11] Dicks AL. The role of carbon in fuel cells. Journal of Power Sources 2006;156(2):128–41. https://doi.org/10.1016/j.jpowsour.2006.02.054.

[12] Gabreab EM, Hinds G, Fearn S, Hodgson D, Millichamp J, Shearing PR et al. An electrochemical treatment to improve corrosion and contact resistance of stainless steel bipolar plates used in polymer electrolyte fuel cells. Journal of Power Sources 2014;245:1014–26. https://doi.org/10.1016/j.jpowsour.2013.07.041.

[13] Dhanushkodi SR, Capitanio F, Biggs T, Mérida W. Understanding flexural, mechanical and physico-chemical properties of gas diffusion layers for polymer membrane fuel cell and electrolyzer systems. International Journal of Hydrogen Energy 2015;40(46):16846–59. https://doi.org/10.1016/j.ijhydene.2015.07.033.

[14] Park S, Lee J-W, Popov BN. A review of gas diffusion layer in PEM fuel cells: Materials and designs. International Journal of Hydrogen Energy 2012;37(7):5850–65. https://doi.org/10.1016/j.ijhydene.2011.12.148.

[15] Mishra V, Yang F, Pitchumani R. Measurement and Prediction of Electrical Contact Resistance Between Gas Diffusion Layers and Bipolar Plate for Applications to PEM Fuel Cells. Journal of Fuel Cell Science and Technology 2004;1(1):2–9. https://doi.org/10.1115/1.1782917.

[16] Park S, Popov BN. Effect of a GDL based on carbon paper or carbon cloth on PEM fuel cell performance. Fuel 2011;90(1):436–40. https://doi.org/10.1016/j.fuel.2010.09.003.

[17] El-kharouf A, Mason TJ, Brett DJ, Pollet BG. Ex-situ characterisation of gas diffusion layers for proton exchange membrane fuel cells. Journal of Power Sources 2012;218:393–404. https://doi.org/10.1016/j.jpowsour.2012.06.099.
[18] Mathias MF, Roth J, Fleming J, Lehnert W. Diffusion media materials and characterisation. In: Vielstich W, Lamm A, Gasteiger HA, Yokokawa H, editors. Handbook of Fuel Cells. Chichester, UK: John Wiley & Sons, Ltd; 2010.
[19] Rüdiger Schweiss, Christian Meiser, Tanja Damjanovic, Ivano Galbati, Nico Haak. SIGRACET® Gas Diffusion Layers for PEM Fuel Cells, Electrolyzers and Batteries. White paper. [July 27, 2020]; Available from: https://www.researchgate.net/publication/295859224_SIGRACETR_Gas_Diffusion_Layers_for_PEM_Fuel_Cells_Electrolyzers_and_Batteries_White_Paper.
[20] Mathur RB, Maheshwari PH, Dhami TL, Tandon RP. Characteristics of the carbon paper heat-treated to different temperatures and its influence on the performance of PEM fuel cell. Electrochimica Acta 2007;52(14):4809–17. https://doi.org/10.1016/j.electacta.2007.01.041.
[21] Chevalier S, Lavielle N, Hatton BD, Bazylak A. Novel electrospun gas diffusion layers for polymer electrolyte membrane fuel cells: Part I. Fabrication, morphological characterization, and in situ performance. Journal of Power Sources 2017;352:272–80. https://doi.org/10.1016/j.jpowsour.2017.03.098.
[22] Xie X, Wang R, Jiao K, Zhang G, Zhou J, Du Q. Investigation of the effect of micro-porous layer on PEM fuel cell cold start operation. Renewable Energy 2018;117:125–34. https://doi.org/10.1016/j.renene.2017.10.039.
[23] Forner-Cuenca A, Biesdorf J, Gubler L, Kristiansen PM, Schmidt TJ, Boillat P. Engineered Water Highways in Fuel Cells: Radiation Grafting of Gas Diffusion Layers. Adv Mater Weinheim 2015;27(41):6317–22. https://doi.org/10.1002/adma.201503557.
[24] Gerteisen D, Sadeler C. Stability and performance improvement of a polymer electrolyte membrane fuel cell stack by laser perforation of gas diffusion layers. Journal of Power Sources 2010;195(16):5252–7. https://doi.org/10.1016/j.jpowsour.2010.03.021.
[25] Gerteisen D, Heilmann T, Ziegler C. Enhancing liquid water transport by laser perforation of a GDL in a PEM fuel cell. Journal of Power Sources 2008;177(2):348–54. https://doi.org/10.1016/j.jpowsour.2007.11.080.
[26] Chun JH, Jo DH, Kim SG, Park SH, Lee CH, Lee ES et al. Development of a porosity-graded micro porous layer using thermal expandable graphite for proton exchange membrane fuel cells. Renewable Energy 2013;58:28–33. https://doi.org/10.1016/j.renene.2013.02.025.
[27] Im Kong M, Choi JW, Kim SI, Lee ES, Kim MS. Experimental study on the self-humidification effect in proton exchange membrane fuel cells containing double gas diffusion backing layer. Applied Energy 2015;145:345–53. https://doi.org/10.1016/j.apenergy.2015.02.027.
[28] Im Kong M, Jung A, Kim MS. Investigations on the double gas diffusion backing layer for performance improvement of self-humidified proton exchange membrane fuel cells. Applied Energy 2016;176:149–56. https://doi.org/10.1016/j.apenergy.2016.05.057.
[29] Kahveci EE, Taymaz I. Experimental study on performance evaluation of PEM fuel cell by coating bipolar plate with materials having different contact angle. Fuel 2019;253:1274–81. https://doi.org/10.1016/j.fuel.2019.05.110.

[30] Wu J, Yuan X, Wang H, Blanco M, Martin J, Zhang J. Diagnostic tools in PEM fuel cell research: Part I Electrochemical techniques. International Journal of Hydrogen Energy 2008;33(6):1735–46. https://doi.org/10.1016/j.ijhydene.2008.01.013.
[31] Netwall CJ, Gould BD, Rodgers JA, Nasello NJ, Swider-Lyons KE. Decreasing contact resistance in proton-exchange membrane fuel cells with metal bipolar plates. Journal of Power Sources 2013;227:137–44. https://doi.org/10.1016/j.jpowsour.2012.11.012.
[32] Ye D, Gauthier E, Benziger JB, Pan M. Bulk and contact resistances of gas diffusion layers in proton exchange membrane fuel cells. Journal of Power Sources 2014;256:449–56. https://doi.org/10.1016/j.jpowsour.2014.01.082.
[33] Millichamp J, Mason TJ, Neville TP, Rajalakshmi N, Jervis R, Shearing PR et al. Mechanisms and effects of mechanical compression and dimensional change in polymer electrolyte fuel cells – A review. Journal of Power Sources 2015;284:305–20. https://doi.org/10.1016/j.jpowsour.2015.02.111.

Chapter 2: State of the art, effects of mechanical compression on GDL physical properties.

This chapter is a review of the different studies and findings with regards to the effect of compression on the GDL's performance, especially electrical properties. The origins of mechanical constraints in PEMFCs are reviewed, followed by the impact of these constraints on the physical properties of GDL. It also presents the usefulness of measuring these properties and a theoretical background on how to do these measurements. The experimental means used to investigate these electrical properties are analysed.

2.1 Types & origins of mechanical compression

The origins of mechanical stresses in PEMFCs can be classified globally into external stresses engendered by the clamping procedure and the working environment, and internal stresses caused by FC operating conditions.

Starting by the main external sources of constraints, FCs need to be clamped to avoid gas-sealing failure and also to decrease electrical and thermal contact resistances between its components. There are multiple clamping ways that are used for FC stacks such as tie-rods and bolts. Millichamp J. et al [1] reviewed stack compression methods and classified them to uniform pressure, dynamic capable and controllable compression methods. They cited the advantages of each compression method. The typical clamping methods are presented in fig. 2.1. The pressure distribution engendered by clamping depends on the used method, the mechanical and geometrical properties of the cell components (thickness, compression modulus…) and the design of the stack (number and position of cells, gaskets, BPP design… etc). The cell is also subject to other external mechanical excitations that will vary depending on the type of transport applications and its working environment such as car bumps, crashes, and all dynamic loads that transport vehicles are subjected to [2] . This environment engenders static and dynamic loads. Different random dynamic load signals, which can be transferred to a cell in a car, have been collected by Hou Y. et al. [3] and the impact of dynamic loads on the FCs has been studied by several authors in the literature [2–12].

Considering internal stresses, the FC operating conditions such as the increase in temperature, the freeze / thaw cycling [13] and the water management generate dimensional changes of cell components. These are the main causes of internal stresses [2,14,15]. Water accumulation leads to a swelling of the membrane and drying leads to its shrinking. Stresses caused by water content [16] and thermal expansions [17] have been simulated and their influences on the performance of FCs have been analysed. To some degree, the pressure of the reactant gases will also enhance the internal constraints.

These various internal and external loads generate an unsteady state of stress inside the FC, especially on the GDL - BPP interface. Besides, because of the nature of the BPP geometry and the GDL structure, the pressure distribution is inhomogeneous. Further, considering the sensitivity of GDL mechanical behaviour with the history of loading, the effect of compression needs to be studied under cyclic compression.

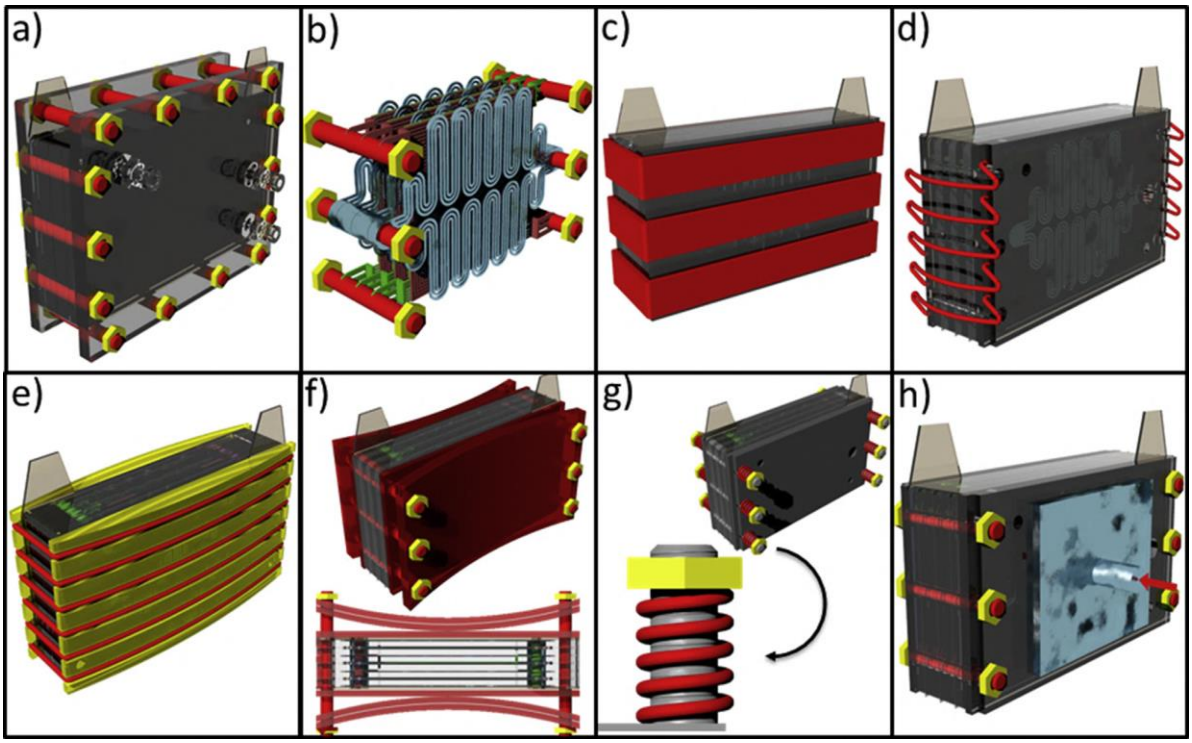

Fig 2. 1: Typical clamping methods [1].

2.2 Effects of mechanical compression on GDL

2.2.1 Mechanical behaviour of GDL

2.2.1.1 Stress-strain constitutive law

The analysis of GDL compression is of paramount importance as this component is responsible for keeping the heart of the FC (the Catalyst Coated Membrane) functional by undergoing mechanical compression. The porous and fibrous structure of a GDL, as well as its very small thickness compared to its other dimensions, engenders anisotropic, inhomogeneous, and non-linear physical properties. Regarding its mechanical behaviour properties, this is translated by a non-linear stress-strain curve with a non-constant and anisotropic Young's modulus [18] as well as a strain hysteresis (sensitivity to the history of applied stresses).

The analysis of the stress-strain curves of GDLs from several authors leads to consider a non-constant compression modulus, which results in a non-linear curve. Several authors have also developed analytical models of this modulus. Mishra et al. [19] noticed that the stress-strain curve can be divided into three linear elastic regions of compression with different Young's Modulus for carbon paper type GDLs, and four linear regions for carbon-cloth type GDLs. Roohparvarzadeh S. [20] analysed and divided this curve into three regions: a short linear region, followed by a non-linear region, then a linear region after 1 MPa. The author has extracted a global polynomial stress-strain relation, and a linear relationship after 1MPa. As in [20] , Norouzifard V. et al. [21] have also confirmed a linear region above 1 MPa of compression. They have developed a model that predicts the mechanical behaviour of the GDL under static compressive forces (see Equation (2.1)). Their model integrates pore size distribution and porosity rate, which are estimated by a microscopy optical analysis and statistical calculations.

$$\sigma = \frac{105\pi Ee}{16\left(\frac{l}{d}\right)^{5}_{eff}} + C \qquad (2.1)$$

With

σ: Stress (MPa).

E: Carbon fibre elastic modulus (MPa).

e: Compressive strain (-).

l: Unit cell length (mm).

d: Fibre diameter (mm).

C: Experimentally determined constant (MPa).

P.A. Gigos et al. [22] found that the GDL behaviour is related to the history of the applied solicitation. In order to consider the sensitivity of GDL to the history of loading and the variation of porosity as function of loading, the model from [21] has been further modified and developed for cyclic compression including the parameter related to porosity. It considers the residual strain resulting from cyclic hysteresis effect and the length between fibres (see Equation (2.2)). The mechanical behaviour of the GDL was stabilised after five cycles of compression due to the fibre rearrangement. Similar results were reported by A. El-Kharouf [23].

$$\sigma = \mu\frac{105\pi E}{16}\left(1 - \sqrt{\frac{\lambda P_0 - \varepsilon}{1-\varepsilon}}\right)^{5}(\varepsilon - \varepsilon_{res}) \qquad (2.2)$$

With:

σ: Stress (MPa).

E: Carbon fibre elastic modulus (MPa).

l: Inter-fibre length (m).

d: Fibre diameter (m).

μ, λ: Constants determined according to the loading-unloading cycles (-).

P_0: Initial porosity (-).

ε: Strain (-).

ε_{res}: Residual strain (-).

The effect of dynamic mechanical loading on the compression modulus of GDLs has been explored by Y. Faydi et al. [24]. The compression modulus is found non-linear and insensitive to the frequency of the dynamic excitation. In addition, this modulus increases with increasing static loads. It was also found that the hysteresis effect decreases when the dynamic load increases.

Anisotropy of the compression modulus is highly observed between in-plane direction (around 1-10 GPa [18]) and through-plane direction (1-10 MPa [18] and around 10-30 MPa in [20]). In the plane, the GDLs also are aligned in preferential directions (Machine & Cross Machine directions) where anisotropy is observed as well [18].

PEMFC environment implies an increase in temperature (60-90 °C) and a humid surrounding. Roohparvarzadeh S. [20] observed no significant effect of temperature on the stress-strain curve while humidity softens the GDL. In the other hand, PTFE was found to increase GDL rigidity [20]. Faydi Y. et al [24] found that compression modulus increase linearly with temperature until 280°C than it decreases linearly. Chen. Y [25] found that the compressive behaviour of GDLs is unchanged until 60°C, then GDLs compression resistance decreases at higher temperatures (90°C). Chien C et al. [17] have developed a 3D-FEM model of PEMFC assembled by 12-bolts to predict the effect of compression on the GDL and the PEM performance. They have simulated a static load (from 1 to 7 MPa) and a thermal load at the centre of the cell. They have detected the maximum deformation of the GDL at the centre of the BPP channel which was in accordance with a 2D model from the literature. It was shown that the deformation due to the smallest mechanical load is much larger than the deformation due to thermal load (four times greater). Sernican M.F et al. [16] studied the effect of water content in the membrane and the GDL rigidity properties. They simulated three configurations of GDL with an isotropic membrane. The first case is a soft isotropic

GDL, the second a rigid isotropic GDL, and the third an orthotropic more realistic GDL (rigid in-plane and less rigid through-plane). They studied multiple water distribution scenarios. The results show that there is a difference when considering an isotropic GDL from real anisotropic properties of the GDL. The soft GDL has the same deformation shape as the orthotropic GDL, and this is due to the dimension ratios favouring a bigger through-plane direction. A close GDL displacement shape between the through-plane water content variation and constant water content is reported, because in both cases water distribution at the membrane-GDL interface is constant.

Fatigue endurance is a significant mechanical property that directly affects service life of the FCs. Dominguez Almaraz G.M. et al. [26] have examined this property with a carbon paper sheet used for GDLs. They have used ultrasonic fatigue testing method. The lifespan of the material decreases when stress increases. The study concluded that crack initiating is related to the debonding at the fibre-matrix interface and to the plastic deformation of the matrix while the crack propagation is caused by high shear stress.

2.2.1.2 Pressure distribution resulting from clamping

In FCs, pressure distribution on GDL should be uniform as inhomogeneous pressure distribution creates hot spots and inhomogeneous current distribution may increase the voltage losses.

Bates et al. [27] found that pressure distribution is not uniform in a single cell. A higher stress is noticed at the edge of the GDL and almost no stress at its centre. Whereas in the stacks, pressure distribution and stress magnitude depend on the location of the cell along the stack axis. Stress magnitude is higher in the GDLs located at the centre-cells of the stack while pressure distribution is more uniform at the GDLs in the cells near the endplates of the stack. Pressure distribution uniformity was found to increase with higher clamping torques, longer preloading times and the use of centre loads which also increased stress magnitude. The stress magnitude is globally higher in the GDLs of single cells. This magnitude depends on the type and thickness of GDL, and on the type and thickness of gasket as gasket were found to withstand most of the clamping pressure (because of their higher young modulus). Stress magnitude was found 10 times higher on gaskets compared to GDLs, and on the type and thickness of GDLs. Actually, the thick MPL coated GDLs held more stress than the thin uncoated ones.

To enhance pressure distribution, Alizadeh E. et al. [28] have developed a new clamping mechanism based on a pocket endplate system. This double endplate is

made of an outer plate and an inner plate that is pushed by pressurised air playing the role of a piston that compresses the whole area of the BPP whereas the outer plates act like a cylinder. By decreasing the high pressure at the edge of the GDL and increasing the low pressure at its centre, this mechanism provides a more uniform pressure distribution with a range of: 1.4-2 MPa compared to a range of 0-4.8 MPa in the traditional systems. Ahmad M. et al. [29] have also studied a new FC compression rig that uses a compression block stressed by a hydraulic press. They observed a non-symmetric pressure distribution and as in [27,30], they found a more uniform pressure distribution for higher clamping force. The model was developed to find the best clamping torque for an optimal GDL compression ratio. Other novel clamping mechanisms, that enhance pressure distribution are reviewed by [1].

2.2.1.3 Optimal clamping pressure

Defining the optimal compression pressure is one of the major issues in PEMFC optimisation. Several performance parameters are directly related to this value. The best pressure level should ensure tightness of the cell and a uniformly distributed pressure to avoid hot spots and mechanical damage, to sufficiently reduce electrical and thermal resistances, particularly interface resistances, and thus decrease ohmic losses. At the same time, this pressure should keep enough porosity for reactant flow. There are multiple clamping methods and several possible configurations of stacks, making it hard to compare the clamping compression level (force, torque, pressure). Finding the optimal GDL compression level is more relevant as all the systems can be controlled with regards to this parameter.

Using their previous model validated by experiments, Ahmad M. et al. [29,31], have predicted a best performance at 16.7 MPa of clamping pressure corresponding to a 1.55 MPa GDL stress. Ul Hassan N. et al. [30] have undertook an experimental investigation to determine this best torque. They found that the highest polarisation curve was found at 1.5 N.m and this matched with the most uniform pressure distribution. With the help of their FEM model developed to study effect of bolt pre-loading in PEMFC, Chien C. et al [17] have determined an optimal clamping pressure of 4 MPa corresponding to a maximum stress of 2.66 MPa on GDLs. This pressure was selected as a trade-off between a decrease of GDL / BPP contact resistance and a diminution of GDL porosity with compression increase.

2.2.1.4 Mechanical behaviour characterisation

Table 2.1 summarises methods used to characterise the mechanical compression on GDL mechanical properties. The different compression modulus models, pressure distribution and optimal pressure determination methods used in literature are depicted. The pressure distribution and GDL types are mentioned.

Property studied	Mechanical solicitation	Type of experiments and other properties studied	GDL used and active area	Results	Ref
- GDL mechanical behaviour under compression	- Static and cyclic compression - Temperature and humidity	- Analytical model validated by experimental and literature data (Ex-situ)	- Carbon paper: SpectraCarb-2050A Toray H 120	Analytical model with a linear fit above 1 MPa: Constants for Polynomial Curve Equation $\sigma = C_1\varepsilon^4 + C_2\varepsilon^3 + C_3\varepsilon^2 + C_4\varepsilon + C_5$ Linear Fit $\varepsilon = \frac{\sigma - b}{E}$	[20]
- GDL mechanical behaviour under compression	- Static load (0-2 MPa)	- Analytical model validated by experimental and literature data (Ex-situ)	- Carbon paper: SGL (24 AA* /25 AA*/10 BA) TGP (H-60/H- 120)	- Developed an accurate analytical model above a 1 MPa compression: $\sigma = \frac{105\pi Ee}{16(l/d)_{eff}^5} + C$ With: $\left(\frac{l}{d}\right)_{eff} = \left(\frac{\mu_f^3 \mu_{A_{pore}}}{\varepsilon\mu_d^5\left(1+6C_f^2\right)\left(1+6C_d^2\right)}\right)^{\frac{1}{5}}$	[21]
- GDL mechanical behaviour under compression	- High cyclic compression loads (10 cycles of 0-7 MPa followed by 10 cycles of 0-12 MPa)	- Analytical model validated by experimental data (Ex-situ)	- Straight carbon fibre paper: with/without PTFE and with/ without MPL. (SGL 24 AA/24 BA/ 24 BC)	- Stabilisation of mechanical behaviour after five cycles of compression - Analytical model: $\sigma = \mu\frac{105\pi E}{16}\left(1-\sqrt{\frac{\lambda p_0 - \varepsilon}{1-\varepsilon}}\right)^5(\varepsilon - \varepsilon_{res})$	[22]
- GDL Mechanical behaviour under compression	- Dynamic excitation (static load from 6-60N) with a dynamic amplitude of 4 N for 10 s. - Frequency from (10-100 Hz)	- Experimental study (Ex-situ)	Carbon paper with PTFE and MPL: SGL 24 BC	- Compression modulus increased non-linearly (from 60 MPa at 1.5 MPa compression to 1683 MPa at 10 MPa compression) - Hysteresis decreased when increasing dynamic load.	[24]
- GDL mechanical behaviour: - Fatigue endurance - Crack initiation and propagation	- Ultrasonic fatigue endurance testing (dynamic excitation of a GDL specimen at resonance frequency (20 kHz) - The displacement applied at the edge was linearly related to the static neck section's stress that consequently ranged in 110-170 MPa.	- Experimental study (Ex-situ)	- Straight carbon fibre paper of 0.3 mm thickness (Freudenberg)	- Material lifetime is $3x10^8$ with a neck stress of 170 MPa and $4{,}5x10^9$ at 117 MPa.	[26]

- GDL mechanical behaviour	- Static pressure (1-7 MPa) -Thermal loading at the centre of the cell	- FEM Model Others: Optimal clamping pressure	- Represented by a graphite composite material (0.35 mm thickness, E= 10 MPa) S=64 cm2	- Linear increase between GDL CR and clamping - Optimal clamping pressure 4 MPa	[17]
- GDL and membrane mechanical behaviour under compression and water content	- Stress due to water content.	- FEM simulation	Carbon fibre paper: TGP H-60	- Deformation of a less rigid isotropic GDL is closer to the real orthotropic GDL. - Water content gradient creates the same stress gradient at the membrane.	[16]
- Pressure distribution over the cell/ stack especially on the GDL	A static clamping torque 10.17 Nm than different central loads and different application durations.	- Simulation + Experimental testing (Ex-situ, or offline)	- Carbon fibre paper with/ without a MPL -S=100 cm2	- In a GDL, stress is higher at the edge and almost zero at the centre. - Stress magnitude is higher in GDLs located at the centre of the stack - Stress distribution is more uniform at GDLs located near the endplates of the stack.	[27]
- Pressure distribution (novel mechanism for uniform pressure distribution)	- Static compression: 7 bars (for pneumatic) 13 Nm (for conventional)	Experimental and FEM Simulation	- GDL Carbon fibre paper (0.235 mm, E=0.01 GPa) BPP : Graphite (3.5 mm, E=5.1 GPa) - S=225 cm2 - End plates (Alu, 30 mm)	- The new clamping mechanism gives better pressure distribution	[28]
- Pressure distribution and clamping process	-Static pressure provided by a hydraulic press: 10, 20 and 30 MPa	- Model development, simulation and experimental validation -Others: best clamping pressure	SGL GDLs (0.3 mm) with E= 8MPa S=158 cm2	- Pressure distribution is not symmetric. - Model validated for optimal pressure prediction by polarisation data in [31]	[29,31]
- Polarisation and power curves	- Static compression load: application of a torque (0.5-2.5 Nm) on the eight bolts of the cell	Experimental (In-situ and Ex-situ) Others: -Pressure distribution -Electrical contact resistance (no result mentioned)	Carbon fibre paper -S=20 cm2	- Best electrical performances and pressure distribution at clamping torque value of 1.5 Nm.	[30]

Table 2. 1: Summarised studies on mechanical properties

2.2.2 GDL morphology

The studies concerning the compression impact on the GDL microstructure show that the essential parameters such as porosity, tortuosity, permeability, surface roughness and all geometrical and physical parameters of the interface, are impacted by the mechanical loading. It is important to consider these parameters as they have a direct impact on the functionality of the GDL and therefore on the performance of PEMFC. Prass S.et al [32]. found that the gaps which were formed between the CL and the MPL depended on the roughness and irregularities of their surfaces. They decreased with compression and a good contact between the CL and the MPL can be achieved as long as the roughness of the surfaces is similar. Zenyuk I.V. et al. [33] used X-ray computed tomography (CT) to study the effect of compression over a range of commercial GDL samples. They found that the compression decreased the porosity for all the GDLs. Banerjee R. et al. [34] studied the impact of rib-channel compression on the GDL porosity distribution via X-ray computed tomography. They found that, under the channel, the porosity profile looks almost like an uncompressed GDL. Under the land region, the GDL thickness decreased. They also found that the fibrous porous transport layer PTL side was the most compressed side compared to the MPL that acted like an incompressible matter. Holzer L. et al. [35] studied the effect of compression on the micro-structure of a GDL. They found that the gas diffusivity varies with compression because of the porosity and geodesy tortuosity change. They also found that through-plane permeability was slightly higher than the In-plane one. For the electrical conductivity, the anisotropy was found to be following the tortuosity (being higher for the through-plane) direction.

2.2.3 GDL thermal properties

GDL compression in FCs also affects its thermal properties such as the thermal conductivity. This property was found to be anisotropic. Thermal conductivity increases with compression [36–42] and decreases with temperature [37,39]. A large part of the thermal resistance is due to the thermal contact resistance [37,40,41]. Yablecki J. et al. [36] found an almost linear increase in the effective thermal conductivity of paper GDLs with the increase of pressure and GDL thickness. The thermal resistance was found to be sensitive to the cycles of compression and the stability is reached after five cycles of compression [38]. This hysteresis effect is more important on the thermal contact resistance compared to bulk resistance [38].

Alhazmi N. et al [39] have noticed that the through-plane thermal conductivity of the GDL increases with an increasing compression and decreases with temperature. This conductivity was lower than the in-plane conductivity of the GDL. Thermal resistance is higher for PTFE treated GDLs. They have noticed that thermal conductivity increases with the presence of MPL. Burheim O. S. et al. [43] has investigated a MPL coated GDL which was divided into three regions the PTL: fibrous Porous Transport Layer part of the GDL, the MPL (MicroPorous Layer), and a composite region [43] (i.e. the contact region between the PTL and the MPL). They found that the thermal conductivity of the composite region is higher than the conductivity of the PTL, which is also higher than the MPL conductivity. Sadeghifar H. et al. [41] found that the thermal GDL-BPP contact resistance decreases with compression, and increases with both MPL and PTFE. Loading-unloading cycles reduce considerably the total thermal BPP-GDL resistance [41]. This reduction is more pronounced for GDLs with lower PTFE rate. Unsworth G. et al [40] have noticed that MPL thickness and thermal resistance remain unchanged until a 1.5 MPa-compression.

2.2.4 GDL electrical properties

Compression pressure influences the electrical properties of the GDL just as the structural and mechanical properties. Both bulk and interface properties of the GDL are impacted by compression. These properties will directly impact the produced electrical power. First, let us define the resistivity, which is the most important property studied:

2.2.4.1 Definitions

Electrical resistivity

The electrical resistivity of a material is its property to oppose the passage of the electrical current through its volume. This property is directly related to the composition and structure of the material. For a simple homogeneous isotropic material, we have Equation (2.3).

$$\rho = \frac{U.A}{I.t} \tag{2.3}$$

With

ρ: electrical resistivity (Ohm.m).

U: Electrical Potential (V).

I: Current Intensity (A).

A: Current cross section (m^2).

t: thickness (m).

Anisotropic material will react differently according to the current passage direction and to the potential field direction of measurements. So that the electrical resistivity of a material can be represented with a 2 D-tensor as in (Equation 2.4).

$$\vec{E} = \begin{pmatrix} \rho_{xx} & \rho_{xy} & \rho_{xz} \\ \rho_{yx} & \rho_{yy} & \rho_{yz} \\ \rho_{zx} & \rho_{zy} & \rho_{zz} \end{pmatrix} \vec{j} \qquad (2.4)$$

With

$\vec{E}$: Electrical field (V/m).

$\vec{j}$: Electrical current density (A/m^2).

ρ_{ik}: Resistivity to current passage in direction "k", for an applied potential in direction "i" (Ohm.m).

This tensor is symmetrical (ρ_{ik}=ρ_{ki}), in most cases [44]. This means that the knowledge of six values allows to completely characterize the materials resistivity. This also means that this tensor is diagonalizable and that a coordinate system exists where only three principal resistivities will represent the resistivity tensor (2.5).

$$\vec{E} = \begin{pmatrix} \rho_1 & 0 & 0 \\ 0 & \rho_2 & 0 \\ 0 & 0 & \rho_3 \end{pmatrix} \vec{j} \qquad (2.5)$$

The through-plane (through thickness) direction of the GDL is taken as a principal direction because of the structure of the GDL. Fig 2.2 represents the in-plane and through-plane direction. The scientists often measure areal specific through-plane resistance of GDL (mOhm.cm^2) instead of through-plane resistivity (mOhm.cm) (The link between these two parameters is the thickness of GDL.). There are two reasons for this choice:

- it is easier to measure the areal specific resistance as we do not have to measure the thickness,
- the through-plane resistance is often compared to the contact resistance of the GDL (mOhm.cm^2) with its neighbouring components, as these two resistances are in series under the rib.

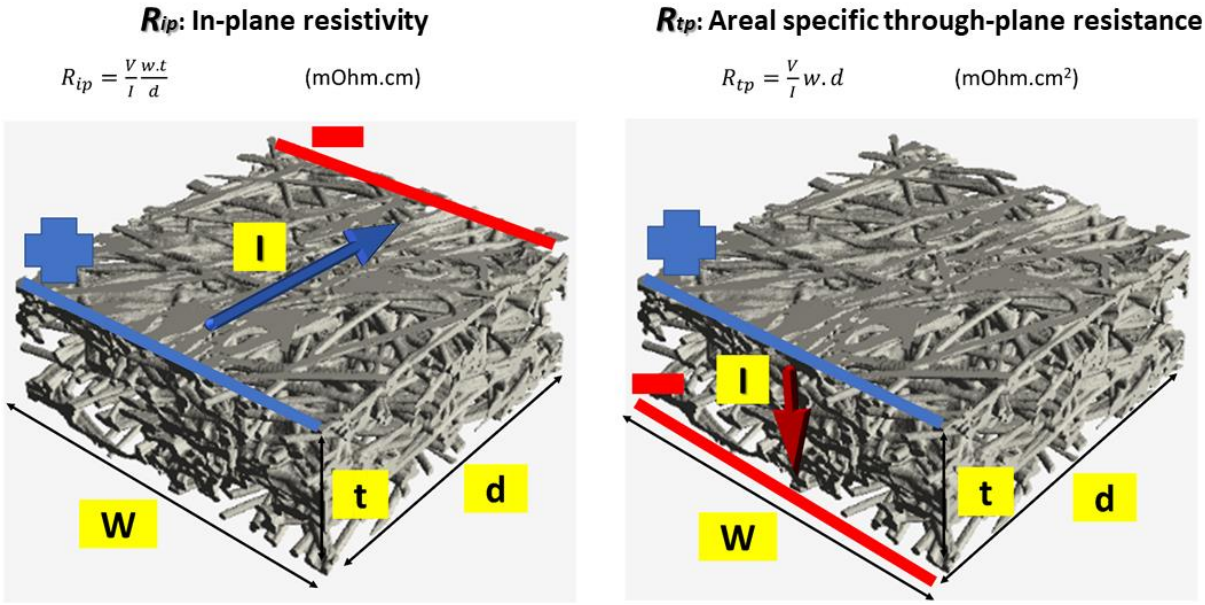

Fig 2. 2: Anisotropy of electrical resistivity of GDLs (www.geodict.com, modified).

The contact resistance represents the difficulty of the electrical charges to pass through one contact surface between two bulk elements. As the contact surfaces are rough and made of asperities, the actual contact area is lower than the apparent contact area. The result is an increase in electrical resistance. This is even worse for GDLs, which are porous fibre composite materials with a much smaller contact area. The mechanical compression increases the actual contact area by flattening the asperities and, in the case of GDL, by increasing the number of fibres in the contact surface [45].

Theoretically, we can define the electrical interface resistivity ρi as expressed in (Equation 2.6) [46] :

$$\rho_i = \frac{\partial V}{\partial J}\Big|_{A\to 0} \qquad (2.6)$$

Where:

ρi : theoretical interface resistivity (mOhm.cm²)
J: *Current density at the contact* (A/cm²)
V: *Voltage* (V)
A: *Contact area.* (cm)

At the difference of bulk resistivity, interface does not have a thickness, and the resistivity is in mOhm.cm^2.
Nevertheless, we cannot measure this quantity, and even in theory, it is difficult to calculate it [47]. Therefore, scientists had defined a measurement quantity that should be close to this interface resistance and this quantity is the specific electrical contact resistance ρc (mOhm.cm^2) [48].
It is defined as:

$$\rho_c = \lim_{\Delta A_c \to 0} (R_c . \Delta A_c) \qquad (2.7)$$

With:

Ac: $Contact\ area$ (cm^2).
ρc: specific electrical contact resistance (mOhm.cm^2)
When the contact is homogenous and the current density is constant, ρc becomes [48]:

$$\rho_c = R_c . A_c \qquad (2.8)$$

GDL Electrical Resistivity

Two main GDL electrical properties are characterised: bulk resistivity and contact resistance with the adjacent components. Defining all the coefficients of the resistivity tensor is a tough task. Therefore, determining a mean bulk resistivity as a first approach can be useful. A common method consists of considering the GDLs as isotropic and estimating the resistivity by the mean of carbon fibre and air resistivities considering the structure porosity.
Globally, the electrical conductivity of the GDL is found to increase with compression [17] while porosity decreases. However, it is important to consider the direction dependence of the electrical resistance. Further, due to the structure of the GDL, this conductivity/resistivity is anisotropic. In [49], the through-plane and in-plane conductivities of carbon paper GDLs were numerically estimated in terms of the porosity. The through-plane conductivity was found to be lower than the in-plane one. These results agree with experimentally measured conductivities with different porosity rates resulting from compression. M.S. Ismail et al. [50] also estimated the effect of GDL anisotropy by comparing isotropic/anisotropic cases. Their model shows that considering isotropic GDLs would over/underestimate the average current density (23–30%). The current density

distribution was more uniform for anisotropic GDL and the in-plane anisotropy found in [51] had no significant impact on FC performance.

2.2.4.2 Effect of compression on in-plane resistivity

Regarding in-plane resistivity, most studies found that the in-plane resistivity decreases with mechanical compression [42,45,52–54]. The increase of this conductivity is non-linear with a higher influence of the smallest pressure values [42].

The in-plane resistivity is lower than the through-plane one. It can be explained by the fact that electrons travel easier along the GDL fibres located in the plane than from one fibre to another situated in the next plane.

Due to the manufacturing process, most GDLs are also anisotropic in the plane [45,52–54]. In-plane resistivity is lower in the machine direction [45] or the fibre alignment direction [54].

In [54] the authors studied the evolution of Rip with the cycles of compression. Rip is found to increase along the cycles of compression.

Basically, Rip influences the contact resistance between the GDLs and the BPP [45,55].

2.2.4.3 Effect of compression on through-plane resistivity

According to the definition of resistivity, the through-plane resistance (or resistivity) is the material capacity to oppose the current travel inside the matter along the axis of the cell. This property of the material is sensitive to compression. Through-plane resistance decreases non-linearly with compression [18,45,52,54,56]. Aydin O. et al. [52] noticed that the resistivity of the felt-carbon paper is higher than the straight fibre graphitised carbon paper. Miyazawa A. et al. [45] found that the contact resistance of the GDLs was smaller than the through plane resistances, and was independent from initial thickness for all GDLs whether the through-plane resistance (area specific resistance) is higher for GDLs with higher thickness. Through-plane GDL conductivity decreases with PTFE, slightly increases with humidity [56]. The through-plane conductivity of MPL is considerably smaller than that of GDLs [56].

2.2.4.4 Effect of compression on contact resistance

The electrical contact resistance is the resistance of electron passage through the interface of two neighbouring elements. Among the ohmic resistances, the contact resistance is reported to reach 50% of these losses [57]. This resistance includes the interfacial resistance between the GDL and the CL [18,58], the contact

resistance between the GDL and the BPP, subject of numerous scientific works, and the contact resistance between the BPP and the current collectors.

This electrical contact resistance was found to decrease with compression [45,56,59–68] non-linearly [56,59,61,65,66] and increase with a PTFE coating [23,56,59,60]. The increase is even greater for cloth GDLs [55]. Contact resistance of cloth GDLs is found higher for the knitted ones compared to the plain ones [19]. Ismail et al. [60] concluded that the mechanical compression reduces the contact resistance and related this observation with the variation of the GDL compression ratio. The presence of a gasket that is generally stiffer and thinner than a GDL limits the compression of GDLs. The GDLs with an initial thickness higher than that of the gasket have a higher level of compression and therefore a lower Rc. This is apparently even more crucial than the increase in Rc due to the PTFE ratio of the GDL. A higher PTFE ratio within the MPL decreases the contact resistance [60]. The presence of an MPL has been found to decrease the resistance [55,59].However, in [56], MPL dramatically increases the electrical contact resistance of GDLs. In [61], for high temperature (120°C-180°C) PEMFCs, the lowest Rc values, decreasing with the mechanical compression, were found for the highest temperature. Zhang et al. [62] found that the pressure [56,60] distribution has a little effect on Rc but affects the average pressure magnitude. Zhou P et al. [63] found that improving pressure distribution was estimated to have a small influence on the reduction of R_C (less than 30%). Contact resistance is also influenced by the BBP geometry. Lai X et al [64] found that increasing the rib round corner minimises Rc. Concerning the metallic BPPs, in [45], entists investigated different BPP coating (Au alone and AU-Ni). First, they found that AU-Ni coating has a smaller contact resistance compared to Au alone coating, which has a smaller Rc compared to a BPP without coating. Contact resistance [45] is related to in-plane resistance. Comparing through-plane resistance to contact resistance (Rc), most studies found that Rc is higher [19,66]. However, in [45], it was found that the contact resistance of the GDLs was smaller than the through plane resistances, especially for GDLs with a higher thickness.

2.3 Importance of analysing GDL electrical parameters under compression

The analysis of the effect of compression on GDL physical parameters, especially electrical properties, is essential to begin to establish the link between the physical properties of the FC constitutive components and its global performance. Analysing GDL resistivities under compression gives a first approach to explain

ohmic losses in FC as a large part of these losses is related to the GDL. A better understanding of ohmic losses is related to the capacity of relating the global resulting resistance and the variation of operating conditions such as compression, temperature, humidity, GDL and BPP structure and dimensions, etc... This is why it is important to have a database of the main GDL structures resistivities and their variation according to several operating parameters. These abacuses can be used in numerical models to define global performance parameters according to local variations of operating conditions. These models and abacuses can be used as a preliminary design tool for fuel cells.

2.4 Experimental tools used in measuring electrical properties of GDLs

Determining ohmic resistance starts by the measurement of the electrical parameters of the GDL. This consists of measuring its contact resistance with neighbouring components, its bulk resistivity, through-plane resistivity which is in series with the contact resistance and in-plane resistivity which is the main conductor under the channels of the BPP. The difficulties of measurement are related to the variation of GDL dimensions with compression. It is a challenge to deconvolute contact resistance and through-plane resistance.

2.4.1 Measurement means of contact resistance

Three main methods are used to determine the contact resistance.

A subtraction method [45,68] can be used by measuring the electrical resistance of two assemblies in such a way that the difference between the assemblies' resistances gives the desired contact resistance. However, most studies that used this method neglect either the bulk resistance or its variation with compression. Another problem is the difficulty of using this method with GDLs having non-identical sides such as one side MPL coated GDLs. Better results can be obtained if the bulk resistivity is measured using special pins or micro-probes that exclude contact resistance with electrodes [45,52,69].

In a second method, the contact resistance is determined by a numerical or experimental estimation that can be achieved using results of the subtraction method. For instance, in [67], T. J. Mason et al. estimated this contact resistance, by placing a GDL between two compressed BPPs and by measuring the resistance under compression. The entire resistance is attributed to the contact resistance. An estimation process can also be used to determine the variation of the through-plane resistance of the GDL with compression, from its porosity such as in the work of M.S. Ismail et al. [60]. A numerical model can also be set to obtain the global

contact resistance using experimental results for instance with a flat graphite plate [62–64].

A third method consists on the use of the Transmission Line Method (TLM) [55,59], that allows a direct experimental determination of the contact resistance of each side of the GDL. This method, initially used to measure Rc between metals and semi-conductors, is based on the fact that the total resistance between two metals related by the semi-conductor will grow linearly with the distance between the metallic contacts (because of the bulk resistance of the semi-conductor that is proportional to its length). The offset of the line curve is the contact resistance that will not vary with the distance between the metals. Fig. 2.3 exhibits the different measurement methods of contact resistance.

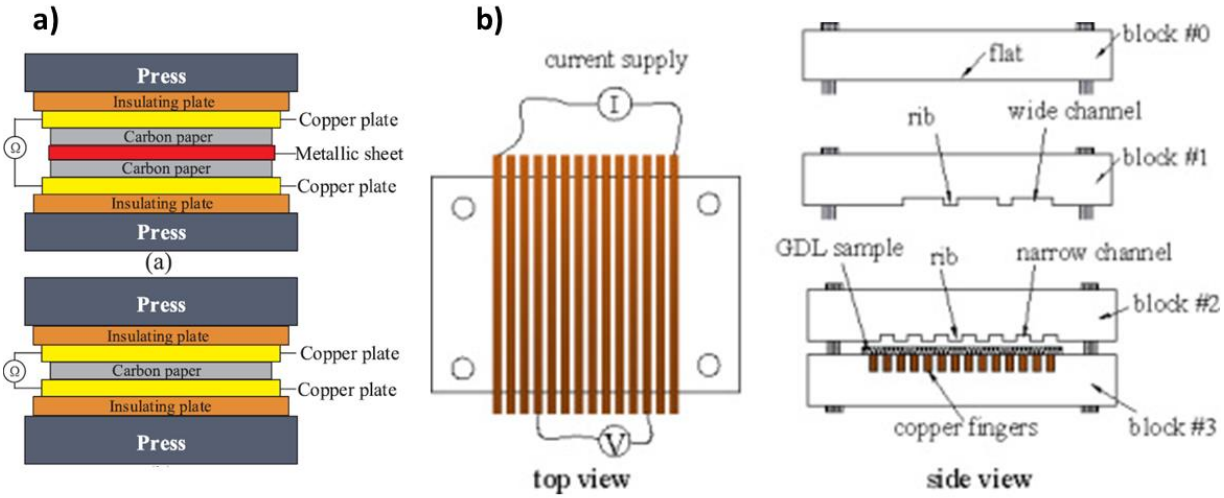

Fig 2. 3: Resistance contact measurement methods a) Example of subtraction method [72], b) Example of Transmission Line Method [55].

2.4.2 Measurement means of through-plane resistance.

The determination of through-plane resistivity is subject to the contact resistance with the electrodes. It is difficult to distinguish the through-plane resistivity from the contact resistance of the measurement mean. These can be minimised using four probe measurement method in order to avoid resistance of wires and electrodes. Golden coated electrodes can be used to decrease contact resistance with electrodes. O. Aydin et al. [52,53] presented the advantages and drawbacks of three methods of through-plane resistivity measurements that are depicted in Fig. 2. 4 using four probe measurement method: the gold electrode method, the gold flat contact pin method and the golden micro-wire probe method.

The first procedure involves a contact resistance (even small) between the electrodes and the GDL which impacts the accuracy of the measurement. However, this method is very rapid to implement.

In the second method, the area of contact is small (a 60 µm diameter contact pin) and consequently, the contact resistance is neglected. But the high isolation area creates a distortion in the equipotential lines. This phenomenon leads to the measurement of small inaccurate resistivities, which are not representative of the resistivity of the other zones far from the electrodes. This phenomenon is especially important for high in-plane resistivity and thin materials such as GDLs. However, this method is accurate for thick materials such as BPP graphite materials.

The last method using golden microwire probes is considered the most accurate. However, it is quite difficult to implement. The microelectrodes are quite fragile materials that need to be handled with great care, contact problems may appear for small compression pressures and other materials may stick on the surface of the wires. Microwires/probes are also used in [45,69]

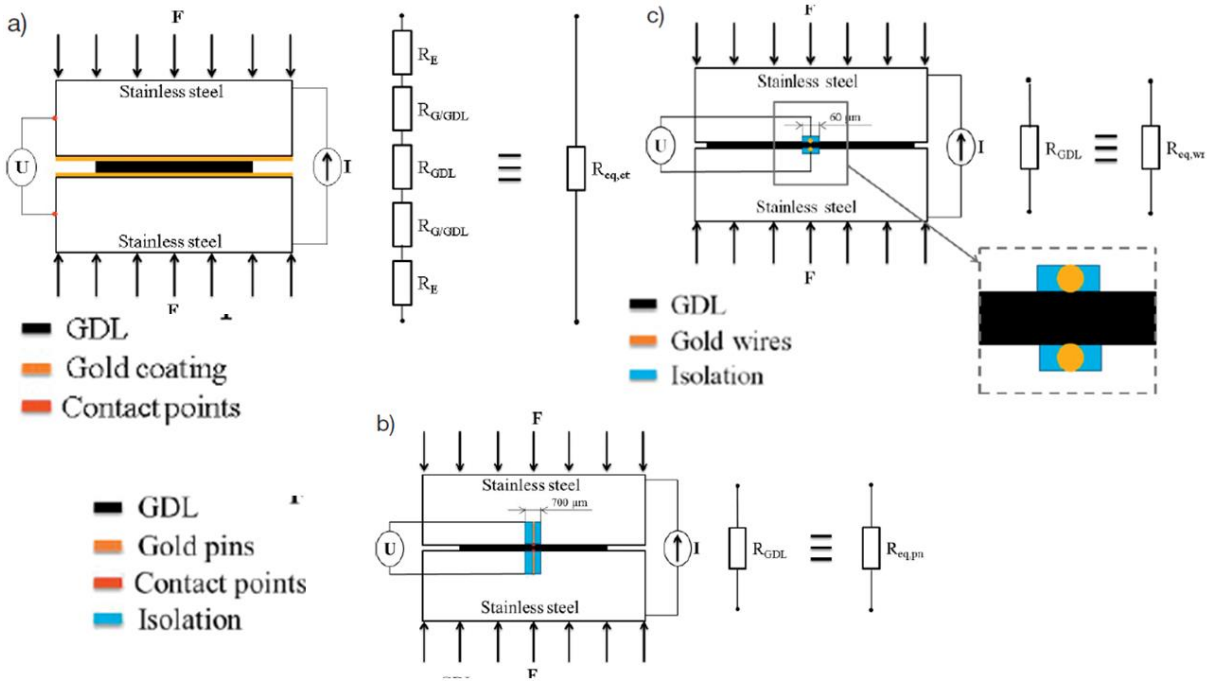

Fig 2. 4: Schematic of the three methods used in this study (a) gold-coated electrodes method; (b) pins method; (c) micro-wire probes method [52]

2.4.3 Measurement means of in-plane resistance.

In-plane resistivity is generally measured using a four-probe method. A current is applied between two points of a surface of a GDL and the voltage is measured

between two other points of the surface along that line. Ismail et al. presented such a measurement apparatus, shown in fig 3.5 [51]. Miyazawa A. et al. [45] measured in-plane resistivity in two principal plane directions using a four-probe method with varying the distance between the probes.

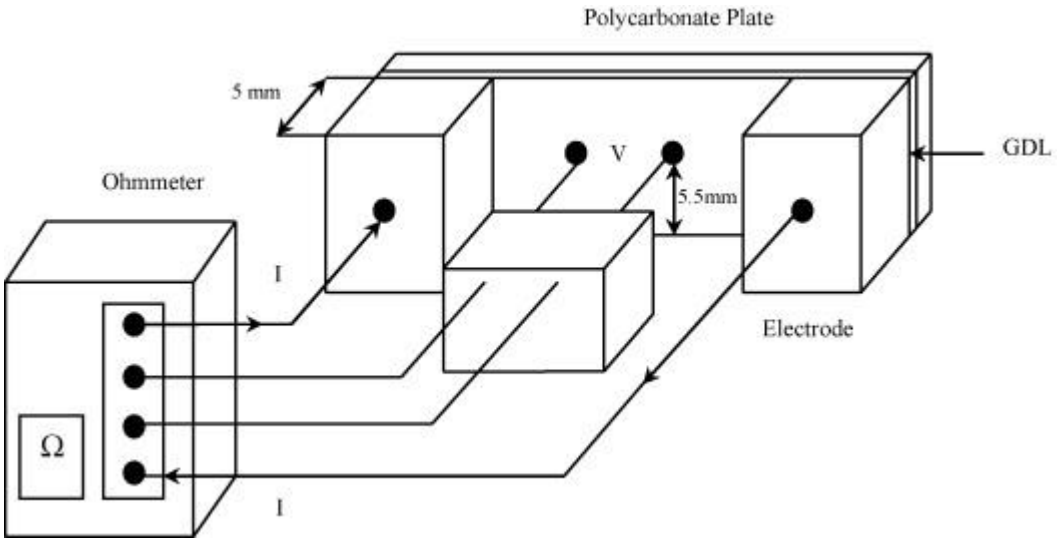

Fig 2. 5: Four Probe In-plane resistivity measurement device [51]

O. Aydin et al. [52,53] measured the in-plane resistivity. They used a four-point measurement method with small gold pins to avoid additional contact resistance. In order to take into account the inhomogeneity of the GDL structure, several points of measurement are used in diagonal, non-perpendicular to the equipotential lines as shown in fig. 2.6.

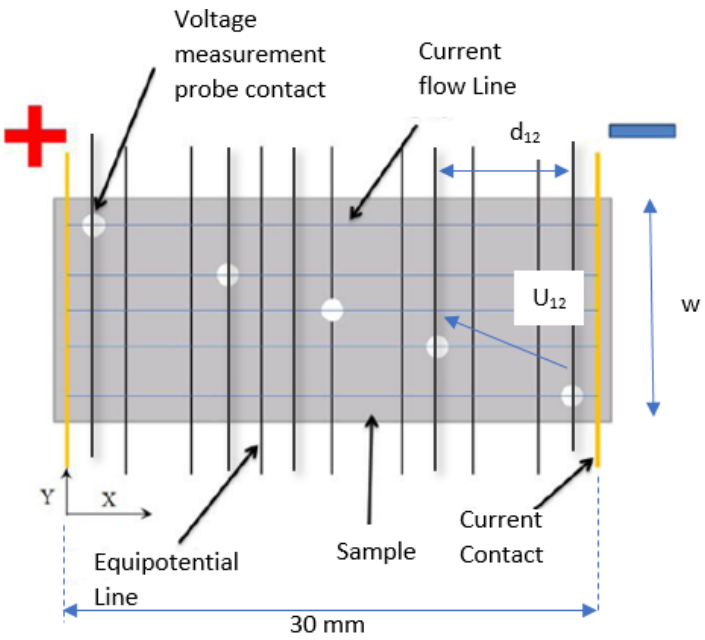

Fig 2. 6: In-plane resistivity measurement device [52]

Another method can be used to measure in-plane resistivity, called the Van Der Pauw method. As depicted in fig. 2.7, a four-point measurement method is developed to measure the in-plane resistivity of an isotropic sample. The measurement points with small contact area are generally equidistant and placed at the edges of the sample. The current is provided by two of the points (1, 2) and the voltage is measured between the two others (3, 4). Then the current is applied between 1 and 3 and measured between 2 and 4 as in fig. 2.7 [70] and characterisation chapter C, 9. By the resolution of equation (2.9,) a geometrical correction factor of the sample is finally obtained [42]

$$e^{\frac{-\pi R_A}{R_S}} + e^{\frac{-\pi R_B}{R_S}} = 1 \qquad (2.9)$$

With:

Rs: Sheet resistance (Ohm/square).

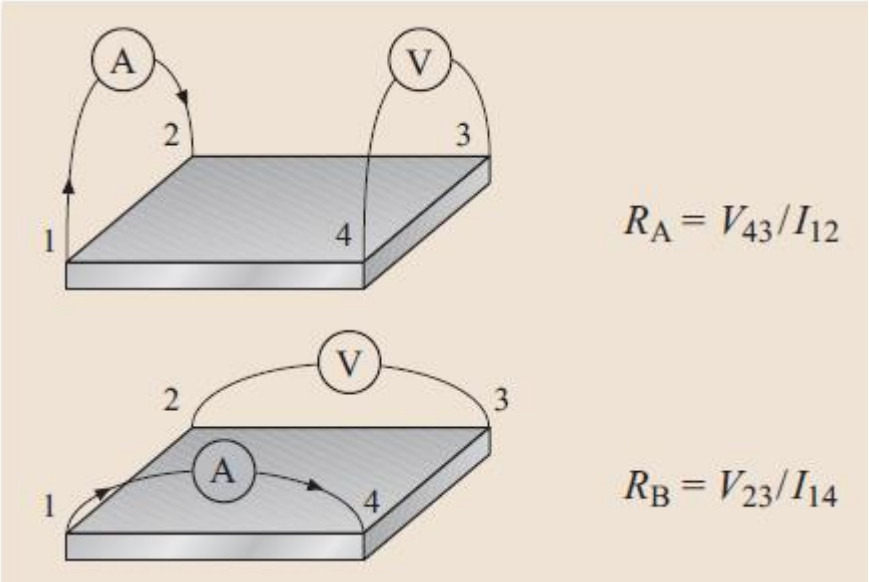

Fig 2. 7: Van Der Pauw method [70]

D. Todd et al. [54,71] measured through-plane resistivity and in-plane resistivities along the fibre and cross fibre direction using a square four-point-probe arrangement (4PP). The in-plane resistivity is measured in several angle directions to consider the anisotropy of the material (Machine and cross machine direction).

Finally the in-plane resistivity can be deduced from the Transmission Line Method as in Ye D. et al. [55]. The authors extracted the bulk resistivity from the slope of this curve using the GDL thickness, which represents the in-plane resistivity.

2.5 Analysis of research issues from literature and thesis roadmap

The performance of fuel cells is strongly related to the influence of mechanical compression. The gas diffusion layer is the most sensitive element to compression. Thus, a literature review of the electrical properties of the GDL under compression pressure has been put forward. Despite the large numbers of studies relating pressure to resistivity, very few studies use real cell operating conditions such as variable compression loads. There is a lack of knowledge of the effect of the different cycles of compression on the different electrical resistances of the GDLs and on its contact resistance with the BPP. Most GDL resistivities found are measured under static compression, and some few times on pre-conditioned GDLs. A lack of analysis is observed for the different electrical resistivities through the cycles of compression is observed. PEMFC operated at temperatures ranging from room temperature to 90°C, and under different humidity/saturated water conditions. However, most measurements of GDL electrical properties are done

under room temperature and dry conditions and there is a lack of analysis and experimental investigation on the effect of these parameters and on the evaluation of their contribution to electronic ohmic losses.

These gaps in GDL resistivity information limit the accuracy and scope of theoretical and numerical models of PEMFC performance that require experimental data for validation.

In the thesis, we aim to contribute to a better understanding of the origin of ohmic losses by associating the effect of operational conditions to the GDL electric resistivities. In order to enhance this knowledge, a wide range of experimental investigations is conducted on several structures of Gas Diffusion Layer, for different electrical resistances of the GDL under mechanical compression and under different operational conditions.

This research work is motivated by the need for data concerning GDL electrical properties under PEMFC operating conditions. This could help stack designers make early choices on GDL structure, composition, and thickness. This also contributes to the availability of input data for more complex Fuel Cell performance models.

The knowledge of the effect of temperature variation and humidity on the electrical resistance can also contribute to better understand the shape of the polarisation curve of the FC.

Decreasing ohmic resistances may contribute to higher fuel cell efficiency. A 1-3% increase in efficiency would not only result in lower hydrogen consumption but also in even more compact and cheaper FC systems.

There is also a lack of relationship between the different resistivities measured. A knowledge of these resistivities helps computing and comparing the cell global resistance and the ohmic losses (contact resistance, bulk resistance).

The aim of this thesis is to enhance the understanding of the influence of real-life operating conditions of a fuel cell on electrical resistivity. The goal is to link these operating conditions and their influence on component properties to the global fuel cell performance.

The electrical properties of some carbon paper GDLs must be analysed under different experimental conditions (cyclic compression, temperature, humidity). The composition of the GDLs and the influence of their structure need to be considered and related to the technical requirements of fuel cells for various applications: for example, the use of GDLs less sensitive to cycles of compression in transport application.

2.6 References

[1] Millichamp J, Mason TJ, Neville TP, Rajalakshmi N, Jervis R, Shearing PR et al. Mechanisms and effects of mechanical compression and dimensional change in polymer electrolyte fuel cells – A review. Journal of Power Sources 2015;284:305–20.

[2] Banan R, Bazylak A, Zu J. Combined effects of environmental vibrations and hygrothermal fatigue on mechanical damage in PEM fuel cells. International Journal of Hydrogen Energy 2015;40(4):1911–22.

[3] Hou Y, Zhou B, Zhou W, Shen C, He Y. An investigation of characteristic parameter variations of the polarization curve of a proton exchange membrane fuel cell stack under strengthened road vibrating conditions. International Journal of Hydrogen Energy 2012;37(16):11887–93.

[4] Liu B, Liu LF, Wei MY, Wu CW. Vibration mode analysis of the proton exchange membrane fuel cell stack. Journal of Power Sources 2016;331:299–307.

[5] Rouss V, Lesage P, Begot S, Candusso D, Charon W, Harel F et al. Mechanical behaviour of a fuel cell stack under vibrating conditions linked to aircraft applications part I: Experimental. International Journal of Hydrogen Energy 2008;33(22):6755–65.

[6] Hou Y, Hao D, Shen C, Shao Z. Experimental investigation of the steady-state efficiency of fuel cell stack under strengthened road vibrating condition. International Journal of Hydrogen Energy 2013;38(9):3767–72.

[7] Hou Y, Zhou W, Shen C. Experimental investigation of gas-tightness and electrical insulation of fuel cell stack under strengthened road vibrating conditions. International Journal of Hydrogen Energy 2011;36(21):13763–8.

[8] Deshpande J, Dey T, Ghosh PC. Effect of Vibrations on Performance of Polymer Electrolyte Membrane Fuel Cells. Energy Procedia 2014;54:756–62.

[9] Hou Y, Hao D, Shen J, Li P, Zhang T, Wang H. Effect of strengthened road vibration on performance degradation of PEM fuel cell stack. International Journal of Hydrogen Energy 2016;41(9):5123–34.

[10] Banan R, Bazylak A, Zu J. Effect of mechanical vibrations on damage propagation in polymer electrolyte membrane fuel cells. International Journal of Hydrogen Energy 2013;38(34):14764–72.

[11] Liu B, Wei MY, Zhang W, Wu CW. Effect of impact acceleration on clamping force design of fuel cell stack. Journal of Power Sources 2016;303:118–25.

[12] Wang X, Wang S, Chen S, Zhu T, Xie X, Mao Z. Dynamic response of proton exchange membrane fuel cell under mechanical vibration. International Journal of Hydrogen Energy 2016;41(36):16287–95.

[13] Dafalla AM, Jiang F. Stresses and their impacts on proton exchange membrane fuel cells: A review. International Journal of Hydrogen Energy 2018;43(4):2327–48.

[14] Kusoglu A, Karlsson AM, Santare MH, Cleghorn S, Johnson WB. Mechanical response of fuel cell membranes subjected to a hygro-thermal cycle. Journal of Power Sources 2006;161(2):987–96.

[15] Kusoglu A, Karlsson AM, Santare MH, Cleghorn S, Johnson WB. Mechanical behavior of fuel cell membranes under humidity cycles and effect of swelling anisotropy on the fatigue stresses. Journal of Power Sources 2007;170(2):345–58.

[16] Serincan MF, Pasaogullari U. Effect of gas diffusion layer anisotropy on mechanical stresses in a polymer electrolyte membrane. Journal of Power Sources 2011;196(3):1314–20.

[17] Chien C-H, Hu Y-L, Su T-H, Liu H-T, Wang C-T, Yang P-F et al. Effects of bolt pre-loading variations on performance of GDL in a bolted PEMFC by 3-D FEM analysis. Energy 2016;113:1174–87.
[18] Kleemann J, Finsterwalder F, Tillmetz W. Characterisation of mechanical behaviour and coupled electrical properties of polymer electrolyte membrane fuel cell gas diffusion layers. Journal of Power Sources 2009;190(1):92–102.
[19] Mishra V, Yang F, Pitchumani R. Measurement and Prediction of Electrical Contact Resistance Between Gas Diffusion Layers and Bipolar Plate for Applications to PEM Fuel Cells. Journal of Fuel Cell Science and Technology 2004;1(1):2–9.
[20] Roohparvarzadeh S. Experimental Characterization of the Compressive Behaviour of Gas Diffusion Layers in PEM Fuel Cells.
[21] Norouzifard V, Bahrami M. Deformation of PEM fuel cell gas diffusion layers under compressive loading: An analytical approach. Journal of Power Sources 2014;264:92–9.
[22] Gigos PA, Faydi Y, Meyer Y. Mechanical characterization and analytical modeling of gas diffusion layers under cyclic compression. International Journal of Hydrogen Energy 2015;40(17):5958–65.
[23] Ahmad El-Kharouf. Understanding GDL properties and performance in polymer electrolyte fuel cells; 2014.
[24] Faydi Y, Lachat R, Meyer Y. Thermomechanical characterisation of commercial Gas Diffusion Layers of a Proton Exchange Membrane Fuel Cell for high compressive pre-loads under dynamic excitation. Fuel 2016;182:124–30.
[25] Chen Y, Jiang C, Cho C. An Investigation of the Compressive Behavior of Polymer Electrode Membrane Fuel Cell's Gas Diffusion Layers under Different Temperatures. Polymers 2018;10(9).
[26] Domínguez Almaraz GM, Ruiz Vilchez JA, Dominguez A, Meyer Y. Ultrasonic Fatigue Endurance of Thin Carbon Fiber Sheets. Metall and Mat Trans A 2016;47(4):1654–60.
[27] Bates A, Mukherjee S, Hwang S, Lee SC, Kwon O, Choi GH et al. Simulation and experimental analysis of the clamping pressure distribution in a PEM fuel cell stack. International Journal of Hydrogen Energy 2013;38(15):6481–93.
[28] Alizadeh E, Ghadimi M, Barzegari MM, Momenifar M, Saadat S. Development of contact pressure distribution of PEM fuel cell's MEA using novel clamping mechanism. Energy 2017;131:92–7.
[29] Ahmad M, Harrison R, Meredith J, Bindel A, Todd B. Validation of a fuel cell compression spring equivalent model using polarisation data. International Journal of Hydrogen Energy 2017;42(12):8109–18.
[30] Ul Hassan N, Kilic M, Okumus E, Tunaboylu B, Soydan AM. Experimental determination of optimal clamping torque for AB-PEM Fuel cell. J. Electrochem. Sci. Eng. 2016;6(1):9.
[31] Ahmad M, Harrison R, Meredith J, Bindel A, Todd B. Analysis of the compression characteristics of a PEM stack, development of an equivalent spring model and recommendations for compression process improvements. In: 2015 6th International Renewable Energy Congress (IREC 2015): Sousse, Tunisia, 24-26 March 2015. Piscataway NJ: IEEE; 2015, p. 1–6.
[32] Prass S, Hasanpour S, Sow PK, Phillion AB, Mérida W. Microscale X-ray tomographic investigation of the interfacial morphology between the catalyst and micro porous layers in proton exchange membrane fuel cells. Journal of Power Sources 2016;319:82–9.

[33] Zenyuk IV, Parkinson DY, Connolly LG, Weber AZ. Gas-diffusion-layer structural properties under compression via X-ray tomography. Journal of Power Sources 2016;328:364–76.
[34] Banerjee R, Hinebaugh J, Liu H, Yip R, Ge N, Bazylak A. Heterogeneous porosity distributions of polymer electrolyte membrane fuel cell gas diffusion layer materials with rib-channel compression. International Journal of Hydrogen Energy 2016;41(33):14885–96.
[35] Holzer L, Pecho O, Schumacher J, Marmet P, Stenzel O, Büchi FN et al. Microstructure-property relationships in a gas diffusion layer (GDL) for Polymer Electrolyte Fuel Cells, Part I: effect of compression and anisotropy of dry GDL. Electrochimica Acta 2017;227:419–34.
[36] Yablecki J, Bazylak A. Determining the effective thermal conductivity of compressed PEMFC GDLs through thermal resistance modelling. Journal of Power Sources 2012;217:470–8.
[37] Sadeghi E, Djilali N, Bahrami M. Effective thermal conductivity and thermal contact resistance of gas diffusion layers in proton exchange membrane fuel cells. Part 1: Effect of compressive load. Journal of Power Sources 2011;196(1):246–54.
[38] Sadeghi E, Djilali N, Bahrami M. Effective thermal conductivity and thermal contact resistance of gas diffusion layers in proton exchange membrane fuel cells. Part 2: Hysteresis effect under cyclic compressive load. Journal of Power Sources 2010;195(24):8104–9.
[39] Alhazmi N, Ingham DB, Ismail MS, Hughes K, Ma L, Pourkashanian M. The through-plane thermal conductivity and the contact resistance of the components of the membrane electrode assembly and gas diffusion layer in proton exchange membrane fuel cells. Journal of Power Sources 2014;270:59–67.
[40] Unsworth G, Zamel N, Li X. Through-plane thermal conductivity of the microporous layer in a polymer electrolyte membrane fuel cell. International Journal of Hydrogen Energy 2012;37(6):5161–9.
[41] Sadeghifar H, Djilali N, Bahrami M. Thermal conductivity of a graphite bipolar plate (BPP) and its thermal contact resistance with fuel cell gas diffusion layers: Effect of compression, PTFE, micro porous layer (MPL), BPP out-of-flatness and cyclic load. Journal of Power Sources 2015;273:96–104.
[42] Hamour M, Garnier JP, Grandidier JC, Ouibrahim A, Martemianov S. Thermal-Conductivity Characterization of Gas Diffusion Layer in Proton Exchange Membrane Fuel Cells and Electrolyzers Under Mechanical Loading. Int J Thermophys 2011;32(5):1025–37.
[43] Burheim OS, Crymble GA, Bock R, Hussain N, Pasupathi S, Du Plessis A et al. Thermal conductivity in the three layered regions of micro porous layer coated porous transport layers for the PEM fuel cell. International Journal of Hydrogen Energy 2015;40(46):16775–85.
[44] Montgomery HC. Method for Measuring Electrical Resistivity of Anisotropic Materials. Journal of Applied Physics 1971;42(7):2971–5.
[45] Miyazawa A, Himeno T, Nishikata A. Electrical properties of bipolar plate and gas diffusion layer in PEFC. Journal of Power Sources 2012;220:199–204.
[46] Schroder DK. Semiconductor material and device characterization. 3rd ed. Hoboken (NJ): IEEE Press; John Wiley & sons; 2006.

[47] Tuttle G. Contact resistance and TLM measurements. [December 07, 2020]; Available from: http://tuttle.merc.iastate.edu/ee432/topics/metals/tlm_measurements.pdf.
[48] Berger HH. Contact Resistance and Contact Resistivity. J. Electrochem. Soc. 1972;119(4):507.
[49] Zamel N, Li X, Shen J. Numerical estimation of the effective electrical conductivity in carbon paper diffusion media. Applied Energy 2012;93:39–44.
[50] Ismail MS, Hughes KJ, Ingham DB, Ma L, Pourkashanian M. Effects of anisotropic permeability and electrical conductivity of gas diffusion layers on the performance of proton exchange membrane fuel cells. Applied Energy 2012;95:50–63.
[51] Ismail MS, Damjanovic T, Ingham DB, Pourkashanian M, Westwood A. Effect of polytetrafluoroethylene-treatment and microporous layer-coating on the electrical conductivity of gas diffusion layers used in proton exchange membrane fuel cells. Journal of Power Sources 2010;195(9):2700–8.
[52] Aydin Ö, Zedda M, Zamel N. Challenges Associated with Measuring the Intrinsic Electrical Conductivity of Carbon Paper Diffusion Media. Fuel Cells 2015;15(3):537–44.
[53] Aydin Ö, Zedda M, Zamel N, Groos U, Hebling C. Comprehensive understanding of electrical conductivity measurements of gas diffusion media of PEM fuel cells: Gwangju, South Korea, 15-20 June 2014. Gwangju, South Korea: Committee of WHEC; 2014.
[54] Todd D, Bennett S, Mérida W. Anisotropic electrical resistance of proton exchange membrane fuel cell transport layers as a function of cyclic strain. International Journal of Hydrogen Energy 2016;41(14):6029–35.
[55] Ye D, Gauthier E, Benziger JB, Pan M. Bulk and contact resistances of gas diffusion layers in proton exchange membrane fuel cells. Journal of Power Sources 2014;256:449–56.
[56] Sadeghifar H. In-plane and through-plane electrical conductivities and contact resistances of a Mercedes-Benz catalyst-coated membrane, gas diffusion and micro-porous layers and a Ballard graphite bipolar plate: Impact of humidity, compressive load and polytetrafluoroethylene. Energy Conversion and Management 2017;154:191–202.
[57] Zhang W, Wu C. Effect of Clamping Load on the Performance of Proton Exchange Membrane Fuel Cell Stack and Its Optimization Design: A Review of Modeling and Experimental Research. Journal of Fuel Cell Science and Technology 2014;11(2).
[58] Prass S. Interfacial morphology and contact resistance between the catalyst and micro porous layers in proton exchange membrane fuel cells: University of British Columbia; 2016.
[59] El Oualid S, Lachat R, Candusso D, Meyer Y. Characterization process to measure the electrical contact resistance of Gas Diffusion Layers under mechanical static compressive loads. International Journal of Hydrogen Energy 2017;42(37):23920–31.
[60] Ismail MS, Ingham DB, Ma L, Pourkashanian M. The contact resistance between gas diffusion layers and bipolar plates as they are assembled in proton exchange membrane fuel cells. Renewable Energy 2013;52:40–5.
[61] Singdeo D, Dey T, Ghosh PC. Contact resistance between bipolar plate and gas diffusion layer in high temperature polymer electrolyte fuel cells. International Journal of Hydrogen Energy 2014;39(2):987–95.
[62] Zhang L, Liu Y, Song H, Wang S, Zhou Y, Hu SJ. Estimation of contact resistance in proton exchange membrane fuel cells. Journal of Power Sources 2006;162(2):1165–71.

[63] Zhou P, Lin P, Wu CW, Li Z. Effect of nonuniformity of the contact pressure distribution on the electrical contact resistance in proton exchange membrane fuel cells. International Journal of Hydrogen Energy 2011;36(10):6039–44.
[64] Lai X, Liu D, Peng L, Ni J. A mechanical–electrical finite element method model for predicting contact resistance between bipolar plate and gas diffusion layer in PEM fuel cells. Journal of Power Sources 2008;182(1):153–9.
[65] Mason TJ, Millichamp J, Shearing PR, Brett DJ. A study of the effect of compression on the performance of polymer electrolyte fuel cells using electrochemical impedance spectroscopy and dimensional change analysis. International Journal of Hydrogen Energy 2013;38(18):7414–22.
[66] Chang WR, Hwang JJ, Weng FB, Chan SH. Effect of clamping pressure on the performance of a PEM fuel cell. Journal of Power Sources 2007;166(1):149–54.
[67] Mason TJ, Millichamp J, Neville TP, El-kharouf A, Pollet BG, Brett DJ. Effect of clamping pressure on ohmic resistance and compression of gas diffusion layers for polymer electrolyte fuel cells. Journal of Power Sources 2012;219:52–9.
[68] El-kharouf A, Mason TJ, Brett DJ, Pollet BG. Ex-situ characterisation of gas diffusion layers for proton exchange membrane fuel cells. Journal of Power Sources 2012;218:393–404.
[69] Sow PK, Prass S, Kalisvaart P, Mérida W. Deconvolution of electrical contact and bulk resistance of gas diffusion layers for fuel cell applications. International Journal of Hydrogen Energy 2015;40(6):2850–61.
[70] Czichos H, Saito T, Smith L. Springer Handbook of Materials Measurement Methods. Berlin, Heidelberg: Springer Berlin Heidelberg; 2006.
[71] Todd D, Schwager M, Mérida W. Three-Dimensional Anisotropic Electrical Resistivity of PEM Fuel Cell Transport Layers as Functions of Compressive Strain. J. Electrochem. Soc. 2015;162(3):F265-F272.
[72] Qiu D, Peng L, Yi P, Lai X, A micro contact model for electrical contact resistance prediction between roughness surface and carbon fiber paper. International journal of Mechanical Sciences 2017;24-125:37-47.

Chapter 3: Electrical properties of the GDL

In this chapter, electrical properties of the gas diffusion layer (GDL) that are related to electronic ohmic losses in PEMFCs are experimentally determined. The electrical bulk resistance of the GDL (namely its through-plane and in-plane resistivity values) is characterized, as well as its contact resistance with the BPP. The contact resistance of the GDL with the BPP measured through the transmission line method is first presented. Then the through plane resistance and in-plane resistivity characterization are presented. Finally, a graphite plate (typical BPP material) is characterized and a comparison between GDL - Graphite BPP and GDL - Gold coated BPP interfaces combinations are discussed. In order to have a good representativity of typical materials used in PEMFC, a number of commercial carbon paper GDLs (12 types) have been characterized These elements are presented in Table 3.1 with their different structure, composition and thickness. They are also reminded in each section according to the examined GDLs.

GDL	Thickness (µm)	Structure	PTFE	MPL
SGL 24 AA	190	Carbonised straight fiber	No	No
SGL 24 BA	190	Carbonised straight fiber	Yes	No
SGL 24 BC	235	Carbonised straight fiber	Yes	Yes
SGL 38 BC	325	Carbonised straight fiber	Yes	Yes
SGL 35 AA	300	Carbonised straight fiber	No	No
SGL 25 AA	190	Carbonised straight fiber	No	No
SGL 10 BA	400	Felt structure	Yes	No
Toray H120	370	Graphitised straight fiber	No	No
Toray H60	190	Graphitised straight fiber	No	No
Toray H90	280	Graphitised straight fiber	No	No
Freudenberg H2315I3	210	Felt structure	Yes	No
Freudenberg H14C9	180	Felt structure	Yes	Yes

Table 3. 1: GDL samples properties.

In order to better approach PEMFC operating conditions, different parameters have been studied such as cyclic compression, temperature, humidity and

compression velocity on the different properties of the GDLs. Fig. 3.1 represents a synthetic diagram of the experimental campaign with investigated parameters, properties, and structures. All the experimental investigations of GDL electrical properties are done under mechanical compression.

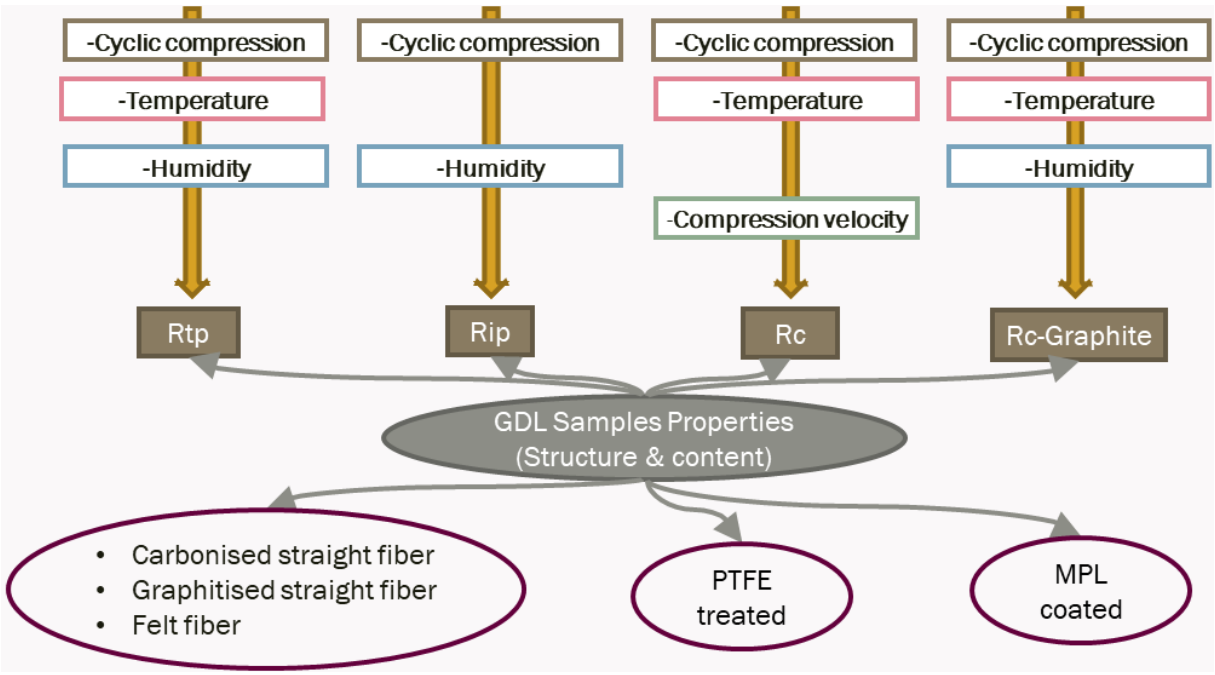

Fig 3. 1: Diagram of GDL electrical properties and operating conditions studied in this thesis.

3.1 Electrical contact resistance

3.1.1 Measurement method

The measurement of the electrical contact resistance Rc was carried out according to the Transmission Line Method (TLM) [1] Rc was measured under different cyclic compression profiles. Several GDL structures were employed. The effect of temperature on Rc was assessed. Fig. 3.2 depicts the experimental set-up used to measure the contact resistance. Fig. 3.3 represents an explained diagram of the sample holder and the deployment of the TLM method.

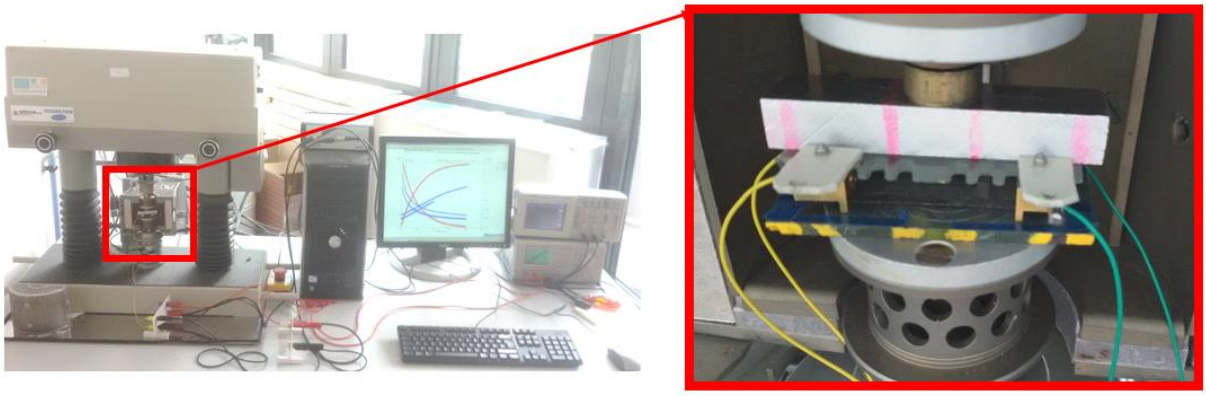

Fig 3. 2: Electrical contact resistance experimental set-up with zoom on sample holder.

3.1.1.1. Samples and sample holder

Different types of carbon paper GDL samples were used under different compression profile (Cf. Table 3.2). The SGL 24 BC is coated with a MPL on one side. Although the MPL usually faces the CL, both the fibers side of the GDL and the MPL side were evaluated.

GDL type	Thickness (µm)	Structure and composition	Applied compression profile
SGL 24 AA	190 +/-30[1]	Straight carbon fibre paper.	All profiles
SGL 24 BA	190 +/-30[1]	Straight carbon fibre paper with 5% PTFE (hydrophobic agent).	(0-8 MPa), (0-4 MPa)
SGL 24 BC	235 +/-30[1]	Straight carbon fibre paper with 5% PTFE + MPL.	(0-8 MPa), (0-4 MPa)
Toray TGP H90	280 [2]	Graphitised straight carbon fibre paper.	(0-8 MPa)
Toray TGP H120	370 [2]	Graphitised straight carbon fibre paper.	(0-8 MPa), (0-4 MPa)
Freudenberg H2315 I3	210 [3]	Felt Carbon fibre paper + hydrophobic agent.	(0-8 MPa)
SGL 10 BA	400	Felt Carbon fibre paper + hydrophobic agent.	(0-4 MPa)

Table 3. 2: GDL sample type.

[1] From SGL carbon company

For GDLs evaluated under a (0-8 MPa), a small area (4x40 mm^2) was employed because the compression machine is limited to 70 N. The samples were cut into two sheets of 2 mm width (W/2) and 40 mm long (fig. 3.3 a). They were placed at each side of the sample holder in order to guarantee some mechanical stability. This homemade sample holder was specifically designed to ensure the application of a homogenous mechanical compression on the samples, thanks to its ball device. The sample holder includes two gold coated metallic indenters with a width L of 1 mm, which is a typical size of BPP rib width. These indenters are in contact with the GDL samples on four contact surfaces of W / 2 x L = 2 x 1 mm^2. The total contact area is therefore 8 mm^2. For other compression profiles, GDLs were cut into only one sheet. Indeed, the area and the width (W) were large enough to ensure stability of the sample holder with one sheet placed in the center.

The GDL-indenter system is electrically insulated from the machine with two glass plates. The upper plate is designed in a way that allows the variation of the distance between the indenters d (d1 to d4) (Table 3.3), which is required to evaluate the contact resistance Rc using the TLM method (fig. 3.3 b). This method is based on the fact that the total resistance Rt (between two metallic contacts and the GDL) is proportional to the distance between the two metallic contacts d.

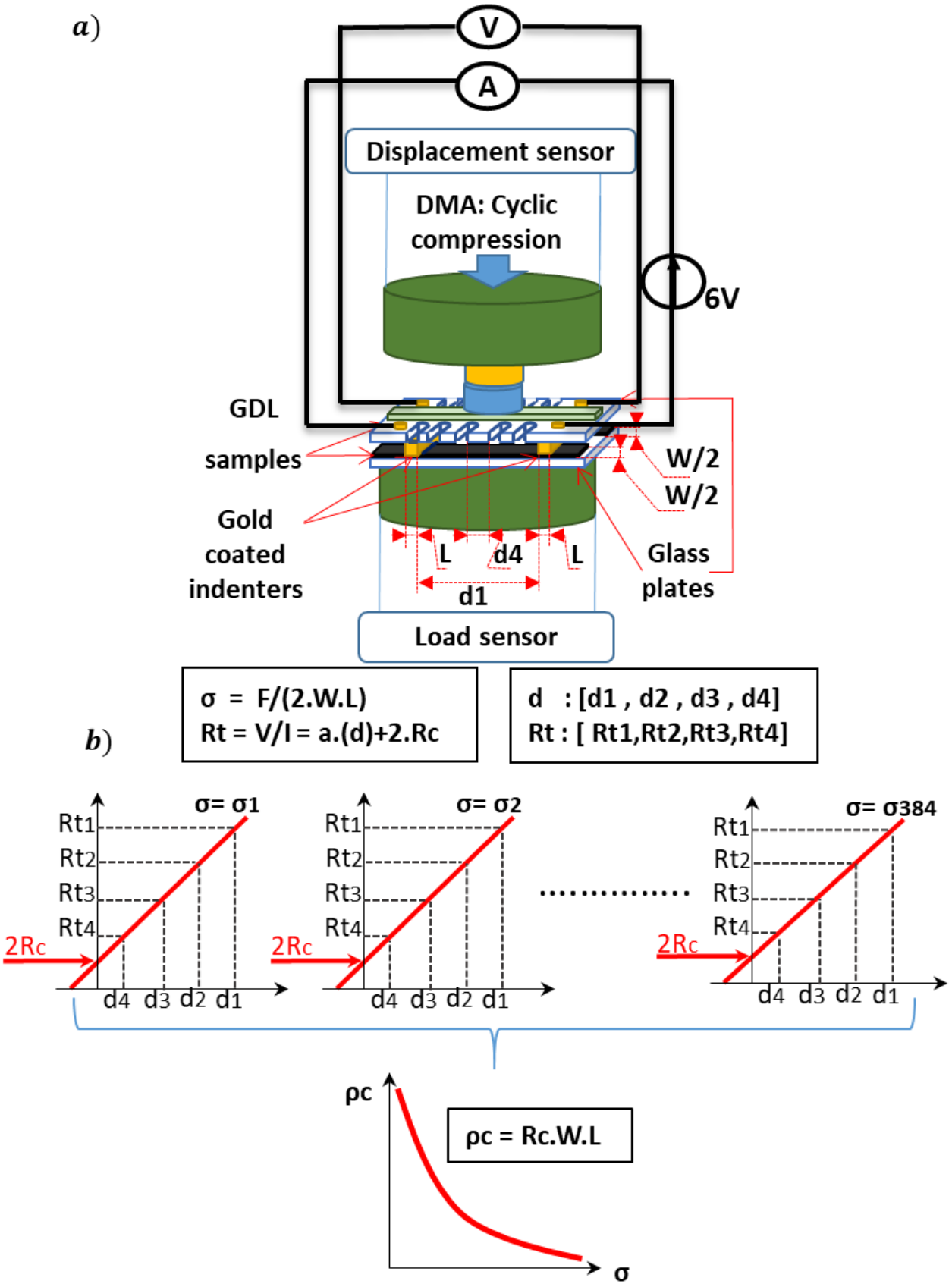

Fig 3. 3: Graphic summarising the experimental procedure to estimate the electrical contact resistance between the GDL and the BPP under cyclic mechanical compression. a) Experimental set-up, b) Contact resistance (Rc) extraction.

3.1.1.2. Applied mechanical load

0-8 MPa compression profile

A cyclic mechanical compression has been applied on the GDL samples using a Dynamic Mechanical Analysis machine - DMA type Metravib VA2000. GDLs were compressed by the indenters. The mechanical force ranged from 0 to 65 N (+/-0.2 N); in terms of applied stress: 0 - 8.25 MPa (+/-0.025 MPa). Five cycles of loading-unloading compression were applied with four levels of pressure as shown in fig. 3.4. This cyclic loading has been applied three consecutive times for every distance d (i.e. d1, d2, d3, d4), on each GDL sample.

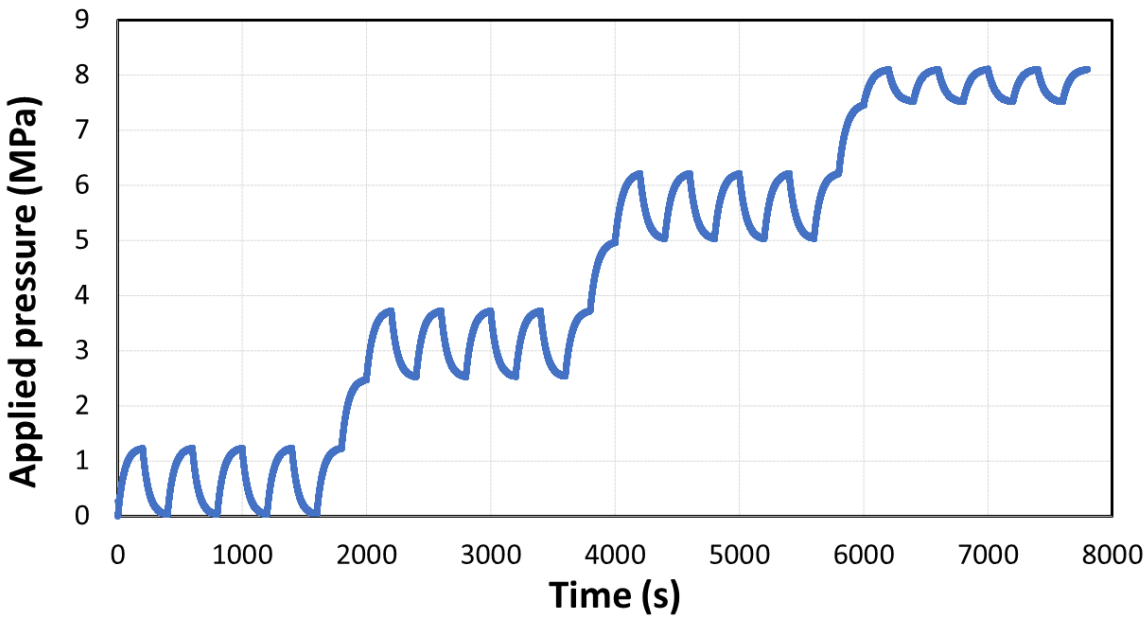

Fig 3. 4: 0-8 MPa compression profile.

The experimental stress-strain curve related to this compression profile is presented in Annex 1.

0-4 MPa compression profile

Rc was also measured under 0-4 MPa compression pressure as depicted in fig 3.5.

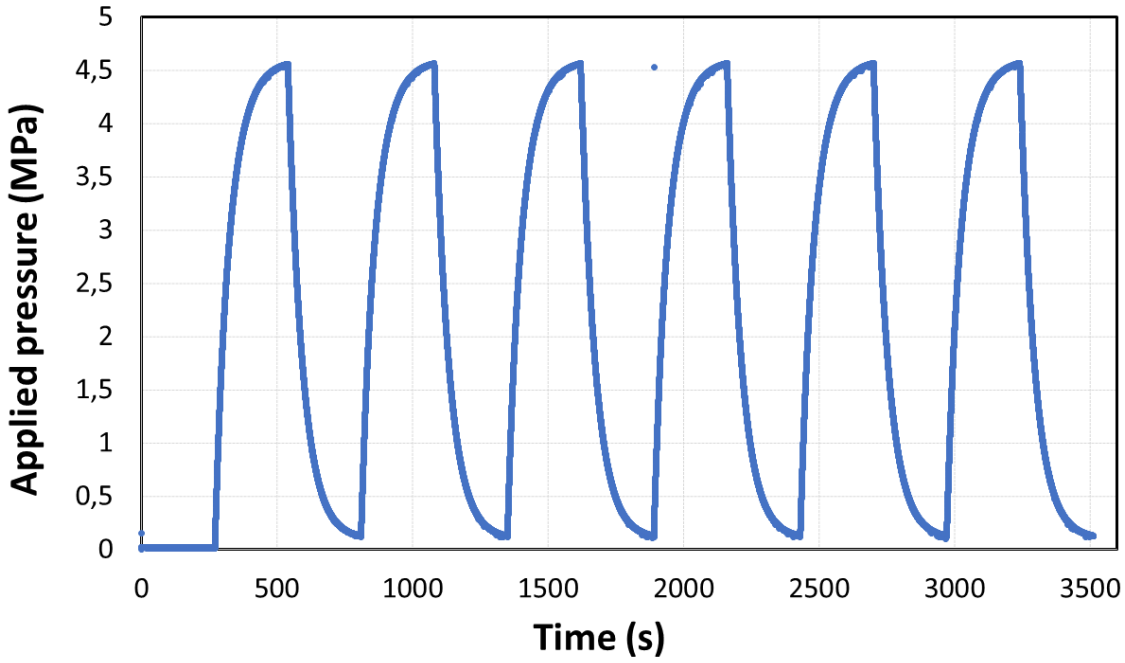

Fig 3. 5: 0-4 MPa compression profile.

As complementary test, the GDL 24 AA was also tested under small compression values as depicted in fig 3.6 in order to evaluate other parameters such as compression speed.

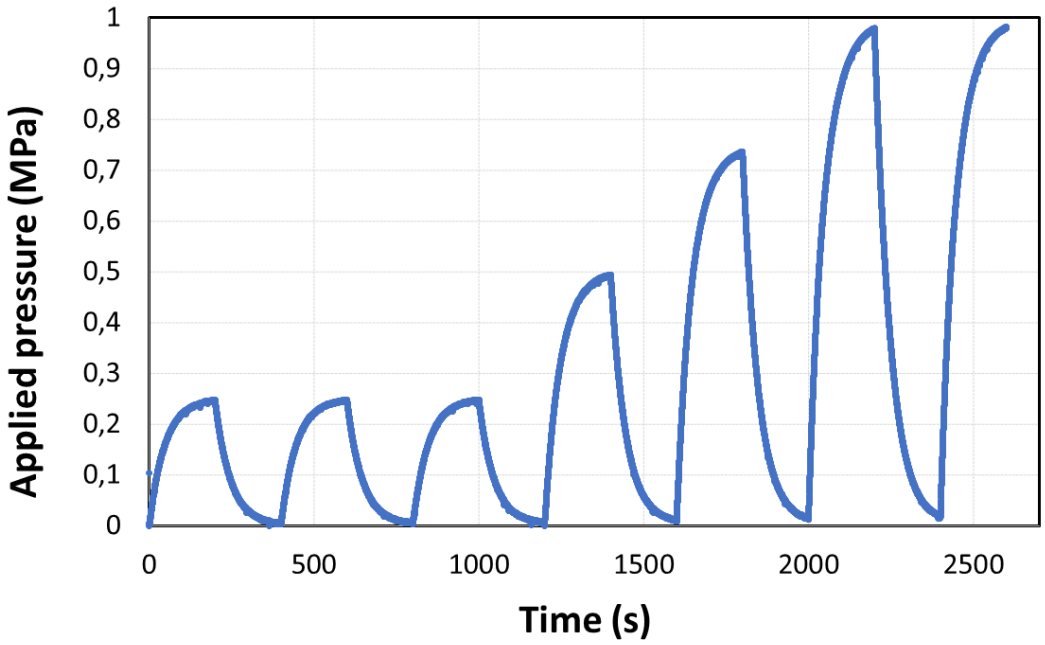

Fig 3. 6: 0-1 MPa compression profile.

3.1.1.3. Specific electrical contact resistance determination

As mentioned earlier, the electrical contact resistance measurement method applied in this research is the TLM method, which is usually used to measure the electrical contact resistance between a metal and a semi-conductor. This method is based on the fact that the total resistance between two metallic contacts and the GDL (Rt) is proportional to the distance between the two metallic contacts (d) following Equation 3.1:

$$Rt = Rs\frac{d}{W} + 2Rc = a.(d) + b \quad (3.1)$$

With:

Rs: the sheet resistance (Ohm / □ or Ohms per square).

W: the width of the GDLs (mm).

Rc: the contact resistance (Ohm).

d: the distance between the metallic indenters (mm).

The contact resistance Rc can be determined by varying the distance between the metallic indenters d in order to find the slope a and the offset b of the linear curve Rt = f(d). In this study, four values of d have been used as shown in Table 3.3.

Pressure profile	For (0-8 MPa)	All other tests
Distance name	Length (mm) (+/-5%)	Length (mm) (+/-5%)
d1	31.1	26.2
d2	18.1	18.3
d3	9.9	9.6
d4	2.2	2.1

Table 3. 3: Distances between the two indenters.

The slope a = Rs / W and the offset b = 2.Rc are then extracted using the least square method. The specific electrical contact resistance is obtained by multiplying the contact resistance by the specific area of one side of the contacts (A_{eff}):

$$\rho c = Rc.A_{eff} \quad (3.2)$$

So that:

$$\rho c = Rc.W.L \quad (3.3)$$

With: $W.L = 4$ mm².

For more details on the mathematical model of the TLM method, the reader is referred to [4-6]. The electric circuit composition is similar to the circuit of [7]. The GDL-indenters set is included in an electrical circuit with a fixed voltage source and a witness resistance. Voltage and current are measured across the system and the total resistance Rt is evaluated as a function of compression for every distance d. The voltage generator is set to 6 V (for 0-8 MPa)(fig. 3.3 a), as El Oualid S. et al. [7].For the other compression profiles, voltage was set to 5 V which does not influence results of ohmic resistances measurement. The voltage and the current resolutions are 2 mV and 0.1 mA, respectively.

For the GDLs evaluated under (0-8 MPa) profile, the uncertainties were determined using the evaluation of type B [8]; which is a way to evaluate uncertainties using non-statistical methods (such as the use of previous data measurement, manufacturer specification, calibration reports…etc). In our case, the manufacturer' specifications were used. Uncertainties on the measured voltage U and current I, were determined according to the user manual of the Oscilloscope used (Tektronix tds2002) with an accuracy of 3% on the measured values. Uncertainty on Rt was calculated according to error propagation laws applied to U and I. Uncertainty on Rc was extracted from the uncertainty on the offset (b) calculated according to the ordinary least-square method, by considering the highest uncertainty on Rt and neglecting the uncertainty on d. This type of uncertainty has been chosen because of the long procedure in this case, which takes more than 30 hours for each GDL type.

For the other compression profiles, the uncertainty was determined using the evaluation of type A, with the use of three samples.

3.1.1.4. Data analysis process

Experimental data were collected by an acquisition card. First, the distance between indenters d was fixed, starting by the longest distance d1, so that the material between the indenters is always uncompressed and not damaged by previous compression. Then, an electrical/mechanical test was done including the mechanical load depicted in fig. 3.3, and the voltage of 6 V was applied to the circuit. The total resistance between the indenters Rt is measured, as well as the displacement of the GDL. The data was stored in one file corresponding to d1. Then, the same test was repeated twice again on the same sample and the data was stored in the same spreadsheet file (tests 1, 2 and 3) for the GDLs tested under

0-8 MPa. The same process was repeated for the three other distances d and the data was recorded in three other files. The four files obtained are treated in order to obtain the contact resistance Rc and the total strain as a function of the applied stress. Every file consists of a number of data sequences. Each data sequence includes: measured force, target force, measured displacement, current intensity, voltage, and time. The number of data sequences in each file is reduced to 384 measurement points by using a simple moving average of the current intensity, the voltage and the displacement by step of 1 N of measured force.

For every GDL, the four files of the measured resistances Rt for the four distances d are combined to calculate the contact resistance using the least square method and the average strain. As an example, let us consider a particular measurement point, Point 5. The measurement Point 5 corresponds to a loading compression of 0.5 MPa for the first cycle of compression. The contact resistance for this point of pressure is calculated using the 4 total resistances Rt (for d1, d2, d3, d4) at this point of compression using the least square method according to Equation 3.1. The steps of the experimental process are depicted in fig. 3.3.

Fig. 3.7 shows the relationship between Rt and d, for the SGL 24 AA. We can observe that the experimental points are quite linear with a regression coefficient of 96%. Accurate measurement of Rc involves a good alignment of the points formed by Rt=f(d) which requires a high regression coefficient.

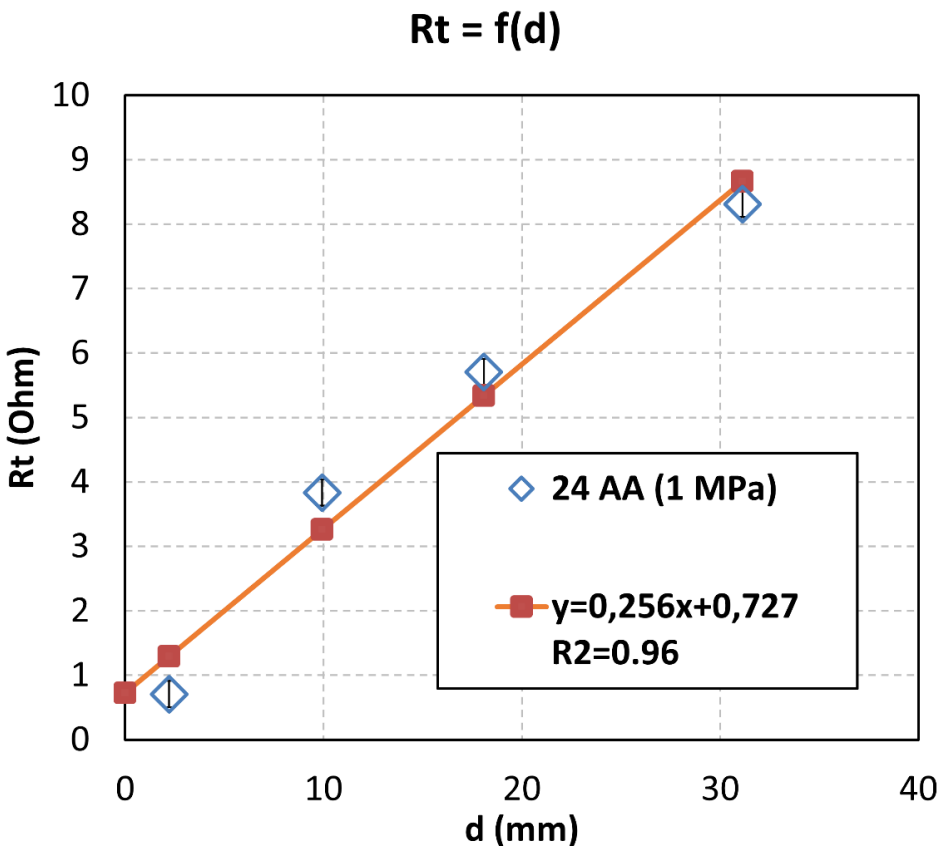

Fig 3. 7: Real Rt = f(d) and least square line for the SGL 24 AA, first test.

For all other compression profiles different from the 0 -8 MPa range, only one test was done on the sample. The same procedure is used to manage the data and extract Rc for every sample. Three samples were used for every GDL. An average Rc is calculated for every sample.

3.1.2. Results

3.1.2.1. Effect of compression

As expected, the experiments described a non-linear decrease of the specific electrical contact resistance ρc with compression as shown in fig. 3.8 a). A very fast reduction of ρc from 0 to 3 MPa can be observed, then a slower one from 3 to 8 MPa. For all the GDLs, more than 75% of the total reduction of ρc is obtained at 2.5 MPa. The applied stress improves the contact between the GDL and the indenters by increasing the contact surface. It also decreases the porosity of the GDL and makes the carbon fibers that conduct electrons closer to each other.

At first glance, the Toray GDLs present a small specific electrical contact resistance ρc (4-20 mOhm.cm²), the SGL GDLs a higher one (4-65 mOhm.cm²), while the Freudenberg has a medium contact resistance (8-32 mOhm.cm²) (fig. 3.8 a)). In the SGL group, the PTL side of the 24 BC shows the highest resistance (27-

65 mOhm.cm²) while its MPL side displays the lowest one (4-23 mOhm.cm²). SGL 24 BA has a higher resistance compared to the SGL 24 AA as shown in fig. 3.8 b). For the Toray Series, the Toray H120 has a comparable resistance with the H90. Some scattered points can be observed when the pressure is lower than 1.25 MPa, even after 2 previous tests reaching 8 MPa as depicted in fig. 3.8.
Uncertainties on ρc are reported in fig. 3.8 b). They will be discussed in the next paragraphs.

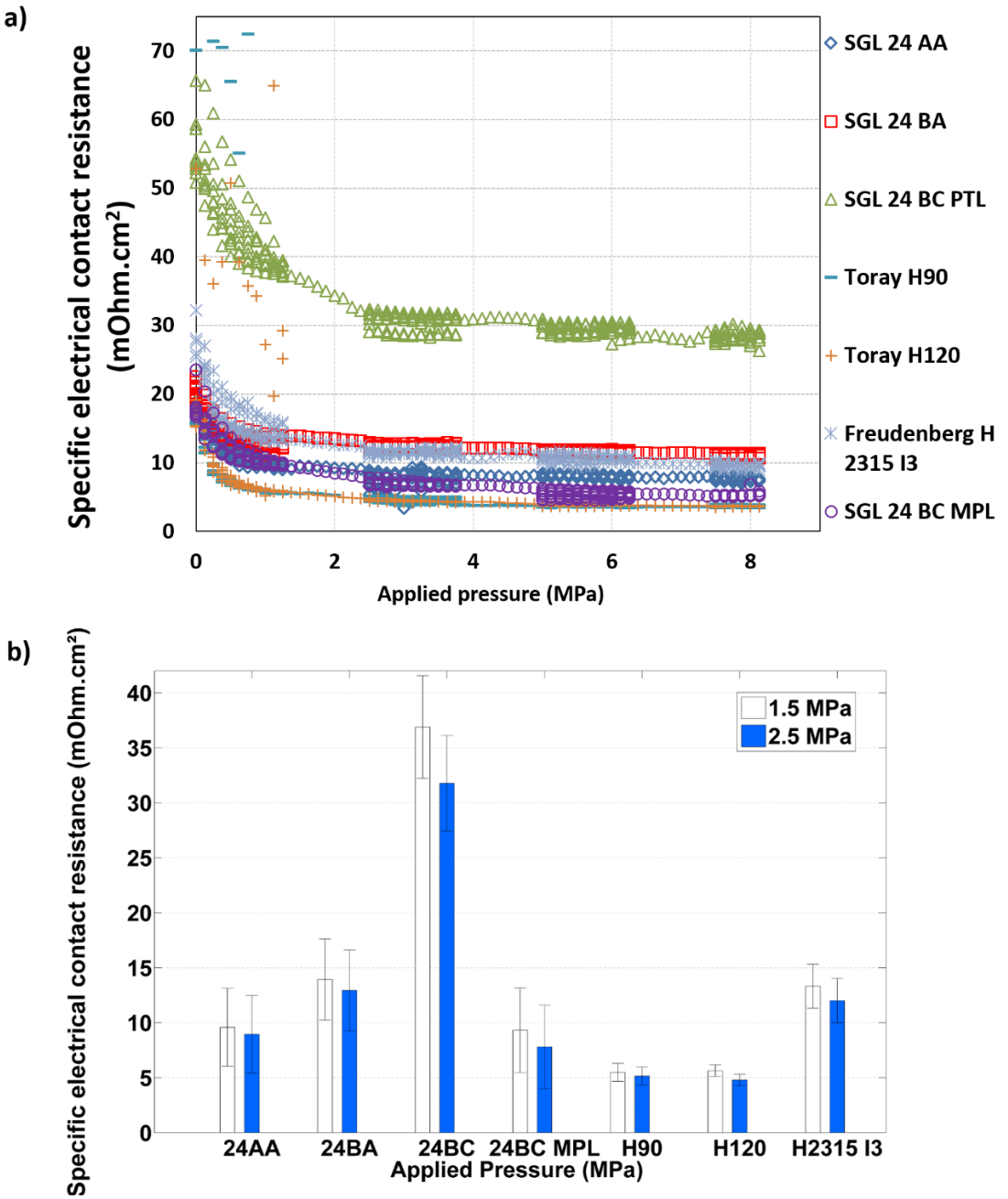

Fig 3. 8: a) Electrical contact resistance as a function of the applied stress for the third test. b) Electrical contact resistance with uncertainties at 1.5 and 2.5 MPa.

Effect of PTFE loading

Analogously to the mechanical behavior, the fact that the SGL 24 BA has a higher electrical contact resistance compared to the SGL 24 AA is ascribed to the PTFE which is added to the reference 24 BA (5 wt%). The PTFE is a non-conductive material that can cover some of the contact surfaces with the indenters. However, more importantly, it increases the mechanical resistance limiting the compression rate of the GDL, which will limit the decrease of the contact resistance attributed to the larger contact area enhanced by compression. This can explain the visible increase of the gap between the resistance of the 24 AA and the 24 BA with compression (from 0 to 1 MPa) that is observed in fig. 3.8 a).

Effect of the MPL

With its smooth surface, the MPL of the SGL 24 BC improves the contact with the indenters, which decreases the contact resistance of the MPL side. The SGL 24 BC PTL side, which originally has the same structure and composition of the SGL 24 BA, exhibited a higher contact resistance compared to the SGL 24 BA's one. Because the contact resistance measured also includes the contact resistance between the MPL and PTL side of the GDL that should also be taken into consideration when analysing Ohmic resistances. We expect that the measurement of Rc at the PTL side of 24 BC contains also the contact resistance between the PTL and the MPL interface. This is not the case when ρc is measured at the MPL side because the MPL bulk resistance might be much lower than the MPL substrate contact resistance and the PTL bulk resistance. Therefore, the current only flows from the first indenter through the MPL layer, then gets back to the second indenter without passing through the lower layer (PTL side, i.e. macro-porous layer side), in the case of the MPL side measurement. Further investigation of the structure of this GDL thickness should be done in order to confirm the nature of the interface between the PTL and MPL, as the interface may depend on different parameters such as the initial porosity of the fibrous structure, the nature of the fiber alignment and the roughness of both surfaces.

Effect of structure and composition

The felt carbon paper exhibited a resistance value between those of the SGL straight carbon paper 24 AA and 24 BA. The smallest resistances were measured for the graphitised straight carbon papers of Toray. Graphitised and felt structure also show smaller uncertainty values compared to the straight paper GDLs as shown in Table 3.4.

GDL		24 AA	24 BA	24 BC	24 BC MPL	H90	H120	H2315 I3
Uncertainty on ρc (mOhm.cm²)	Min.	3,52	3,61	4,18	3,56	0,71	0,51	1,97
	Max.	3,68	3,92	4,99	4,33	1,23	0,74	2,25
	Average	3,54	3,68	4,54	3,79	0,81	0,53	2,05
Average relative uncertainty (%)		41,89	29,62	13,84	55,52	18,16	11,47	17,29

Table 3. 4: Uncertainties of the contact resistance (3rd test).

3.1.2.2. Effect of compression Cycles

Effect on the contact resistance ρc

While measuring the electrical contact resistance, the GDLs were compressed from 0 to 8.25 MPa. They were subjected to five cycles of loading-unloading mechanical compression upon four levels of compression (0-1.25 MPa, 2.5-3.75 MPa, 5-6.25 MPa, and 7.5-8.25 MPa) (fig. 3.4).

The effect of the cycles of compression has been evaluated with two methods by calculating an absolute value and a relative one. The absolute difference of contact resistance ρc between the cycles, Cρc, has been evaluated by determining the average of the absolute value of the difference between ρc at the loading of the 2nd, 3rd, 4th, and 5th cycle and ρc at the loading of the 1st cycle (Cf. Equation 3.4). The rate of this difference RCρc was extracted by dividing it by the value of ρc at the 1st cycle (Cf. Equation 3.5). The effect of the cyclic compression on the mechanical properties has been evaluated in the same way, using the strain instead of ρc. One pressure value has been chosen for every compression level: 1, 3, 6, and 8 MPa. Standard deviation has been evaluated for absolute values.

$$C\rho c = \frac{\sum_{i=1}^{5}(\rho c_1 - \rho c_i)}{4} \quad (3.4)$$

$$RC\rho c = \frac{C\rho c}{\rho c_1} \text{x} 100\% \quad (3.5)$$

With:

$C\rho c$: Contact resistance absolute difference between cycles (mOhm.cm2).

$RC\rho c$: Contact resistance relative difference between cycles (%).

ρc_i: Specific electrical contact resistance at cycle i (mOhm.cm2).

The electrical contact resistance is globally affected by the number of cycles of compression. As expected, we observe a general trend of decrease of the difference between the cycles (Cρc and RCρc) with compression for all GDLs, as well as the difference for strain values. The difference between the cycles for compression values of 1 and 3 MPa is much higher than for values of 6 and 8 MPa (fig. 3.9). This decrease is higher in absolute values Cρc and less evident in relative values RCρc because the contact resistance itself decreases with compression (fig. 3.9). Values of Cρc depicted a maximum mean value of 8.9 mOhm.cm² for the SGL 24 BC substrate sample.

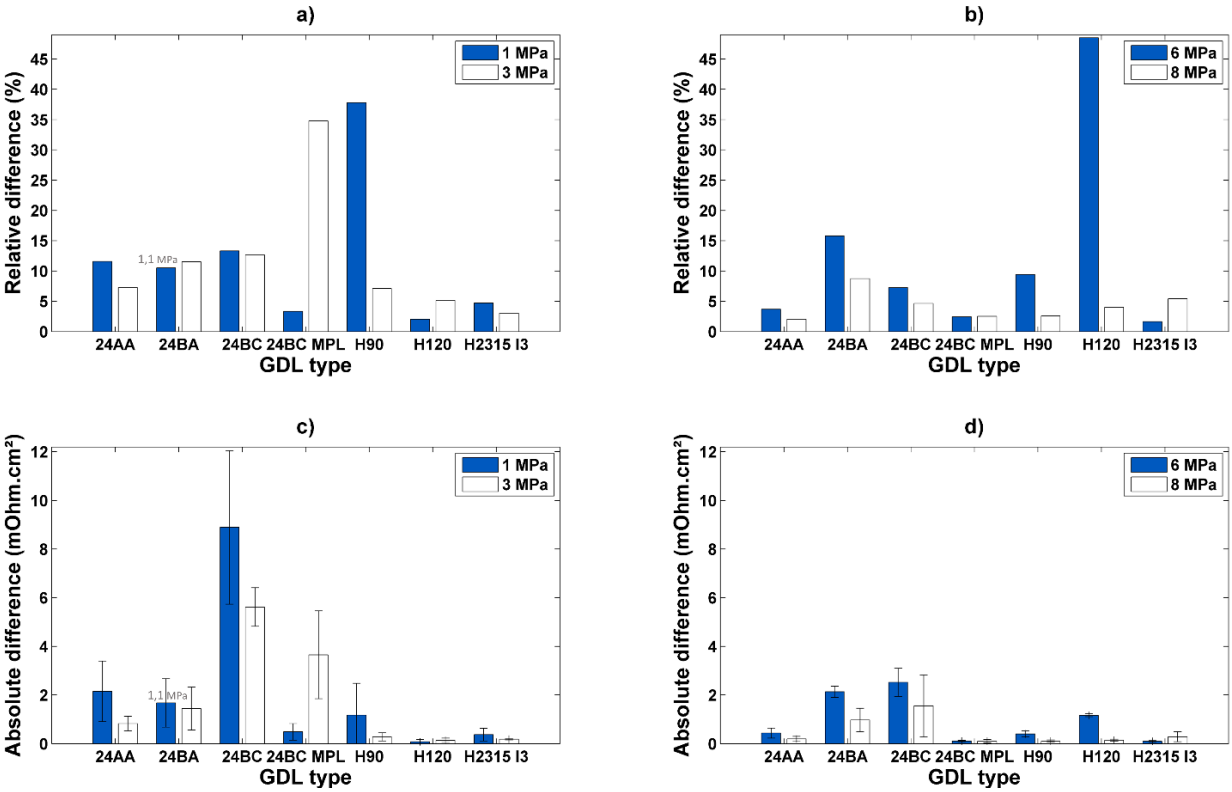

Fig 3. 9: The difference of contact resistance between the cycles as a function of compression pressure: the relative difference RCρc at low pressure and b) at high pressure. The absolute difference Cρc c) at low pressure and d) at high pressure

When analysing the absolute values (fig. 3.9), the Toray H120 manifests a low difference between cycles followed by the Freudenberg H2315 I3, while the highest ones were presented by the SGL 24 BC substrate side (PTL) followed by its MPL side. We can imagine that the Toray graphitised structure is the least sensitive to the mechanical cyclic issues. Yet, when observing the relative values, this H120 had to some degree higher difference rates. This is explained by the fact that its

contact resistance is so low compared to other GDLs that even values of less than 1.2 mOhm.cm² give relative differences RCρc of about 48%. The Freudenberg GDLs, on the other hand, has the lowest difference rate RCρc (fig. 3.9 a) and b)), which is attributed to its 3D felt structure being less sensitive to cyclic effects compared to the 2D straight carbon fibre structures. Observing the mechanical properties regarding the difference between the cycles, it is visible that, for absolute and relative difference of strain, the Freudenberg H2315 I3 has the lowest value as well (fig. 3.10), which confirms that its structure is the least sensitive to cyclic compression and therefore its ρc as well. Qiu D. et al. [9] also concluded that the felt carbon structure has the highest stability in terms of electrical resistance and microstructure after applying cyclic and steady loads. We also notice that the SGL 24 BC is mechanically the most sensitive GDL to strain difference between the cycles just as it is in terms of Cρc.

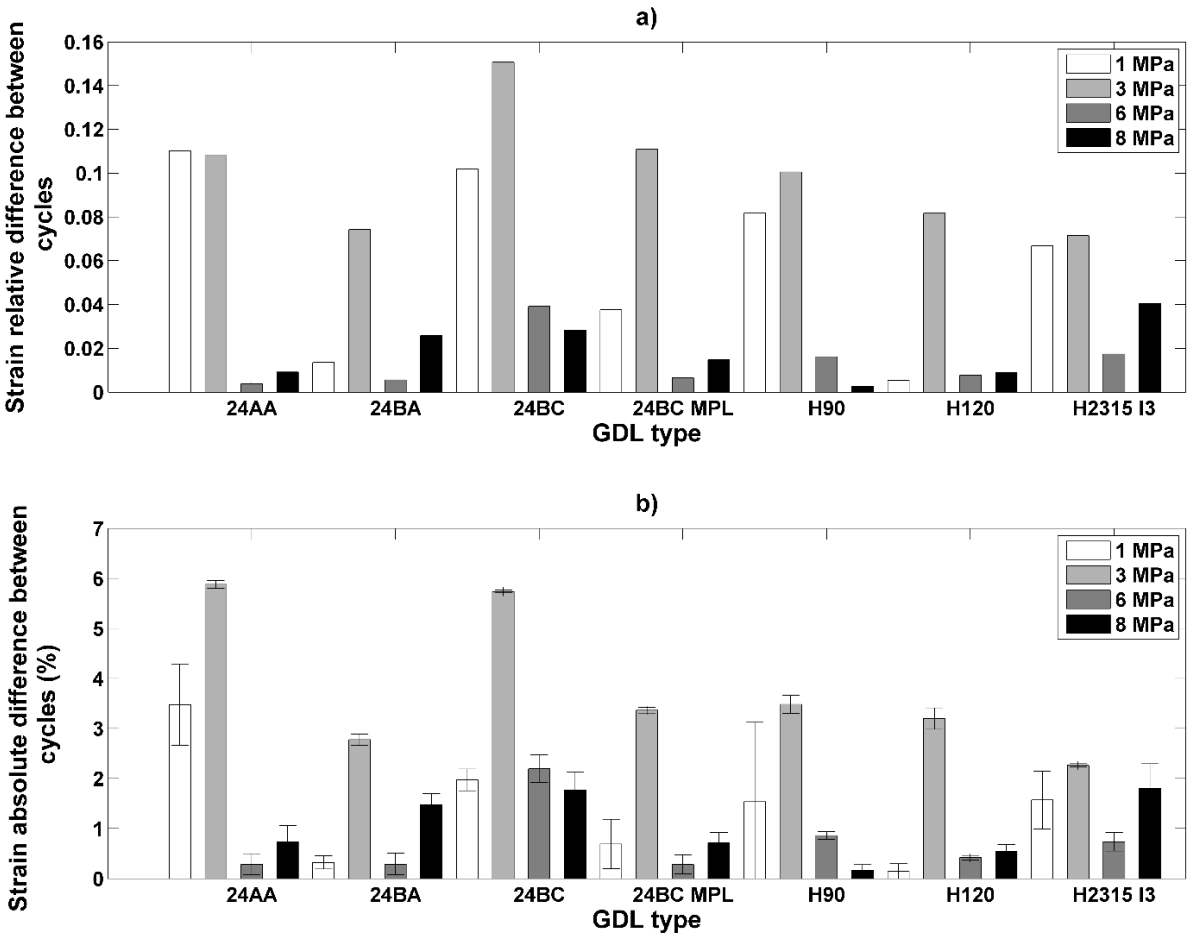

Fig 3. 10: Strain difference between cycles for 1, 3, 6 and 8 MPa, with standard deviations.

Effect of PTFE

The difference between cycles Cρc of the 24 BA increased unexpectedly compared to the SGL 24 AA. It appears that the PTFE increases the electrical sensitivity to cyclic compression. This is not explained by the mechanical difference between cycles, which decreased with PTFE. The increase of the Cρc may be attributed to the PTFE deterioration with cycles.

Effect of MPL loading

The SGL 24 BC substrate, which has originally the same structure as the SGL 24 BA, exhibited a higher absolute and relative difference Cρc and RCρc. The MPL side of the 24 BC also showed a higher RCρc at low pressure. Adding a MPL increased the difference between cycles of the GDL substrate side, electrically and mechanically.

Effect of the three tests of mechanical compression

The mean electrical contact resistance is almost constant over the three consecutive compression tests for all the GDL types with a trend of a slight decrease of ρc along the tests for the SGL GDLs (fig. 3.11) and a little increase of ρc for the other GDLs. The Cρc tends generally to decrease with the tests.

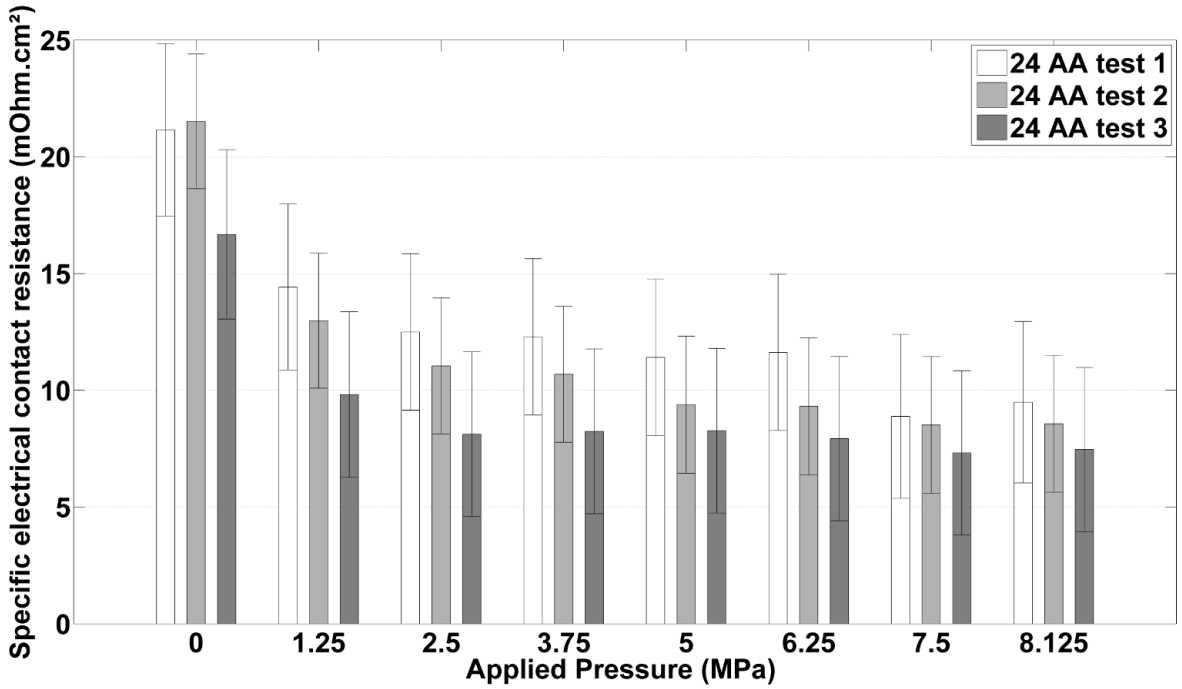

Fig 3. 11: Electrical contact resistance as a function of the applied stress for the three tests performed with SGL 24 AA.

.

3.1.2.3. Effect of the velocity of pressure application

Fig. 3.12 depicts Rc of the first loading step of compression for GDL 24AA, for the three types of compression tests. The compression range studied is 0-0. 5 MPa.

The Rc curve for (0-8 MPa) was conducted under an average compression velocity of (1.25 MPa/200s). The Rc curve for (0-1 MPa) was conducted under an average velocity of (0.25 MPa/200s). The Rc curve for (0-4 MPa) has the highest compression velocity (3 MPa/200s). We observe an effect of the velocity of pressure application on the Rc decrease. Deeper investigations could be interesting to launch in order to explain this phenomenon.

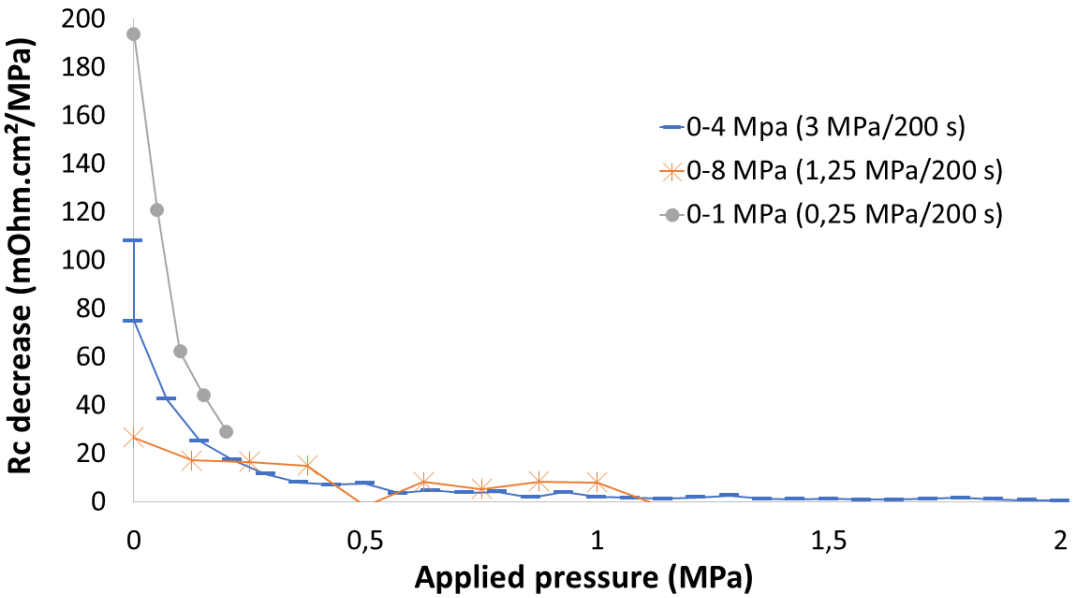

Fig 3. 12: Rc of GDL 24 AA using three compression profiles, for the first cycle of compression.

3.1.2.4. Effect of temperature

In fig. 3.13, Rc is measured under three levels of temperature, for one compression cycle (compression from 0 to 1.35 MPa, then unloading to 0.07 MPa). A very small increase of the contact resistance, with temperature varying from room temperature to 70°C is observed. But at very low pressure, Rc is higher for low temperatures, the change occurs in the range [0.07 -0.21 MPa]. The reduction of Rc with compression seems more substantial for low temperatures.

First, we observe that contact resistance of uncompressed GDLs (or compressed with a very low pressure) decreases with temperature. We know that contact resistance also decreases with compression (observed earlier) because of the compression of the GDL structure. Higher temperature tends to expand materials,

meaning that compression is harder at higher temperature and the reduction of GDL thickness will be lower at high temperatures. This may explain why contact resistance of the GDL decreases more importantly with compression pressure at low temperatures (blue curve) while it decreases with a smaller rate at higher temperatures (green and red curves) with compression. Thus, the curves intersect at [0,07 MPa-0,021 MPa].

If we compare loading-unloading cycles, we notice that the gap between the loading curve and the unloading one increases with temperature.

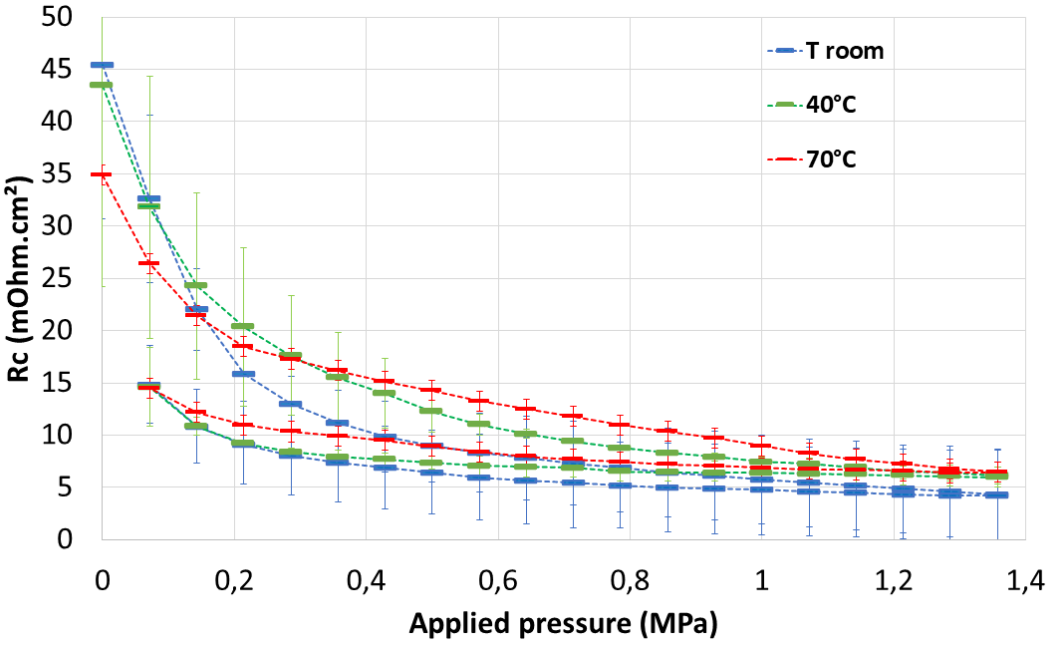

Fig 3. 13: Effect of temperature on Rc.

3.2. Through plane resistance

3.2.1. Measurement method

The electrical area specific through-plane resistivity - Rtp (mOhm.cm²) - of GDLs is measured using gold coated electrodes and under mechanical compression. Two set-ups of measurement have been used. In the first set-up, the pressure was created by putting static weight loads over the electrodes. In the second set-up, the mechanical compression was controlled by a press. The effect of cyclic compression effect and temperature variation on the through-plane resistance was evaluated.

3.2.1.1. GDLs investigated

Different structures and compositions of carbon paper GDLs, from SGL and Toray, were evaluated. They are described in Table 3.5.

GDL reference	Thickness (from supplier) (µm)	Structure and composition
SGL 24 AA	190 +/- 30	Straight fibre
SGL 24 BA	190 +/- 30	Straight fibre +5% PTFE
SGL 24 BC	235 +/- 30	Straight fibre +5% PTFE (in substrate) + MPL
SGL 10 BA	400	Felt fibre + 5% PTFE
Toray H 120	370	Graphitised straight fibre

Table 3. 5: GDLs used.

3.2.1.2. Measurement using static weights set-up

The area specific through-plane resistance Rtp was measured by placing a GDL between two circular gold coated electrodes (1 cm^2). These electrodes were supported by two plates. Different weights were placed on the upper plate leading to known loads (1-2 MPa). A current of 1 A was applied on these electrodes and the voltage drop was measured with an Agilent digital multi-meter. Two GDLs types were evaluated using this method: SGL 24 AA and SGL 24 BA. Three samples were used for every type. The cyclic compression was applied by altering higher and lower weights. The values of voltage drop were measured after a time of stabilisation (some minutes).

Let the reader note that the zero-compression value corresponds to the application on the GDL of the upper plate without extra-weight and not to an absolute zero.

Compression profile followed the curve depicted in fig. 3.14.

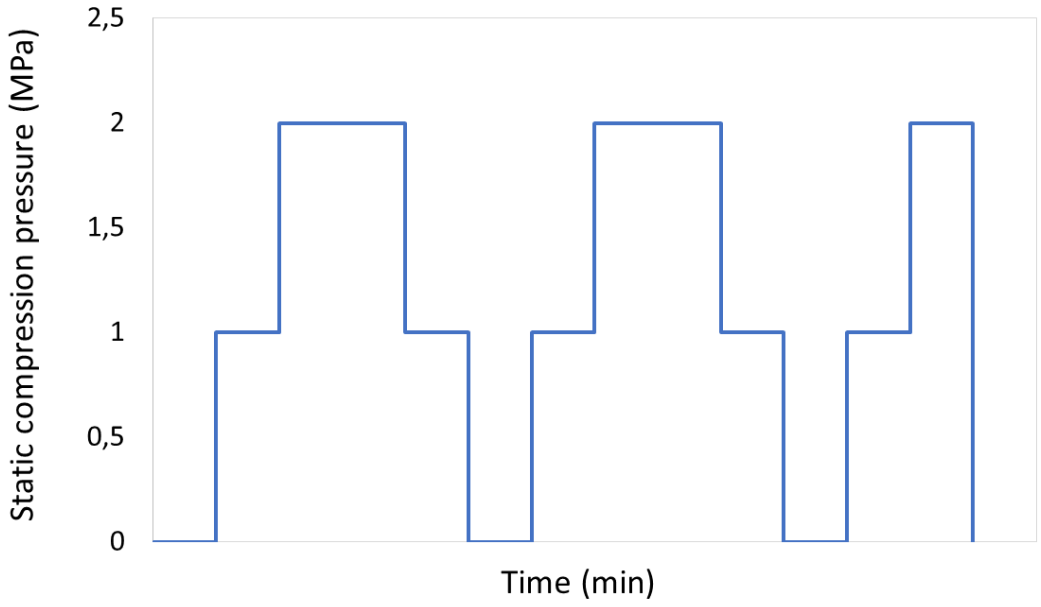

Fig 3. 14: Static weight compression profile.

3.2.1.3. Measurement under controlled compression

In this method, Rtp was measured by placing a GDL between two square gold coated electrodes (2.25 cm^2), and by applying a four-probe measurement set-up. A current of 1 A was applied on these electrodes and the voltage drop was measured using two probes placed on the electrodes. The compression was controlled by a mechanical press that can hold ten compression levels. Three samples were used for each GDL. Rtp was measured under low pressure (up to 2 MPa) and high pressure (up to 4 MPa). The cyclic compression was evaluated by altering higher and lower loads. For the SGL 24 BC, another way was also used, by repeating the same procedure three times on the same GDL sample (which means that the same mechanical loading-unloading procedure is applied three times on the GDLs). The temperature variation effect was evaluated by heating the press holding plates to a fixed temperature (45°C and 70°C) and measuring the Rtp in the same way as the high-pressure procedure.

Fig. 3.15 shows the Rtp measurement apparatus.

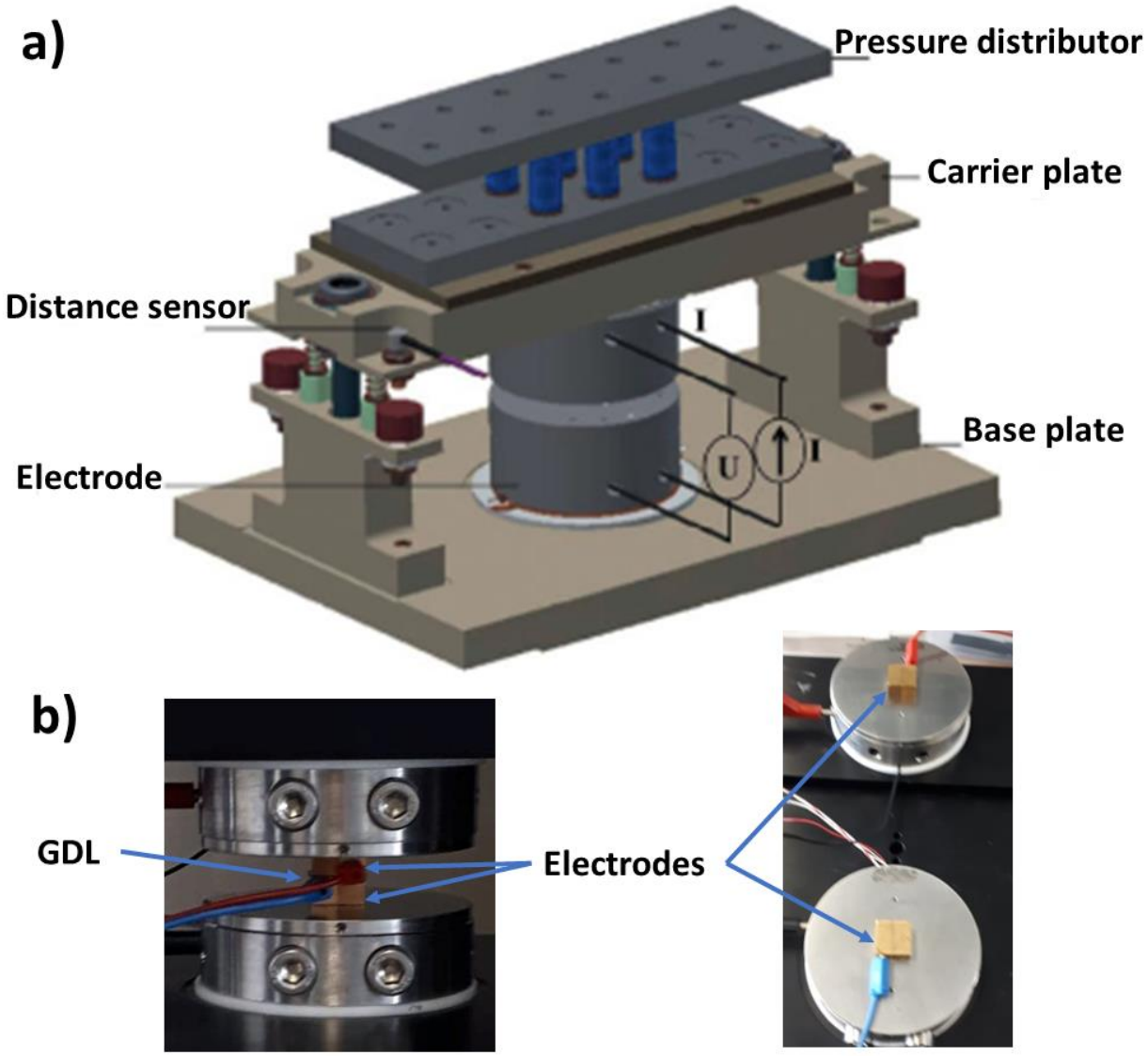

Fig 3. 15: Gold coated electrode apparatus used to measure Rtp: a) Rtp measurement apparatus [10], b) golden electrodes.

Various compression cyclic compression profiles of ten levels (press limit) were used, such as in fig. 3.16.

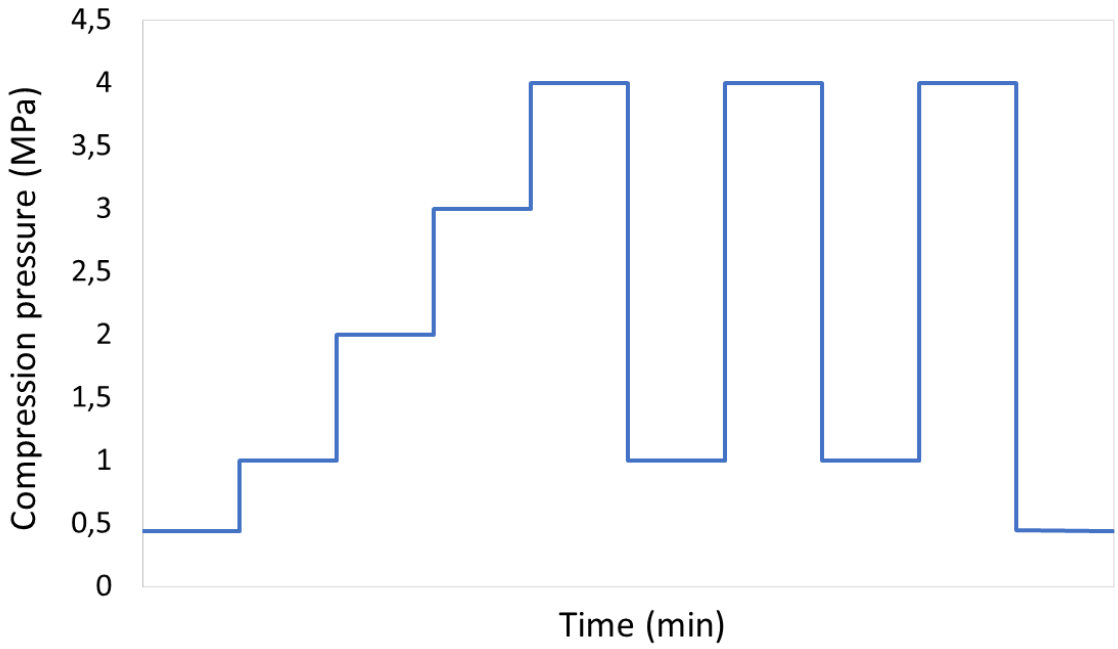

Fig 3. 16: A profile of controlled compression pressure.

3.2.2. Experimental results

3.2.2.1 Measurement using static weights set-up

These measurements are done at room temperature. The compression force applied is depicted in fig. 3.17.

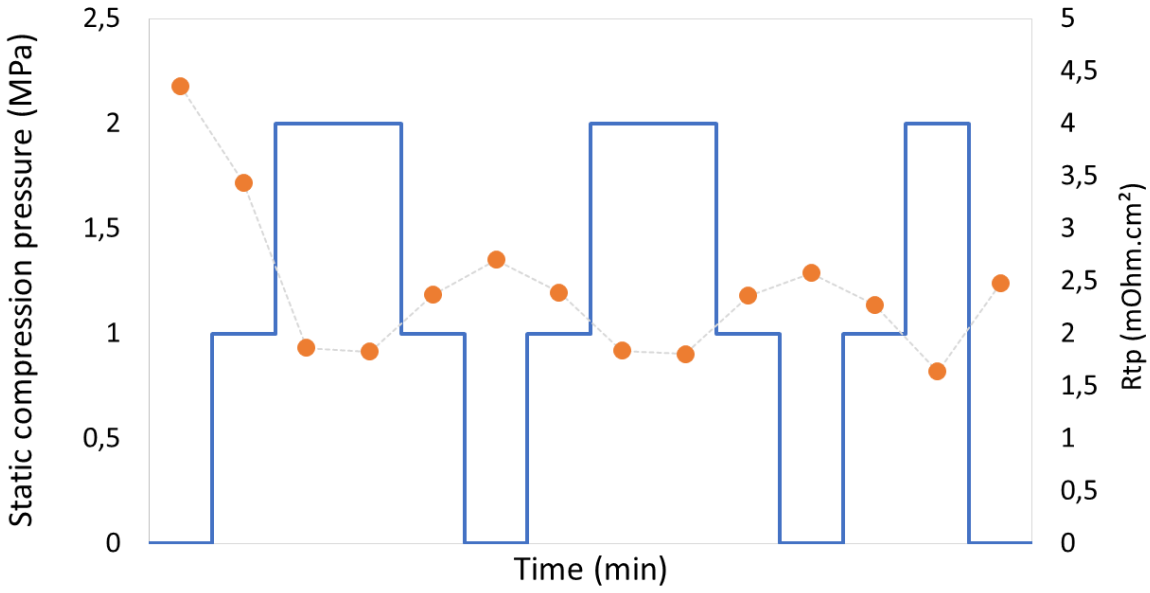

Fig 3. 17: Static weight compression pressure (blue line) and corresponding Rtp of GDL 24 BA as a function of time (orange dots).

The results of Rtp are depicted in fig 3.16.

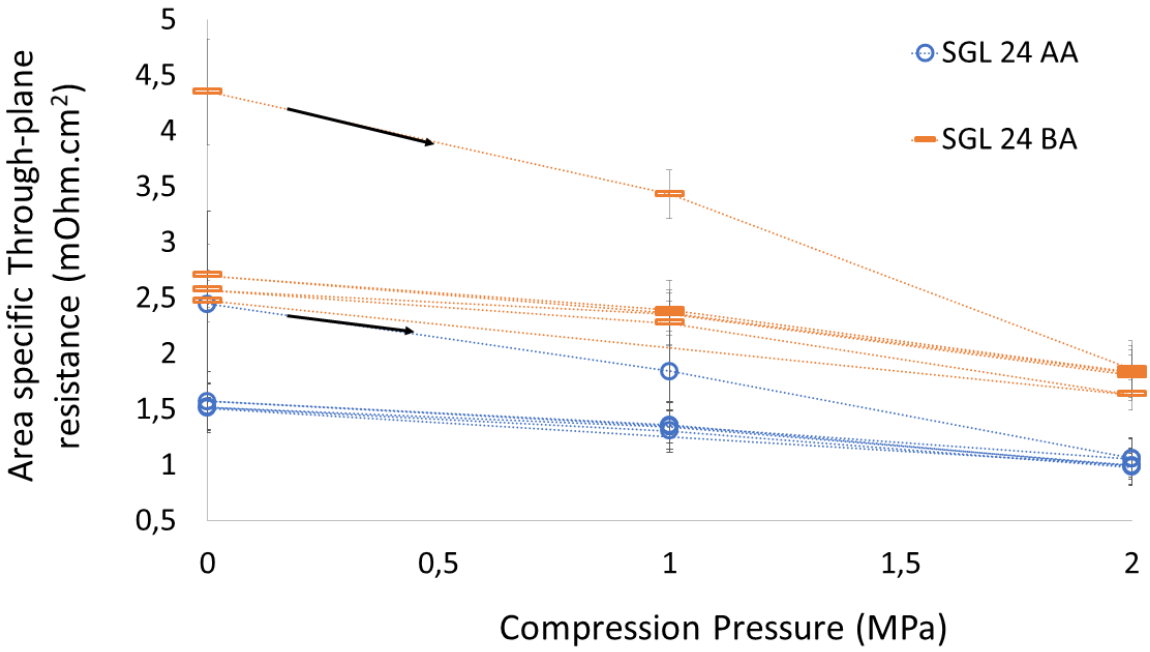

Fig 3. 18: Trough-plane resistance with static weights for SGL 24 AA & SGL 24 BA.

We can observe in fig 3.18:

- A decrease of Rtp with compression.
- A higher Rtp value for SGL 24 BA compared to those obtained for SGL 24 AA. The values for SGL 24 BA range from 1.81 to 4.35 mOhm.cm². The values for SGL 24 AA from 0.98 to 2.45 mOhm.cm².
- A decrease of Rtp along the cycles of compression, especially between the first compression loading and the rest of the cycles.

3.2.2.2 Measurement under controlled compression

The compression pressure is applied following the profile displayed in fig 3.19.

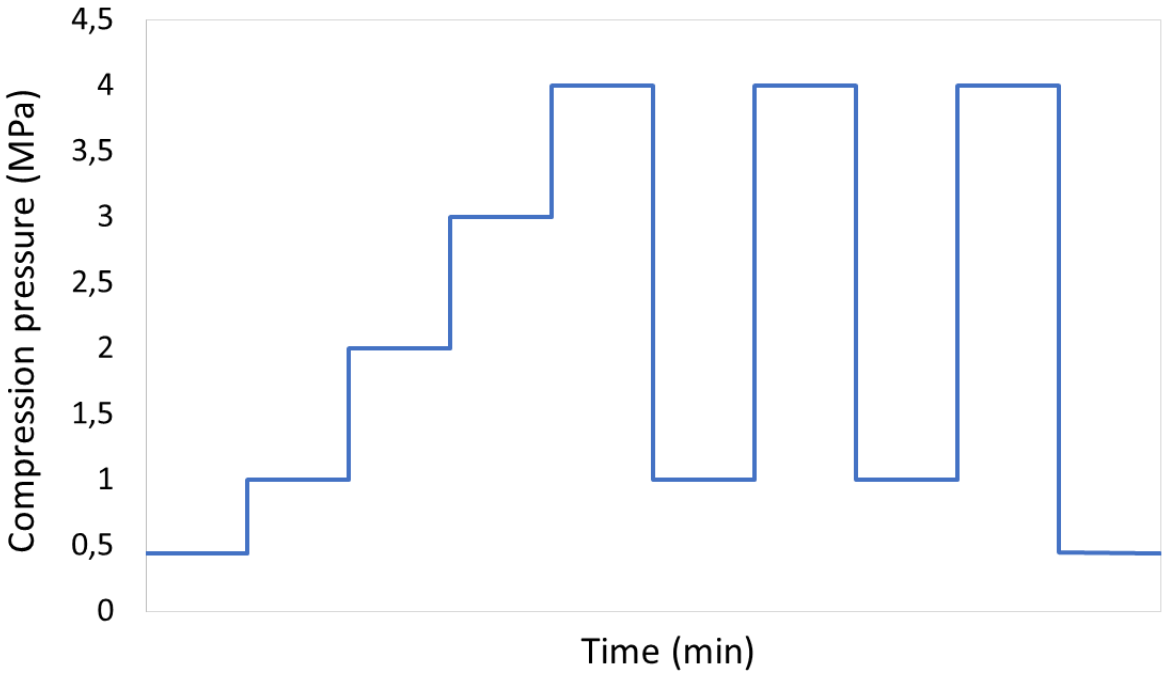

Fig 3. 19: High compression pressure applied on GDLs while measuring Rtp.

Fig 3.20 represents the Rtp of the different GDLs as a function of compression pressure.

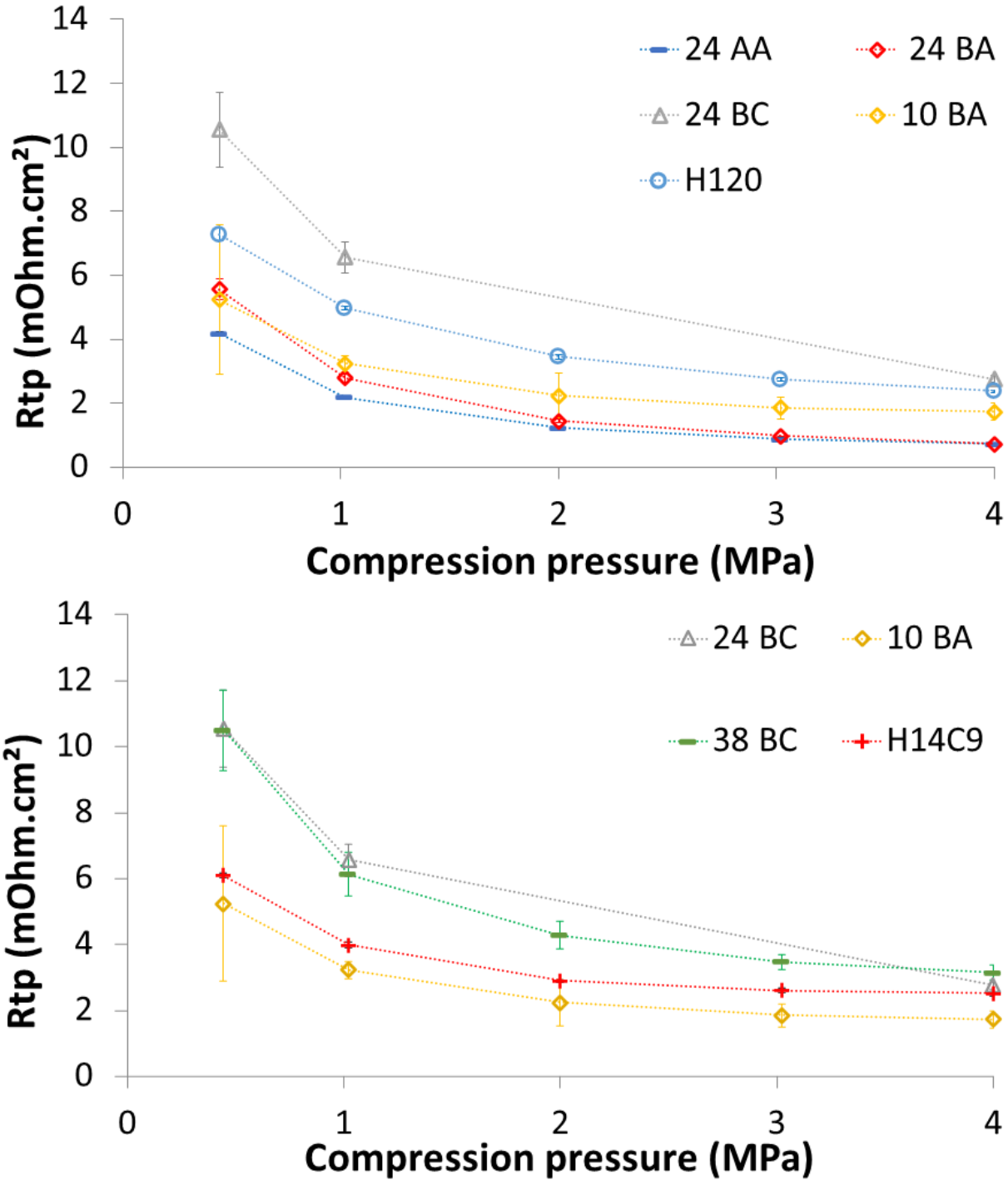

Fig 3. 20: Rtp Vs applied compression pressure (First cycle of compression).

Area specific electrical Rtp varies between 0.66 and 13.53 mOhm.cm² for all GDLs between 0.44 and 4 MPa.

A non-linear decrease of Rtp with compression is observed in fig 3.20. An important decrease is observed from 0 to 2 MPa, then a lower one above 2 MPa.

SGL 24 AA and 24 BA show the smallest Rtp. The higher Rtp values are observed for SGL 10 BA, H14C9, H120, 24 BC, and 38 BC.

3.2.3. Discussion

3.2.3.1. Comparison between the static-weight method and the press-compression method

The results of Rtp obtained for SGL 24 BA following the compression profile presented in fig 3.19, using static-weight method and controlled-compression method, are depicted in fig 3.21.

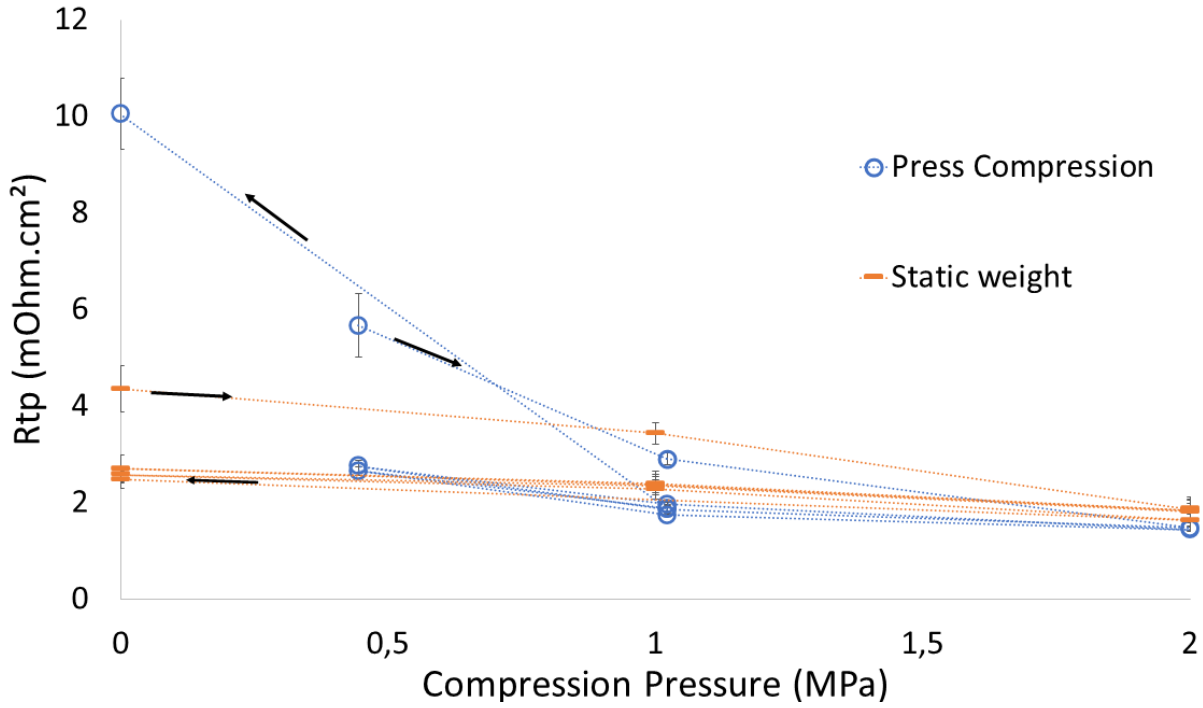

Fig 3. 21: Static weights Vs Press compression method.

The curves seem quite similar at compression values for 1 MPa and 2 MPa compression. For instance, 2 MPa values of Rtp are 1.64 +/-0.13 and 1.45 +/-0.05 mOhm.cm², which means that using either method is reliable.

3.2.3.2. Effect of cyclic compression

Effect of cyclic compression

The cyclic compression induces a Rtp decrease with cycles, especially for lower loads as can be shown in fig. 3.22 for 1 MPa and for all GDLs. The greatest decrease is observed from Cycle 1 to Cycle 2. Then, a lower rate of decrease is observed as seen in Table 3.6.

SGL 24 BA demonstrates the highest difference percentage (54 %) while the H14C9 has the lowest one (21%).

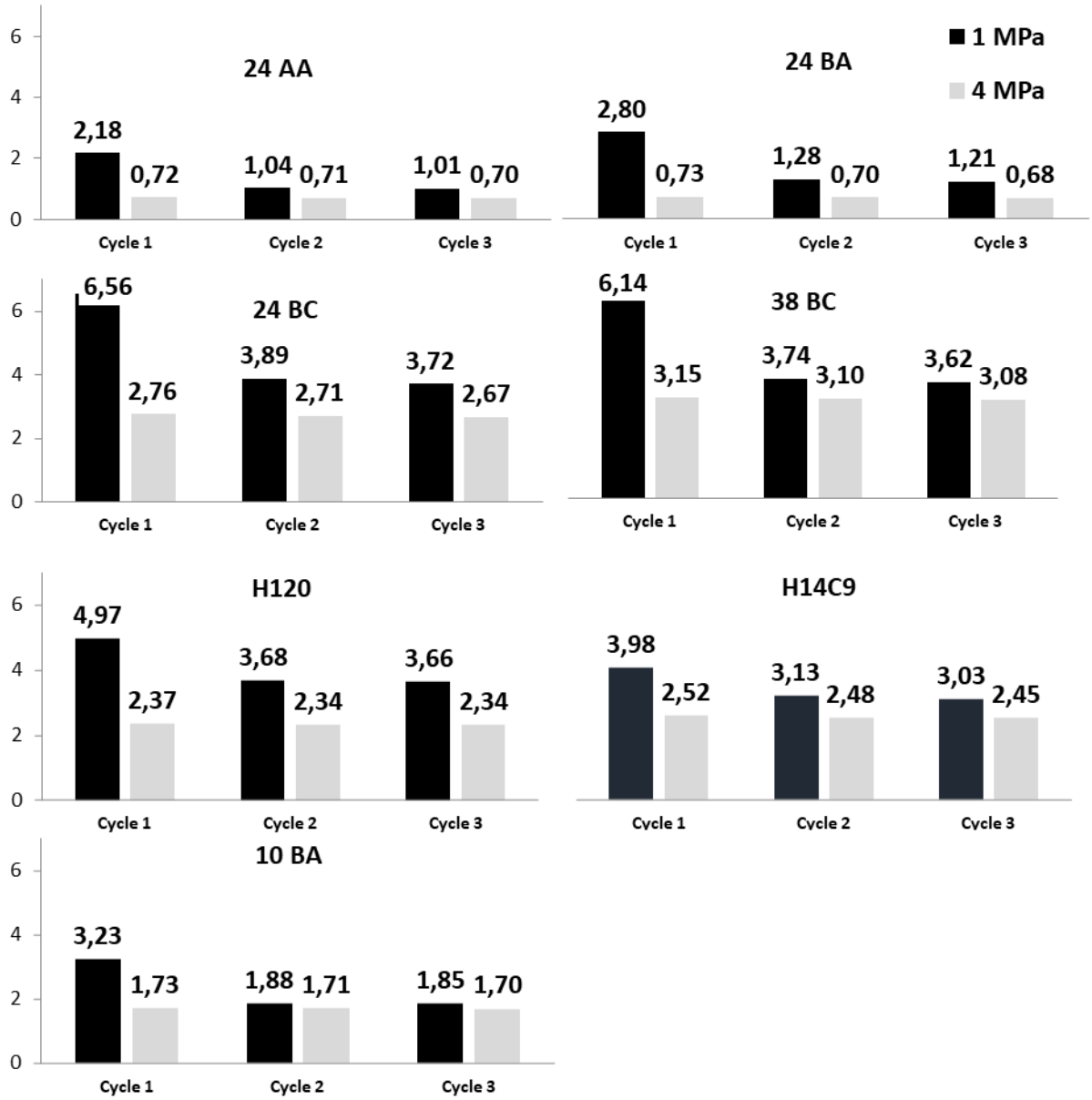

Fig 3. 22: Rtp values at different cycles of compression for 1 and 4 MPa.

	Pressure	24 AA	24 BA	24 BC	10 BA	H 120	H14C9	38 BC
Cycle2/Cycle1 (%)	1 MPa	52.58	54,42	40.62	42.00	26.02	21.47	39.12
	4 MPa	1.04	4,12	1.90	1.30	1.42	1.79	1.67
Cycle3/Cycle2 (%)	1 MPa	2.17	5,29	4.43	1.2	0.61	3.12	3.21
	4 MPa	2.11	2,15	1.39	0.44	0	0.91	0.73

Table 3. 6: Rate of Rc decrease along the cycles of compression.

Effect of cycle's peak load value/ methods of compression for SGL 24BC

For the 24 BC, a second method was also used to determine the effect of cyclic compression.

The cycle of compression used in fig 3.23 was repeated three times on the same GDL sample. The results for Rtp are depicted in fig 3.24.

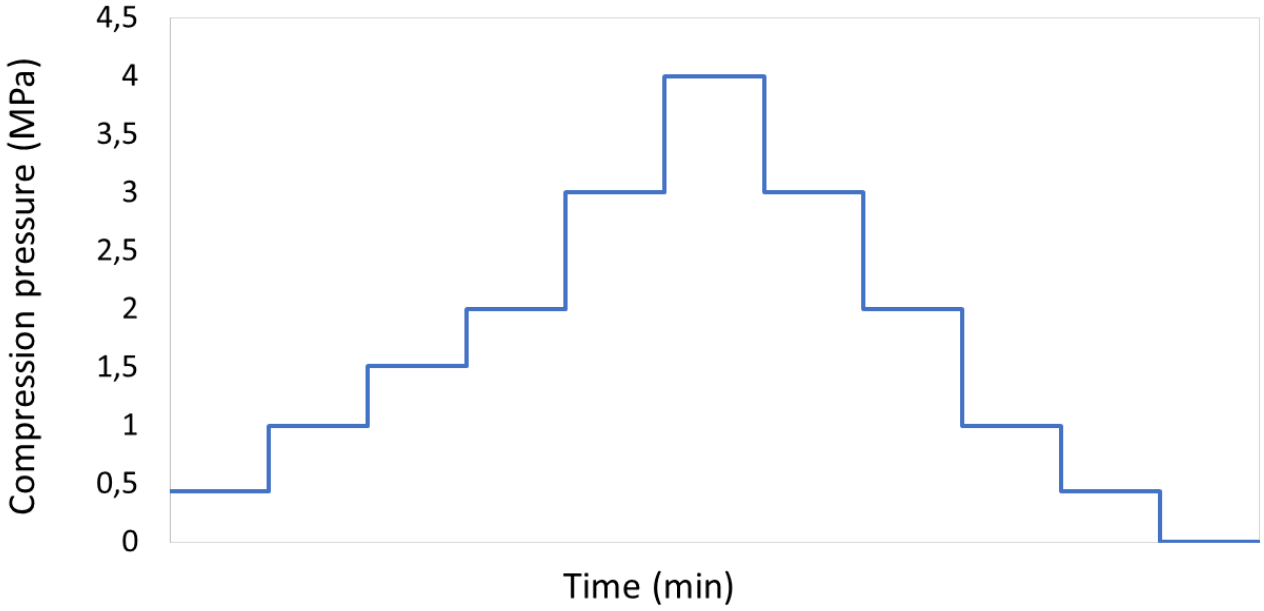

Fig 3. 23: One cycle of compression pressure profile for 24 BC.

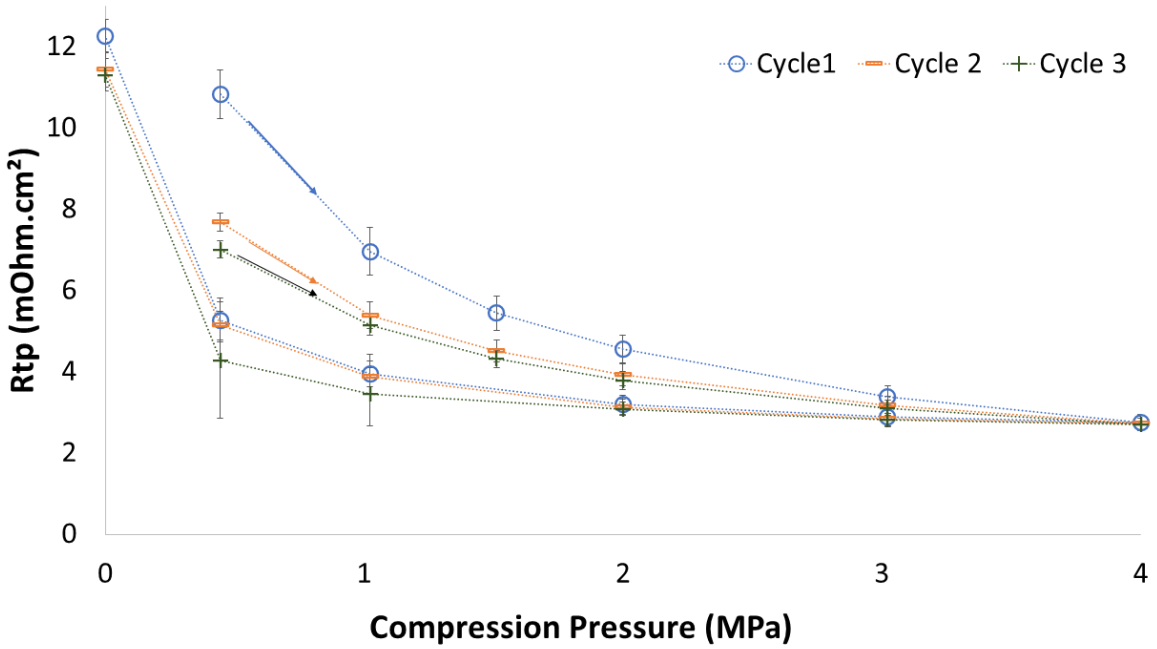

Fig 3. 24: Rtp for the three cycles of compression.

The effect of the cycles of compression is shown in fig 3.24. First, we can clearly see that the values of Rtp are different between the loading and the unloading phases of the cycles of compression. There is also a difference of value between the different cycles of compression. In a single cycle, Rtp is higher at the loading phase. Added to that, Rtp decreases along the cycles as it can be observed (the blue curve representing the first cycle has the highest Rtp values).

The rate of difference of Rtp between the cycles of compression is illustrated in Table 3.7 for all the values of compression.

Pressure (MPa)	**0.44**	**1.02**	**1.51**	**2**	**3.02**	**4**	**3.02**	**2**	**1.02**	**0.44**	**0**
Cycle 2/Cycle 1 (%)	29.11	22.52	17.22	13.96	5.78	1.09	1.30	1.88	1.99	2.42	6.73
Cycle 3/Cycle 2 (%)	8.60	4.73	4.16	3.63	2.12	0.55	1.05	1.20	10.47	16.62	1.15

Table 3. 7: Difference of Rtp between the cycles of compression.

The difference rate between cycles seems less important using this method compared to the first method (40.62% for 1 MPa and 1.90% for 4 MPa) for Cycle 2/Cycle 1 (%) rate. Hysteresis is calculated at 2 MPa in Table 3.8, (16 to 17%), for the three cycles of compression.

24 BC	**(Yload-Yunload) / (Ymax-Ymin)×100%**
Cycle1	17.12
Cycle 2	16.24
Cycle 3	16.23

Table 3. 8: Hysteresis rate for the cycles of compression measured for a medium value of compression equal to 2 MPa.

Effect of a low maximum pressure

Table 3.9 compares the difference of Rtp when the highest compression pressure is 2 MPa. The applied pressure is presented in fig 3.25.

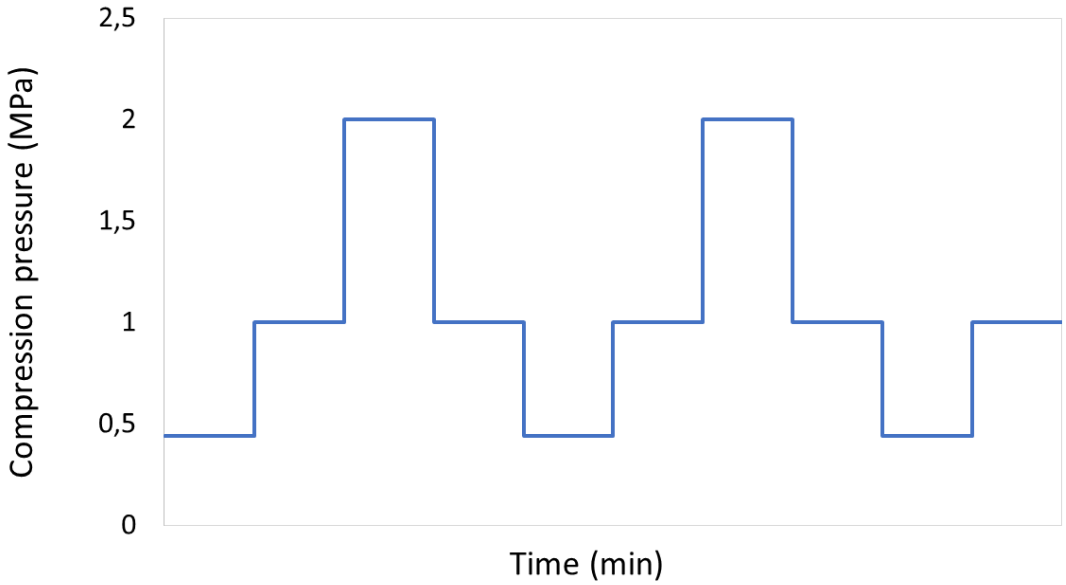

Fig 3. 25: Low compression pressure profile.

	Cycle 2/cycle 1					Cycle 3/cycle 2
GDL/Pressure (MPa)	0.44	1.02	2	1.02	0.44	1
24 BA	51.32	32.30	2.03	6.43	3.80	4.20
24 BC	44.65	21.30	2.25	3.68	3.93	3.47
10 BA	38.47	21.96	1.05	2.29	2.25	2.00
H 120	20.53	8.66	0.26	0.73	1.44	2.00

Table 3. 9: Cycle 2 to cycle 1 relative difference of Rtp and cycle3/cycle2 for 1 MPa.

Unexpectedly, a lower difference for a lower compression maximum value is observed for 1 MPa when comparing Table 3.9 with Table 3.6. This might be due to the difference between the two compression methods, the second one being slower, passing by all the intermediate values when loading and unloading. This is not the case for the third to second cycle of compression, for 1 MPa, for the 24 BA and 24 BC.

3.2.3.3. Effect of PTFE, MPL and GDL structure

We can see that SGL 24 BA has a higher Rtp compared to SGL 24 AA, which means that PTFE increases through-plane resistance. We also observe that GDLs with a

MPL have a higher Rtp, probably because of a higher thickness, as we also observe that thicker GDLs (10 BA, H120, 38 BC, and H14C9) have higher Rtp values. The decrease of Rtp with compression is due to two physical facts: first, the decrease of its thickness, meaning a decrease of the distance traveled by the current between two electrodes, and secondly the increase of the density of the GDL with compression as fibers tend to fill the pores and void space making the GDL more conductive. The decrease of Rtp (area specific through-plane resistance (in $mOhm.cm^2$) for example for GDL Toray H120 between 0,44 MPa and 4 MPa is about 67%; this is due to both factors. If we compare with the through-plane resistivity (mOhm.cm) by dividing the Rtp by the thickness value of H 120 at that pressure (0,44 and 4 MPa), we found a decrease of 47% of the resistivity which confirms that point (if the decrease of Rtp was only due to the change in thickness, the resistivity would have remained constant).

3.2.3.4. Effect of temperature variation

Rtp measured at different temperatures (room temperature, a medium one (45-50 °C, and at high temperature 70°C) under compression is depicted in fig 3.26.

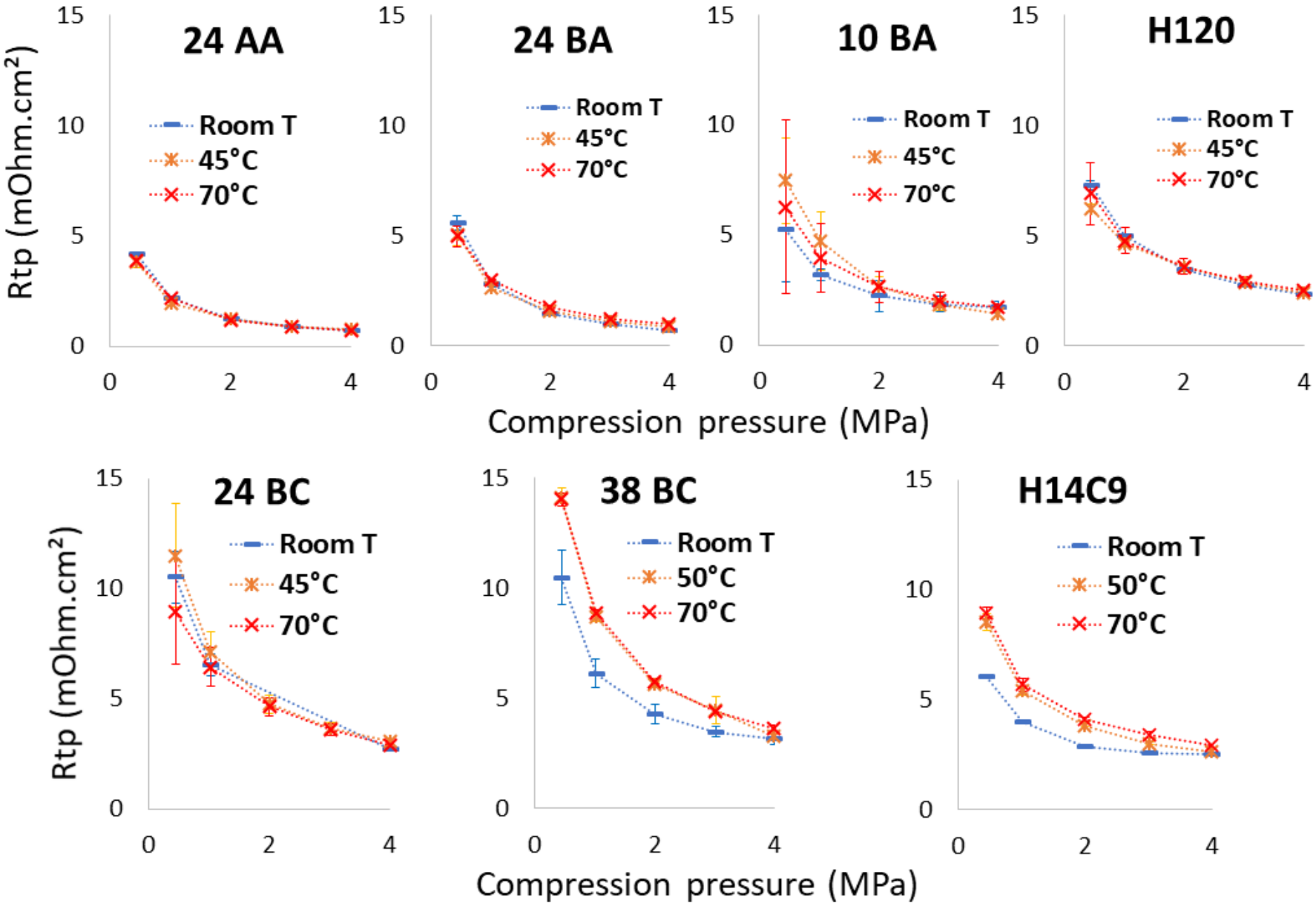

Fig 3. 26: Rtp as a function of applied compression and temperature (loading of first cycle).

At this stage, it is difficult to have accurate conclusions on the temperature effect. The following observations can be made:

When heating the press, the Rtp decreases with temperature, However, four among seven GDLs show a higher Rtp for temperatures higher than room temperature (24 BA, 10 BA, H14C9, 38 BC). Temperature effect seems more visible at lower pressure.

For pressure values higher than 2 MPa for all GDLs (except 10BA and 24 AA), Rtp increases with temperature (still the increase is not necessarily out of the error bars).

Up to 2 MPa:

- For the GDLs 24 AA and H120, Rtp decreases with temperature if Rtp at room temperature is compared with Rtp at 45°C and 70°C (but this is not the case between 45°C and 70°C).
- For the GDLs 10 BA, 24 BA, 38 BC, and H14C8, Rtp increases with temperature if Rtp at room temperature is compared with Rtp at 45°C and 70°C (but this is not the case between 45°C and 70°C for the 10 BA).
- For the 24 BC, Rtp decreases with temperature (when comparing only GDLs compressed for at least 1 min 15 s).

3.2.3.5. Humidity effect

FC produces water and can be fed by humidified reactant gases. Hence, an accurate study on GDL physical properties should not only consider dry GDLs, but also the effect of humidity / water saturation.

Experimental Procedure

Measurements were done using water saturated GDLs instead of controlled humidity because it is easier to monitor.

We started our study by a simple carbon paper GDL, the SGL 24 AA (which is untreated with hydrophobic agent). GDLs were cut into 1x1=1 cm^2 sheets (24 pieces), and weighted dry (before water soaking), using a "Sartorius scale" with a 10 µg resolution.

First, we had to find a way to saturate the GDLs at 100%. First, GDLs were simply soaked for different duration (1 h, 2 h, …, 8 h) in deionised water to find a way to determine the 100% saturation point. However, this was not possible as the water uptake was high (more than theoretical 100% saturated pores). GDLs were soaked in small bottles containing 20 ml of deionised water. We also used magnetic stirring to rotate the water and we had the same results.

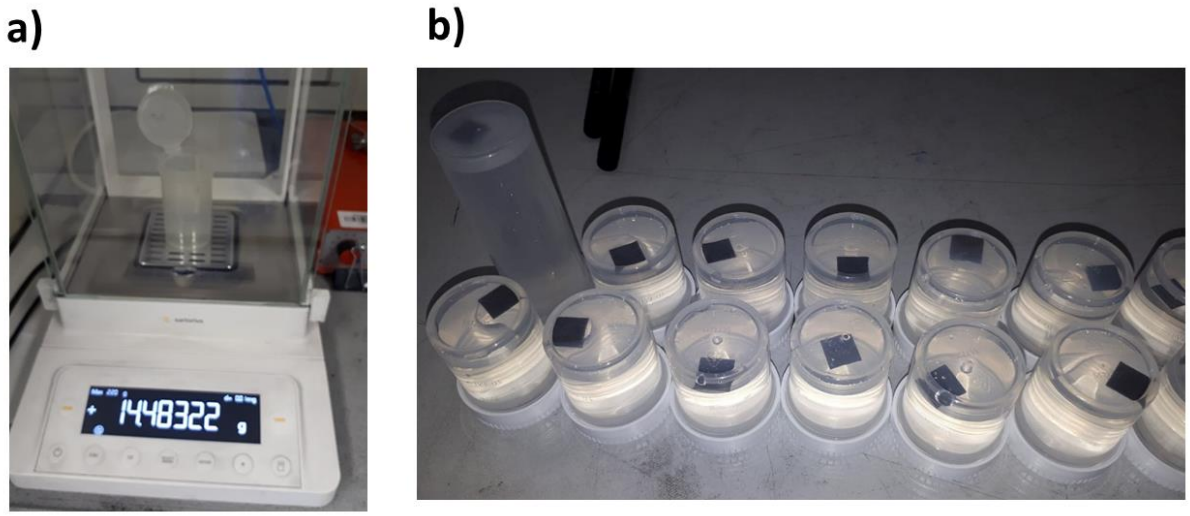

Fig 3. 27: GDLs soaked in deionised water for different hours. a) weighing scale, b) GDLs soaked in deionised water.

Fig 3.28 and fig 3.29 show the evaluation of GDL weight with time of evaporation for the different GDLs that were soaked without and with magnetic stirring.

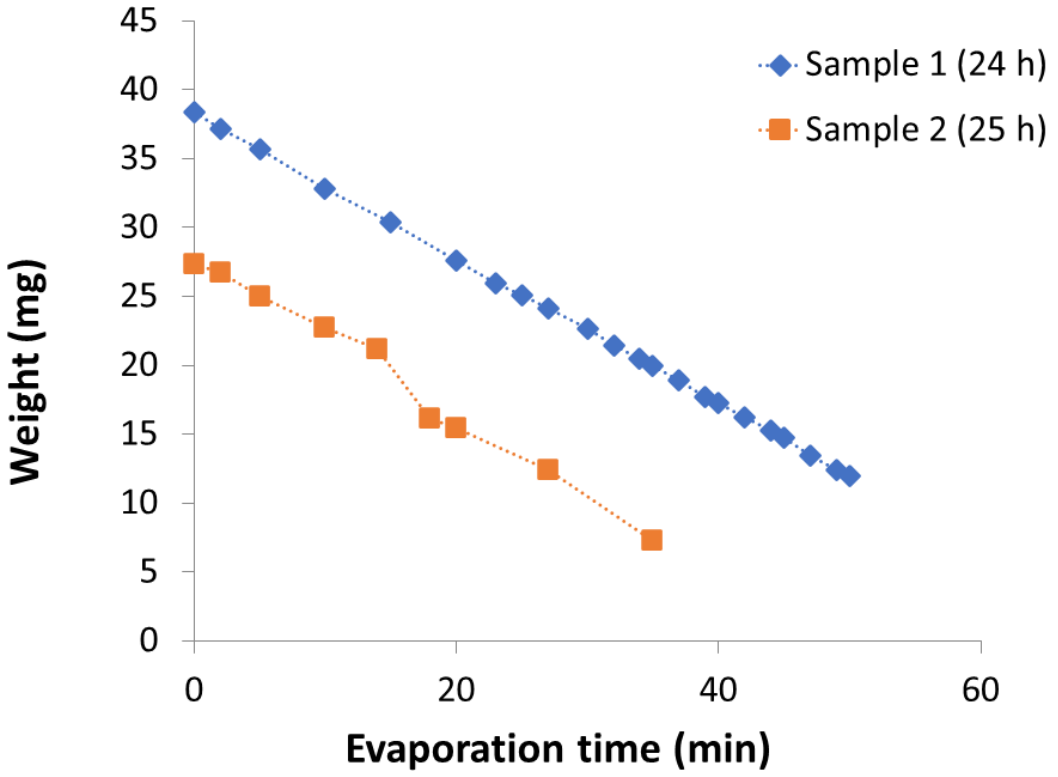

Fig 3. 28: Evaporation speed rate of wet GDL after 24 h of deionised water soaking (GDL 24 AA).

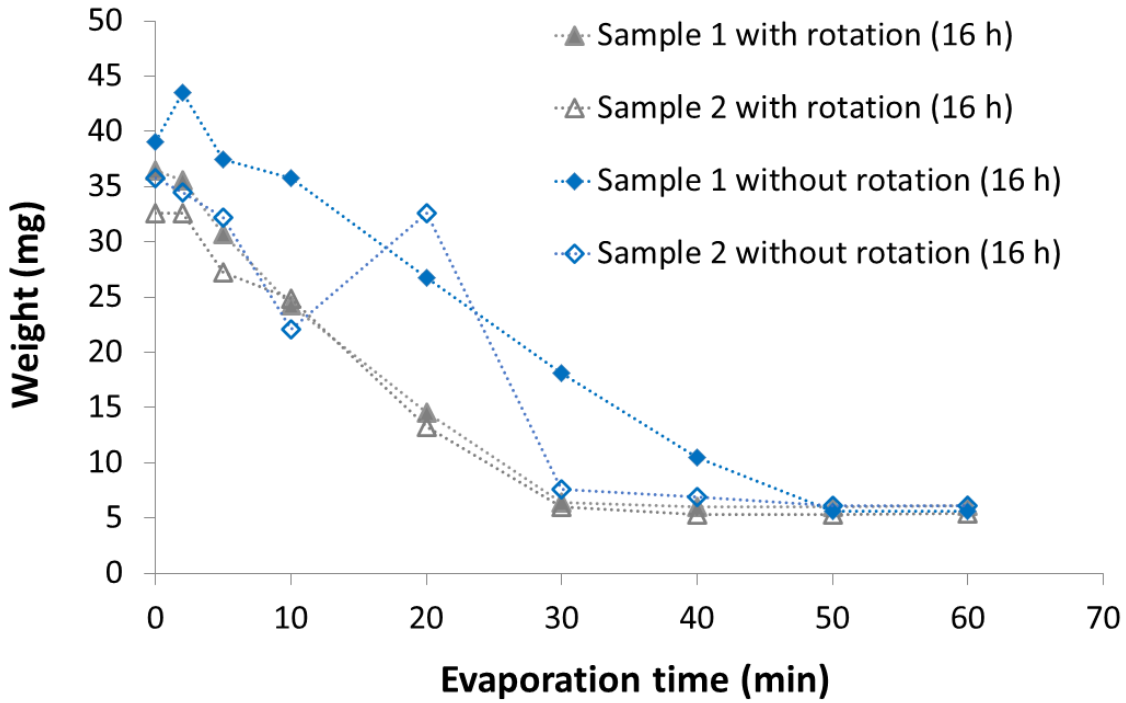

Fig 3. 29: Evaporation speed rate of wet GDL after 24 h of deionised water soaking with/without magnetic stirring (GDL 24 AA).

Although the water intake is different from one experience to another, the speed of evaporation is practically the same as we observe the slope of the different curves (see figures below). The time of complete evaporation only depends on the quantity of water intake.

To get 100% saturated GDLs, we followed a method, called Vapor impregnation method. It is used in many works investigating the effect of saturation on the diffusion coefficient of the GDL [11].

In our study, we choose to use a vacuum pump of -0.95 bar meaning a pressure of 5 kPa, and for 30 min. GDLs were put into water. With this method 100% saturated GDLs were obtained. Fig 3.30 shows the GDL inside the depressurised chamber.

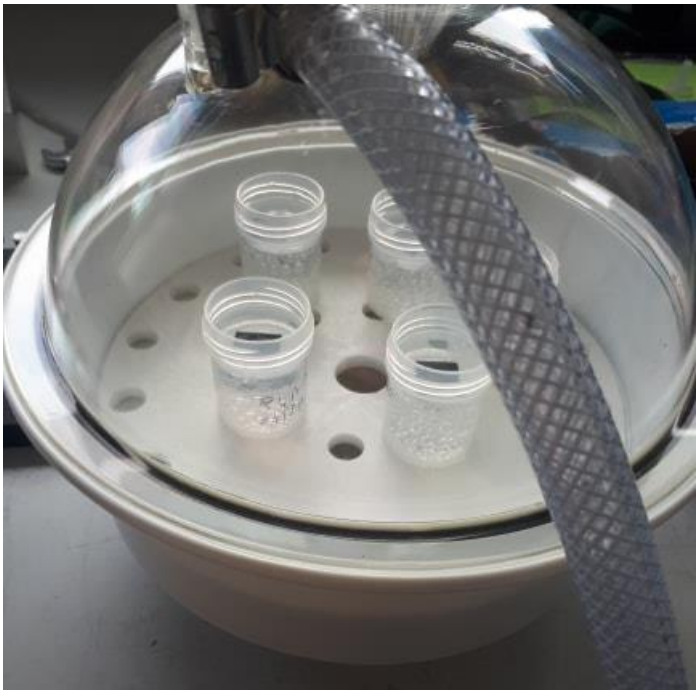

Fig 3. 30: GDLs inside a chamber connected with a vacuum pump.

The electrical areal specific through-plane resistivity of some carbon paper GDLs has been measured using gold-coated electrodes under cyclic mechanical compression from 0 to 4 MPa and under saturated water obtained using the method described above.
Untreated GDLs of various thicknesses and porosities of both SGL (24 AA, 25 AA, 35 AA) and Toray (H 60, H120) were investigated. GDL 24 BA containing PTFE and GDL 24 BC coated with an MPL were also examined.
GDLs H120 and 24 AA were also put between two graphite plates and the total resistance was measured under saturated and dry GDL conditions.

Results

GDLs were saturated with water. Rtp was measured using the same apparatus as in fig 3.15 and the results were compared to dry Rtp GDLs. The results of all characterised GDLs are presented in the following figures. Fig 3.31 shows Rtp results for GDL 24 AA and H120. Similar results were found when measuring the total resistance of these two GDLs sandwiched between two graphite plates.

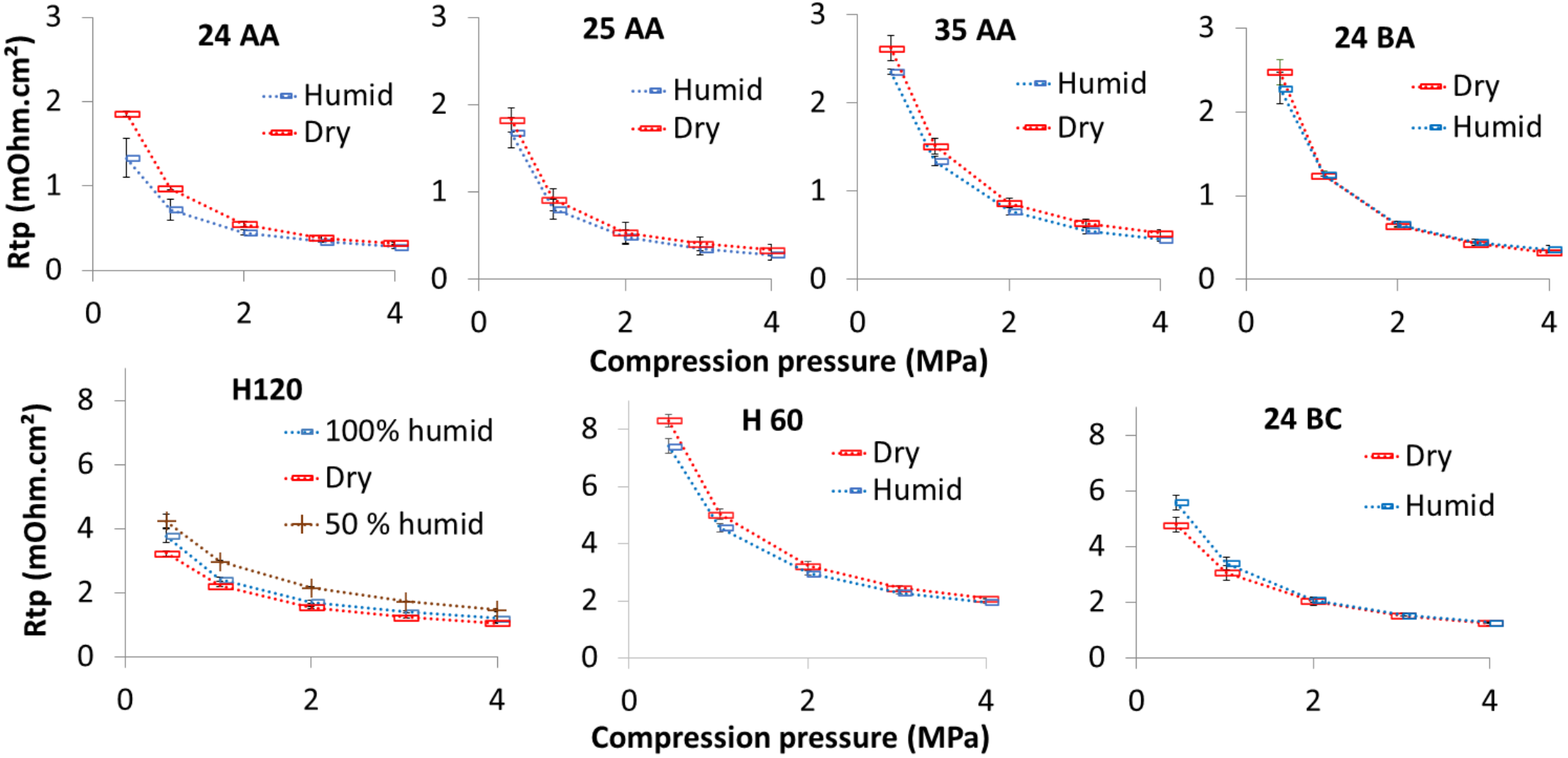

Fig 3. 31: Fig. 3. 31: Rtp as a function of compression under saturated water conditions for GDLs 24 AA and H 120.

First two carbon papers were specifically investigated: a thick graphitised GDL Toray H120 and a thin carbonised GDL SGL 24 AA. The through-plane resistance for thick GDLs increases with water saturation while for thin GDLs Rtp decreases with water saturation. This behaviour was found when these two types of GDLs were put between two graphite plates.

Then, other simple carbon paper GDLs from both manufacturers with different porosity ratios or thicknesses were analysed. All these GDLs resistances decrease with water saturation following the behaviour of the thin SGL 24 AA. This behaviour can be attributed to a higher compression of humid GDLs compared to dry GDLs as they were found to be softer in the study of S. Rahapood [13]. We notice also that the gap between the dry and humid GDLs are higher at low pressure.

GDLs with PTFE and MPL, which make them more difficult to saturate with water were investigated with a low humidity rate. Their resistances increased with humidity. This may be attributed to an extra non-conductive layer made by the deionised water that tends not to stay inside the hydrophobic GDL, which increases the measured through-plane resistance. GDL H120 has a different behaviour compared to all other untreated GDLs. Its resistance increases with water saturation. However, this increase is not monotonous as a higher resistance is observed for a 50% initially saturated GDL compared to a 100% saturated GDL. Further investigations are needed to explain this behaviour.

3.3. In-plane resistance

3.3.1. Measurement method (apparatus, method, uncertainty, GDLs used)

The electrical in-plane resistivity “Rip” of several GDLs is measured under cyclic mechanical compression (from 0 to 4 MPa).

3.3.1.1. Measurement devices

The Rip is measured using a Fraunhofer ISE-home-made apparatus based on the four points method [10,12], using five probes for potential measurements and two current contact bars for load current application. The GDL is placed under the golden bars and the voltage probes. An electrical current (I) of 1 A is applied between the two golden bars and the potential difference (U1j) is measured between probe 1 and probes 2, 3, 4, and 5. The distance, measured on the x-axis, between two probes is equal to 4.2 mm (5 mm from probe-to-probe canters since the diameter of a probe is 0.8 mm). The compressed area has the following sizes: 30 mm (distance on the x-axis between the two golden bars) × w (the width of the sample on the y-axis), (See fig 3.32).

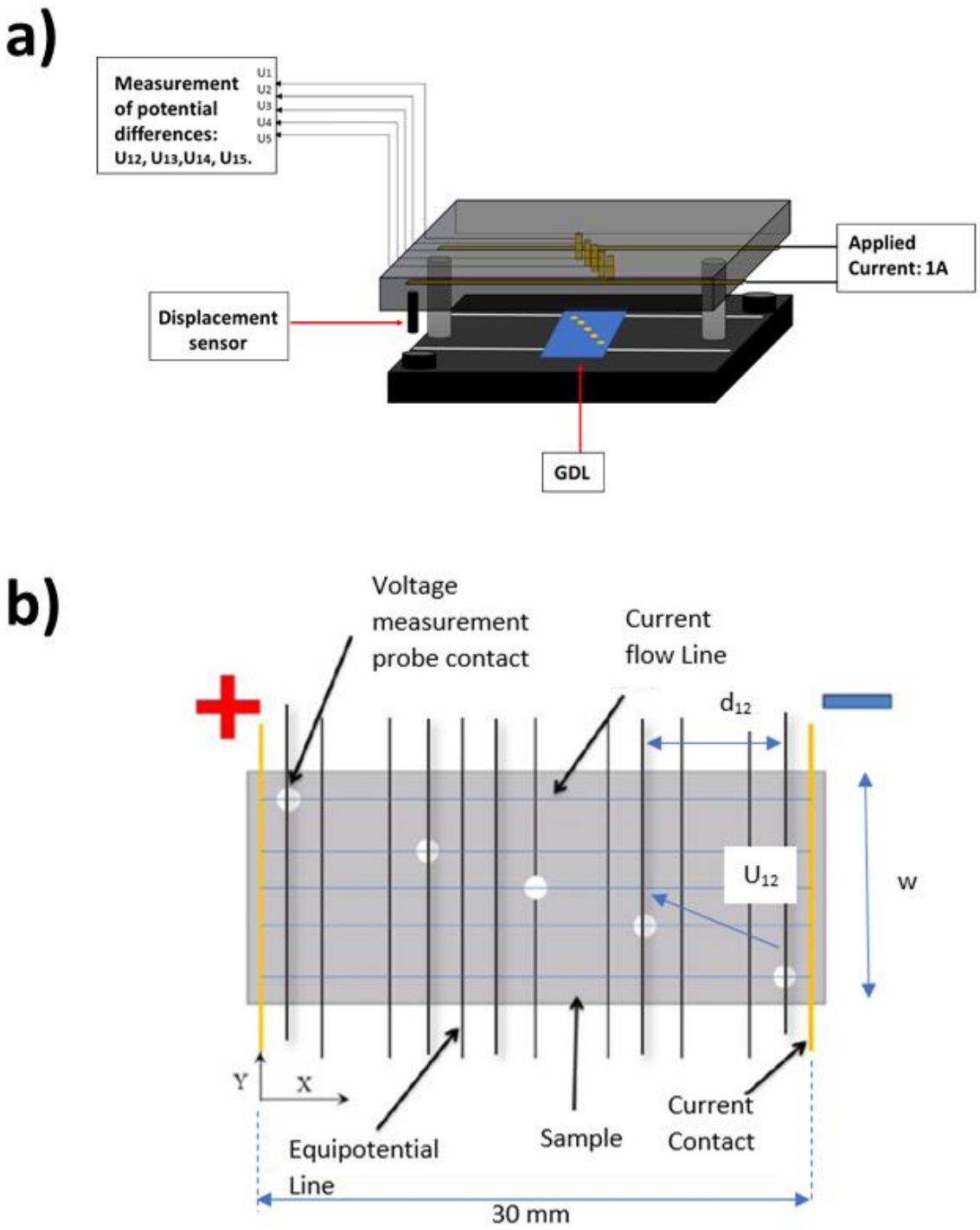

Fig 3. 32: Electrical in-plane resistivity measurement apparatus developed by the Fraunhofer ISE: a) apparatus, b) GDL sample [12].

The measurement method is based on (Equation 3.6):

$$Rip = \frac{1}{4}\sum_{j=2}^{5}\frac{U_{1j}}{I}\frac{w.t}{d_{1j}} \qquad (3.6)$$

With:

Rip : in-plane resistivity (mOhm.cm),

U_{1j}: the voltage drop measured between probe 1 and probe j (mV),

w: the sample width (following y-axis in the fig. 3.32) (cm),

t: the GDL thickness (mm),

d_{1j}: the distance on the x-axis between the two equipotential lines related with the probes 1 and j; this distance is equal to= ((j-1)*5-0.8) (mm),

I: the applied current intensity (A).

The thickness "t" is determined by measuring the displacement of GDLs through compression using a proximity sensor from *Waycon Positonmesstechnik*, located on the top part of the apparatus. The sensor is connected to an electronic device and the signal is translated to a voltage value. A linear relationship is used between the displacement measured and the corresponding voltage with the maximum range of 2 mm corresponding to a 10 V value. Once the displacement corresponding to a particular compression point is determined, the offset due to the displacement of the apparatus is deduced using this linear relationship. This apparatus displacement is selected from previous experimental values obtained by the Fraunhofer ISE using the same compression forces (See Table 3.10). Once this offset has been removed, the thickness is deduced by subtracting the displacement from the initial thickness of the GDL.

Compressed surface 3 × 3 = 9 cm²				Compressed surface 1.5 × 3 = 4.5 cm²		
P (MPa)	F (N)	Vs (µm)		P (MPa)	F (N)	Vs (µm)
0	0	0		0	0	0
0.11	100	0		0.11	50	0
1	900	5.6		1	450	0
2	1800	13		2	900	5.6
3	2700	19		3	1350	9.8
4	3600	25.8		4	1800	13
1	900	5.6		1	450	0
4	3600	25.8		4	1800	13
1	900	5.6		1	450	0
4	3600	25.8		4	1800	13
0.5	450	0		0.51	230	0

Table 3. 10: Displacement of the measurement apparatus as a function of pressure P.

Additional information on the measurement devices

The current is applied with a dual power supply apparatus from AIMTTi (EX354RD) with a resolution of 1 mA and an accuracy of 0.5% of reading +/-3 digits. (from "AIMTTi (EX354RD) data sheet").

The voltage was measured using a multimeter from UNI-t: UT61C with a voltage measurement specification 60 mV / 600 mV +/- (0.8%+3); 6 V / 60 V / 600 V +/ - (0.5%+1). (from UNI-t: UT61C user manual).

The proximity sensor is of type magnetic sensor with a 0.05 µm resolution related to a source of voltage Agilent (E3648A) with an accuracy of < 0.01% + 3 mV).

3.3.1.2. Applied mechanical compression

For all the experiments, the same cyclic mechanical compression was applied. The cycle was defined according to fig 3.33.

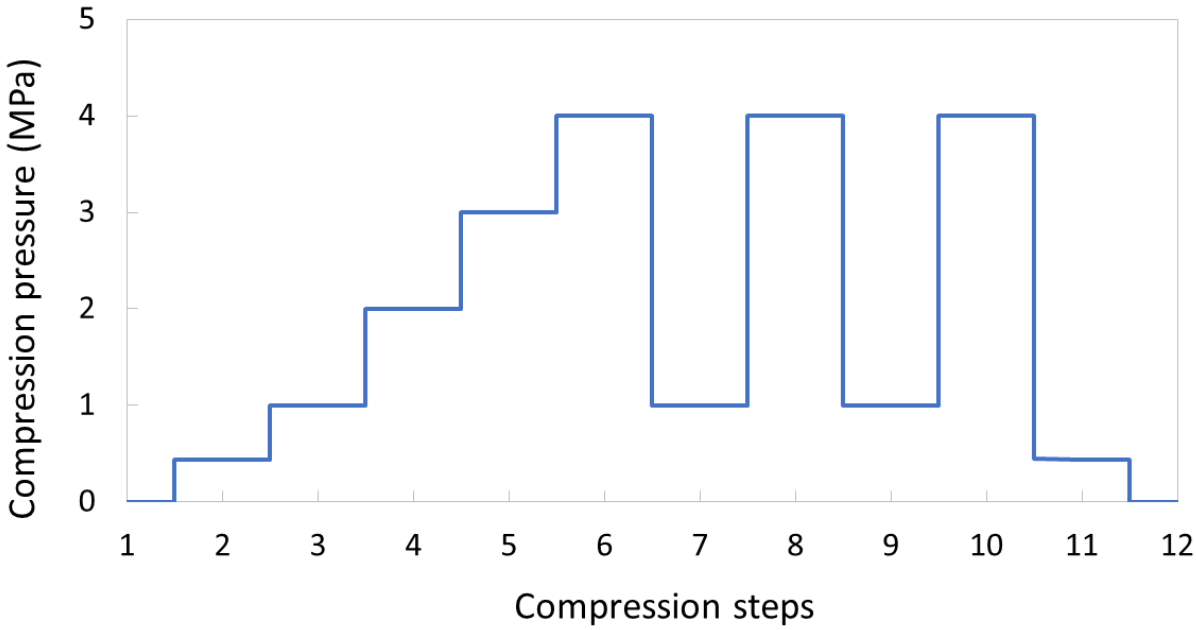

Fig 3. 33: Compression profile applied on the GDLs.

The compression was applied by a hydraulic press on the apparatus. GDLs were compressed under the whole area between the two golden bars. Two compression areas were investigated: 3 × 3= 9 cm^2 and 1.5 × 3= 4.5 cm^2. GDLs were cut into rectangular sheets.

3.3.1.3. Sample type

Table 3.11 summaries the type of GDLs used with their physical properties and with the thickness measurement methods that were applied to determine the Rip.

GDL reference	Thickness (from GDL supplier) (µm)	Structure and composition	Number of samples tested
SGL 24 AA	190 (at a pressure of 0.025 MPa)	Straight fibre	3
SGL 24 BA	190 (at a pressure of 0.025 MPa)	Straight fibre + 5% PTFE	3
SGL 24 BC	235 (at a pressure of 0.025 MPa)	Straight fibre + 5% PTFE (in substrate) + MPL	2/3
SGL 10 BA	400	Felt fibre + 5% PTFE	2
Toray H 120	370	Graphitised straight fibre	3
SGL 38 BC	325 (at a pressure of 0.025 MPa)	Straight fibre + 5% PTFE (in substrate) + MPL	3
Freudenberg H14 C9	180	Felt fibre structure + hydrophobic treatment + MPL	3

Table 3. 11: GDLs used (details on the methods used for thickness measurement / calculation (column 4) will be given in 2.4.2).

An average thickness (t) variation of three samples of one type of GDL was measured under the cyclic mechanical compression profile depicted in fig. 3.33. Electrical parameters (U_{1j} & I) of the same type of GDL were measured under the same compression profile, using three samples and Rip of each sample was determined using the average thickness (t).

The first point of compression was 0.44 MPa when measuring the electrical parameters and 0.11 MPa for the thickness measurement.

This first point was chosen very small (0.11 MPa) for thickness determination, because it is taken as the reference voltage of the starting zero displacement point (corresponding to the voltage of the initial thickness of GDL). The reference voltage is measured at the first level of compression, and not before starting the compression process, for the following reason: the hydraulic press moves very quickly at the start when the compression plates are set to the correct level and then the compression program starts immediately, which causes instability of the voltage related to the displacement sensor without having any real compression / displacement of the GDL.

Even the known GDL thicknesses (for SGL at least and Freudenberg) are given under a minimal compression of 0.025 MPa by the manufacturers (from SGL GDL data sheet, and Freudenberg GDL data sheet).

This method was used for all GDLs, except 38 BC and H14C9, where both thickness and electrical parameters were measured at the same time for every sample.
For GDL 10 BA, thickness variation was extracted from previous data of Fraunhofer Lab experiments under a static compression from 0 to 4 MPa. The values for 1 and 4 MPa were unchanged when determining Rip for the 2nd and 3rd cycles of compression.

3.3.1.4. Anisotropy/MPL

For all GDLs, except SGL 10 BA, measurements were done according to two perpendicular directions D1 and D2 (see fig 3.34), in order to analyse the anisotropy of the in-plane resistivity.

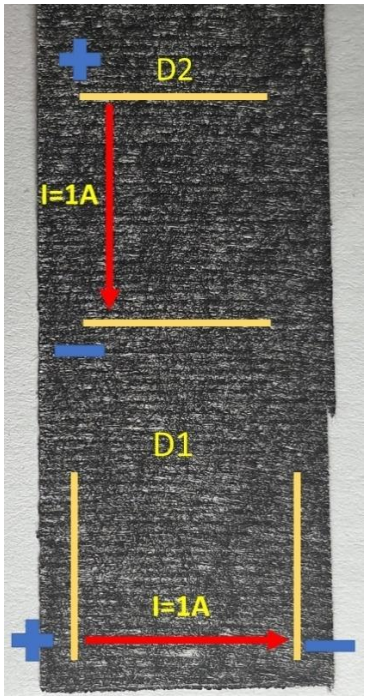

Fig 3. 34: GDL H14C9 Rip measurement direction (D1 Direction; D2 Direction, the golden bars represent the current contacts of fig 3.30).

For GDLs with a MPL (24 BC, 38 BC, H14C9), measurements were done with fibre substrate in the upper side (face to the two golden bars) and only one sample of GDLs has been used with a MPL in the upper side, for every type of GDL, just in order to check that results are identical.

3.3.2. Results

3.3.2.1. Rip variation

The Rip of the GDLs was evaluated under cyclic mechanical compression. In fig 3.35, the Rip of the GDL type SGL 24BA in both directions D1 and D2 is depicted as a funtion of the applied compression. The blue curve represents the first loading part (corresponding to steps 1 to 6, in fig 3.33). The purple curves represent the cyclic region (steps 6 - step 10, in fig 3.33) and the green curve the unloading part (step 10 - step12). These curves show a non-linear decrease of the Rip with compression pressure, an anisotropy of the Rip between the directions D1 and D2, and a sensitivity to the cycles of compression (especially for the first cycles, steps 6-8). These properties are going to be studied in the next three subsections with more details. Table 3.12 summarises the ranges of Rip according to the GDL. The Rip ranges from 3 to 38 mOhm.cm for the different GDLs.

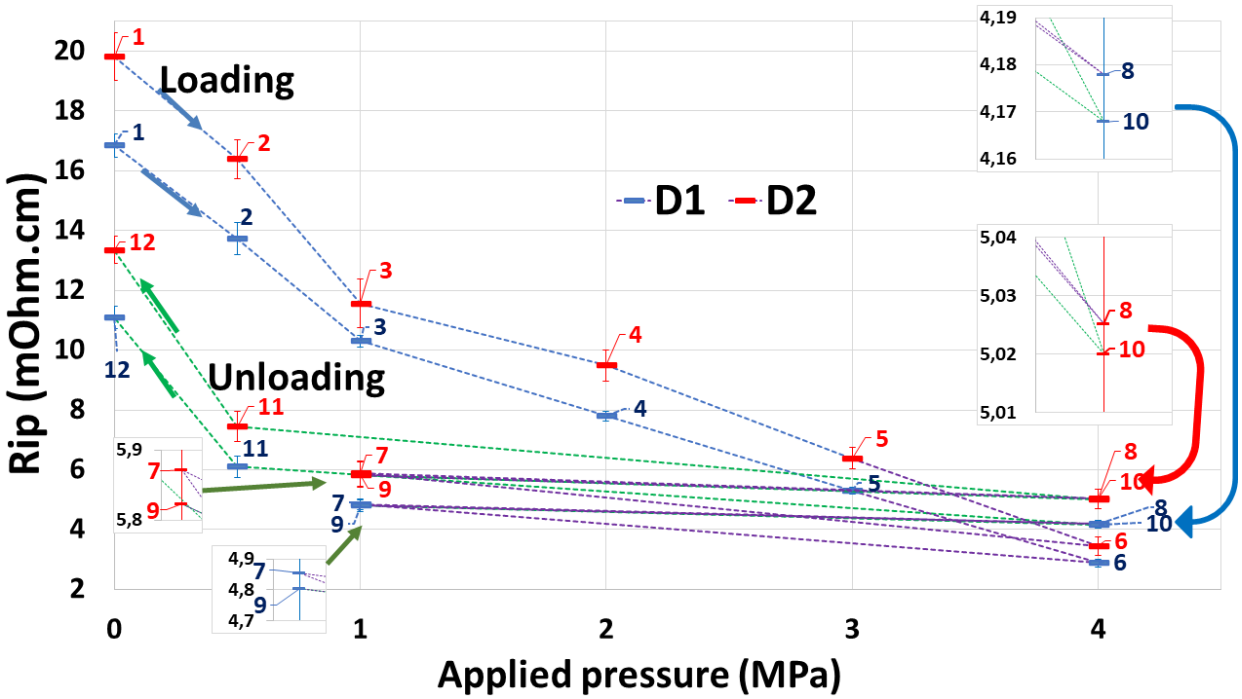

Fig 3. 35: Rip as a function of applied pressure, GDL 24 BA D1 & D2.

GDL	Rip min (mOhm.cm)	Rip max (mOhm.cm)
24 AA	5	18
24 BA	3	20
24 BC	10	30
H120	3	11
38 BC	9	27
H14C9	5	38
10 BA	**11**	**32**

Table 3. 12: Minimum and Maximum of Rip as a function of the GDLs.

3.3.2.2. Effect of compression

Table 3.13 illustrates the evolution of Rip with the compression steps. It contains the Rip values, the slope and the rate of decrease of Rip with pressure. The in-plane electrical resistivity decreases non-linearily with pressure. The decrease rate is higher before 1 MPa (See fig. 3.36). In order to evaluate the linearity of Rip with pressure after 1 MPa, the slopes of Rip with pressure were investigated. In a linear behaviour, the slope should not vary a lot with compression steps. So, the slopes of 1 MPa steps (See Table 3.13 column 9-11) were compared to the [1 - 4] MPa slope (Column 5, Columns 13-15) the GDLs with a sum of the three relative differences (Column 16) higher than 60% were considered as non-linear. After 1 MPa, some GDLs (H120, 24 BA, and 10 BA) have a quite linear behaviour (i.e. Rip as a linear function of pressure). GDLs 24 BC and 38 BC behave non-linearily. GDLs H14C9 and 24AA are the most non-linear ones. Regarding all the investigated GDLs, the Rip values in the first cycle of compression vary from 3 to 30 mOhm.cm.

Regarding the rate of decrease with compression, in Table 3.13, column 7, the GDL that has the highest decrease of Rip with compression is 24 BA (more than 70%). The one with the least decrease is H120 (25-27%), then: 10 BA (32%), 24 BC and 38 BC (33-38%), H14C9 and 24 AA (44-49%), except H14C9 MPL (37%).

The rate of decrease and the slope between 1-4 MPa have close values between D1 /D2 or MPL of the same type of GDL. This can be considered as a property of the GDL. To show this effect, columns 7 and 8 of the table are depicted in fig. 3.37. The slope between 1-4 MPa is around 1.5-3 mOhm.cm/MPa for SGL GDLs, 1-2 mOhm.cm/MPa for the Freudenberg GDLs, and arround 0.5 mOhm.cm/MPa for the Toray GDLs.

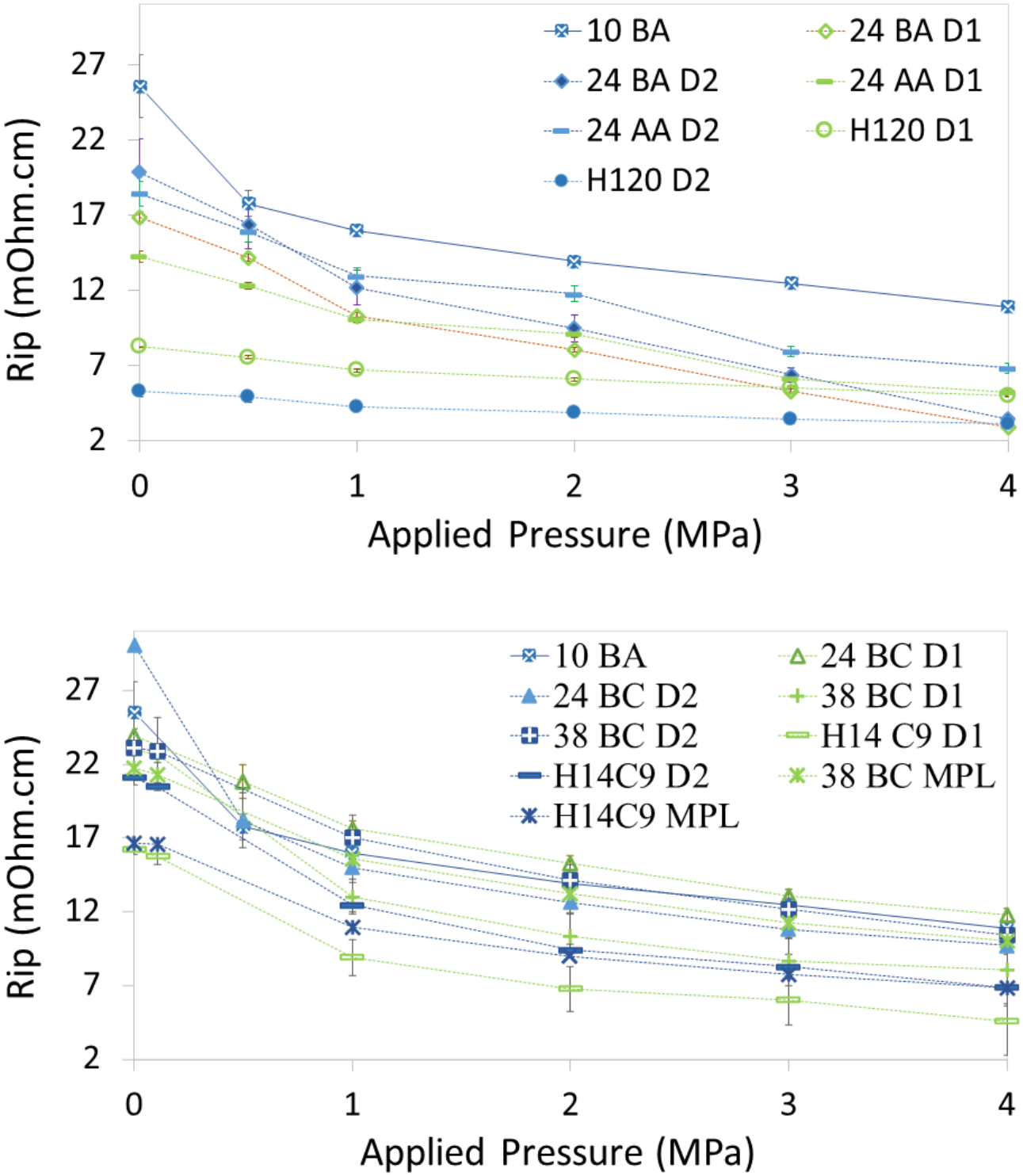

Fig 3. 36: Rip as a function of compression (first cycle for all GDLs).

Rip Pressure	1,00	2,00	3,00	4,00	Sum (1-4 MPa)	Rip decrease* (1-4 MPa) (%)	Slope S (1-4 MPa) ** (mOhm.cm. MPa^{-1})	Slope S1(1-2) mOhm.cm. MPa^{-1})	Slope S2 (2-3) mOhm.cm. MPa^{-1})	Slope S3(3-4) mOhm.cm. MPa^{-1})	Dif% S-S1	Dif% S-S2	Dif% S-S3	T=Sum of Dif	Linearity (T<60 %)
Column number	2	3	4	5	6	7	8	9	10	11	12	13	14	15	16
10 BA	15,98	13,90	12,45	10,91	53,24	31,75	-1,69	-2,08	-1,44	-1,55	23,11	-14,56	-8,55	46,22	Linear
24 BA D1	10,31	8,03	5,29	2,88	26,51	72,10	-2,48	-2,28	-2,74	-2,41	-8,17	10,71	-2,54	21,41	Linear
24 BA D2	12,16	9,49	6,38	3,45	31,47	71,60	-2,90	-2,67	-3,11	-2,93	-7,96	7,12	0,84	15,91	Linear
24 AA D1	10,02	9,05	6,09	5,21	30,38	48,00	-1,60	-0,97	-2,96	-0,88	-39,76	84,63	-44,88	169,27	non-linear
24 AA D2	12,93	11,74	7,92	6,81	39,41	47,33	-2,04	-1,19	-3,82	-1,11	-41,46	87,06	-45,60	174,12	non-linear
24 BC D1	17,64	15,25	13,05	11,81	57,75	33,04	-1,94	-2,39	-2,20	-1,24	22,88	13,16	-36,05	72,09	non-linear
24 BC D2	15,01	12,65	10,82	9,70	48,17	35,39	-1,77	-2,36	-1,83	-1,12	33,27	3,25	-36,52	73,05	non-linear
H120 D1	6,68	6,09	5,52	4,97	23,26	25,54	-0,57	-0,59	-0,57	-0,55	4,23	-0,55	-3,68	8,45	Linear
H120 D2	4,27	3,85	3,40	3,10	14,62	27,49	-0,39	-0,42	-0,44	-0,31	8,03	13,37	-21,41	42,81	Linear
38 BC D1	13,03	10,35	8,64	8,04	40,06	38,27	-1,66	-2,68	-1,71	-0,60	61,19	2,91	-64,10	128,19	non-linear
38 BC D2	17,00	14,15	12,19	10,39	53,73	38,89	-2,20	-2,86	-1,95	-1,80	29,63	-11,40	-18,22	59,25	Linear
38 BC MPL	15,55	13,25	11,25	10,06	50,11	35,32	-1,83	-2,30	-2,00	-1,19	25,76	9,16	-34,92	69,83	non-linear
H14C9 D1	8,91	6,77	6,01	4,59	26,27	48,53	-1,44	-2,14	-0,76	-1,42	48,49	-47,02	-1,48	96,99	non-linear
H14C9 D2	12,45	9,39	8,28	6,88	37,00	44,78	-1,86	-3,06	-1,12	-1,40	64,65	-39,89	-24,76	129,30	non-linear
H14C9 MPL	10,95	8,95	7,74	6,83	34,47	37,66	-1,38	-2,01	-1,20	-0,91	45,92	-12,45	-33,47	91,83	non-linear

** Rip decrease= (Rip (1MPa)-Rip (4MPa))/(Rip (1MPa))* x *100* *(%)*

***Slope (1-4MPa) S=(Rip (1MPa)-Rip (4MPa))/(1-4 MPa)* *(mOhm.cm.MPa^{-1})*

Table 3. 13: Rip as a function of pressure and GDLs, decrease rate, slope, and linearity analysis.

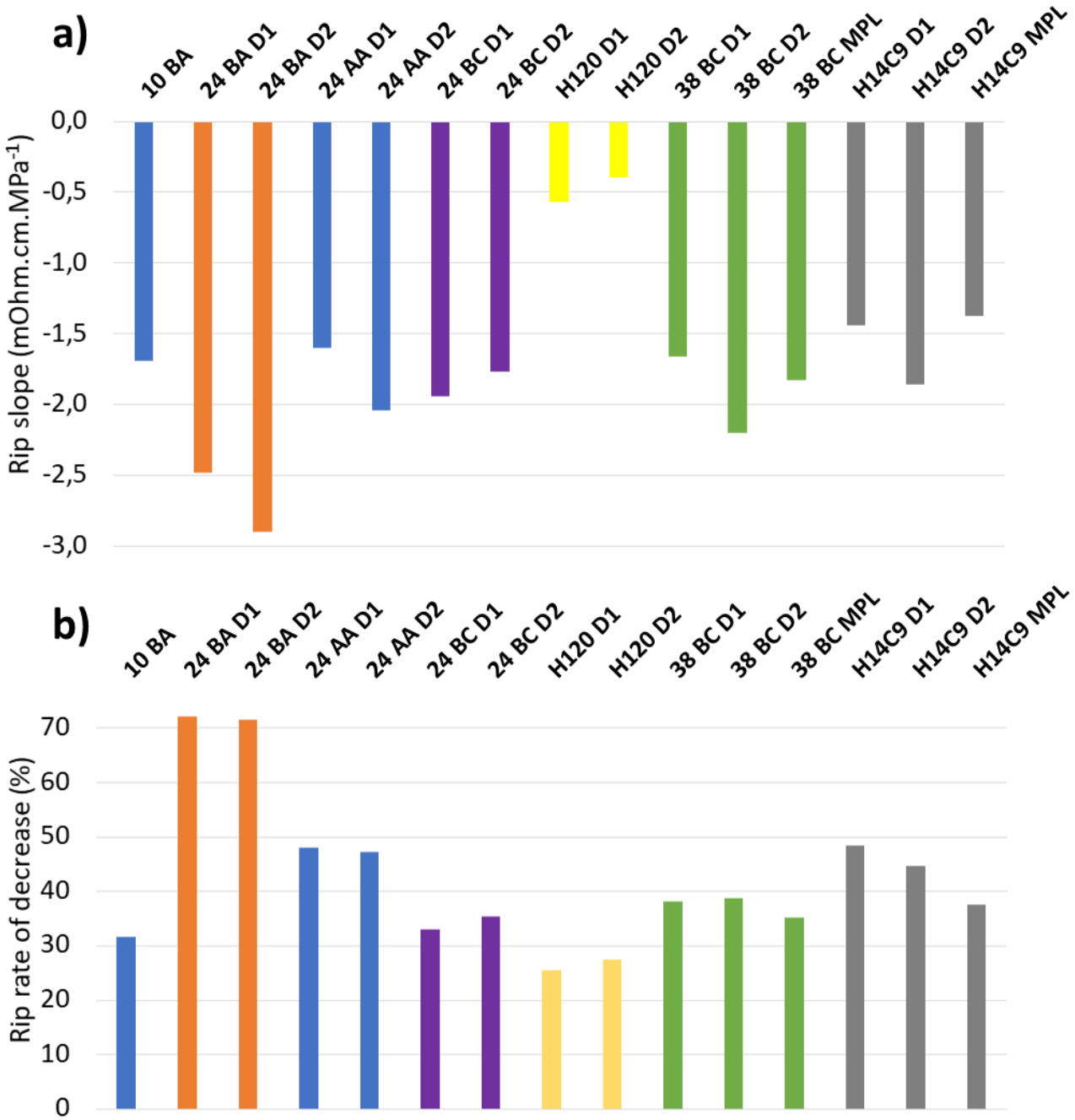

Fig 3. 37: Slope and rate of decrease of Rip between 1 and 4 MPa

In fig. 3.38, the average value of Rip between D1, D2 and MPL are depicted as a function of the compression between 1-4 MPa, for all GDLs. We can see that the Toray GDL has the smallest value of Rip, while the SGL Series presents the highest levels of Rip. The Freudenberg H14C9 has a medium Rip value similar to MPL free SGLs.

Three levels can be identified:

- a high Rip level including the GDLs 10BA, 24BC, and 38 BC with values between 9 and 16 mOhm.cm,
- a medium Rip level formed by 24 AA, H14C9, and 24 BA with values between 3 and 11 mOhm.cm,
- and a low level Rip including H120 (4-5 mOhm.cm).

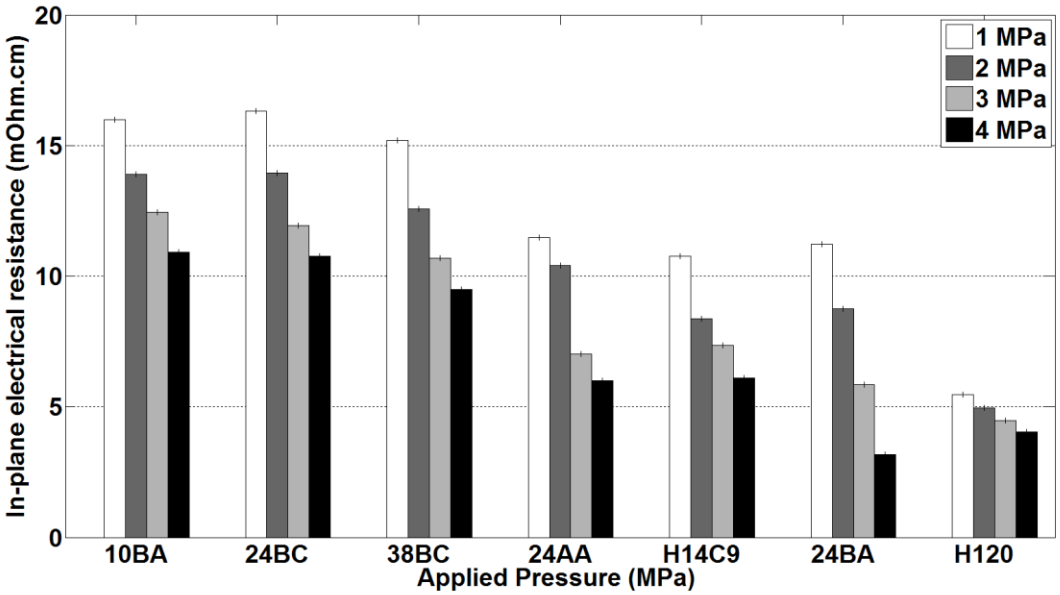

Fig 3. 38: Rip as a function of the applied pressure and GDLs used, for all GDLs except 10BA. Average value between D1 and D2 was taken. For 38BC and H14C9, Rip of MPL was also considered.

Effect of PTFE

The PTFE is a non-conductive substrate coating the carbon fibres that will conduct the electrons in the plane. Regarding the GDLs 24 BA and 24 AA, the Rip values are quite similar. At low pressure, 24 AA has a lower Rip. But after 2 MPa, as the reduction rate of Rip with compression is the highest (70%) for 24 BA, the Rip value of 24 BA becomes lower. It is supposed to make the GDLs stiffer, which means we should expect a higher Rip with compression. This does not seem the case here, as 24 BA's thickness decreased more than 24 AA with compression, which explains the lower Rip value.

Effect of MPL

Comparing the 24 BA and 24 BC GDLs (which has the substrate of 24 BA, but coated with a MPL), it can be stated that the MPL increases the Rip. We also notice a lower decrease of Rip with compression when the GDL is MPL-coated. Regarding linearity, the MPL coated GDL exhibits a non-linear behaviour even after 1 MPa compression, whereas 24 BA has a quite linear behaviour after 1MPa. The GDL 38 BC, which is MPL coated, has also a nonlinear Rip behaviour as a function of pressure. The GDLs 38 BC and 24 BC have also close Rip values especially 38BC D1 and 24 BC D2 and similar rates of decrease around (30-40%).

Effect of structure

Graphitised fibre paper GDLs have the smallest Rip even with a higher thickness. Globally, low thickness GDLs (24 AA, 24 BA, and H14C9) exhibit lower Rip values.

3.3.2.3. Effect of the cycles of compression

The cyclic behaviour of the Rip has been evaluated by calculating the difference of the Rip between different cycles at 1 and 4 MPa. The hysteresis at 1 MPa was calculated for the first cycle of compression. The difference between cycles (Ci+1/i) is computed as follows:

$$C_{i+1/i} = \left(\frac{Rip_i - Rip_{i+1}}{Rip_i}\right) \times 100 \quad (\%) \qquad (5)$$

With:

i: the number of the cycle considered,

Rip_i: the in-plane resistance for the cycle i (mOhm.cm).

The hysteresis at 1 MPa (H) is defined as:

$$H = \left|\frac{Rip_{loading}(1Mpa) - Rip_{unloading}(1MPa)}{Rip_{\max\,(cycle1)} - Rip_{\min\,(cycle1)}}\right| \times 100 \quad (\%) \qquad (6)$$

So:

$$H = \left|\frac{Rip_1(1Mpa) - Rip_2(1MPa)}{Rip_1(0.5MPa) - Rip_1(4MPa)}\right| \times 100 \quad (\%) \qquad (7)$$

And specifically, for SGL 38 BC and Freudenberg H14C9:

$$H = \left|\frac{Rip_1(1Mpa) - Rip_2(1MPa)}{Rip_1(0.1MPa) - Rip_1(4MPa)}\right| \times 100 \quad (\%) \qquad (8)$$

In table 3.14, these three parameters (C2/1, C3/2 and H) are listed for all GDLs. Regarding the majority of GDLs, the cyclic difference C2/1 is positive for 1 MPa and negative for 4 MPa. This means that the Rip is going to decrease between the loading and the unloading of the first cycle. But then, the values in the second cycle are going to be higher than in the first cycle. C3/2 is generally positive which means that the second cycle also behaves as the first: having the Rip decreasing between the loading and the unloading phases. This behaviour is illustrated in fig. 3.39. The value of the Rip at 4 MPa in the third cycle is generally between the 1st and the 2nd cycle (as C3/2 is generally positive at 4 MPa). The Rip values between 1 and 4 MPa are getting closer to each other.

Load (1 MPa)	GDL	C2/1 (%)	C3/2 (%)	Hysteresis at 1 MPa (H)	GDL	C2/1 (%)	C3/2 (%)	Hysteresis at 1 MPa (H)
1	*24 BA D1*	52,91	1,06	48,41	*38 BC D1*	8,41	27,01	7,5
4		-45,24	0,24			-5,19	-7,54	
1	*24 BA D2*	51,69	0,82	48,56	*38 BC D2*	25,51	1,67	41,92
4		-45,54	0,10			-6,32	0,83	
1	*24 AA D1*	34,14	-0,12	48,33	*38 BC MPL*	21,82	0,39	30,30
4		-2,46	0,66			0,72	-0,19	
1	*24 AA D2*	33,14	0,14	47,26	*H14 C9 D1*	32,83	2,03	26,16
4		-2,95	1,11			-26,92	-0,16	
1	*24 BC D1*	18,90	0,67	37,01	*H14 C9 D2*	30,22	2,51	27,66
4		-2,79	0,26			-7,20	1,29	
1	*24 BC D2*	21,63	0,76	38,23	*H14 C9 MPL*	26,49	1,28	29,76
4		-3,99	0,27			-8,66	/	
1	*H120 D1*	12,32	0,31	32,05	*10 BA*	-9,32	-0,72	21,74
4		-6,54	-0,03			-0,91	-0,45	
1	*H120 D2*	15,99	0,95	38,48				
4		-6,55	0,24					

Table 3. 14: Effect of cyclic compression on Rip (negative rates in red).

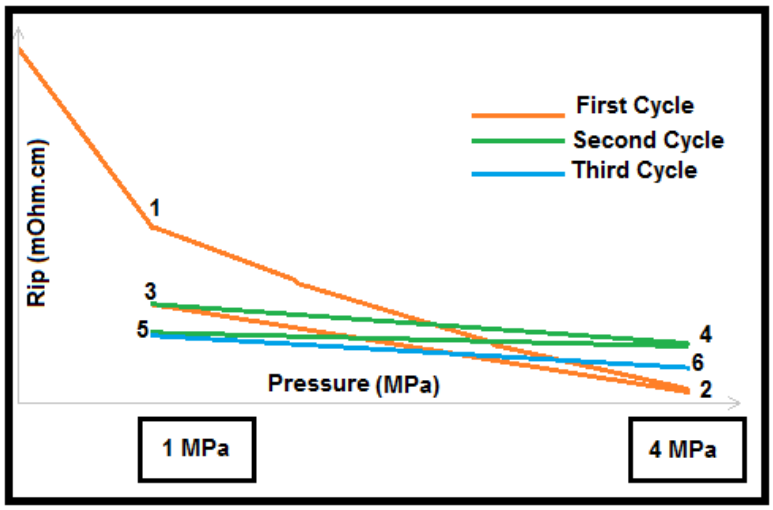

Fig 3. 39: Typical behavior of the Rip with cycles of compression.

Regarding the values of cyclic difference, higher values are observed for the first cycles (C2/1) and for lower compression pressures (1 MPa). This can also be observed in fig. 3.40, where values of Rip are generally smaller in the 2nd cycle, compared to the 1st cycle. But in the 3rd cycle, the values are close to those of the 2nd cycle. Generally, D1 and D2 of the same type of GDL have close values of C2/1 at 1 MPa. The hysteresis calculated at 1 MPa for the first cycle of compression also gives close values between D1 and D2 of each GDL. The highest effect of cyclic compression is observed for GDLs 24 BA, then 24 AA as C2/1 is up to 30-50% and H is up to 47-49 %. The lowest effect can be observed for the GDL SGL 10 BA.

Effect of PTFE

The cyclic effect of compression on the Rip is higher with the PTFE loaded SGL 24 BA, compared to the PTFE free SGL 24 AA substrate.

Effect of MPL

Using an MPL decreased the cyclic effect on Rip values, as we can observe the decrease of the rates between the values of SGL 24 BC and SGL 24 BA.

Structure effect

Observing the C2/1, the felt structure (10 BA) and the graphitised substrate (H120) are the least affected by the cycles of compression, in terms of Rip.

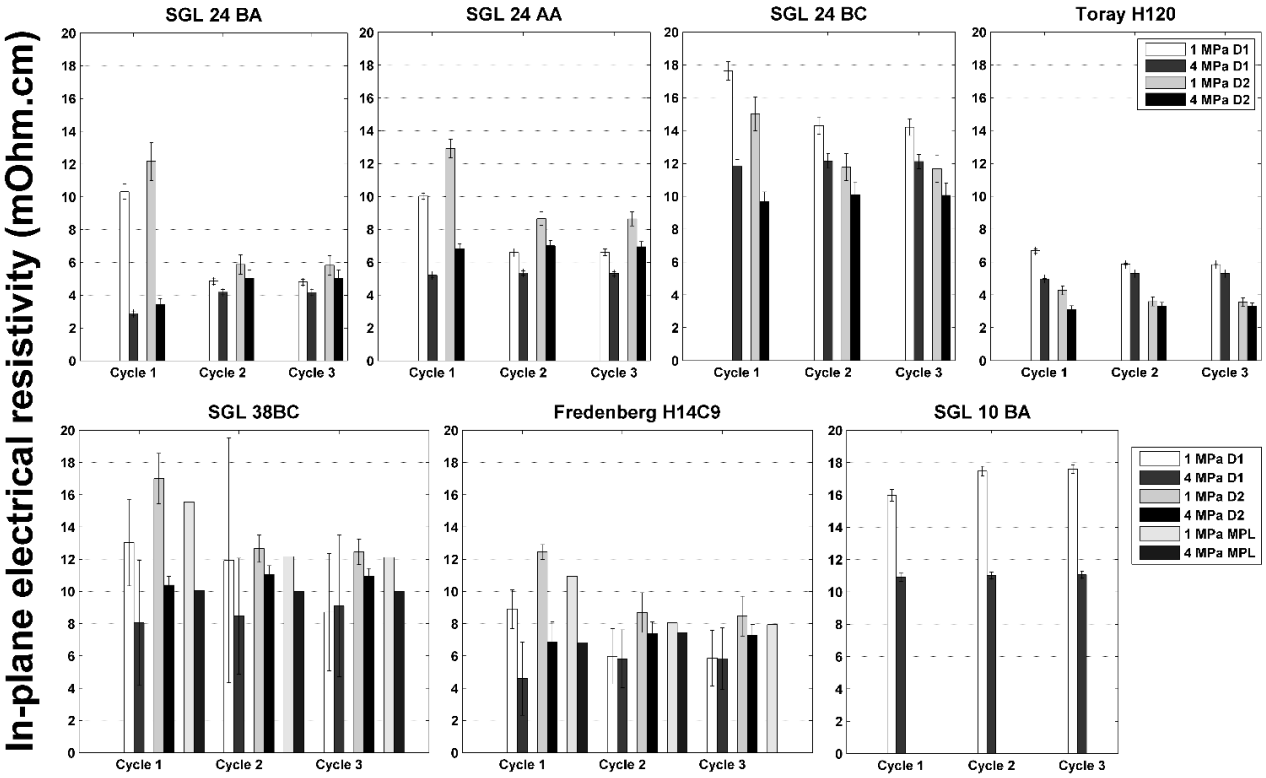

Fig 3. 40: Cyclic compression Rip as a function of the compression cycles.

3.3.2.4. Anisotropy investigation

Along with the difference of the resistivity between the through-plane direction and the in-plane direction, there is also a difference of Rip between the different in-plane directions. In order to investigate this anisotropy, for all GDLs (except 10 BA), the in-plane resistivity was measured through a direction D1 and its perpendicular direction D2.

In order to investigate this resistivity anisotropy, an anisotropy rate "a" is defined as the difference between the resistivities of the two directions over their average value:

$$a = \frac{\left|R_{ip_{D1}} - R_{ip_{D2}}\right|}{(R_{ip_{D1}} + R_{ip_{D2}})/2} \times 100\ \% \qquad (9)$$

Where $R_{ip_{D1}}$(mOhm.cm), $R_{ip_{D2}}$ (mOhm.cm) are respectively the in-plane resistivities through the directions D1 and D2.

In fig. 3.41, this parameter is depicted as a function of compression steps (see fig. 3.33) for the different GDLs.

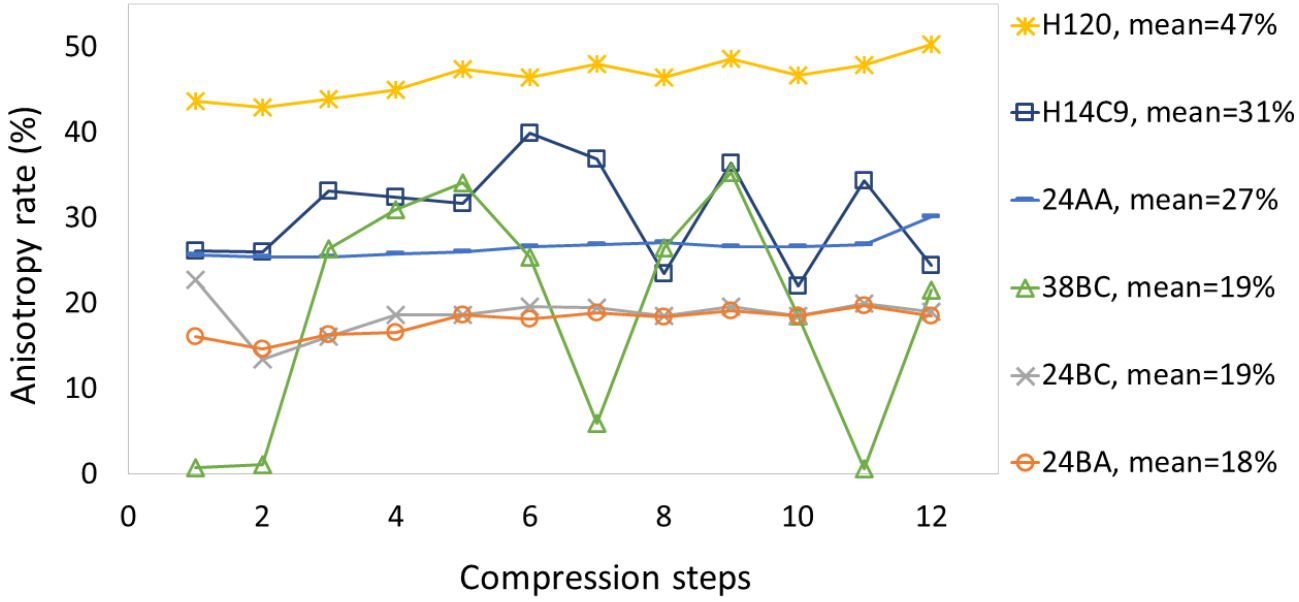

Fig 3. 41: Anisotropy rate of different GDLs as a function of the compression steps.

Observing fig. 3.41, we can note that anisotropy rate's average varies from 18 to 47% depending on the GDLs, with the highest anisotropy observed attributed to the GDL Toray H120 and with the lowest one attributed to the GDL SGL 24 BA. The anisotropy slightly increases with the compression steps with the different GDLs, but the variations are quite small. However, for GDL H14C9, the anisotropy behaviour varies with the cycles of compression. The variation is even higher for GDL SGL 38BC. Note that in these GDLs, (H14C9 and 38 BC), every sample of GDL was given its own thickness, while in the other GDLs, the thickness

attributed to each sample for the Rip calculation was an average value of the investigation of other samples.

3.3.2.4.1. Effect of the use of an average thickness in measurement protocol

In order to observe this effect, the anisotropy rates of the GDLs H14C9 and 38BC, calculated using an average thickness for all samples, are depicted in fig. 3.42. An average thickness is calculated from the seven different samples used in this investigation (three in D1, three in D2, one with the MPL upside). The same average thickness is then used for all samples to determine Rip using equation 3.6. As it can be noticed, using an average value of thickness between D1 and D2, instead of real thickness values for every sample, gives more stable anisotropy rates.

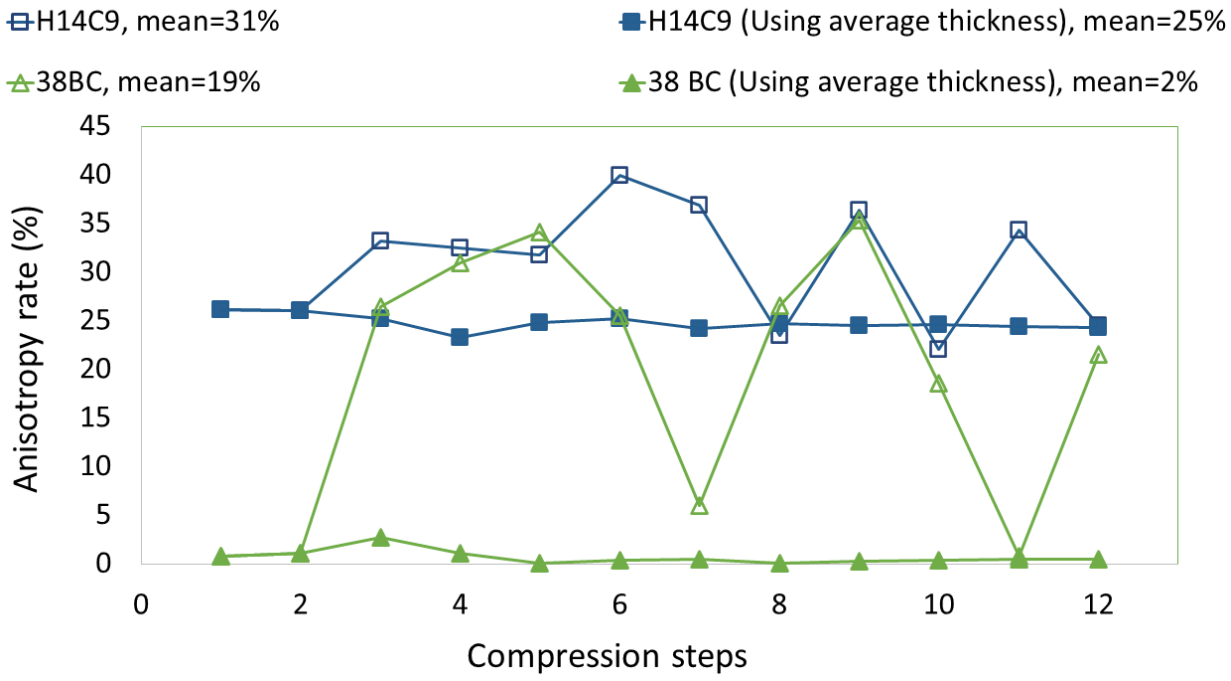

Fig 3. 42: Anisotropy rates vs. compressions steps. The use of an average thickness value for all samples vs. the use of one average thickness value between D1 and D2.

Effect of PTFE

The PTFE decreases the effect of anisotropy as the rate of anisotropy is higher for 24 AA (27%) compared to 24 BA (19%).

Effect of MPL

When comparing the anisotropy rates of 24BA (19%) and 24BC (18%), we can observe that the curves are nearly the same, concluding that there is no substantial effect of MPL on the anisotropy.

Effect of compression cycles

The only apparent effect of the cycles of compression on the anisotropy rate is in the 2nd cycle, where an increase of "a" is observed for 1 MPa (point 9). Then a decrease for 4 MPa can be noticed for almost all the GDLs (except 24 AA).

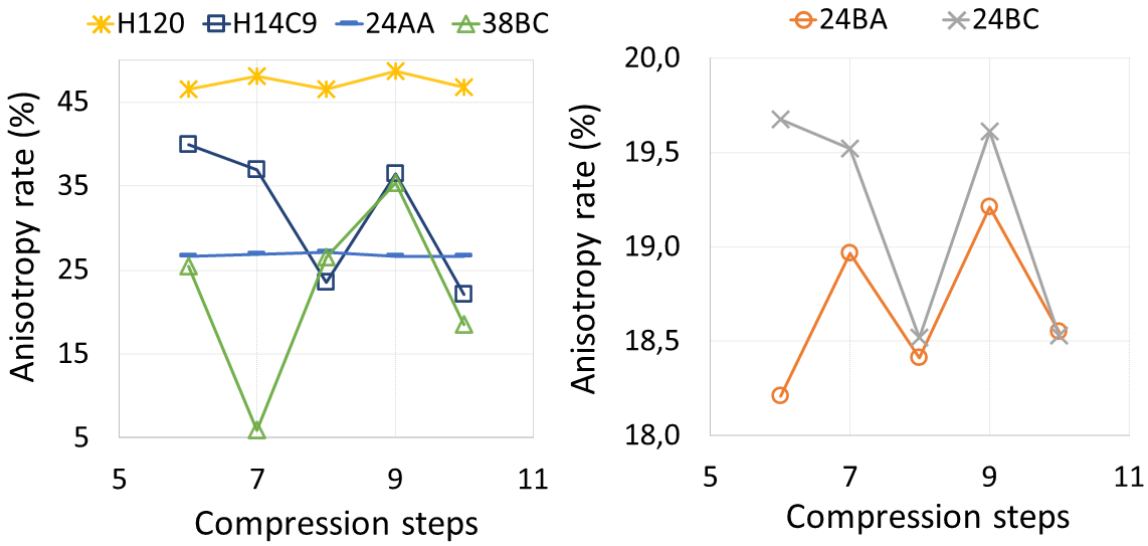

Fig 3. 43: Fig. 3. 43: Anisotropy rate of different GDLs as a function of the compression steps. Zoom on Fig. 3.37

Effect of Structure

Globally, we can see that carbonised straight carbon fibres GDLs_(SGL) exhibit the smallest values of anisotropy. Graphitised fibre GDLs (Toray) show the highest rate of anisotropy. When observing with bare eye the felt structure of H14C9, parallel straight lines can be seen. This predicts a high anisotropy, which is confirmed here (30-40%).

3.3.2.5. Effect of thickness variation on Rip

In order to see the effect of the thickness variation with compression on the behaviour of Rip, the Rip of the GDLs 24 BA and H120 (respectively with the highest and lowest rates of Rip decrease vs. compression) has been evaluated: under constant thickness values and compared to the Rip determined considering thickness variation with compression (D1 and D2).

Two constant thicknesses were investigated to extract Rip: the initial (highest thickness) (D1-H, or D2-H) and the smallest thickness that the GDL has observed during the compression process (D1-S, or D2-S). The various curves of Rip are depicted in fig. 3.44. We can notice that the biggest variation of Rip with compression is due to the thickness variation. The variation in Rip due to electrical parameters is only around 5-10% while considering thickness variation with compression varies Rip up to 70%. This means, it is important to take into consideration the variation of thickness with compression.

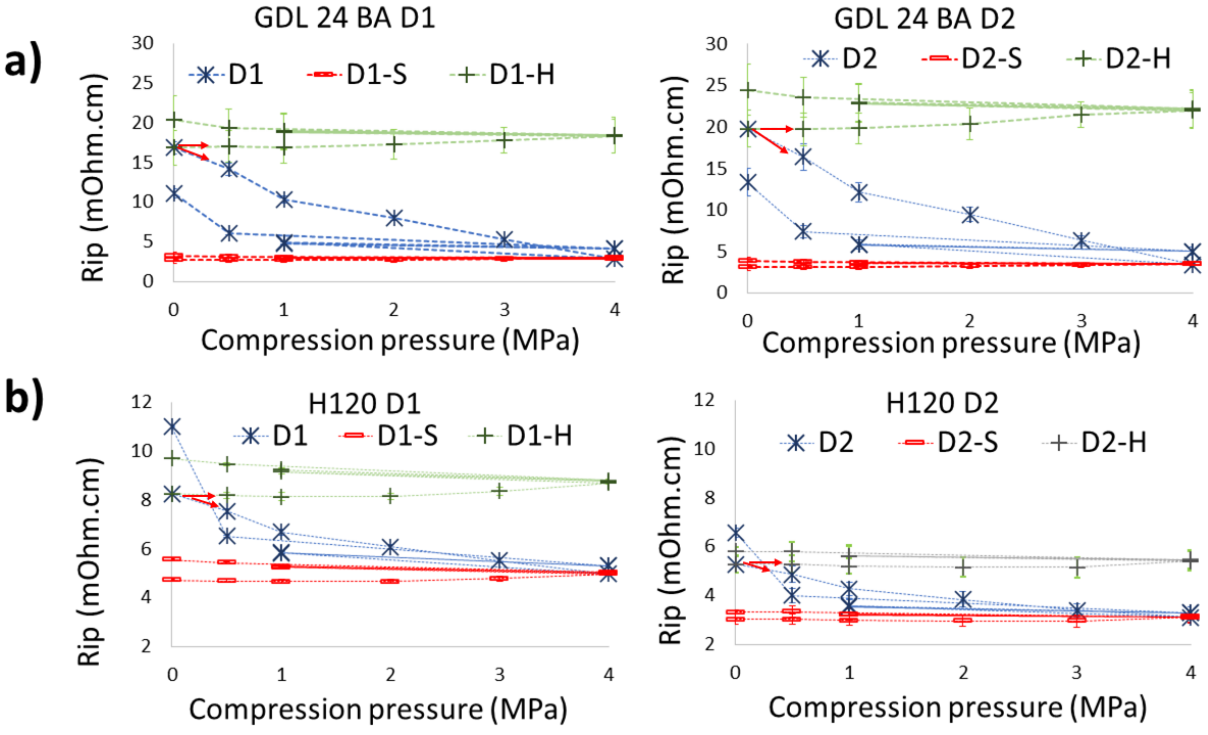

Fig 3. 44: Rip considering constant thickness, Highest initial thickness (H), and Smallest thickness (S).

3.3.2.6. Effect of Humidity

Rip of GDL 24 AA has been measured under compression (fig. 3.33) and water saturated GDL (40% and 80%) in order to see the effect of humidity on in-plane resistivity. The same water saturation method used for Rtp investigation has been used (see section 3.2.3.5). Fig. 3.45 shows in-plane resistivity measured for the first cycle of compression.

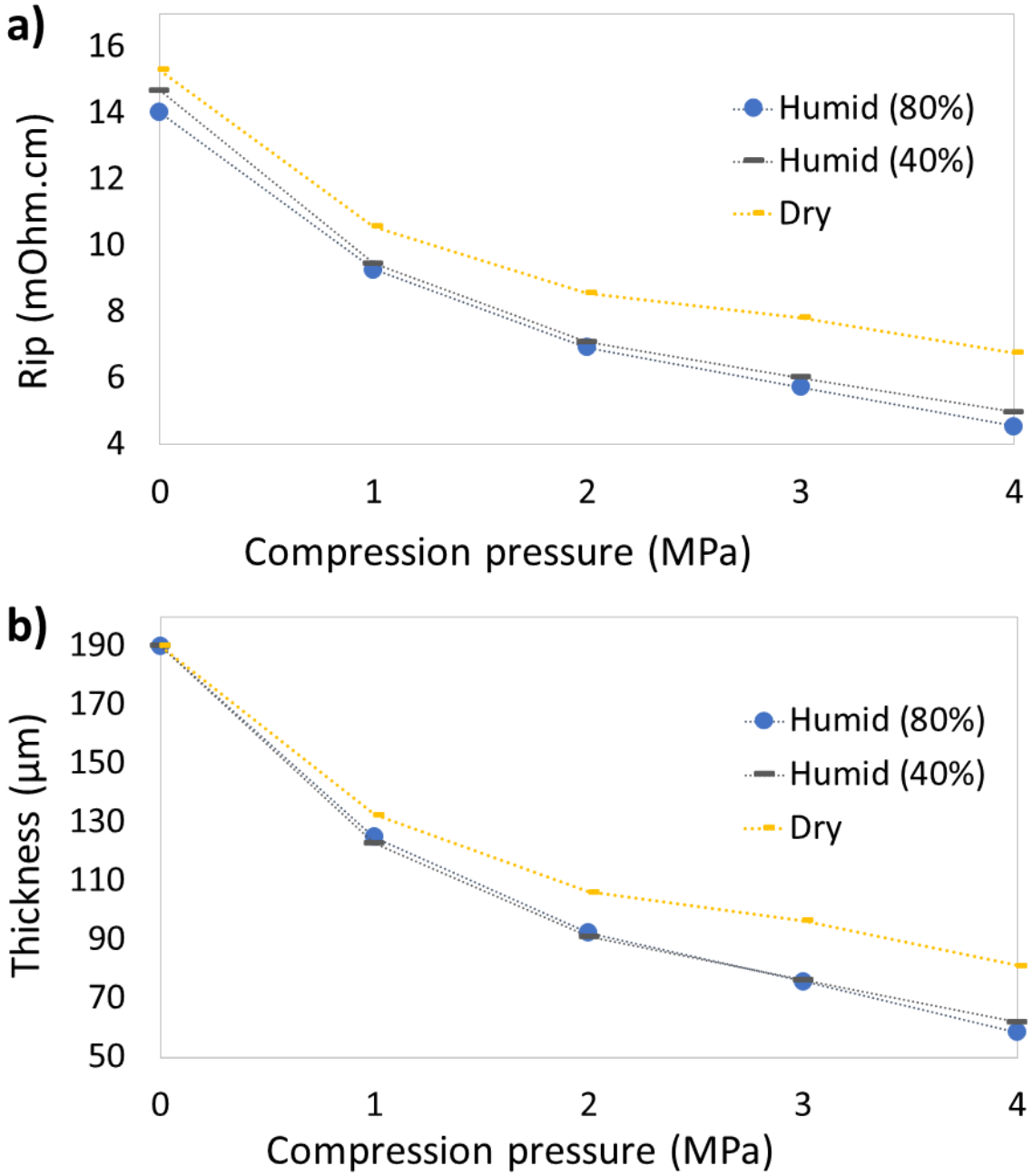

Fig 3. 45:Effect of humidity at room temperature (20°C) for SGL 24 AA a) on in-plane resistivity b) on thickness variation.

Humidity seems to decrease in-plane resistivity (fig. 3.45 a), especially between a completely dry GDL and a saturated one (40%). Degree of saturation does not seem

to influence much the results as the curves of Rip under 40% RH and 80% RH seem to lay on each other. The decrease of Rip seems to be related to the higher decrease of thickness with compression when the GDL is saturated (fig. 3.45 b). We observe the same phenomena following the cycles of compression, as it is depicted in fig. 3.46 which represents Rip and thickness of GDL 24 AA following the cycles of compression. Variation of rip and thickness between the loading and unloading phase seems lower with humidity. This result is consistent with those of S. Rahapood [13] who found that GDL were softer under humid conditions when the strain-stress of a GDL was compared under 0% and 85% humidity rates at 85°C.

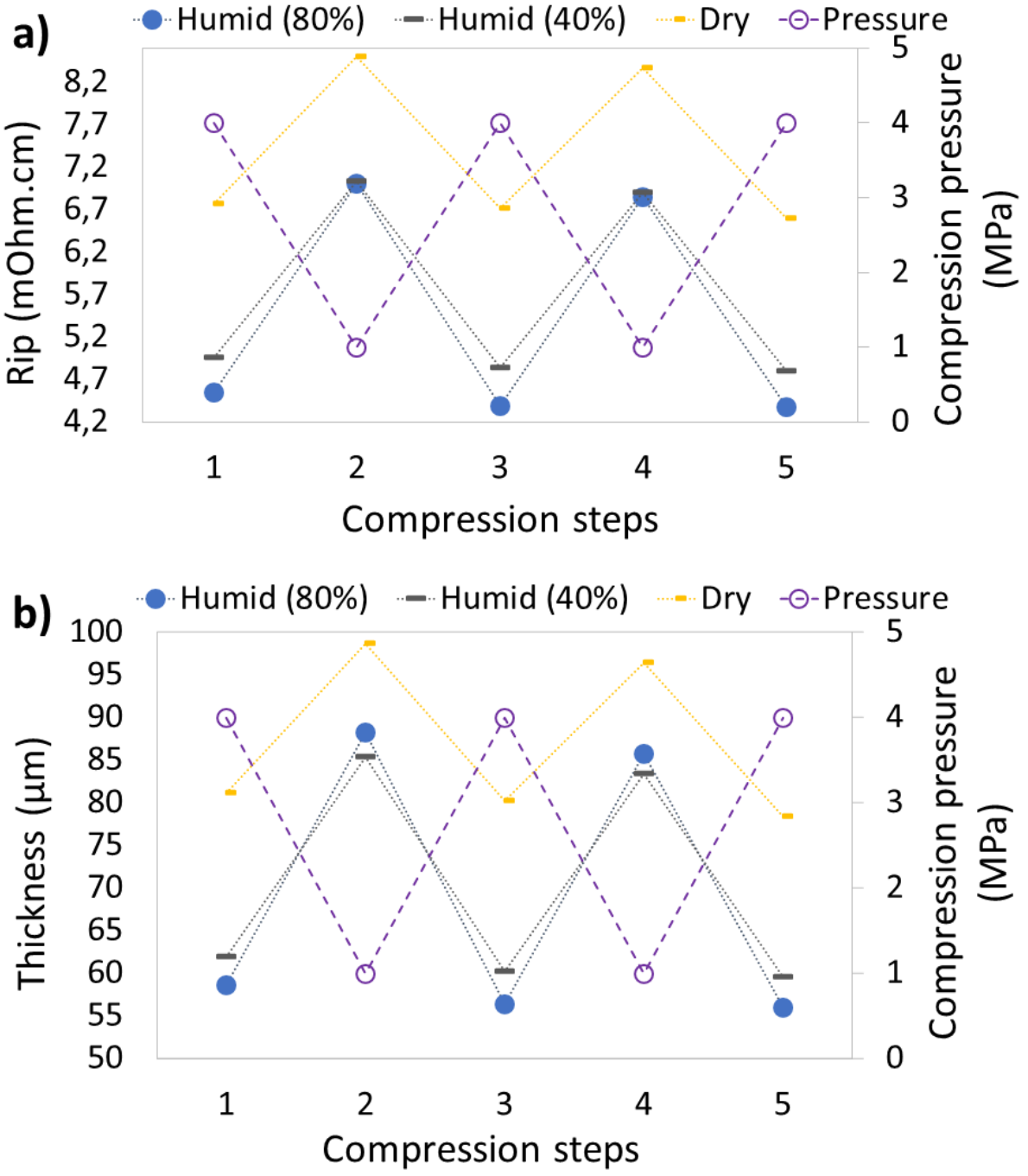

Fig 3. 46: Effect of humidity at room temperature (20°C) for SGL 24 AA during cyclic compression a) on in-plane resistivity b) on thickness variation.

3.3.3. Conclusion

The in-plane electrical resistivity Rip decreases non-linearily with compression. Regarding the different GDLs, three levels of Rip are identified. The GDL with the lowest Rip values is the graphitised Toray H120. Regarding the rate of decrease with compression, the GDL that has the highest decrease of Rip with compression is 24 BA (more than 70%, from 1 to 4 MPa) and the one with the lowest decrease is H120.

Rip is sensitive to the cycles of compression. In the same cycle, the Rip is decreasing between the loading and the unloading compression phase. Comparing cycles to each other, the values of Rip between 1 and 4 MPa are getting closer to each other with the cycles. The effect of cycles is larger for the first cycles. The GDLs that are the most affected by the cycles of compression are the SGL with straight paper substrates while the least affected GDLs are the felt structures and the graphitised one.
An anisotropy of Rip is observed in the plane between the directions D1 and D2, with the highest anisotropy observed for the GDL Toray H120, and the lowest for the GDL SGL 24 BA. The average rate of anisotropy varies between 18 and 47%.

The rate of Rip decrease, the slope of Rip between 1 and 4 MPa and the hysteresis of Rip with the cycles of compression have close values between D1 /D2 of the same type of GDL. Therefore, this can be considered as a property of the GDL.

The PTFE increases the sensitivy to the cycles of compression and decreases the anisotropy. The MPL increases the Rip, decreases the rate of Rip decrease with compression, and it decreases the sensitivity to the cycles of compression.

3.4. Rc extraction with subtraction method-Rc/Rtp of Graphite / Gold coated surface.

In order to compare different Rtp / Rc of GDLs with a graphite or golden interface, the eVlectrical parameters of one type of graphite and combined graphite-GDL sets were determined.

3.4.1. Graphite investigation

Rtp and Rip of a 4 mm thick resin filled, molded graphite type FC-GR347B from Graphtek LLC has been measured under compression.

Table 3.15 summarizes the main physical properties of the graphite [14] given by the manufacturer.

Density (g/cm^3)	1.99
Particle size (cm)	0.00254
Shore Hardness	76
Flexural strength (MPa)	65
Maximum Temperature (°C)	170
Porosity (%)	0
Electrical resistivity (ohm.cm)	0.0012

Table 3. 15: FC-GR347B graphite properties

3.4.2. Rtp Measurement

The through-plane of the graphite has been measured using the pin method described in [10,12], which was found to be an accurate method for thick pieces such as graphite. This method avoids having contact resistance with the electrodes.

The Rtp apparatus is the same as the one used for GDLs (section 3.2), except the electrodes. Fig. 3.47 shows the pin electrodes used.

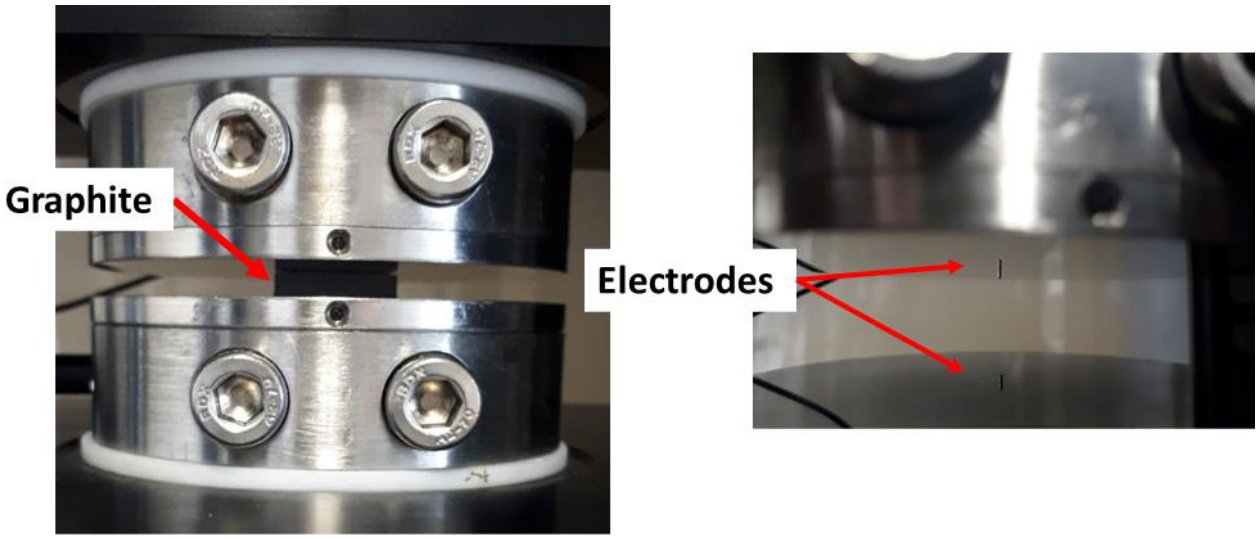

Fig 3. 47: Pin electrodes.

3.4.3. Results

3.4.3.1. Through-plane resistance (Rtp)

Fig. 3.48 shows the through-plane resisitivity of a graphite sample using the pin electrodes. Uncertainties are important may be due to the displacement of the pins. The values of Rtp are very small (5-20 µOhm.cm²).

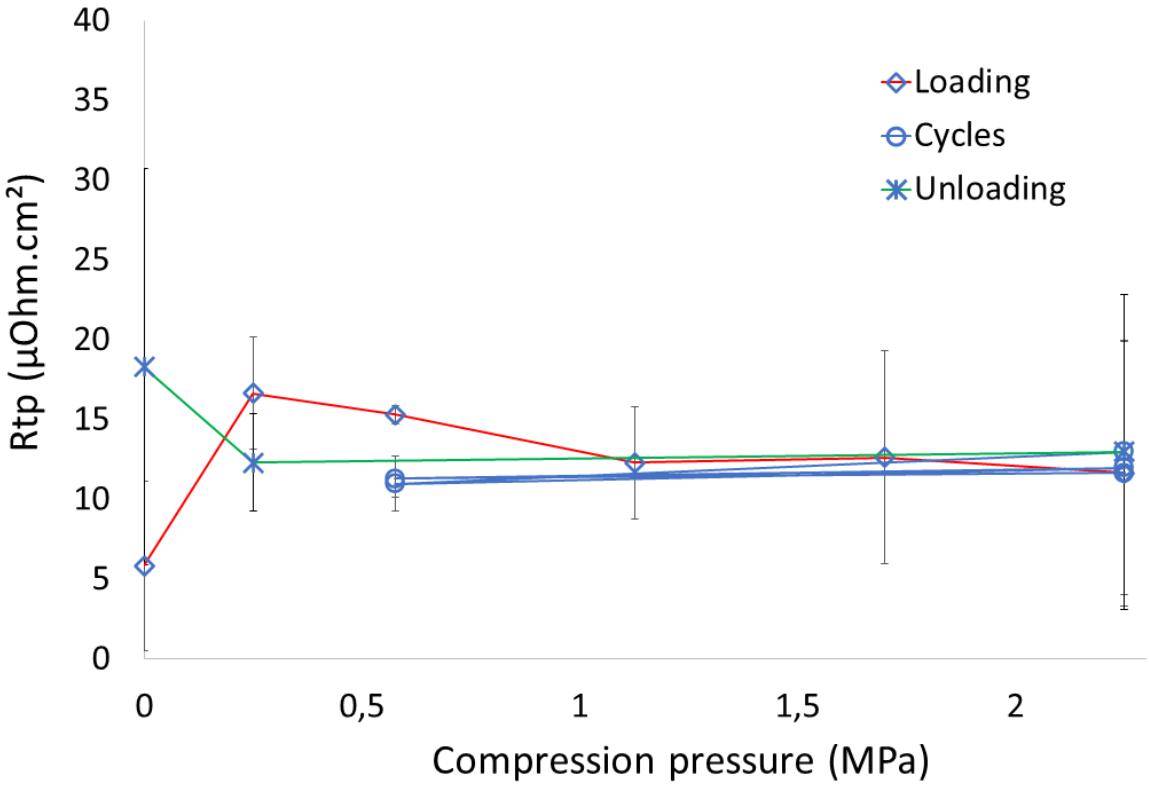

Fig 3. 48: Area specific through-plane resistivity (using pin electrodes) as a function of compression pressure.

In order to evaluate the contact resistance between the gold electrodes and the graphite, a 2x2 cm² graphite sample was investigated under golden electrodes (the same as that used to measure Rtp for the GDLs). Fig. 3.49 depicts this contact resistance determined by substracting the Rtp of graphite.

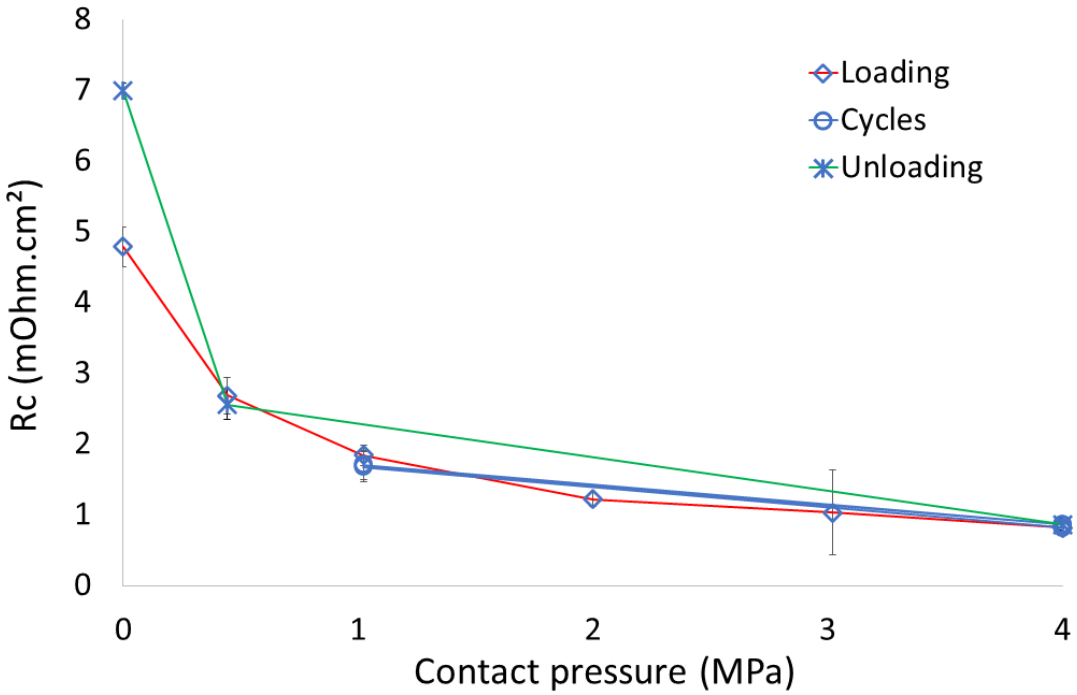

Fig 3. 49: Contact resistance between gold and graphite under compression.

The contact resistance of the gold coating and the graphite is higher than the through-plane resistance of graphite with two orders of magnitude.

3.4.3.2. In-plane resistance (Rip)

The in-plane resistivity was measured using the same apparatus as in section 3.3, on a 4 mm thick 20 × 40 mm sample. Two samples were used. Thickness was considered unchanged with compression. Fig. 3.50 represents this in-plane resistance as function of compression.

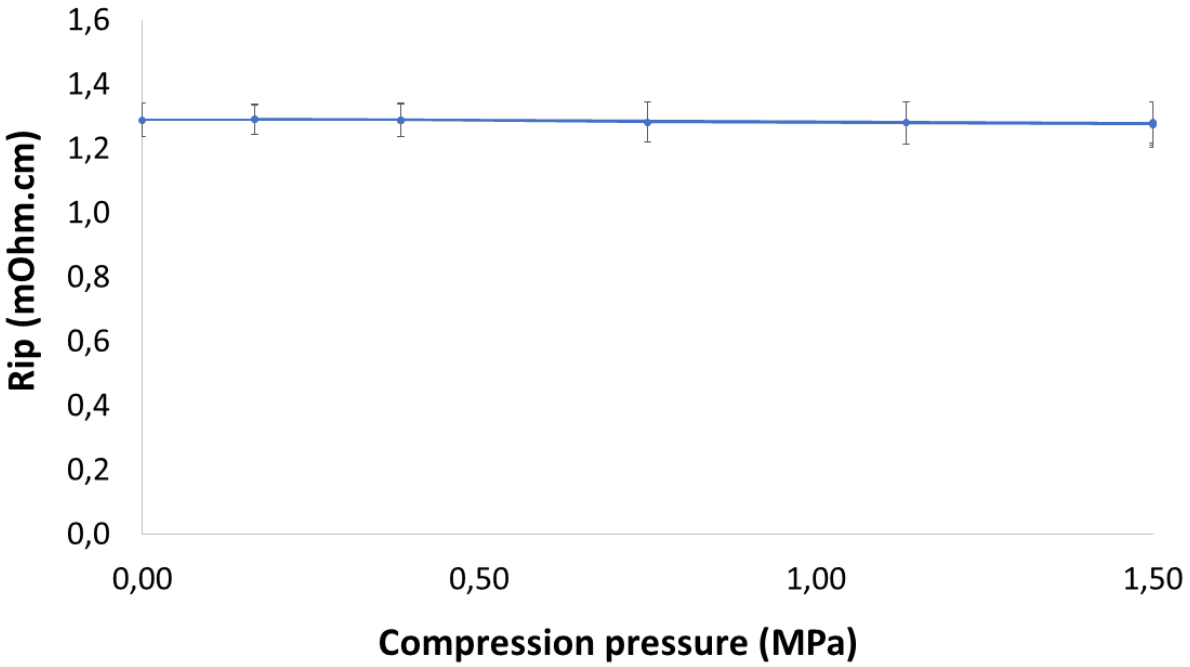

Fig 3. 50: In-plane resistivity of Graphite.

The in-plane resistivity is around 1,3 mohm.cm, a value close to the resistivity given by the constructor. The resistivity remains unchanged with compression and is smaller than GDL resistivity.

Comparaison of GDL Rtp measured under golden electrodes:

Fig. 3.51 shows the resistance of a stack made up of one graphite plate - one GDL - one graphite plate which was measured with the gold electrodes method; then the contact resistance between the golden electrodes and the graphited was removed, as well as the Rtp of GDLs measured previously using gold coated electrodes (section 3.2).

The contact resistance of GDLs with graphite is higher than with the golden electrodes, especially for low compression levels.

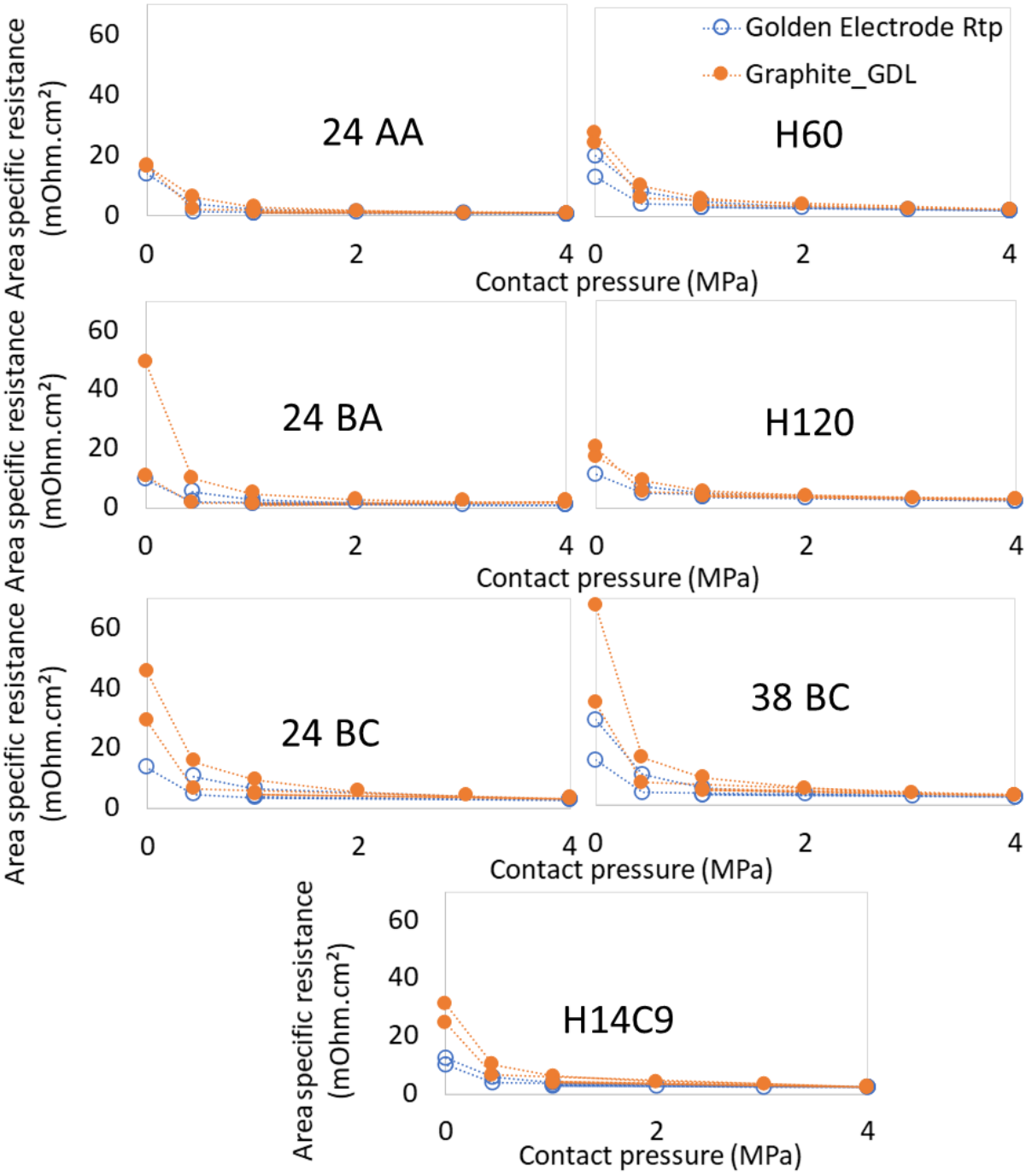

Fig 3. 51: Contact resistance of GDL with graphite and through-plane resistance with gold coated surface for one loading-unloading cycle.

3.4.3.3. Effect of temperature

In fig. 3.52, graphite resistance was measured under gold coated electrodes at room temperature and at a temperature of 75°C. It appears that the resistance increased with temperature especially under low compression pressure; the increase could reach more than 25%. This resistance is mainly due to the contact resistance between the graphite and the gold coated electrodes.

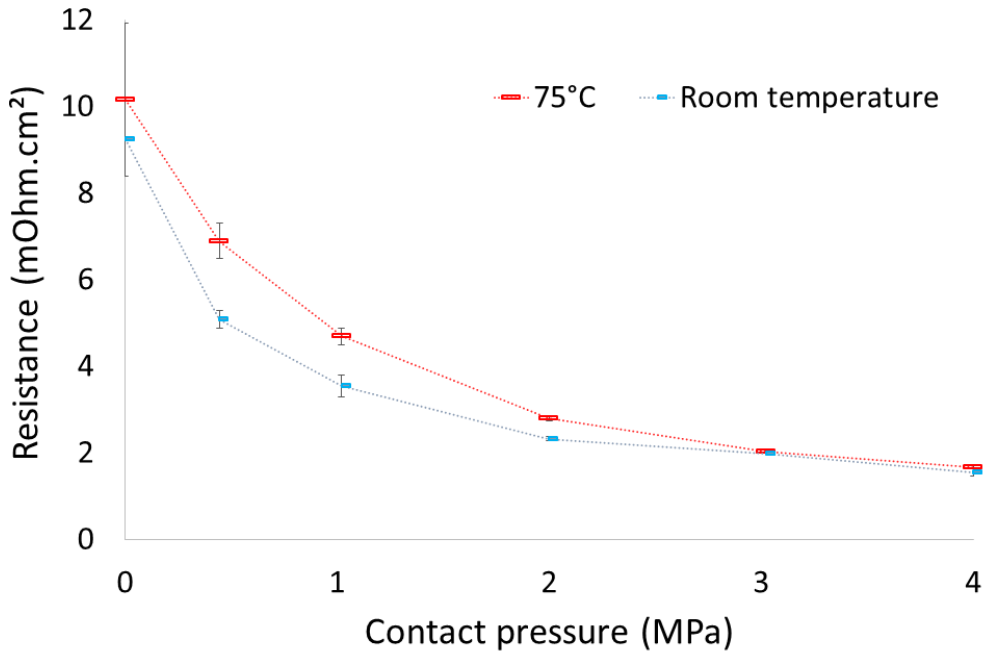

Fig 3. 52: Effect of temperature on graphite resistance.

The effect of temperature on the total resitance of a graphite - GDL - graphite set was also investigated using a Toray H120 GDL. Fig. 3.53 shows the total resistance of graphite - GDL - graphite measured with gold coated method under compression at room temperature and at 75°C. It apears that contrary to the contact resitance between the graphite and the golden electrodes, the total resistance decreased with temperature. So this decrease, is due to the sum of the contact resitance of graphite with the GDL and the Rtp of the GDL. This can be explained as GDL H120 shows a small Rtp decrease with temperature for pressures up to 2 MPa and contact

resistance of GDLs with gold seems to decrease with temperature at very low pressure (lower than 0.2 MPa). The effect of temperature is more important at low pressure.

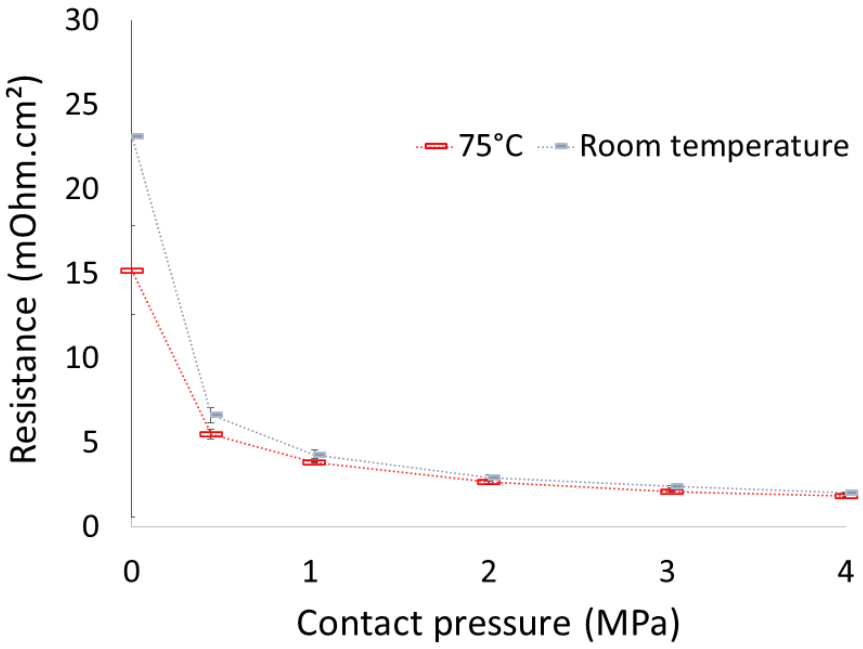

Fig 3. 53: Effect of temperature on total resistance.

3.4.3.4. Comparison of different Rtp-Rc techniques. Particular case of GDL H120

For the GDL H120, exact through-plane resistance has been measured previously with the gold electrodes. Fig. 3.55 shows the Rtp of GDL H-120 using gold coated electrodes (presented earlier), Rtp of the same GDL using microwire methodes extracted from [10] and the contact resistance between the GDL and the gold coated electrodes that has been determined by substraction between the two curves.

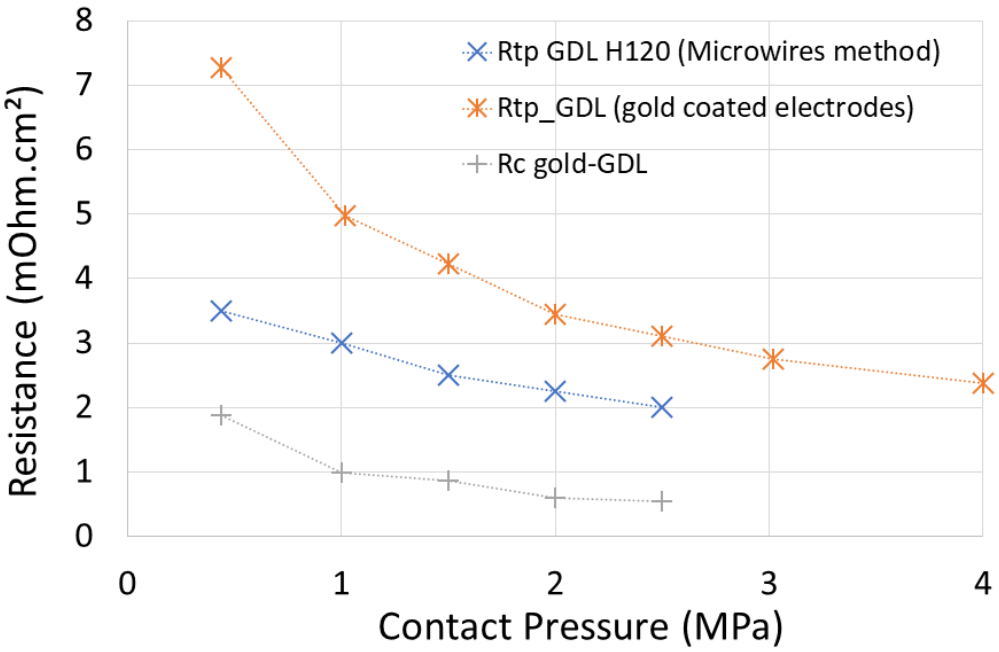

Fig 3. 54: Contact and through-plane resistances for GDL H120.

The contact resistance between the golden electrodes and the GDL has values between 0 and 2 mOhm.cm² which is low compared to the through-plane resistance (2-4 mOhm). However, this contact resistance is lower than the one predicted by the TLM method used earlier (0-5 mOhm.cm²).

In the next section, the Rc between GDL and graphite will be extracted.

3.4.3.5. Contact resistance between graphite and the GDL

In order to extract the contact resistance between graphite and GDL, two stack configurations were used, added to the previous extracted data (contact resistance between the GDL and the golden cotaed electrodes (Rc gold - GDL), the contact resitance between the graphite and the gold coated electrodes (Rc graphite - gold) and the through-plane resitance of GDL measured with microwires method (Rtp(m)). Both stacks were investigated under gold-coated electrodes. Fig. 3.55 represents the stack configuration for Rtot1 and Rtot2.

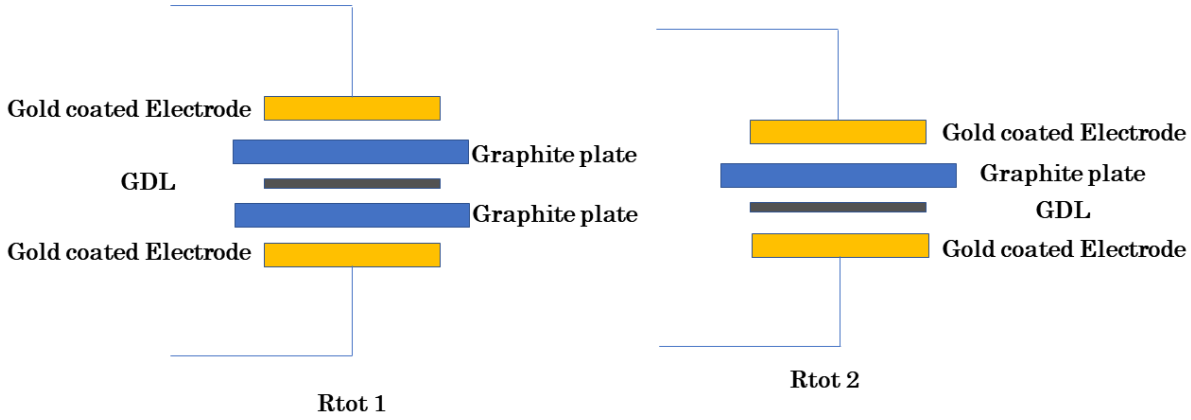

Fig 3. 55: Stack configuration

The first configuration is a stack of: one graphite plate - one GDL - one graphite plate. Two stacks were evaluated every time with three different GDL samples. The total resitance measured is called R_{tot1}:

$$R_{tot1} = 2 . R'_{cgraphite-gold} + 2 . R'_{cgraphite-GDL} + R'_{TP-GDL} + 2 . R'_{TP-Graphite} \quad (3.7)$$

$$R'_{cgraphite-gold} = \frac{R_{tot1} - (2 . R'_{cgraphite-GDL} + R'_{TP-GDL} + 2 . R'_{TP-Graphite})}{2} \quad (3.8)$$

$$R_{cgraphite-Gold} = R'_{cgraphite-GDL} . A_{cgraphite-Gold} \quad (3.9)$$

R_{tot1}: Total resistance of stack 1 (mOhm)

$R'_{cgraphite-gold}$: Electrical contact resistance between graphite and a gold coated surface(mOhm)

R'_{TP-GDL}: GDL Electrical through-plane resistance (mOhm)

$R'_{TP-Graphite}$: Graphite Electrical through-plane resistance (mOhm)

$R_{cgraphite-gold}$: Specific electrical contact resistance between graphite and a gold coated surface(mOhm.cm^2)

$A_{cgraphite-Gold}$: Contact area between graphite and electrode (2.25 cm^2)

The second configuration is a stack of: one GDL - one Graphite plate. One stack was evaluated with three different GDL samples. The total resitance measured is called R_{tot2}:

$$R_{tot2} = R'_{cgraphite-gold} + R'_{cgraphite-GDL} + R'_{TP-GDL} + R'_{TP-Graphite} + R'_{cgold-GDL} \quad (3.10)$$

$$R'_{cgraphite-GDL} = R_{tot2} - (R'_{cgraphite-gold} + R'_{TP-GDL} + R'_{TP-Graphite} + R'_{cgold-GDL}) \quad (3.11)$$

$$R_{cgraphite-GDL} = R'_{cgraphite-GDL} \cdot A_{cgraphite-GDL} \quad (3.12)$$

R_{tot2}: Total resistance of stack 2 (mOhm)

$R'_{cgraphite\text{-}GDL}$: Electrical contact resistance between graphite and GDL (mOhm)

$R'_{cgold\text{-}GDL}$: Electrical contact resistance between a golden coated surface and GDL (mOhm)

$R'_{cgraphite\text{-}GDL}$: Specific electrical contact resistance between graphite and GDL (mOhm)

$A_{cgraphite-GDL}$: Contact area between graphite and GDL (2.25 cm^2)

An average value of the contact resitance was then evaluated from these three stacks.

fig. 3.56 depicts the contact resistance of the GDL and the graphite (Rc graphite-GDL) and the contact resistance of the GDL with the gold coated electrodes (Rc GDL gold). It appears that Rc graphite-GDL is higher than the Rc-gold especially at low compression pressure. This contact resistance also decreases non-linearily with compression.

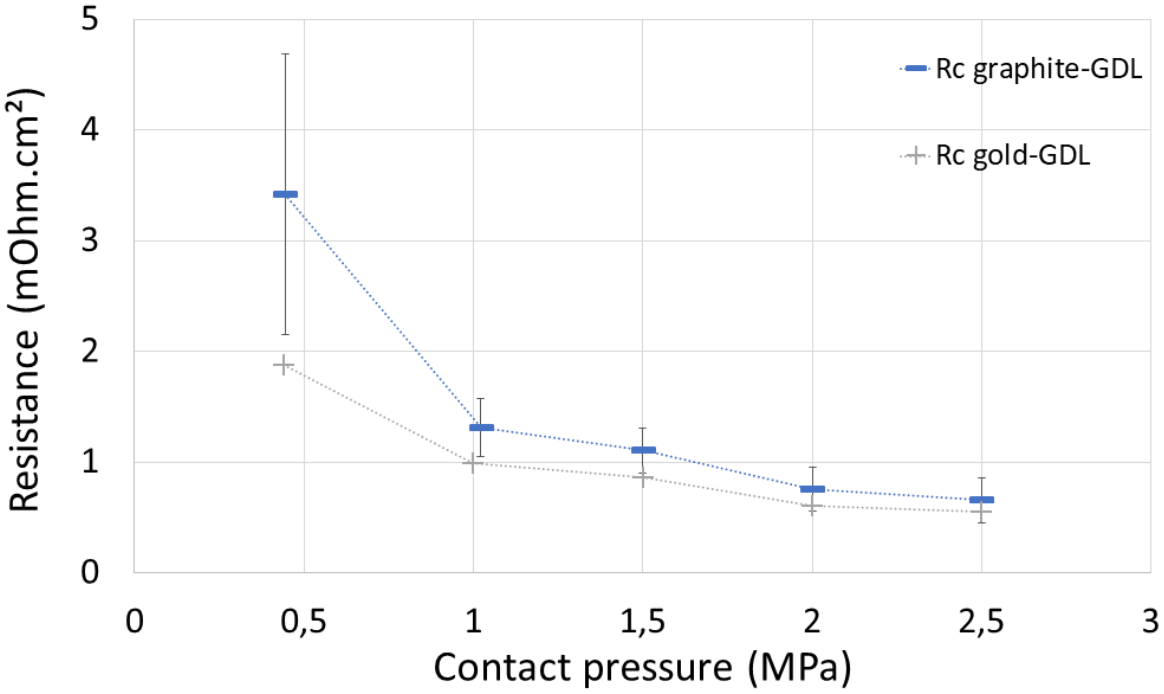

Fig 3. 56: Contact resistance of graphite and gold coated surfaces with GDL.

3.5. Conclusion

In this chapter, the electrical properties of different types of carbon paper GDLs have been experimentally investigated under cyclic mechanical compression and in different operating conditions (temperature, humidity) as can be seen in fig 3.57. The effects of structure and composition have been analysed. The use of BPP or a golden coated surface in contact with a GDL has been examined.

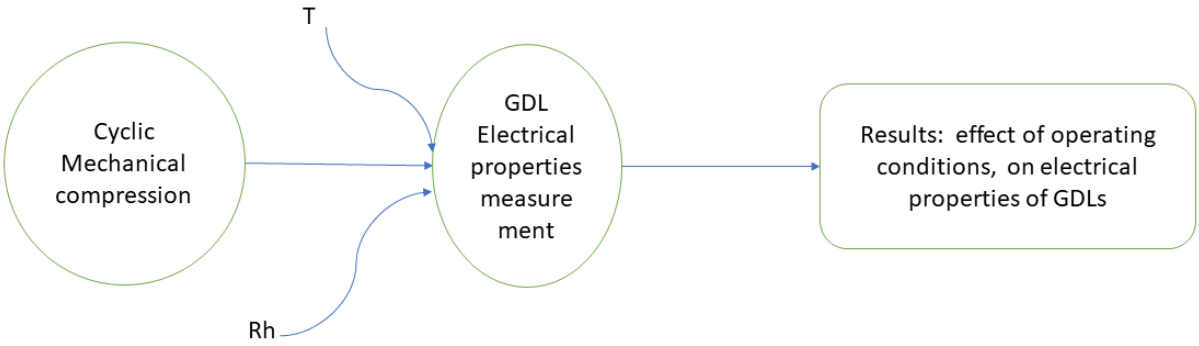

Fig 3. 57: Experimental method and results.

The different electrical resistivities (in-plane, through-plane, and contact resistance with the BPP) are influenced by various parameters and with different degrees of influence.

All electrical resistances decrease non-linearly with compression. An important decrease is observed at low pressure. Then a smaller one is measured at higher pressure values. The electrical contact and through-plane resistances are comparable in terms of values at medium pressure values. Rc varies from 2 to 70 mohm.cm^2, Rtp from 0.6 to 13,6 mohm.cm^2, and Rip from 3 to 38 mohm.cm. Let us consider a decrease of the specific electrical contact resistance between the GDL and the BPP of 20 mOhm.cm^2 for example after compression, with a cell crossed by 1 A/cm^2 current density. Let us also assume that the contact area between BPP and GDL is about half the total active area of the cell. The decrease of the specific electrical contact resistance will save 40 mV at each of the cell sides (anode and

cathode), leading to a total of 80 mV for the cell, which corresponds to a power density of 80 mW/cm². This is not negligeable as it corresponds to 5-6% of 1,3 W/cm² fuel cell (such as Toyota Mirai 2016 version)[3]. These resistances are all subject to hysteresis with the cycles of compression. This sensitivity to the cycles of compression is higher for the first cycles of compression and for lower compression values. The cycles of compression that can illustrate the variation of compression inside the FC in operation also influence other parameters such as permeability. This has been observed in [15] where permeability was measured for a number of GDLs before and after cyclic compression and was found to decrease, in different percentages. Related studies to explain these changes found in other GDL physical properties with the cycles of compression in relation to its structure and composition should be explored further to establish structural rules that may allow correlation between different GDL important properties, that are considered as factors impacting FC performance, and their behavior towards the cycles of compression (and generally towards FC operating conditions).

The effects of composition and structure on the different resistivities, and their behavior under cyclic compression are observed. Table 3.16 summarizes the influence of different parameters on the electrical resistances.

The PTFE increases both Rc and Rtp. It also decreases the anisotropy rate of Rip but increases its sensitivity to the cycles of compression. Rtp of GDLs containing PTFE increases with humidity.

The MPL decreases Rc, increases Rtp, and the sensitivity of Rc to the cycles of compression. The MPL increases Rip and in opposite to Rc. It also decreases the sensitivity of Rip to the cycles of compression. Rtp of GDLs containing MPL increases with humidity.

Globally, the most stable structures to the cycles of compression are the felt 3D structures. They are thus adequate GDLs for FCs subject to compression change such as in transportation applications. Graphitized fibers have also a quite stable

[3] According to (Henning Lohse-Busch, Kevin Stutenberg, Toyota Mirai Testing report which assumes an area of 237 cm² for a 114 kW fuel cell with 370 individual cells).

behavior and generally the smallest values of resistances. The less stable GDLs are straight carbonized fiber GDLs.

The contact resistance seems to be influenced by compression velocity and temperature. Humidity impacts the though-plane resistance and it also influences the in-plane resistivity.

The contact resistance of GDLs with graphite is larger than with gold-coated surfaces.

The experimental data gathered in this chapter can be used in numerical models in order to calculate the total ohmic resistance of GDLs and BPPs, and to estimate the total potential drop inside PEMFCs.

In this chapter, water saturated GDLs were investigated under cyclic compression, to see the effect of humidity on Rtp and Rip. Most water saturated GDLs which were untreated (with PTFE or MPL), depicted a Rtp smaller than dry GDLs. This is explained by a higher compression with humidity. Preliminary experiments show the same results for Rip.

The impact of humidity is estimated % on Rtp. Experiments were hold under 100% saturated GDLs for straight carbon paper GDLs. The impact of intermediate saturation levels can be interesting to explore, the case of the GDL H120 showing a higher Rtp with humidity and higher Rtp for 50% saturated GDL compared to 100 % should be explored. Experiments were conducted under water saturated GDLs; future investigations can be done under humidity conditions and for other GDL structures such as the felt structure.

Electrical potential drop in PEMFCs is related to the variation of the electrical resistances of its components with the different operating conditions. Mechanical compression, as shown in this chapter, impacts the different resistances. The distribution of the contact pressure at the interfaces between components, depends on several parameters and should be optimized to get the smallest possible resistances without damaging the FC components. In the next chapter, a mechanical finite element model (FEM) of the PEMFC combined with a design of experiment (DoE) is developed in order to investigate the effects of the thickness of the different PEMFC components and GDL compression behavior law on stress

and contact pressure distribution. The aim of the study is to obtain preliminary design rules to optimize contact pressure and stress distribution PEMFCs.

	Compression	Output characteristics	Velocity	Humidity / water saturation	Temperature	PTFE	MPL	Structure (Lowest values / most stable for cycles)
Rip	▼	Rip vs compression behaviour	/	▲	/	▼	▲	Graphitised fibre paper
		Sensitivity to cycles	/	▼	/	▲	▼	Felt and Graphitised fiber paper
Rtp	▼	Rtp vs compression behaviour	/	▼ (in most cases)	+	▲	▲	Thin straight fiber GDL
		Sensitivity to cycles	/	?	?	▲	▼	Felt with MPL and Graphitised fiber paper
Rc	▼	Rc vs compression behaviour	+	/	▲	▲	MPL side ▼ PTL side ▲	Graphitised fibre paper
		Sensitivity to cycles	/	/	▲	▲	▲	Felt structure

Table 3. 16: Influence of different parameters on the electrical resistances.

▼ : decrease ▲ : increase, +: influence;, /: not studied in this thesis, ?: not analysed.

3.6. References

[1] K. Bouziane, E.M. Khetabi, R. Lachat, N. Zamel, Y. Meyer, and D. Candusso, Impact of cyclic mechanical compression on the electrical contact resistance between the gas diffusion layer and the bipolar plate of a polymer electrolyte membrane fuel cell. Renewable Energy 153, 349–361 (2020).

[2] Fuel Cell store, Toray Carbon Fiber Paper "TGP-H". https://www.fuelcellsetc.com/store/DS/Toray-Paper-TGP-H-Datasheet.pdf (accessed 14 May 2019).

[3] Fuel Cell store, FREUDENBERG Gas Diffusion Layers for PEMFC and DMFC, http://www.fuelcellstore.com/spec-sheets/freudenberg-gdl-technical-data.pdf.

[4] H. Murrmann and D. Widmann, Current crowding on metal contacts to planar devices. IEEE Trans. Electron Devices, 1969;16:12:1022–1024.

[5] H. Murrmann and D. Widmann, Messung des Übergangswiderstandes zwischen Metall und Diffusionsschicht. Si-Planarelementen. Solid-state Electronics 1969;12:879–886.

[6] Tuttle. G, Contact resistance and TLM measurements, http://tuttle.merc.iastate.edu/ee432/topics/metals/tlm_measurements.pdf.

[7] El Oualid S, Lachat R, Candusso D, Meyer Y. Characterization process to measure the electrical contact resistance of Gas Diffusion Layers under mechanical static compressive loads. International Journal of Hydrogen Energy 2017;42(37):23920–31.

[8] Joint Committee for Guides in Metrology. Evaluation of measurement data — Guide to the expression of uncertainty in measurement. September 2008. https://www.bipm.org/utils/common/documents/jcgm/JCGM_100_2008_E.pdf (accessed 23 January 2020).

[9] D. Qiu, H. Janßen, L. Peng, P. Irmscher, X. Lai, W. Lehnert, Electrical resistance and microstructure of typical gas diffusion layers for proton exchange membrane fuel cell under compression, Applied Energy 231 (2018) 127–137

[10] Ö. Aydin, M. Zedda, and N. Zamel, Challenges Associated with Measuring the Intrinsic Electrical Conductivity of Carbon Paper Diffusion Media. Fuel Cells 15 (3), 537–544 (2015).

[11] S. Wang, Y. Wang. Investigation of the through-plane effective oxygen diffusivity in the porous media of PEM fuel cells: Effects of the pore size distribution and water saturation distribution. International Journal of Heat and Mass Transfer 98 , 541-549 (2016).

[12] Ö. Aydin, M. Zedda, N. Zamel, U. Groos, and C. Hebling, Comprehensive Understanding of Electrical Conductivity Measurements of Gas Diffusion, in 20th World hydrogen energy conference 2014.

[13] Sogol Roohparvarzadeh. Experimental characterization of the compressive behaviour of gas diffusion layers in PEM fuel cells, [Thesis, Master of Applied Science in Mechanical Engineering] University of Waterloo, Ontario, Canada (2014), p. 89.

[14] Graphtek manufacturer data sheet, available at (https://www.graphitestore.com/core/media/media.nl?id=9561&c=4343521&h=10193ebc1eef07343903) ((accessed May 2021)

[15] Aldakheel, F.; Ismail, M. S.; Hughes, K. J.; Ingham, D. B.; Ma, L.; Pourkashanian, M.; Cumming, D.; Smith, R. Gas permeability, wettability and morphology of gas diffusion layers before and after performing a realistic ex-situ compression test, Renewable Energy (2019), doi:10.1016/j.renene.2019.11.109

Annex 1: GDL compression stress-strain curve

Figure A1 represents resulting experimental stress-strain curves for GDLs investigated under 0-8 MPa cyclic compression while measuring specific electrical contact resistance [A1].

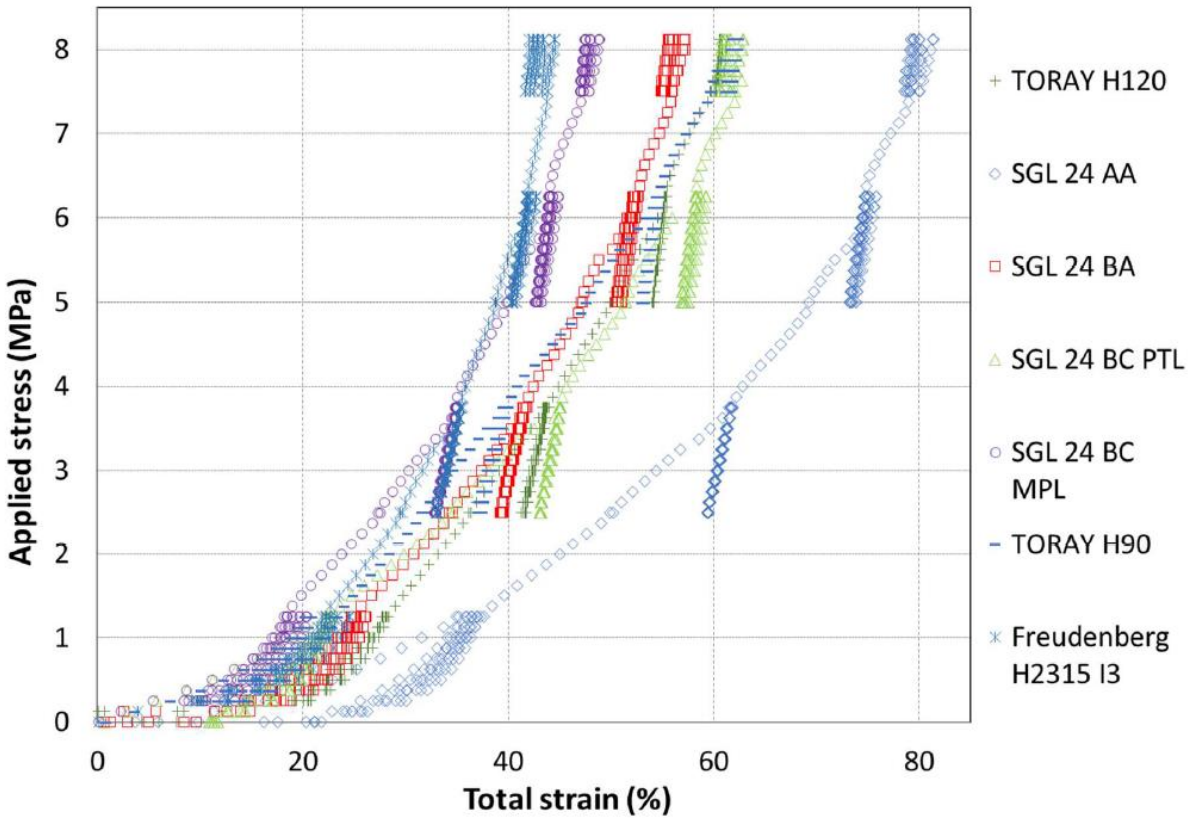

Figure A1: experimental stress-strain curves of compressed GDLs

[A1] Khadidja Bouziane, El Mahdi Khetabi, Rémy Lachat, Nada Zamel, Yann Meyer, Denis Candusso. Impact of cyclic mechanical compression on the electrical contact resistance between the gas diffusion layer and the bipolar plate of a polymer electrolyte membrane fuel cell. Renewable Energy 153 (2020) 349-361.

Annex 2: Water saturation investigation

In Table A1, weights of dry and wet GDLs that were soaked in deionised water (just after taking the GDL out of the water recipient) are presented with the number of hours of soaking. Two samples (Sample 1 and Sample 2) were used for every hour.

Method	Simple DI soaking in water				
GDL Type	24 AA				
GDL	Soaking time (h)	Dry Weight (g)	Wet Weight (g)	after 2 min	after 10 min
Sample 1	1	5.23	30.4	29.14	20.38
Sample 2	1	5.21	38.32	37.05	30.66
Sample 1	2	5.42	31.58		24.33
Sample 2	2	5.18	38.25	37.17	24.39
Sample 1	3	5.18	11.4	10.4	6.33
Sample 2	3	5.79	47.01	46.64	9.55
Sample 1	4	5.46	31.24	30.39	14.41
Sample 2	4	5.54	39.32	38.27	22.41
Sample 1	5	5.15	23.61	22.61	16.41
Sample 2	5	5.17	26.11	24.82	13.04
Sample 1	6	6.12	30.35	29.2	19.17
Sample 2	6	4.94	30.3	29.55	9.82
Sample 1	7	4.62	37.36	36.34	26.94
Sample 2	7	5.61	38.03	37.26	13.23
Sample 1	24	5.54	38.38	37.19	
Sample 2	25	5.75	27.38		
Dry mean weight		5.37			

Table A1.: GDL weight by simple soaking in water.

Table A2 presents the wet and dry GDLs weights when using magnetic stirring.

Sample name	Soaking time (h)	Dry weight (g)	Wet weight after evaporation time (min)								
			0	2	5	10	20	30	40	50	60
Night rotation 1	16	5.97	36.46	35.56	30.74	24.27	14.55	6.43	6.	5.98	6.07
Night rotation 2	16	5.23	32.55	32.55	27.27	24.82	13.22	5.98	5.29	5.35	5.38
Night rotation 6	16	4.98	39.07	43.47	37.43	35.76	26.75	18.08	10.48	5.62	5.62
Night rotation 7	16	5.23	35.73	34.49	32.19	22.11	32.61	7.63	6.88	6.14	6.14
Night rotation 3	23	4.63	17.2	15.31	9.18	7.54	5.3	5.27	0	0	0
Night rotation 4	23	5.71	34.75	30.02	27.15	21.58	7.71	6.04	5.95	0	0

Table A2.: GDL weight using magnetic stirring

Chapter 4: PEMFC model

4.1 Introduction

The link between the energetic performance of a PEMFC and external-internal mechanical excitations [1], as well as environmental conditions is one of the significant factors influencing its industrialization [2].

In the previous chapter, the electrical properties of several structures of GDLs have been investigated experimentally under the effect of FC environmental and operational conditions. It appears that mechanical compression has a substantial impact on the electrical bulk and contact resistances which affect the global electrical performance of the FC, as these resistances result in ohmic losses. Besides, the response of the electrical resistance decrease with compression is not linear leading to potentially an optimal pressure state (as has been seen in the thesis of El Mahdi Khetabi where in-situ means were employed to study the effect of compression on PEMFCs) and to consider more realistic GDL mechanical behavior laws. Especially, that mechanical compression also affects the material strength of the different components. It is interesting to know how these mechanical constraints are influenced by the different parameters resulting from the choice of the FC components by developing and using numerical mechanical models. The literature on these mechanical aspects and the selection criteria of cell components are relatively limited [3].

Besides, laws relating GDL electrical properties (resistances) as a function of mechanical compression need to be used in these numerical models in order to link this local ex-situ (i.e. outside of the FC) investigated properties with the global FC performances that are measured in-situ (while the FC is operating).

To enhance the design lifecycle of these FC systems, it is thus necessary to have preliminary design models meeting the requirements of reliability and performance, reducing PEMFC cost and increasing lifespan, that consider the above properties. A preliminary design model is developed to allow the initial exploration of the design space with a limited computation cost. The early-stage design is important because the major design choices are made at this stage, in

particular the product architecture. For example, this could enable to design new stack compression systems for assembly procedures and FC operation by reducing Ohmic losses in the electrical power generator. After this stage, the possibilities for product innovation or modification are quite limited [4]. Consequently, from the beginning of the design process, it is important to have a better understanding of the parameters that play a role in electrical power generation, such as the electrical Contact Resistance (CR) which influences the electronic losses. As shown in the previous chapters, this resistance is strongly dependent on the contact pressure resulting from mechanical excitations. It is thus important to study the parameters influencing this contact pressure.

Among the external excitations of a PEMFC, there are assembly procedures, operational and environmental aggressive conditions. Here, we will be interested in the mechanical clamping of stack [5] which is used in order to assemble different components of the PEMFC. As presented previously, this mechanical stress influences the GDL physical properties and the global FC performance [6-8]. To optimize the performance of a PEMFC, the mechanical excitations must be handled. The mechanical compression during mechanical clamping reduces ohmic losses due to the resistance of the GDLs and rise of mass transport losses by reducing the porosity of the GDL. The experimental analysis given in the previous chapter shows that both contact and bulk electrical resistances of different GDL structures decrease with mechanical compression non-linearly.

Among the components of PEMFC, GDLs play a major role in the cell performance by allowing a homogeneous distribution of gas from the channels to the membrane and ensuring thermal and electrical conduction. In fact, even though most physical properties of GDL show non-linear trend with compression [9-13] (See Chapter 2), most studies treating PEMFC analysis and modelling use a linear GDL constitutive law. Articles focusing on GDLs sometimes consider a hyper-elastic constitutive law [14]. However, the comparison between these linear and hyper-elastic behaviours is little explored. The experimental analysis of several GDL structures given in the previous chapter concludes on a non-linear decrease of

contact resistance with compression with more than 75% of total reduction that was attained at 2.5 MPa.

The representativeness of the preliminary models involves the study of non-linearities, in particular for GDL [15]. In this study, we are especially interested in the influence of the GDLs constitutive law (linear and hyper-elastic constitutive laws) and the layer thicknesses of PEMFC components on the contact pressure (CP_{RESS}) on the performance of PEMFC. Geometry, especially all the layer thicknesses, plays an important role in the performance of PEMFC. The layer thicknesses influence the variation of the mechanical stresses and therefore affects performance. The PEMFC performance is associated with contact pressure CPress which is defined by Equation (4.1).

$$CPress = \frac{N}{a \times b} \tag{4.1}$$

With

- N: Normal plan force [N],
- a: Contact width (x direction see Fig. 4.1 and Table 4.2).
- b: Contact height (z direction see Fig. 4.1 and Table 4.2).
- a×b: the real contact surface between interface [m²].

The performance in terms of power generation depends on protonic losses and electronic losses. About 50% of electronic losses stem from Contact Resistance (CR) [16,17]. At each interface, there will be a loss of current intensity due to insufficient surface-to-surface contact. Studies have found that Mechanical CPress can strongly affect CR [5,6] and a relation between CR and CPress was observed [7,18]. The most important electronic ohmic losses in FC are at the BPP - GDL interface with the electrical CR [1, 19]. The aim of this preliminary design model is therefore to have the optimal contact pressure in order to reduce the CR as much as possible [20,21].

The study goes further by using a Design of Experiments (DoE) with a 2D Finite Element (FE) Model including contact friction to study the effect of geometry and constitutive law of materials, on the mechanical and electrical performance of a

PEMFC stack. To validate and assess numerical results, comparisons are made with experimental results from literature. The combined DoE & FEM methodology is presented in the next section, followed by the results on the effect of parameters and a critical discussion of the study.

The numerical investigation presented in this chapter was first published in the International Journal of Hydrogen Energy - Elsevier. The present chapter is, therefore, an updated version of the previously published paper [22].

4.2 Methods

The main purpose of this study is to investigate the effects of geometry and GDL constitutive law on CPress. A 2D Finite Element (FE) model with contact friction has been developed to simulate the mechanical properties to obtain CPress and von Mises yield criterion. An effective approach is proposed to save CPU time with DoE methods, by using Taguchi approach. DoE provides also an optimal simplified model to maximize the pressures for each interface and minimize the constraints.

4.2.1. Finite element Model

A FE model has been developed with the commercial software Abaqus [23]. This software uses the Finite Element Method (FEM) to solve engineering and mechanical problems. The FE Modelling permits to build a representation of a problem in a model and to give the structure behaviour subjected to environmental conditions and to external / internal mechanical excitations.

4.2.2. Finite Element Model & geometry

A 2D symetric plane strain FE model with contact friction has been developed to simulate the mechanical properties to obtain Contact pressure “CPress” and Von Mises yield criterion using commercial software Abaqus [23].

This modeling is aimed to obtain a global mechanical behavior and not a local one. In order to limit the computation (CPU) time, the model is simplified without BPP distribution channels. Elastomeric gaskets are not included as the force on the gasket used represents only 5% of the total clamping force [24]. A single fuel cell

was simulated. Due to symmetry of a cell, only half of the single fuel cell has been modelled. The model components are EP (End Plate), BPP, GDL, and MEA as shown in Fig. 4.1.

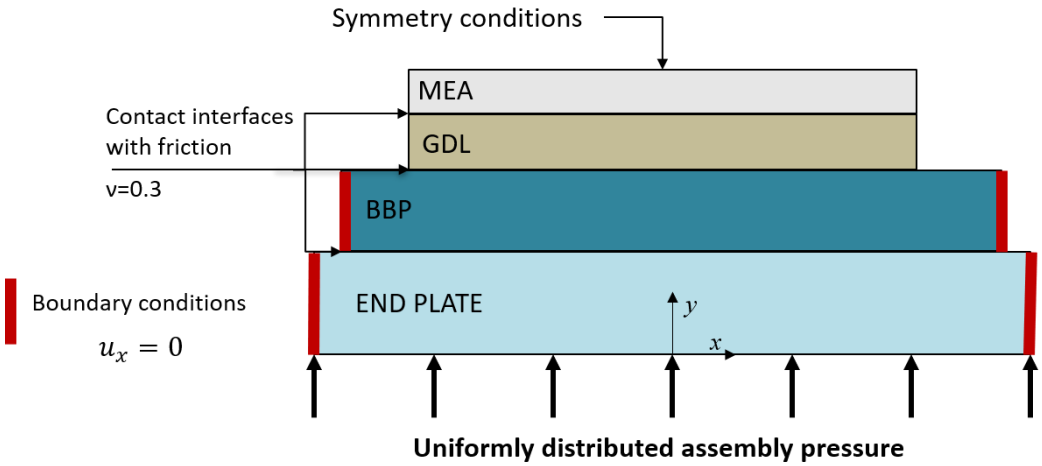

Fig. 4. 1: A single fuel cell model.

The model is built with the following assumptions:

- Assembly pressure of 1 MPa uniformly applied on the End plate.
- Boundary conditions applied on BPP and EP are $u_x = 0$ (see fig. 4.1).
- Symmetry conditions applied on MEA.
- Coefficient of adhesion friction is μ=0.3,
- Contact follows Coulomb's law T= N.μ = N.tanφ [24].

With :

T: Tangentiel force.(N)

N: Normal Plan force (N).

μ: Coefficient of adhesion friction.

φ: Grip angle.

u, u_y: Displacement following direction x, direction y.

Constant widths and the heights in direction x and z are presented in fig 4.1 and Table 4.1; the thicknesses in y direction are variable. The first objective of the

study is to quantify the impact of thickness on CPress and then on electrical contact resistance. The second objective is observing the constitutive law on the mechanical and electrical behaviour of a PEMFC. For this purpose, the model developed by Mishra [25] is applied to link mechanical contact pressure and electric contact resistance (and thus the PEMFC performance). Thus, it is possible to take into account analytically the geometry of the BPP and limit the loss of accuracy. A balance between computation time and accuracy was sought.

	Width (a) [mm]	Height (b)[mm]
EP	350	350
BPP	295	295
GDL	200	200
MEA	200	200

Table 4. 1: Description of the model geometry.

4.2.3. Material properties

The mechanical behavior is included in the assembly model with homogeneous and isotropic materials. The constitutive laws applied derive from mechanical stress-strain tests [26]. The elastic material properties of EP, BPP, GDL, and MEA are listed in Table 4.2. The mechanical properties of the Nafion membranes (112, 115, and 211) are given for 90 % RH at 40 °C [27]. For simplicity, this hydration level is assumed to be constant throughout the compression process, although in real applications this may not be necessarily true. This study focuses on the influence of GDL constitutive law on contact pressure with hyperelastic and linear constitutive law. The GDL hyperelastic constitutive law was extracted from uniaxial experimental data with a Marlow deformation energy potential model [26] where linearity was only found for little deformations. The value of Poison's ratio for GDLs is taken according to different literature studies that considered this value of 0.25 [28-31].

Cell component	Material	Young modulus [MPa]	Poisson's ratio
EP	Aluminium alloy	70 000	0.33
BPP	Graphite	5 100	0.25
GDL	TGP-H-90	60	0.25
MEA	Nafion	190	0.25

Table 4. 2: Mechanical properties of the PEMFC components.

The GDL has a hyperelastic behaviour due to its microstructure. Therefore, the assumption of a linear constitutive law should be used carefully. As shown in fig. 4.2, for a GDL strain smaller than ε=0.14, the linear nominal stress will be lower (up to 56.12% max) than Marlow's stress (non-linear). Near to zero and for ε=0.14, the differences between these laws are slight. The hyper-elastic law is only used in the model to analyse the non-linear behaviour of the loading in the first cycle compression. Cyclic behaviour is not studied in this numerical analysis.

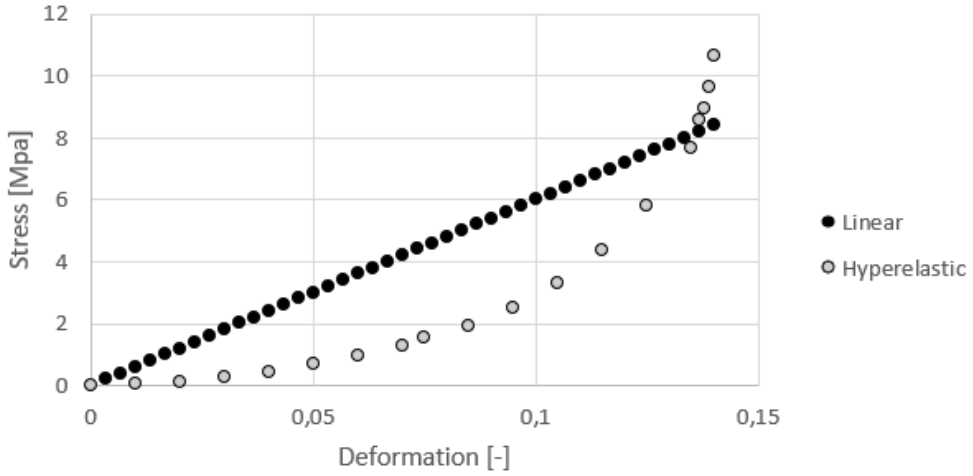

Fig. 4. 2: Relation stress/strain of GDL - comparison between linear/hyperelastic laws.

4.2.4. Meshing

In this FE modelling, the greatest difficulty is to keep a continuity in the mesh with a great variation in thickness. The MEA can be five hundred times smaller than BPP. The mesh has element shape quad dominated with CPE4RH element type a 4-node bilinear plane strain quadrilateral in linear interpolation [23]. This element type is imposed by the choice of the hyperelastic law for the GDL. The number of nodes and elements resulting from the mesh of the half-single fuel cell according to the different tests are given in Table 4.3.

Test	Nodes number	Elements number
1	142 294	121 976
2	181 601	161 284
3	11 602	8 735
4	25 655	19 484
5	222 898	202 568
6	147 107	133 750
7	30 987	26 000
8	35 000	39 013
9	-	-

Table 4. 3: Mesh description.

The FE number is investigated to have a good mesh quality on the entirety of the model. The aim is to have a sufficiently fine mesh so that the results are consistent and the CPU time short. Hence the size mesh of the model is adapted in function of the variations in thickness as shown in fig 4.3. To guarantee the quality of the results, a mesh with at least two elements in the thickness of each component has been chosen. The compromise for the overall mesh size is between 0.01 and 2.5 depending on thickness size.

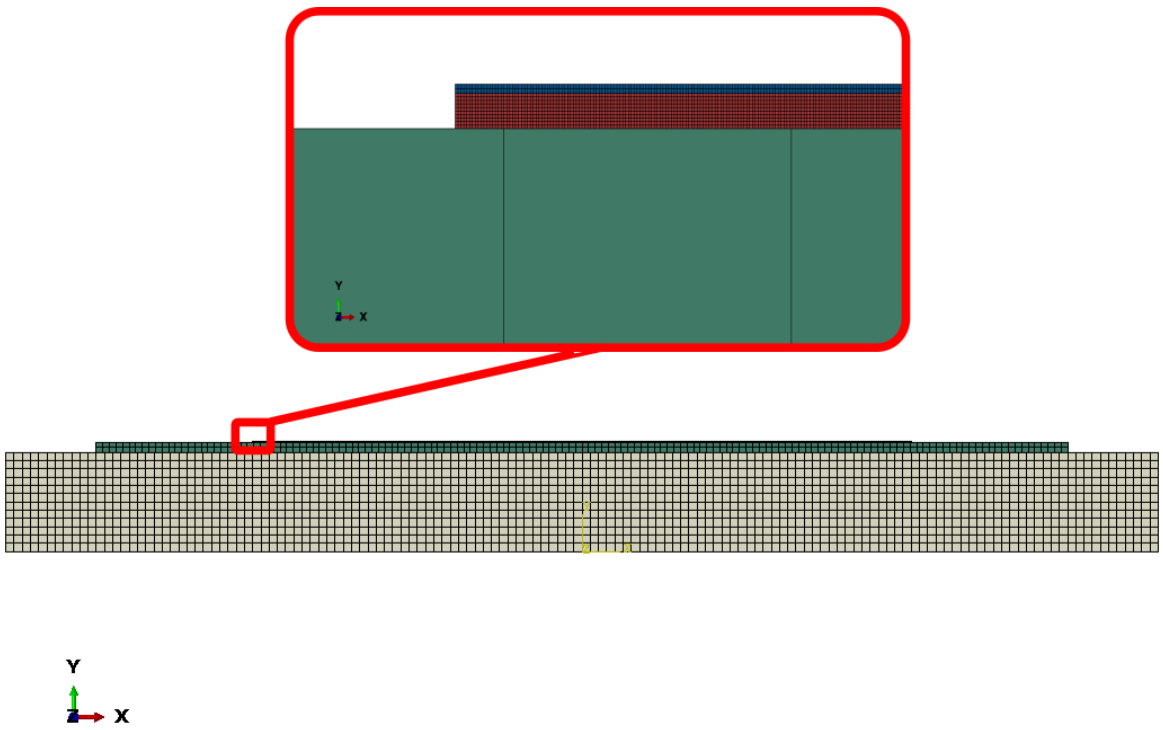

Fig. 4. 3: Mesh used for computations.

4.2.5. Parameterization of Abaqus

Models are set under two steps to simulate the assembly procedure. An initial step at 0 “time” period and another one at 1 “time” period. In a nonlinear analysis, a step takes place over a finite period of "time", although this "time" has no physical meaning unless inertial effects or rate-dependent behaviour are important. The incrementation is automatic with a maximum number of 100 increments. The initial increment size is between 0.0001 and 0.01. The maximum increment size is 1 and the minimum lies between 1E-30 and 1E-05. The other step parameters are the selection of the direct solver method and the full Newton solution technique. A linear extrapolation, in “time”, of the previous incremental solution is used to begin with the non-linear equation solution for the current increment. The uniform pressure is 0 MPa at initial step and loaded of 1 MPa at charge step. The boundary conditions are applied on BPP and EP. The BPP and EP have the boundary condition u_1 (corresponding to ux) blocked and a symmetry on the MEA with $u_2=0$ as seen in fig. 4.1. The representations used in Abaqus for the interactions between

components are: surface-to-surface contact (standard) type with master surface and slave surface. The contact interaction property is a tangential behaviour isotropic with a friction coefficient of 0.3, which was the most suitable value for the convergence of the model. To avoid interpenetration between each element, a non-penetration constraint is applied. The analysis is run in Abaqus/Standard with the Newton-Raphson method on 4 processors and 1 GPGPU acceleration. To ensure the convergence of the calculations, the initial increment size could be decreased.

4.2.6. Design of Experiments with Taguchi approach

4.2.1.1. Explanation for simplification

A DoE allows saving time thanks to a series of tests organized in advance to understand and quantify multiple parameters in a minimum of tests. It avoids combining all the modalities of all the parameters. Using a DoE table, the number of tests is given in Equation (4.2).

$$model\ number = LEVEL^{factor} \tag{4.2}$$

With:

- Factor: number of parameters to vary; factors are independent variables,
- Level: numbers of factor values.

The Taguchi approach permits the reduction of the model number thanks to standard tables which list the most common combinations of levels and factors [32].

4.2.1.2. Modalities

The model has 4 factors: thicknesses of EP, GDL, BPP, and MEA with three levels. To highlight the influence of geometry with a classical DoE method, 3^4 meaning 81 different models have to run. Moreover, as the influence of the constitutive law on the contact pressure is also studied, we would have two tables of DoE: one table with GDL hyperelastic constitutive law and the other one with GDL linear constitutive law. Consequently, 162 models should run.

For 4 factors with 3 levels, the table for the Taguchi approach is an experimental matrix L_9 with 9 the model number. Tables 4.4 and 4.5 respectively give the description of models and the details of the different factors and levels. The Taguchi method allows the reduction of the number of models from 162 to 18.

Test Nr.	Levels of controlled factors				Results
	A	B	C	D	
1	1	1	1	1	R1
2	1	2	2	2	R2
3	1	3	3	3	R3
4	2	1	2	3	R4
5	2	2	3	1	R5
6	2	3	1	2	R6
7	3	1	3	2	R7
8	3	2	1	3	R8
9	3	3	2	1	R9

Table 4. 4: Description of models in the Taguchi approach.

Factors	Level 1	Level 2	Level 3
A - MEA	Nafion-112	Nafion-115	NR 211
	0.05	0.127	0.0254
B - GDL	TGP-H-060	TGP-H-090	TGP-H-120
	0.19	0.28	0.37
C - BPP	Bipolar Graphite Plate		
	3	6.35	12.7
D - EP	30	15	7.5

Table 4. 5: Description of the levels (thicknesses) in the DoE.

4.2.7. Coupling FEM and DoE

In a first step, the geometry and material characteristics are chosen in the literature dedicated to PEMFCs [33-36]. In a second step, the mechanical properties given are simulated with the software Abaqus [23]. Finally, the DoE factors are extracted following the flowchart in fig. 4.4. This methodology implied to simulate a configuration of mechanical properties individually. 9 tests have been modelized. For every model, CPress and the Von Mises yield criterion are extracted for each step of increment. All the curves presented in this study are related with the loading step at 1 s.

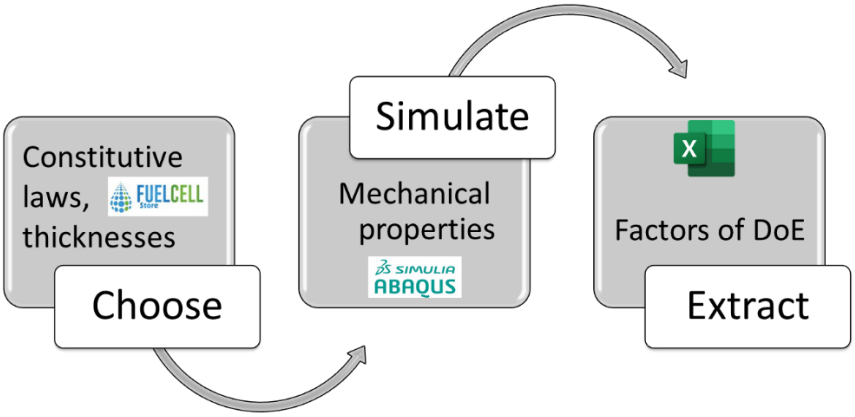

Fig. 4. 4: Methodology for coupling FEM and DoE.

4.3. Results

The mechanical behaviours of the PEMFC components are described in the following section, which also includes a detailed comparison between numerical results and those from the literature.

4.3.1. Geometry effects and most influential components

4.3.1.1. Geometry effects on the model convergence

Concerning the choice of the factor D-EP to level 3 (D3) in the selected Taguchi table, a first set of simulations with a value of 1.588 mm was achieved. Tests 3, 4, 8, and 9 could not converge. In the analysis of the inconclusive tests, we observed that there could not be a smaller End Plate (EP) than the BPP. On the one hand, with a BPP thickness below 10% of the EP thickness, the numerical calculations did not run. We assume that is due to a significant penetration of the materials with each other. Thanks to a new value of 7.5 selected for D3, we were able to run Tests 3, 4, and 8. On the other hand, regarding Test 9, we concluded that a very thin MEA in front of the GDL and/or EP has a negative impact on the convergence of the calculation. Indeed, in Test 9, the MEA-GDL thickness ratio (7%), and especially the MEA-EP thickness ratio (0.08%), are smaller compared to the thickness ratios of the other tests. There are no results for the Tests 9 because their thickness ratios have remained disadvantageous for the calculation in Table 4.6. By analyzing the inconclusive tests, it is possible to establish preliminary

design rules for the numerical model (and maybe the physical stack) based on thickness ratios: the MEA/GDL ratio must be greater than 9%, the MEA/EP ratio between 0.7% and 1.7%, the GDL/EP ratio less than 12% and the BPP/EP ratio less than 190%. A detailed study on the thickness ratios effects on the numerical model would surely be very interesting.

Hyperelastic GDL						
Results	Max. von Mises yield criterion [MPa]			Max. contact pressure [MPa]		
	Contact GDL-MEA	Contact BPP-GDL	Contact EP-BPP	Contact GDL-MEA	Contact BPP-GDL	Contact EP-BPP
R1	7.81	2.75	7.27	8.2	8.2	7.62
R2	14.37	5.87	2.29	14.45	14.27	9.75
R3	23.57	15.56	16.15	23.84	31.61	8.58
R4	30.84	34.34	107.85	34.66	62.51	15.49
R5	14.37	2.75	7.27	8.05	8.04	7.62
R6	13.86	5.95	14.5	15.52	15.34	13.29
R7	13.98	13.83	7.98	13.18	5.6	8.66
R8	42.93	48.45	30.4	41.13	115.2	22.25
R9	-	-	-	-	-	-

Table 4. 6: Maximum pressure and von Mises yield criterion for hyperelastic GDL.

4.3.1.2. Geometry effects on mechanical behaviour

First, let us note that we aim to minimize the von Mises yield criterion in order to limit the load on the components and thus avoid the definitive failure of the materials. On the other hand, the contact pressure at the interfaces needs to be

maximized since the more surface will be in contact, the better the contact resistance and therefore the FC performance.

Table 4.6 shows the maximum von Mises yield criterion and the maximum contact pressures at the interfaces of the models with a hyperelastic constitutive law for the GDL. The lowest and highest values are calculated for Tests 2 and 8, respectively. In Test 2, the smallest von Mises yield criterion is between the EP and the BPP: 2.29 MPa. In Test 8, the highest stress pressure is between the BPP and the GDL: 115.2 MPa.

By only changing the thicknesses, there is a variation of 97.9% between extreme values of von Mises yield criterion at the EP-BPP interface and 95.1% for the contact pressure at BPP-GDL interface. This observation confirms that thickness plays a key-role in the performance of the FC.

4.3.1.3. Most influential constitutive components

In Table 4.7 summarizing the factor effects, the EP factor (called D in the DoE) has the highest numerical values. So, the EP thickness has a greater influence on stress and contact pressure. The EP thickness controls the behaviour of stress and pressure in the other components. A thin EP considerably increases the CPress and especially the stress as shown in Table 4.7.

		Total effect on von Mises yield criterion [MPa]	Total effect on contact pressure [MPa]
MEA	A1	-28,74	-21,96
	A2	16,63	-3,96
	A3	18,18	38,88
GDL	B1	14,93	-9,42
	B2	-4,38	16,12
	B3	-15,82	-10,04
BPP	C1	-2,64	18,12
	C2	37,16	11,43
	C3	-22,13	-25,74
EP	D1	-39,51	-40,27
	D2	-29,74	-27,45
	D3	56,08	54,29

Table 4. 7: Total effects of the DoE study with hyperelastic GDL.

It is certain that the EP is an important element to obtain a maximum contact pressure. The smaller thickness of the EP (7.5 mm) increases the contact pressure and especially the stress. For EP thickness of 30 mm, there is an effect of 54.29 MPa on the contact pressure and 56.08 MPa on von Mises yield criterion.
To find the best EP thickness, it is therefore necessary to choose an EP thickness that can increase the contact pressure without overstraining the EP and the BPP. It will certainly be necessary to look for the best trade-off in the interval [7.5mm; 15mm].

4.3.2. Effect of the GDL constitutive law

The comparison between the linear and hyperelastic constitutive laws is presented in Table 4.8. For the linear constitutive law, there are high reductions or little rises

of the stresses and pressures, comparatively to the tests done with hyperelastic constitutive law. This is due to the different evolutions of the constitutive law in linear and hyperelastic modes.

Difference between hyperelastic and linear laws						
Results	von Mises yield criterion [MPa]			Contact pressure [MPa]		
	Contact GDL-MEA	Contact BPP-GDL	Contact EP-BPP	Contact GDL-MEA	Contact BPP-GDL	Contact EP-BPP
R1	2.17	-4.79	-1.74	2.32	-2.94	2.39
R2	2.53	-3.67	-5.85	3.50	-1.26	2.57
R3	3.67	-2.14	0.65	5.74	0.21	-0.415
R4	5.39	10.83	-0.84	6.35	23.17	0.46
R5	9.31	-4.89	-2.18	2.76	-4.16	4.09
R6	3.19	-6.92	3.23	3.97	-4.65	3.61
R7	4.21	4.02	0.08	2.05	-9.06	0.13
R8	10.73	21.15	4.6	15.33	52.6	4.35

Table 4. 8: Difference for maximal pressure and maximal von Mises yield criterion between the hyperelastic and linear laws.

Surprisingly, the change in the GDL constitutive law is not directly related to its thickness. It appears that the influence of thickness ratios between them are predominant for the stress. It seems that the contact pressure is influenced by the thickness of the EP. When it is small or equal to 15, there is a decrease at the GDL-MEA and EP-BPP interfaces, and an increase at the BPP-GDL interface, in comparison with the results of the hyperelastic behaviour law. When the thickness of the EP is 7.5mm, another distribution can be observed.

The GDL constitutive law does not influence the characteristics of the best thicknesses which optimize the FC performance. On the contrary, the constitutive

law affects the extremum of the DoE according to the thickness ratio. This confirms that the GDL constitutive law plays a role in the FC performance. Nevertheless, it seems to have less impact than the variation in thickness.

4.3.3. Behaviour of compression and stress at interface

In order to understand the performance, the contact between the interfaces is studied with the von Mises yield criterion. The behaviour of CPress and stress changes according to the thickness ratios and the GDL constitutive law for a given interface.

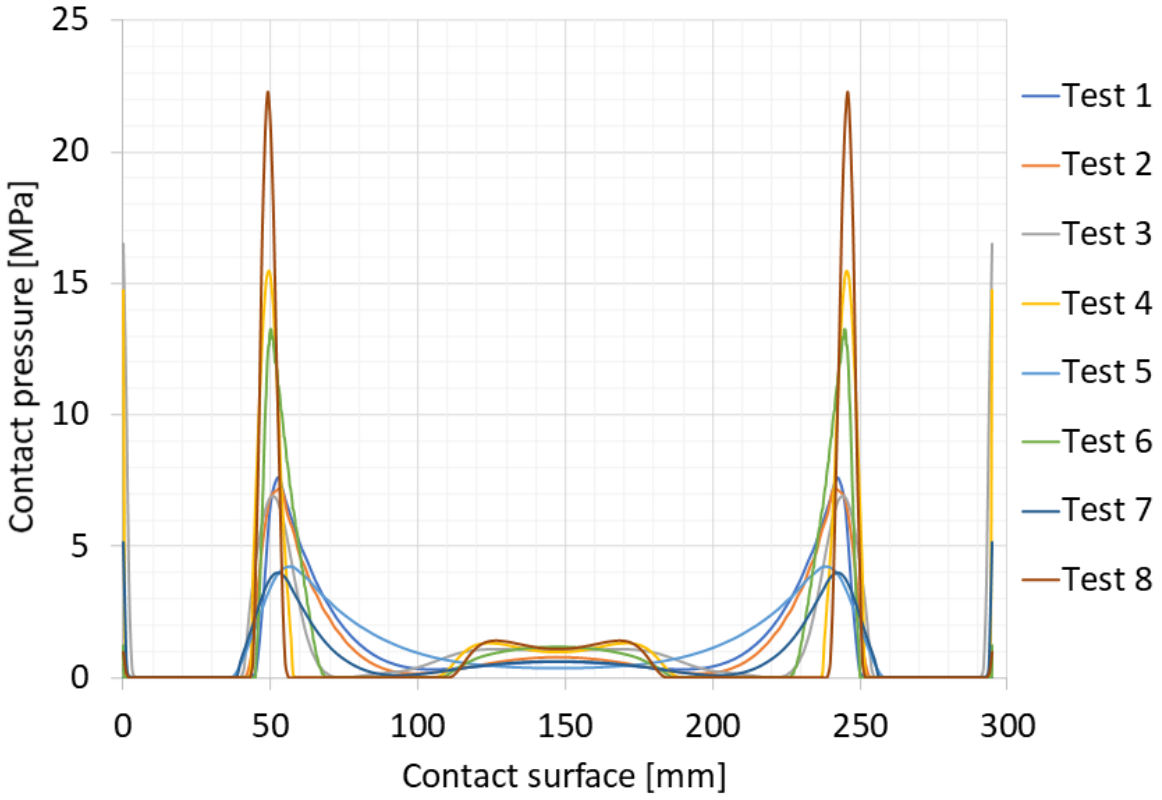

Fig. 4. 5: CPress at the EP-BPP interface with hyperelastic GDL.

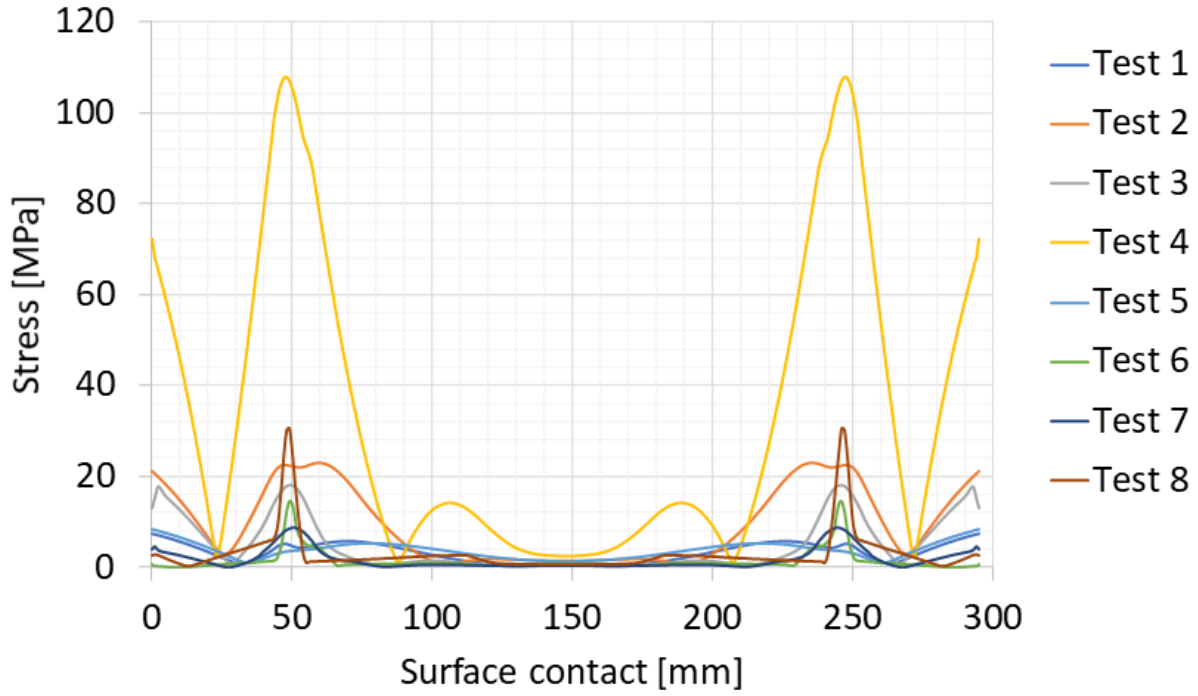

Fig. 4. 6: Von Mises yield criterion at the EP-BPP interface with hyperelastic GDL.

For the EP-BPP interface, the simulations led to inhomogeneous but symmetrical behaviours along the surface, as shown in fig. 4.5 and 4.6. There is a pressure drop on the edge and in the middle of the interface. A pressure drop means a bad contact between the two interfaces, leading therefore to a debonding. This bad contact can cause an increase in the electric contact resistance inside the fuel cell and therefore induce a loss of performance. As presented in fig. 4.5, the pressures vary between 5 and 22 MPa as a function of the thickness ratios.

Overall, for the tests with low pressures under 13.5 MPa, there is a correlation between pressure and stress as presented in fig. 4.5 and 4.6. When the pressures are low, so are stresses. This is the case for Tests 1, 6, and 7. Others, such as Tests 2, 3 and 6, have medium pressures, and the stresses extend from the maximum pressure area to the center of the interface. This can sometimes be noticed for a

surface contact of 40 mm, as it is the case for Test 2. This suggests that there is slippage and shear between the EP and BPP interfaces.

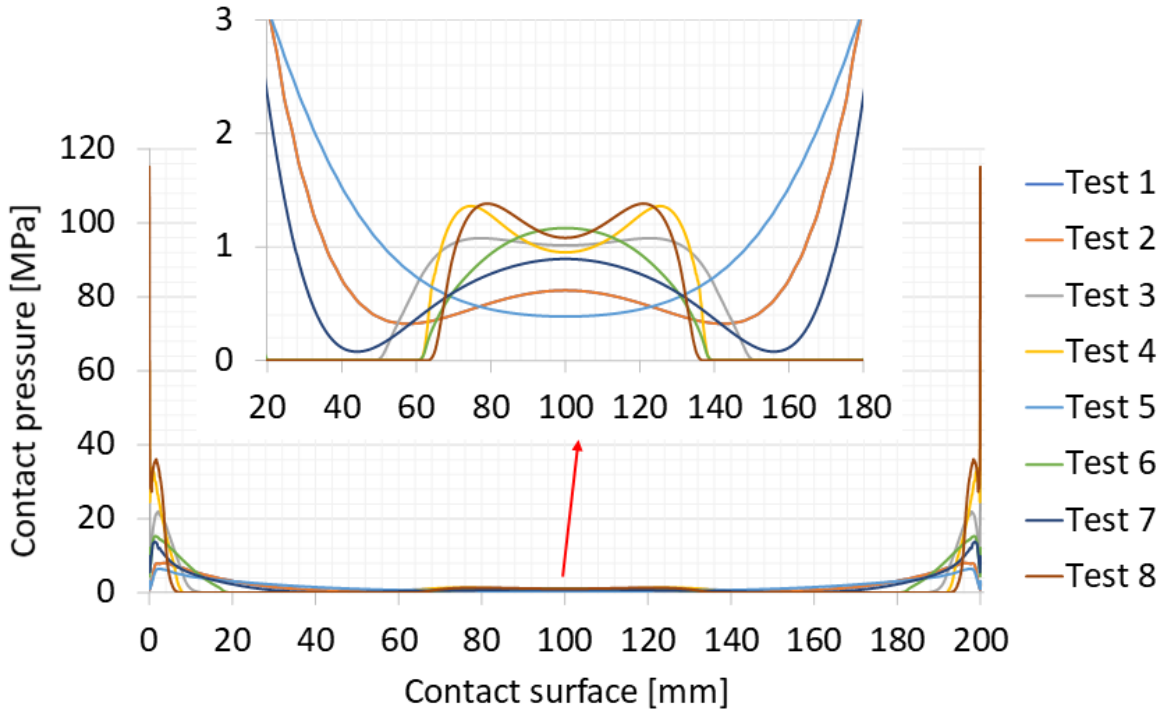

Fig. 4. 7: CPress at the BPP-GDL interface with hyperelastic GDL.

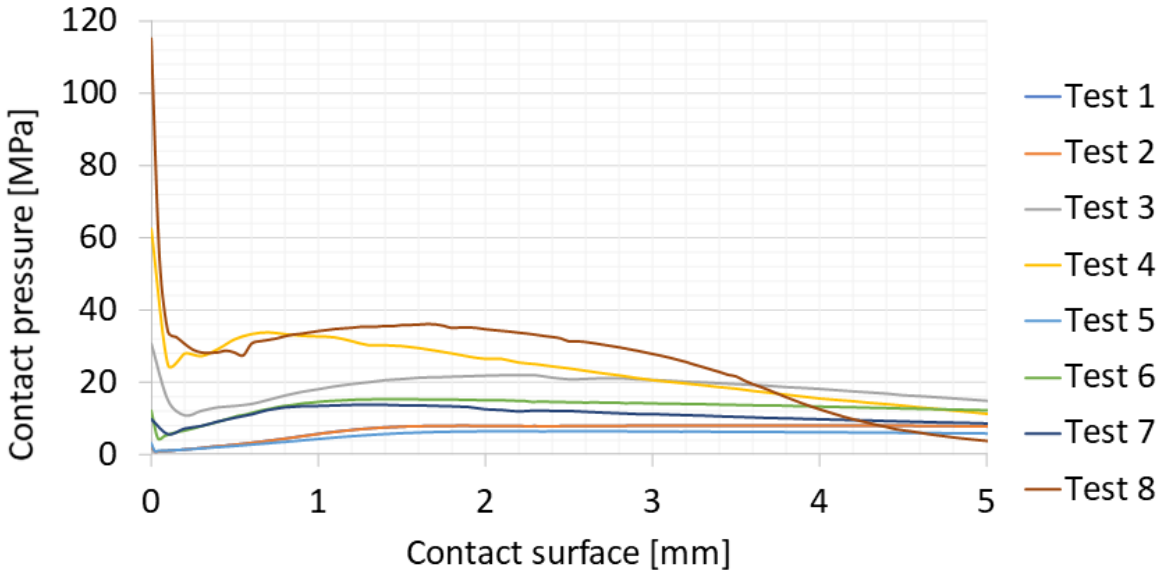

Fig. 4. 8: Zoom-in for CPress at the BPP-GDL interface with hyperelastic GDL sssssssssss

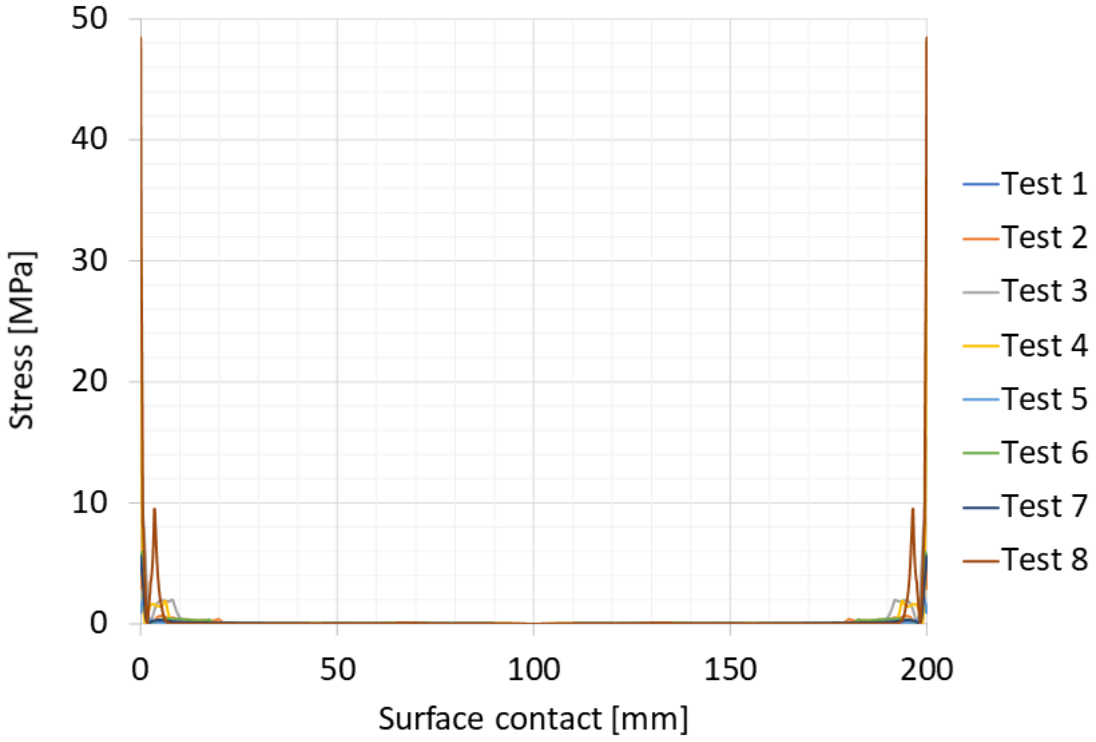

Fig. 4. 9: Von Mises yield criterion at the BPP-GDL interface with hyperelastic GDL

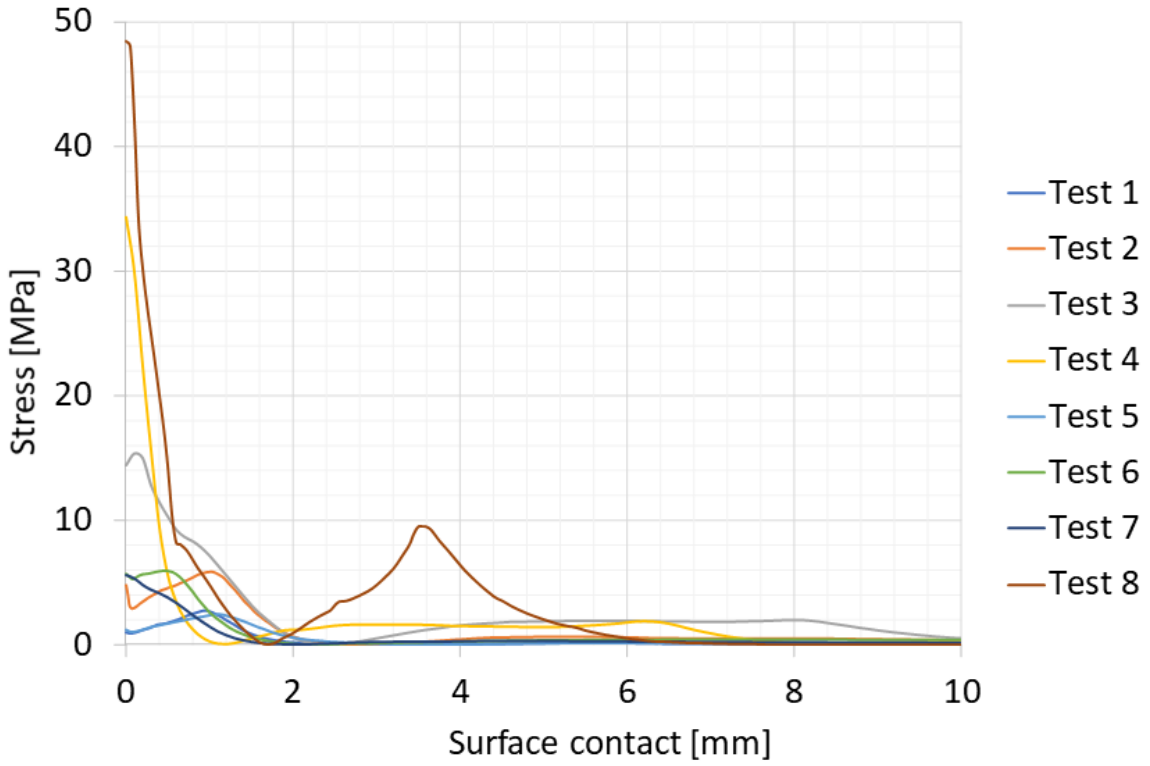

Fig. 4. 10:Fig. 4. 10: Zoom-in Von Mises yield criterion stress at the BPP-GDL interface with hyperelastic GDL.

At the BPP-GDL interface, the pressures have their highest values at the edge of the interface. But in the middle of the edge, the mechanical pressures are close to 0. Overall, these pressures range from 0 to 118 MPa. It is two times more than the maximum stress of the BPP-GDL interface. The behaviours in pressure and stress at this interface are similar, except at the ends. Further analysis of the tests shows that for each test the highest value of pressure and stress is at the edges of interface, as depicted in fig. 4.7, 4.8, 4.9, and 4.10. In the range [0; 5 mm], the contact pressure is greater than the stress. After 5 mm, the values are near to 0. The contact pressure behaves in a similar way for all the tests: with an overpressure at the edges, then with a depression close to the edge, and a new overpressure until approaching 0 after 5 mm as in fig 4.7. When observing the zoom of fig 4.7 along the internal low contact pressure area, it is interesting to note that tests 1, 2, 5, and 7 show a pressure higher than 0.07 MPa, meaning that

contact is insured along all the interface. The behaviour of the stresses fluctuates more between the different tests, with the same overstress and under-stress pattern as the contact pressures, except for Test 7 given in fig. 4.9. For example, in fig. 4.9 and for Test 7, there is no under stressing close to the edge and for Test 9, there is considerable overstressing close to 4 mm. There is therefore a real interest in choosing thickness ratios that maximize contact pressures and minimize stress, in order to reduce electronic losses as much as possible and to avoid any mechanical rupture in the PEMFC.

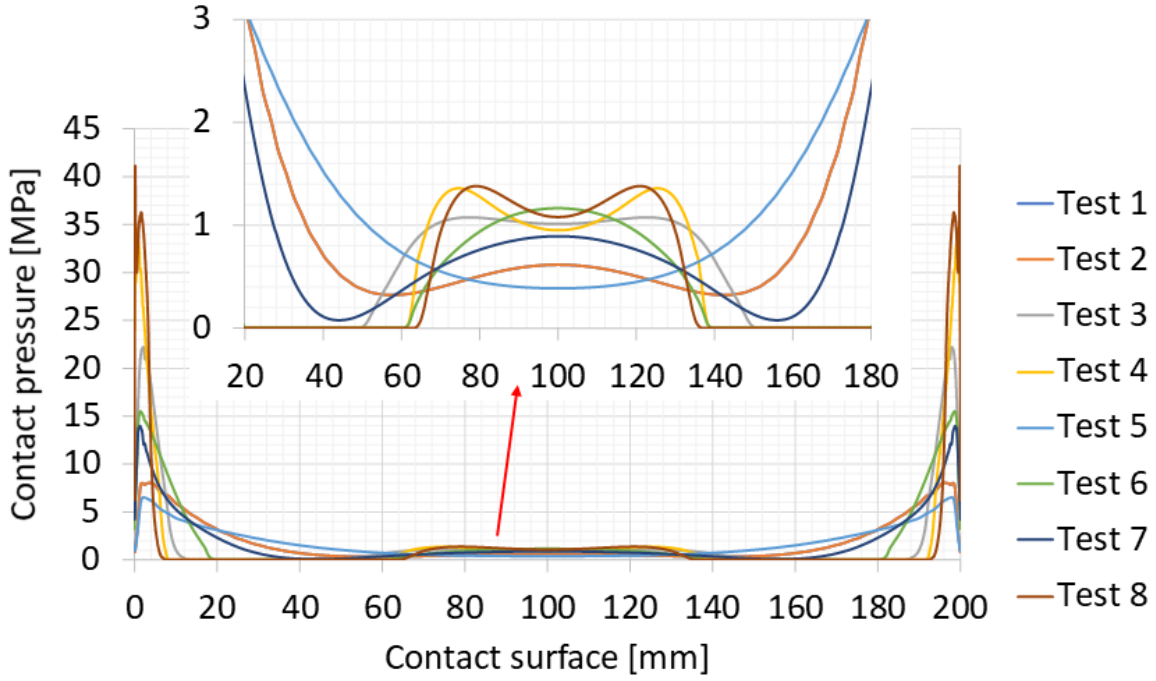

Fig. 4. 11: CPress at the GDL-MEA interface with hyperelastic GDL.

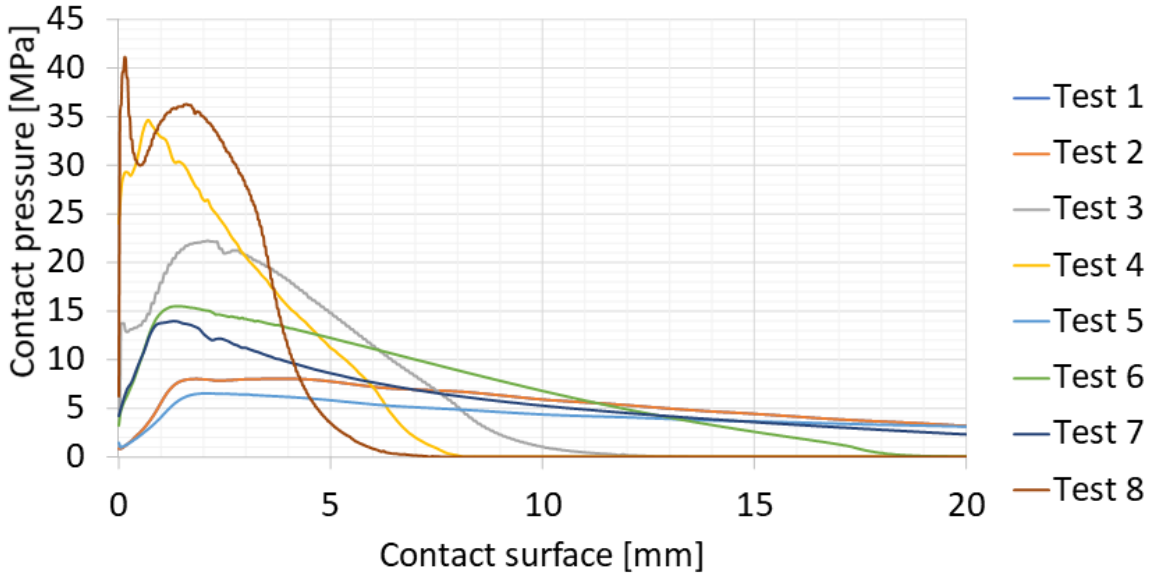

Fig. 4. 12: Zoom-in for CPress at the GDL-MEA interface with hyperelastic GDL.

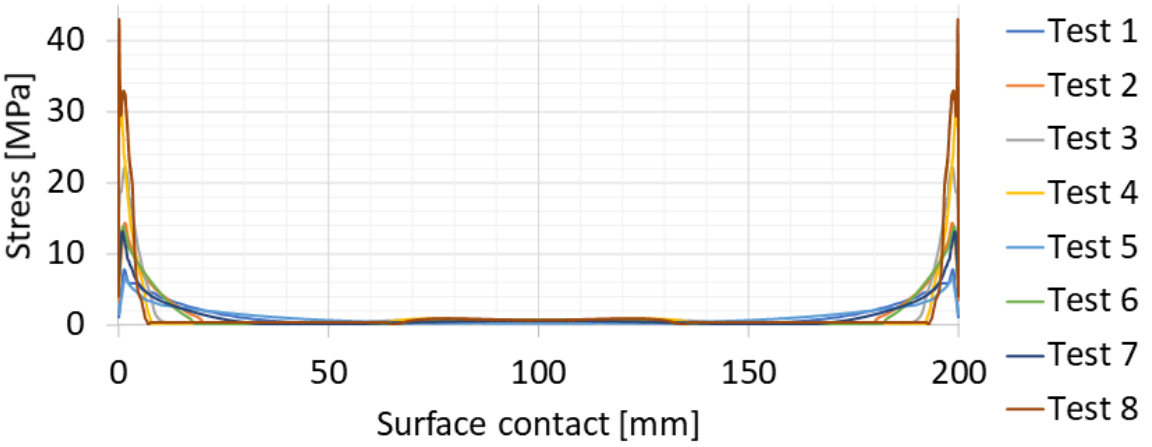

Fig. 4. 13: Von Mises yield criterion at the GDL-MEA interface with hyperelastic GDL.

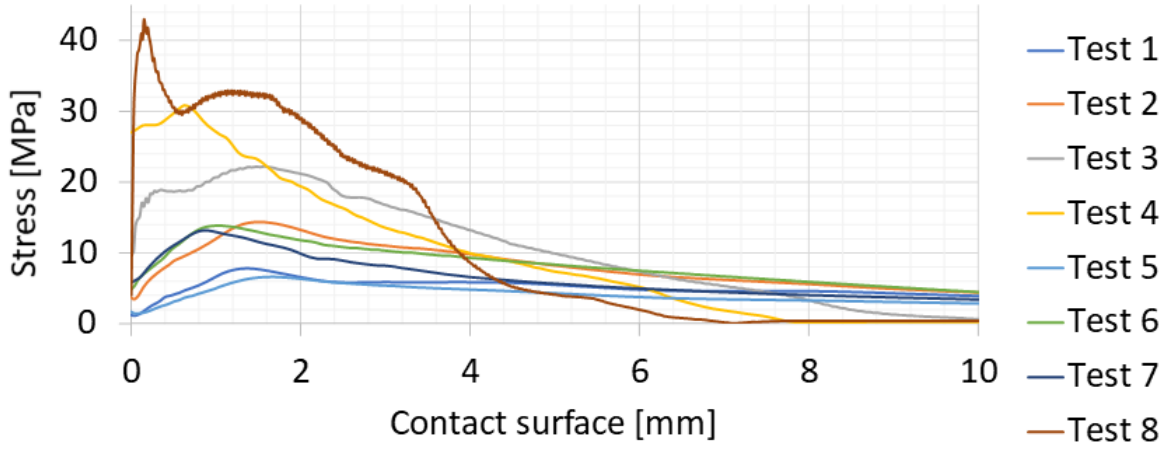

Fig. 4. 14: Zoom-in for von Mises yield criterion stress at the GDL-MEA interface with hyperelastic GDL.

Fig. 4.11, 4.12, 4.13, and 4.14 show that the GDL-MEA interface has the same behaviour as the BPP-GDL interface. The pressures are at their highest at the ends and drop sharply to 0 MPa. Therefore, we have a pressure concentration at the ends and then a bonding and a debonding in the middle of the structure. This creates a high variation in resistance throughout the structure. Just like the GDL-BPP interface, when observing the zoom of fig 4.11 along the internal low contact pressure area, tests 1, 2, 5, and 7 show a pressure higher than 0.07 MPa, meaning that contact is also insured along all this interface.

A closer examination at the ends shows that, for this interface, the behaviour of the stresses is identical to the pressures. When the pressure is at its highest, the stresses are at their highest. Even when it is minimal, so are the stresses. This observation is similar for each test.

4.3.4. Best set of parameters

According to the effect analysis table, the best EP thickness seems to be in the [7.5mm; 15mm] interval. We chose the thickness of 15 mm (D2) with the least negative influence on the contact stress and pressure as presented in Table 4.5. The best compromise for the MEA is the thickness of 0.05 mm (A1) in Table 4.4. The contribution of the thickness of the MEA to the performance of the FC is quite significant after the EP. As far as the GDL is concerned, it is certain that the best

choice is that of B2 and therefore the thickness 0.28 mm which will reduce the stress by maximizing the contact pressure. Finally, for the BPP, the best parameter according to Table 4.7 is C1 with a thickness equal to 3 mm.
Our most unfavourable case is with the linear behaviour because the lowest value of von Mises yield criterion increases and drastically reduces the greater value of CPress, compared to the tests with the hyperelastic constitutive law. That is why for the model of best sets of parameters, the constitutive law for GDL is hyperelastic.
An optimal simulation is performed with 182 189 nodes and 161 725 elements. The maximum values of von Mises yield criterion do not exceed the elastic limit that each component can withstand as given in Tables 4.9 and 4.10.
The von Mises yield criterion is significant in contact with the GDL-MEA and EP-BPP interfaces, but it allows to have a high contact pressure.

Optimal results		
Contact type	Max. von Mises yield criterion [MPa]	Max. contact pressure [MPa]
Contact GDL-MEA	15	16
Contact BPP-GDL	6	16
Contact EP-BPP	29	13

Table 4. 9: Max von Mises yield criterion and CPress.

Component	Material	Elastic limits (MPa)
End Plate (D)	Aluminium alloy	220 [33]
BPP (C)	Graphite	50 [34]
GDL (B)	Carbon paper (TGP-H-90)	40 [35]
MEA (A)	Nafion	23-32 [36]

Table 4. 10: Elastic limits of different constitutive materials.

4.3.4.1. Effect of the pressure distribution on the electrical contact resistance

The electrical contact resistance between GDL and BPP is calculated using data of Toray H-90 presented earlier (Chapter 3) [37]. The TLM method is used to measure the contact resistance under 5 compression cycles over several mechanical pressure stages ranging from 0 to 8 MPa. The most interesting values to compute the contact resistance are obtained for the loading phase applied during the first cycle. We focused on the data linked to the GDL ref. Toray H90 with a 0.28 mm thickness. From fig. 4.5, it is possible to obtain the distribution of contact resistances shown in fig. 4.15 by applying the approach described in [25, 38]. The electrical contact resistance of the BPP-GDL interface is a non-linear function with respect to the thickness of the BPP. The model can also be used to compute the electrical resistance of the BPP-GDL interface: 3.49 mΩ for Test 2, 3.09 mΩ for Test 5 and 19.9 mΩ for Test 8, here for a rib surface.

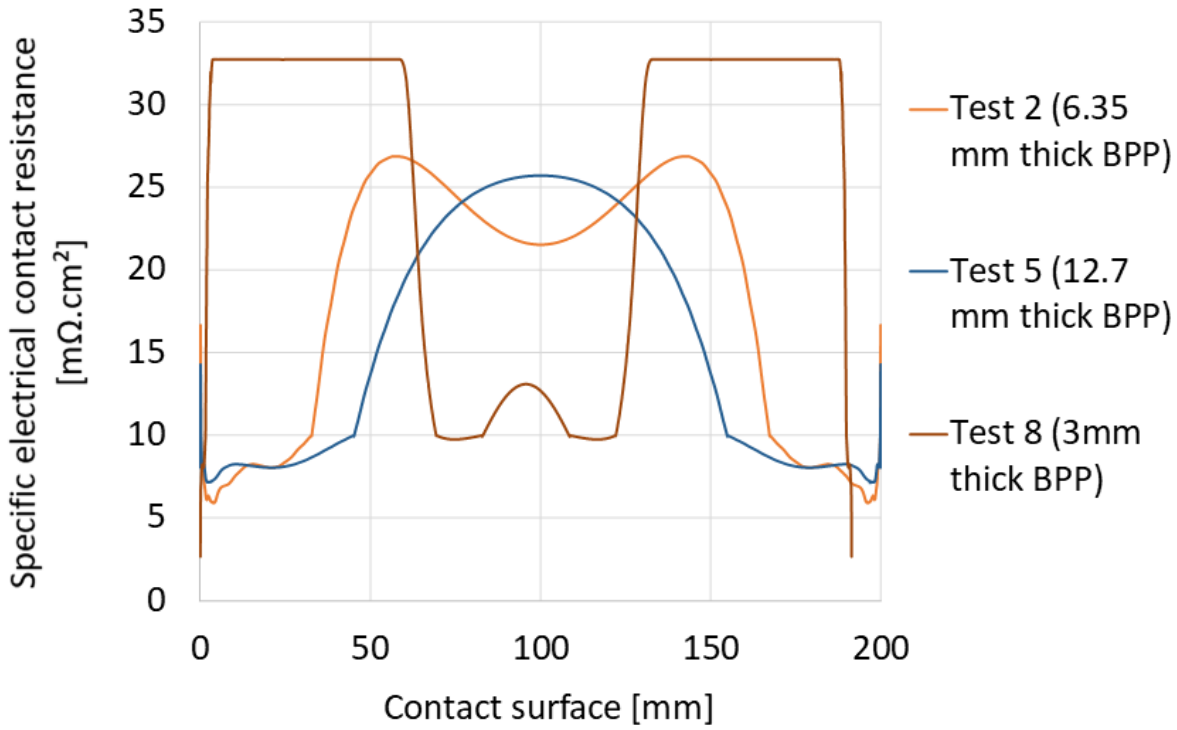

Fig. 4. 15: Distribution of the electrical contact resistance at the GLD-BPP interface for the GDL ref. Toray H90.

The comparison between Test 2, Test 5, and Test 8 shows that increasing the size ratio between the MEA and the BPP spreads the resistance at the edges of the GDL, and also increases the contact resistance on the surface of the GDL. Increasing the size ratio between EP and BPP increases the contact pressure thus decreases the contact resistance. Adopting thin components increases the contact resistance. Therefore, the most favourable case seems to have thick and equivalent thicknesses between the different components.

4.3.5. Comparison with literature

To verify the validity of our model, we compare the pressure distributions on GDL and MEA from experiments and numerical models.

Experimentally, there are two major in-situ techniques used to measure contact pressure distributions [2]. The first technique uses pressure sensitive films composed of two polyester based sheets which one of them is coated with a layer of micro-encapsulated color forming material and the other one is coated with a layer of color developing material [39]. Pressure is approximated depending on the density of red spots. The second tool for evaluating the pressure distribution is the use of piezoelectric sensors, as in the work of Dey et al. [40].

Most of the works are not usable since the clamping system is with nuts and bolts. The distributed pressure is therefore not uniform. As pointed out in the work of Wen et al. [39], positions of nuts and their number have considerable influence on the pressing process. This is partly due to the buckling of the endplate.

The experimental work of Alizadeh [19] makes possible to validate the stress distribution for the MEA and the pressure distribution on the GDL. The loading conditions are identical to our model. They used pneumatic clamping system which can compress the cell at 7 bars. The contact pressure distribution over the active area of the PEMFC is obtained using super low-pressure Fujifilm used with a range of [0.5; 2.5] MPa inserted between two GDLs as depicted in fig. 4.16. Their work confirms the behavior obtained on the MEA and the GDL for both the numerical model and the experimental test. However, the values of pressures and

stresses are not similar. This may possibly be explained by the hyperelastic constitutive law used to model the GDL behavior.

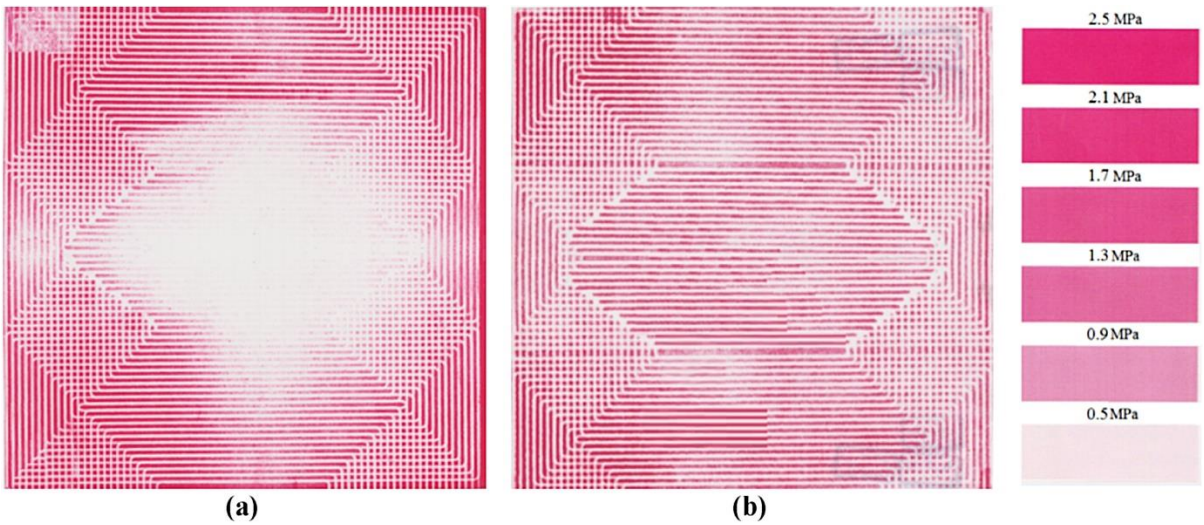

Fig. 4. 16: Contact pressure distributions over the MEA of PEM Single cell: (a) Stainless steel end plate with 30 mm thickness, (b) Stainless steel end plate with 50 mm thickness [19].

In their work, Bates et al [41] have obtained the same behavior of the von Mises constraints, although the clamping system does not match our model. In their model, the clamping system consists of nuts and bolts. They have performed two simulations: a single-cell and a 16-cell stack were run under various clamping pressures. In both models, a linear behavior law is applied to the GDL and to all other elements. Only the single-cell model is used and compared to our test with the closest thicknesses. The same stress distribution is seen on the EP/BPP and GDL/MEA interfaces as shown in Fig. 4.17, but the presence of the BPP channels considerably changes the mechanical behaviour of the BPP/GDL interface.

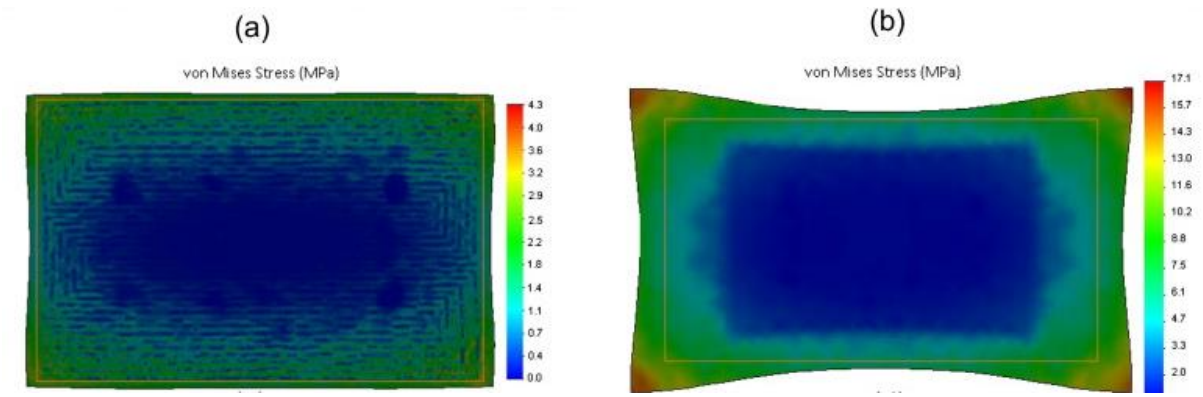

Fig. 4. 17: Von Mises stress distribution (single cell, active area = 100 cm²): a) deformed GDL stress plot, (b) deformed MEA stress plot [41].

With the work of Zhang et al. [38], a numerical comparison of the pressure distribution obtained at the BPP/GDL interface is possible. They have experimentally obtained a contact resistance–pressure constitutive relation for the contact between the BPP and the GDL, and estimated the contact pressure in a real fuel cell stack based on either geometrical relations or FEM analysis. The load corresponding to our model corresponds to a uniform load distribution. The numerical results of the pressure distribution on the BPP/GDL interface are in line with the results obtained in this paper although there are channel print marks.

4.4. Conclusion

This chapter presents a study of the mechanical behaviour of a PEMFC with a focus on the contact pressure distribution at different layer interfaces in the stack and electrical contact resistance between BPP and GDL. A numerical development was initiated in order to quantify the influences of thickness of cell components and constitutive law of the GDL on the PEMFC performances expressed in terms of electrical resistances at the early-stage design of a PEMFC. To reach this aim, a 2D finite element model including contact friction was developed and combined with a DoE. Concerning the GDL, a hyperelastic experimental constitutive law and a linear constitutive law were implemented. An optimal set of geometric and mechanical parameters were determined. During the computation process, it appeared that the ratios between the thicknesses of the cell components influence the computation stability. After reviewing the simulation results, we noted that the electrical and mechanical responses are more impacted by the layer thicknesses than by the GDL constitutive law.

The mechanical model presented in this chapter offers interesting rules to design FCs with adequate thickness layer combinations, giving the optimal contact pressure that reduces the electrical contact resistance and the optimal von-Mises stress. This model can be used as a preliminary decision tool. The FEM 2D model coupled with the DoE can be further developed by integrating variation of material properties with temperature and humidity that can add additional MEA stress. The variation of Membrane/GDL/BPP type also needs to be considered, with additional GDL structures and the study of the influence of the CL-MPL layers. In this model, the fuel cell compression was modelled by an imposed pressure, for simplification and because most of experimental investigations on GDL properties are done under imposed pressure loading conditions, even if it does not completely represent real clamping conditions. Further numerical investigations can be done

with more realistic loading conditions. The additional parameters that influence pressure distribution such as the clamping procedure and the clamping pressure level can be considered. The DoE method can also help extracting design rules using regression equations according to degrees of influences of parameters without the need of simulation.

Once the choice of elements done, a 3D model can be used to validate the electrical performance of the FC, by integrating the different resistances of the layers, such as the bulk resistance of the GDL (in and through-plane resistivities which are related to stress inside the layer), and the specific electrical contact resistance between the layers which is related to the contact pressure. The specific electrical contact resistance is still the most important to consider. It has higher values, and it involves a smaller surface in comparison with the through-plane resistivity because of the BPP channels, which implies a higher total resistance. Total ohmic losses can be predicted through the simulation according to clamping pressure conditions.

4.5. References

[1] Hou Y., Zhang X., Lu X., Hao D., Ma L., Li P., AC impedance characteristics of a vehicle PEM fuel cell stack under strengthened road vibrating, Int. J. Hydrog. Energy 2014; 39:32:18362-18368.

[2] Khetabi E.M., Bouziane K., Zamel N., François X., Meyer Y., Candusso D., Effects of mechanical compression on the performance of polymer electrolyte fuel cells and analysis through in-situ characterisation techniques - A review, J. Power Sources 2019;424:8–26.

[3] Saadat, N., Dhakal, H. N., Tjong, J., Jaffer, S., Yang, W., Sain, M. Recent advances and future perspectives of carbon materials for fuel cell. Renewable and Sustainable Energy Reviews 2021; 110535.

[4] Diampovesa, S., Hubert, A., Yvars, P. A., Meyer, Y., Zimmer, L. (2019). Optimal design for electromagnetic devices: A synthesis approach using intervals and constraint-based methods. International Journal of Applied Electromagnetics and Mechanics 2019; 60(S1), S35-S48.

[5] Alizadeh E., Ghadimi M., Berzagui M., Momenifar M., Saadat S., Development of contact pressure distribution of PEM fuel cell's MEA using novel clamping mechanism, Energy 2017;131:92-97.

[6] Wang X., Song Y., Zhang B., Experimental study on clamping pressure distribution in PEM fuel cells, J. Power Sources 2008;179:305-309.

[7] Hou Y., Zhou B., Zhou W., Shen C., He Y., An investigation of characteristic parameter variations of the polarization curve of a proton exchange membrane fuel cell stack under strengthened road vibrating conditions, Int. J. Hydro. Energy 2012;37:11887-11893.

[8] Zhou Y., Jiao K., Du Q., Yin Y., Li X., Gas diffusion layer deformation and its effect on the transport characteristics and performance of proton exchange membrane fuel cell., Int. J. Hydrog. Energy 2013;39:12891-12903.

[9] Kleemann J, Finsterwalder F, Tillmetz W. Characterisation of mechanical behaviour and coupled electrical properties of polymer electrolyte membrane fuel cell gas diffusion layers. Journal of Power Sources 2009;190(1):92–102.

[10] Roohparvarzadeh S. Experimental Characterization of the Compressive Behaviour of Gas Diffusion Layers in PEM Fuel Cells.

[11] Hamour M, Garnier JP, Grandidier JC, Ouibrahim A, Martemianov S. Thermal-Conductivity Characterization of Gas Diffusion Layer in Proton Exchange Membrane Fuel Cells and Electrolyzers Under Mechanical Loading. Int J Thermophys 2011;32(5):1025–37.

[12] Todd D, Bennett S, Mérida W. Anisotropic electrical resistance of proton exchange membrane fuel cell transport layers as a function of cyclic strain. International Journal of Hydrogen Energy 2016;41(14):6029–35.

[13] Sadeghifar H. In-plane and through-plane electrical conductivities and contact resistances of a Mercedes-Benz catalyst-coated membrane, gas diffusion and micro-porous layers and a Ballard graphite bipolar plate: Impact of humidity, compressive load and polytetrafluoroethylene. Energy Conversion and Management 2017;154:191–202.

[14] García-Salaberri, P. A., Vera, M., & Zaera, R. (2011). Nonlinear orthotropic model of the inhomogeneous assembly compression of PEM fuel cell gas diffusion layers. International Journal of Hydrogen Energy, 36(18), 11856-11870.

[15] Zhang, Z., He, P., Dai, Y. J., Jin, P. H., & Tao, W. Q. (2020). Study of the mechanical behavior of paper-type GDL in PEMFC based on microstructure morphology. International Journal of Hydrogen Energy, 45(53), 29379-29394.

[16] Netwall CJ, Gould BD, Rodgers JA, Nasello NJ, Swider-Lyons KE. Decreasing contact resistance in proton-exchange membrane fuel cells with metal bipolar plates. J. Power Sources 2013;227:137–44.

[17] Ye D, Gauthier E, Benziger JB, Pan M. Bulk and contact resistances of gas diffusion layers in proton exchange membrane fuel cells. J. Power Sources 2014;256:449–56.

[18] Zhou P., Wu C.W., Ma G.J. Contact resistance prediction and structure optimization of bipolar plates. J. Power Sources 2006;159:2:1115–1122.

[19] Alizadeh A., Barzegari M., Momenifar M., Ghadimi M., Saadat S., Investigation of contact pressure distribution over the active area of PEM fuel cell stack. Int. J. Hydrog. Energy 2016;41:3062-3071.

[20] Atyabi, S. A., Afshari, E., Wongwises, S., Yan, W. M., Hadjadj, A., Shadloo, M. S. Effects of assembly pressure on PEM fuel cell performance by taking into accounts electrical and thermal contact resistances. Energy 2019;179,490-501.

[21] Lai, X., Peng, L., Ni, J. A mechanical–electrical finite element method model for predicting contact resistance between bipolar plate and gas diffusion layer in PEM fuel cells. Journal of Power Sources 2008;182(1),153-159.

[22] Charbonné C., Dhuitte M.-L., Bouziane K., Chamoret D., Candusso D., Meyer Y. Design of experiments on the effects of linear and hyperelastic constitutive models and geometric parameters on polymer electrolyte fuel cell mechanical and electrical behaviour. Int J Hydrog Energy; (Available online 13 March 2021).

[23] (ABAQUS 2018) ABAQUS/Standard User's Manual, Version 6.13. Providence, RI: Dassault Systèmes Simulia Corp, 2018. [accessed 27 April 2020]

[24] Carral C, Mele P. A numerical analysis of PEMFC stack assembly through a 3D finite element model. Int J Hydrog Energy 2014;39:9:4516-4530.

[25] Mishra, V., Yang, F., Pitchumani, R., Measurement and prediction of electrical contact resistance between gas diffusion layers and bipolar plate for applications to pem fuel cells, J. Fuel Cell Sci. Technol. 2004;1:1:2-9.

[26] Gigos P.A., Faydi Y., Meyer Y., Mechanical characterization and analytical modeling of gas diffusion layers under cyclic compression, Int. J. Hydrog. Energy 2015;40:17:5958-5965.

[27] Choi, P., Jalani, N. H., Thampan, T. M., Datta, R. Consideration of thermodynamic, transport, and mechanical properties in the design of polymer electrolyte membranes for higher temperature fuel cell operation. J. Polym. Sci. B Polym. Phys. 2006;44:16:2183-2200.

[28] D. Bograchev, M. Gueguen, J.-C. Grandidier, S. Martemianov, Stress and plastic deformation of mea in running fuel cell, Int J Hydrog Energy 2008;33:20:5703-5717.

[29] A. Kusoglu, A. M. Karlsson, M. H. Santare, S. Cleghorn, W. B. Johnson, Mechanical behavior of fuel cell membranes under humidity cycles and effect of swelling anisotropy on the fatigue stresses, J. Power Sources. 2007;170:2:345-358.

[30] M. A. S. Al-Baghdadi, H. A. S. Al-Janabi, Effect of operating parameters on the hygro-thermal stresses in proton exchange membranes of fuel cells, Int J Hydrog Energy 2007;32:17:4510-4522.

[31] A. Kusoglu, A. M. Karlsson, M. H. Santare, S. Cleghorn, W. B. Johnson, Mechanical response of fuel cell membranes subjected to a hygro-thermal cycle, J. Power Sources. 2006;161:2:987-996.

[32] Joneja A., Design Principles, The Hong Kong University of Science and Technology, 2001.

[33] http://www.almet-metal.com/informations-techniques/donnees-aluminium [accessed 27 April 2020]

[34] https://www.sceram.com/graphite/ [accessed 27 April 2020]

[35] https://www.fuelcellstore.com/toray-carbon-paper-060 [accessed 27 April 2020]

[36] https://www.fuelcellstore.com/spec-sheets/chemours-nafion-211-212-spec-sheet.pdf [accessed 27 April 2020]

[37] Bouziane, K., Lachat, R., Zamel, N., Meyer, Y., & Candusso, D. Impact of cyclic mechanical compression on the electrical contact resistance between the gas diffusion layer and the bipolar plate of a polymer electrolyte membrane fuel cell. Renewable Energy 2020;153:349-361.

[38] Zhang L., Liu Y., Song H., Wang S., Zhou Y., Hu S. J., Estimation of contact resistance in proton exchange membrane fuel cells. J. Power Sources 2006;1162:2:1165-1171.

[39] Wen C.-Y., Lin Y.-S., Lu C.-H. Experimental study of clamping effects on the performances of a single proton exchange membrane fuel cell and a 10-cell stack. J. Power Sources 2009;192:2:475-485.

[40] Dey, T., Deshpande, J., Singdeo, D., Ghosh, P. C. Study of PEM fuel cell end plate design by structural analysis based on contact pressure. Journal of Energy 2019; 11 pages. Article ID 3821082.

[41] Bates A., Mukherjee S., Hwang S., Lee S. C., Kwon O., Choi G. H., Park S. Simulation and experimental analysis of the clamping pressure distribution in a PEM fuel cell. Int. J. Hydrogen Energy 2013;38:15:6481-6493.

Conclusion and perspectives

Enhancing PEMFC performance by the decrease of its ohmic losses requires a better understanding of the relationship between the electrical properties of its components and their variation with regards to the operating conditions, such as mechanical compression resulting from several internal and external sources of excitation. This research work focuses mainly on the GDL, one of the FC components most impacted by mechanical compression. The porous fibrous structure of carbon paper GDLs made it sensitive to the varying mechanical compression inside the FC. Their physical properties are also modified by mechanical compression leading to a change of the cell performance. A review of literature on the relationship between mechanical compression and physical properties of GDL shows the non-linearity of compression modules and a sensitivity to the cycles of compression. Both the electrical and thermal resistances were found to decrease with compression as well as permeability and porosity. A trade-off must be found between decreasing ohmic resistances and increasing mass transport resistance. Despite the large numbers of studies relating mechanical pressure to electrical resistivity, very few studies used real cell operating conditions such as variable compression loads, temperature and humidity.

In the present study, a number of carbon paper GDLs with different structural and composition parameters has been investigated in order to assess the influence of different FC operation parameters.

Electrical-mechanical characterization has been conducted under cyclic mechanical compression with variable operating conditions in order to have an adequate data base of electrical-structural properties of carbon paper GDLs. Both bulk (in and through-plane) resistance of the GDL and its interface contact resistance with the BPP were characterized. This data base can be used to feed FC numerical models and help fuel cell designers for the choice of their GDLs according to their application requirements. As an example of such a development, a coupled DoE - 2D mechanical FEM model of a half-cell has been conducted. The idea is to help choose the best set of FC components according to their thickness in order to optimize interface parameters, i.e. to increase contact pressure that is

beneficial to reduce contact resistances and decrease equivalent Von Mises stress to avoid material damage.

All GDLs electrical contact and bulk resistances were shown to decrease non-linearly with compression, with a substantial decrease at low compression levels. More than 75% of the decrease of contact resistance is obtained when applying 2,5 MPa. Moreover, when GDLs were initially kept for some minutes under a small compression before starting the cyclic compression process, more than 75% of decrease was obtained at 0,5 MPa. A decrease of more than 75% is obtained for through-plane resistance for pressures over 2 MPa and for in-plane resistance for pressure over 3 MPa. This means that a contact pressure of 3 MPa on the GDLs is completely sufficient to insure reduced electrical resistance. If we estimate that GDL surface is around 50% of the active area because of rib and channels of the BPP, a recommended pressure on the active area would be around (1,5 MPa). Moreover, optimum pressure levels could be reduced by initial GDL conditioning under small compression levels. This would be sufficient to ensure adequate resistances levels, especially that compression may decrease porosity which increases mass transport losses and too much compression could damage the GDLs.

These different resistances are sensitive to the cycles of compression with various degrees of sensitivity. GDLs can be conditioned before being used in a PEMFC with one or two cycles of compression at higher pressure values or by a sufficiently long initial compression. A first very small compression level on GDLs for some minutes shows a more stable electrical behavior and can be used in conditioning GDLs before using them in PEMFCs.

Designers of PEMFC need to take into account the ratio of different components thickness to insure optimal interfacial compression pressures. The numerical model has shown that GDL-BPP contact pressure interface was not uniformly distributed even with a uniform applied pressure. Indeed, compression pressure can locally reach very high levels, while some places experience very low contact pressure. This indicates a possible explanation of hot spots as ohmic losses can be unevenly distributed.

Felt structure was the least sensitive to the cycles of compression with adequate resistance levels. Thus, this type of GDLs can be recommended for transport applications.

The lowest resistances were found for graphitized GDLs that are suitable for stationary application to have the smallest resistances possible. They also have acceptable levels of sensitivity to the cycles of compression.

Contact resistance is influenced by velocity of compression and temperature. Humidity influences both in and through-plane resistance. These parameters' influence is particularly important at low compression values. This should be taken into consideration, as it had been shown in the numerical model that some points of the interfaces experience very low compression pressures.

Future works:

In this thesis, several parameters related to electrical properties of GDLs were examined. Further research can be conducted to more accurately predict the PEMFC ohmic losses and overall, its electrical performance as a function of its operating conditions.

PEMFC are getting more and more used in transportation applications and specific conditions related to air, marine, or road conditions need to be conducted to optimize systems and reduce the costs.

It seems that velocity of compression affects electrical-mechanical behavior of GDLs and further research may be done in this area to adjust initial compression methods and monitor service compression methods along the FC life.

Water saturation affects in and through-plane resistance. Preliminary studies on in-plane resistance show a variation with water saturation. Further investigation should be done to properly evaluate the relationship between in-plane resistance humidity rate and different GDLs structure.

To predict the exact ohmic losses as a function of humidity, temperature, and compression, the data of different resistances with their anisotropy should be used in FEM models, by integrating ionic membrane resistance which is a function of temperature and water content and correlated with the experimental data.

The part of contact resistance of GDLs is not negligeable as the contact interfaces have a smaller surface, especially for thin and humidified membranes. In this study, porosity of GDLs was not investigated. This parameter needs to be taken into consideration to evaluate mass transport losses. Additionally, in this work, a number of carbon paper GDLs with different structures and compositions have been investigated under different operating conditions. Some properties were examined such as PTFE rate and thickness. In order to establish performant GDL design rules, its is important to correlate the results of this study with more structural and composition parameters of the GDLs, such as density / porosity, fiber diameters, MPL-substrate interface microstructure, and the variation of this microstructure through the cyclic compression and other operating conditions such as temperature and humidity. Experimental results of this study can also be used to validate analytical models for predicting effective electrical properties.
Finally, data should be correlated with different stack configurations, this means taking into account different local compression, temperature and humidity levels.

Résumé étendu :

Etude des liens entre les performances de composants de pile à combustible PEM et leurs comportements à l'intérieur de la pile observés en fonctionnement. Développement de caractérisations électriques et mécaniques in-situ et ex-situ.

Plan :

1. Introduction

La réduction des émissions de gaz à effet de serre implique le déploiement de sources d'énergies alternatives telles que les piles à hydrogène. L'hydrogène est actuellement considéré comme un vecteur d'énergie potentiel pour le stockage d'énergies renouvelables et pour l'alimentation des véhicules électriques. Il pourrait également être considéré comme une source d'énergie primaire suite à la découverte récente d'hydrogène naturel issu de sources géologiques. L'hydrogène est, en tout cas, appelé à prendre une plus grande place dans le mix énergétique de demain. Les piles à combustible à membrane polymère basse température (PEMFC) sont les technologies de pile les plus matures et elles peuvent être utilisées dans différentes applications (transport, espace, stationnaire, portable).

La puissance produite et les surtensions des PEMFCs dépendent des conditions de fonctionnement et des propriétés physiques des composants des cellules. L'amélioration du rendement de la pile passe par une diminution des pertes liées notamment aux pertes ohmiques. Cela implique de développer une meilleure compréhension de la relation entre les propriétés physiques des matériaux, la variation de ces propriétés avec les conditions de fonctionnement et l'influence de cette variation sur les pertes ohmiques. Les pertes ohmiques sont en bonne partie dues à la résistance protonique de la membrane mais également liées à des résistances électroniques volumiques dans les composants de cellule et à des résistances de contact entre ces éléments. Ces résistances sont fonction de la nature du matériau, de sa structure et des conditions de fonctionnement telles que l'humidité, la température et également la compression mécanique exercée sur l'assemblage. Les travaux menés dans cette thèse contribuent à la compréhension de l'origine des pertes ohmiques électroniques, en particulier celles liées à la couche de diffusion de gaz (GDL).

2. PEMFCs, GDL et effet de la compression mécanique.

Une PEMFC est constituée d'une membrane électrolyte échangeuse de protons constituée d'un polymère et couverte de deux couches catalytiques (CL), placées entre deux couches de diffusions de gaz (GDLs), elles-mêmes tenues et compressées par deux plaques bipolaires (BPPs). Cet empilement est présenté dans la Figure1 :

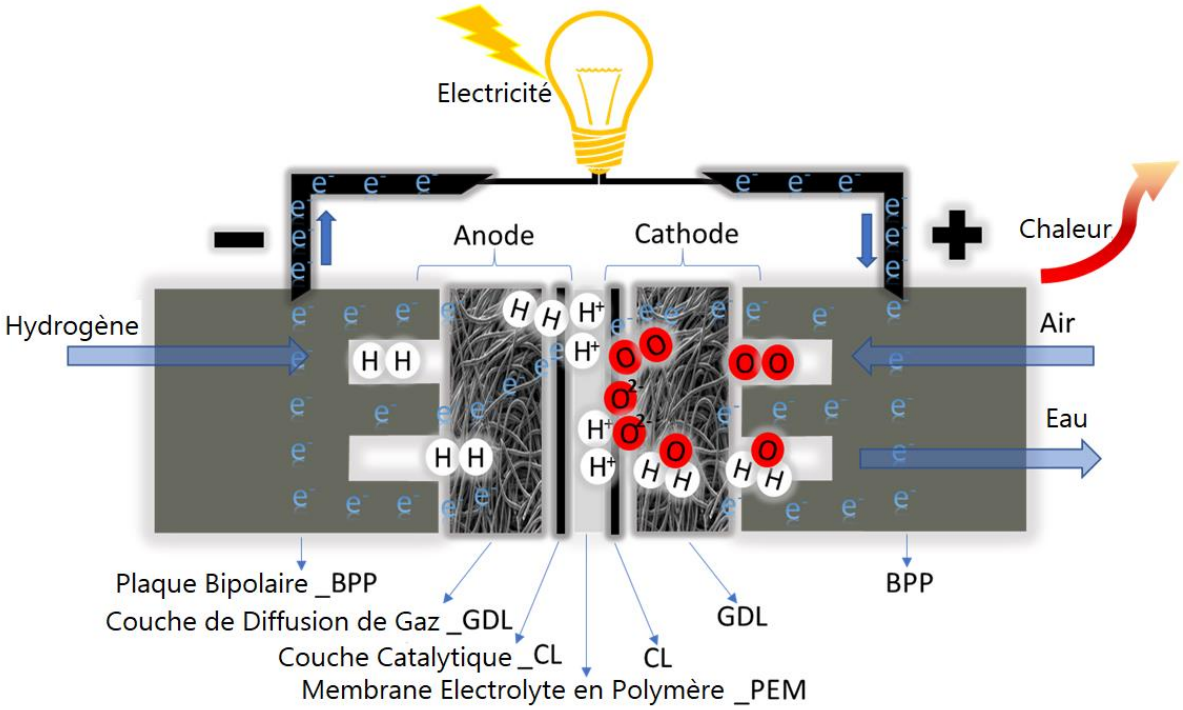

Figure 1: Schéma d'une Pile à combustible PEMFC.

Le générateur électrochimique convertit l'hydrogène et l'oxygène en électricité, en chaleur et en eau, via une réaction globale d'oxydoréduction (équation 1).

$$H_2 + \frac{1}{2}O_2 \rightarrow H_2O \qquad (1)$$

La GDL joue plusieurs rôles dans une PEMFC. Elle diffuse les gaz réactifs de la plaque bipolaire vers les électrodes et évacue les gaz inutilisés. Elle conduit les électrons et la chaleur. Elle permet d'évacuer l'eau produite et joue un rôle important dans la gestion de l'eau à l'intérieur de la pile. De plus, elle doit maintenir mécaniquement le cœur de pile pour garantir son bon fonctionnement. Les structures qui permettent communément toutes ces fonctions sont des structures composites poreuses en fibres de carbone qui peuvent se présenter sous forme de papier ou de « tissu » (incluant éventuellement un traitement hydrophobe et une couche micro-poreuse (MPL)). Cette structure poreuse est très sensible à la sollicitation mécanique et ses propriétés physiques, telles que ses résistances électrique et thermique et sa porosité, sont également affectées par cette sollicitation mécanique. Celle-ci a diverses origines :

- externes comme le serrage de la pile, les vibrations ou les chocs,

- internes, liées au fonctionnement de la pile tels que le gonflement-rétrécissement de la membrane, l'expansion thermique et les variations de pression des gaz.

Ces sollicitations mécaniques génèrent un état de contrainte variable. De plus, le comportement mécanique de la GDL est non-linéaire et laisse apparaitre une hystérésis de déformation avec les cycles de charge-décharge en compression. Les propriétés physiques de la GDL, à l'instar de sa résistance électrique, sont affectées par le comportement de la structure vis-à-vis des cycles de compression. Il est par conséquent nécessaire d'étudier cette influence de la charge mécanique en utilisant une compression cyclique afin de s'approcher au mieux des conditions de fonctionnement réelles de la pile et, in fine, mieux appréhender le rôle de la GDL dans les pertes ohmiques globales. Les niveaux optimaux de compression mécanique font notamment l'objet d'un compromis entre de faibles pertes ohmiques et des performances en diffusion élevées.
La Figure 2 présente de manière synthétique l'effet de la compression mécanique sur les propriétés physiques de la GDL.

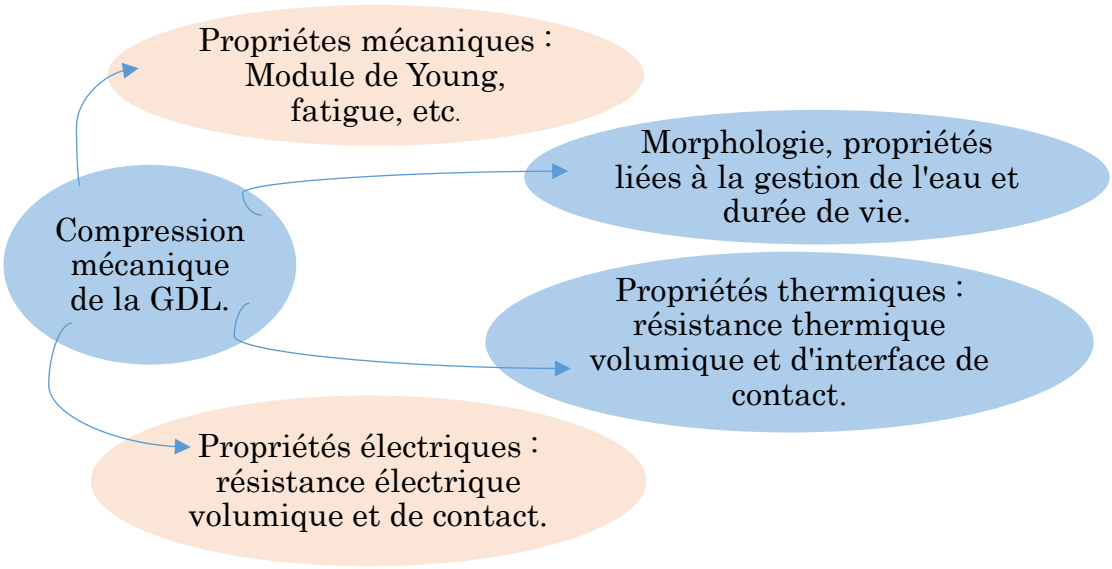

Figure 2 : Effet de la compression mécanique sur les propriétés physiques de la GDL.

3. Propriétés électriques des GDLs

Dans cette thèse, des investigations expérimentales et des analyses des propriétés électriques ont été menées sur plusieurs types de GDLs à base de papier carbone disponibles dans le commerce. Des techniques de caractérisation ex-situ ont été utilisées pour mesurer, d'une part, la résistance dans le plan suivant deux directions perpendiculaires et, d'autre part, la résistance à travers le plan sous une contrainte mécanique cyclique. Les effets des variations de température et d'humidité ont également été analysés. La résistance de contact entre la GDL et la plaque bipolaire a été mesurée en utilisant la méthode de transmission de ligne TLM.

Une diminution non-linéaire de toutes les résistances a été observée avec l'augmentation de la compression mécanique. Cette observation implique l'existence d'un niveau optimal de compression à utiliser pour la pile, compte tenu des variations de la porosité de la GDL et de ses propriétés de diffusion. Ces résistances sont plus ou moins sensibles aux cycles de compression, selon la structure des GDLs. La structure en feutre est la moins sensible aux cycles. L'hystérésis de la résistance électrique décroît avec le niveau de compression et le nombre de cycles. Malgré l'anisotropie de la GDL observée pour la résistance dans le plan, quelques propriétés restent invariantes avec la direction de mesure, comme le taux de décroissance de la résistance avec la compression mécanique ou l'hystérésis. Enfin, l'humidité a tendance à faire décroitre la résistance à travers le plan de la GDL.
Le Tableau 1 résume les principaux effets des conditions opérationnelles sur les propriétés électriques de la GDL.

Résistances	**Compression**	**Caractéristiques de sortie**	**Vitesse de compression**	**Humidité / saturation en eau**	**Température**	**PTFE**	**MPL**	**Structure (valeurs les plus faibles / les plus stables suivant les cycles)**
Rip (dans le plan)	▼	Rip vs comportement avec la compession	/	▲	/	▼	▲	Papier carbone de fibre graphitisées
		Sensibilité aux cycles de compression	/	▼	/	▲	▼	Structure en feutre et papier carbone de fibre graphitisées
Rtp (à travers plan)	▼	Rtp vs comportement avec la compession	/	▲ (en majorité)	+	▲	▲	Structure en fibre droite et fine
		Sensibilité aux cycles de compression	/	?	?	▲	▼	Structure en feutre couverte de MPL et papier carbone de fibres graphitisées
Rc (de contact)	▼	Rc vs comportement avec la compession	+	/	▲	▲	MPL ▼ PTL ▲	Papier carbone de fibres graphitisées
		Sensibilité aux cycles de compression	/	/	▲	▲	▲	Structure en feutre

Tableau 1 : Influence des differents paramètres sur les résistances électriques (▼ : diminue, ▲ : augmente, + : influence, / : hors du cadre de cette thèse, ? : non-analysé).

4. Modèle numérique d'une PEMFC

Afin d'optimiser le choix des différents composants d'une PEMFC, un modèle numérique mécanique élément-finis 2D combiné à un plan d'expérience a été développé. Deux critères d'optimisation ont été considérés : la pression de contact des interfaces qui doit être maximisée (afin de réduire les résistances de contact électriques et donc les pertes ohmiques) et la contrainte équivalente de Von-Mises qui doit être minimisée afin de garantir que les composants ne s'endommagent pas. Les paramètres à optimiser sont l'épaisseur de chaque composant (Plaque terminale, BPP, GDL, MEA). Trois niveaux d'épaisseurs choisis pour chaque composant (correspondant à des valeurs de référence disponibles dans le commerce). Par ailleurs, le comportement mécanique non-linéaire de la GDL a été pris en compte via l'implantation d'une loi contrainte/déformation mesurée. Une comparaison a également été menée par rapport à un modèle intégrant une loi de comportement mécanique linéaire via un module de Young constant. La Figure 3 présente le modèle de la pile utilisé.

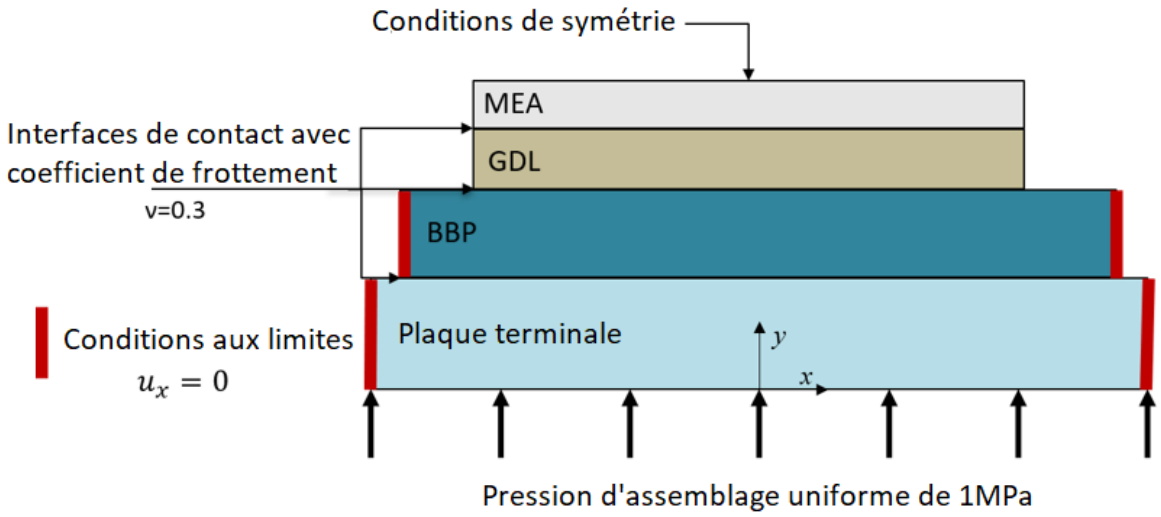

Figure 3 : Modèle d'une cellule PEMFC.

Le modèle montre une courbe de distribution de pression de contact non-uniforme aux interfaces, quel que soit le choix du comportement mécanique de la GDL (linéaire-ou pas). Il montre également que certaines combinaisons d'épaisseurs ne semblent pas possibles. Par conséquent, certaines règles de conception peuvent être déduites des résultats de simulation obtenus. Par exemple, l'épaisseur de la plaque terminale doit être supérieure à celle de la BPP. Ce modèle permet également de prédire la résistance de contact électrique d'une interface, grâce à la loi reliant résistance de contact et pression de contact.

5. Conclusion

L'amélioration des performances d'une PEMFC à travers la réduction de ses pertes ohmiques implique une meilleure compréhension de la relation entre les propriétés électriques des composants et leurs variations avec les conditions opératoires telles que la compression mécanique, la température et l'humidité. Cette thèse s'est focalisée principalement sur les GDLs et leurs propriétés électriques-mécaniques. Un certain nombre de GDLs de type papier carbone (fibres droites et feutres) ont été caractérisées sous compression mécanique cyclique et sous différents paramètres environnementaux.

Une pression optimale d'assemblage de stack de 1,5 MPa permet d'assurer des niveaux de résistances assez faibles pour les GDLs analysées. Les GDLs peuvent être conditionnées avec une faible compression initiale pendant quelques minutes afin d'assurer une diminution et une stabilisation des paramètres électriques par la suite.

Les structures feutres semblent les plus stables vis-à-vis des cycles de compression et sont donc les mieux adaptées aux applications sujettes à des changements de compression mécanique, comme les transports par exemple. Les GDL avec des fibres graphitisées ont les résistances les plus faibles.

Les valeurs des différentes résistances des GDLs mesurées dans cette thèse sous différentes conditions peuvent être utilisées pour enrichir des modèles numériques multiphysiques dédiés à la prédiction des performances électriques des PEMFCs.

université PARIS-SACLAY

ÉCOLE DOCTORALE
Physique et ingénierie : Electrons, Photons, Sciences du vivant (EOBE)

Titre : Etude des liens entre les performances de composants de pile à combustible PEM et leurs comportements à l'intérieur de la pile observés en fonctionnement. Développement de caractérisations électriques et mécaniques in-situ et ex-situ.

Mots clés : Compression mécanique cyclique, GDL, pile PEM, résistance de contact, résistivité.

Résumé : L'amélioration du rendement des piles à combustible à membrane polymère basse température (PEMFC), passe par une diminution des pertes liées aux surtensions, telles que les pertes ohmiques, qui dépendent des conditions de fonctionnement et des propriétés des composants. Cela implique une meilleure compréhension de la relation entre propriétés physiques des matériaux, leur variation avec les conditions de fonctionnement et son influence sur les pertes ohmiques. Cette pile à hydrogène est constituée d'une membrane électrolyte en polymère, échangeuse de protons, couverte de deux couches catalytiques, placées entre deux couches de diffusions de gaz (GDLs), maintenues par deux plaques bipolaires (BPPs). Les pertes ohmiques sont en bonne partie dues à la résistance protonique de la membrane, mais également liées à des résistances électroniques volumiques dans les composants de cellule et à des résistances de contact entre ces éléments. Ces résistances sont fonction de la nature du matériau, de sa structure et des conditions de fonctionnement telle que l'humidité, la température et la compression mécanique exercée sur l'assemblage. Les travaux menés contribuent à la compréhension de l'origine des pertes ohmiques électroniques, en particulier celles liées à la GDL.

La GDL diffuse/évacue les gaz réactifs de/vers la BPP, conduit les électrons et la chaleur, contribue à la gestion de l'eau à l'intérieur de la pile et maintient mécaniquement l'ensemble membrane-couche catalytique. Les structures permettant ces fonctions sont des structures composites poreuses en fibres de carbone sous forme de papier ou de « tissu ». Cette structure est très sensible à la sollicitation mécanique d'origines diverses générant un état de contrainte variable. De plus, le comportement mécanique de la GDL est non-linéaire et laisse apparaitre une hystérésis de déformation avec les cycles de charge-décharge en compression. Les propriétés physiques de la GDL, à l'instar de sa résistance électrique, sont affectées par ce comportement de structure. Ce qui nécessite l'utilisation de compression cyclique pour étudier l'influence de la charge mécanique afin de s'approcher au mieux des conditions de fonctionnement réelles de la pile et in fine mieux appréhender le rôle de la GDL dans les pertes ohmiques globales. Les niveaux optimaux de compression mécanique font l'objet d'un compromis entre de faibles pertes ohmiques et des performances en diffusion élevées.

Dans cette thèse, une investigation des propriétés électriques a été menée sur plusieurs types de GDL papier carbone disponible dans le commerce :

- Des techniques de caractérisation ex-situ ont été utilisées pour mesurer d'une part la résistance dans le plan suivant deux directions perpendiculaires et d'autre part, la résistance à travers le plan sous une contrainte mécanique cyclique. Les effets des variations de température et d'humidité ont également été analysés.
- La résistance de contact entre la GDL et la plaque bipolaire a été mesurée en utilisant la méthode de transmission de ligne TLM.

Une diminution non-linéaire de toutes les résistances avec l'augmentation de la compression a été observée, ce qui implique l'existence d'un niveau optimal de compression à utiliser pour la pile, compte tenu de la porosité de la GDL et de ses propriétés de diffusion. Ces résistances sont plus ou moins sensibles aux cycles de compression, selon la structure des GDLs (la structure en feutre étant la moins sensible aux cycles). L'hystérésis de la résistance électrique décroît avec le niveau de compression et le nombre de cycles. Malgré l'anisotropie de la GDL observée pour la résistance dans le plan, quelques propriétés restent invariantes avec la direction de mesure, comme le taux de décroissance de la résistance avec la compression mécanique ou l'hystérésis. Enfin, l'humidité a tendance à faire décroitre la résistance à travers le plan de la GDL.

Maison du doctorat de l'Université Paris-Saclay
2ème étage aile ouest, Ecole normale supérieure Paris-Saclay
4 avenue des Sciences,
91190 Gif sur Yvette, France

Title : Study of the relations between the performances of PEM fuel cell components and their behaviors in stacks operated in the complete system. Development of electrical and mechanical characterization techniques

Keywords : Cyclic mechanical compression, PEM fuel cell, GDL, electrical contact resistance, resistivity

Abstract : Low Temperature Polymer Electrolyte Membrane Fuel cell (PEMFC) is the most mature fuel cell technology, and it can be used in a variety of applications, (transport, space, stationary and portable applications). This electrochemical generator converts Hydrogen and Oxygen into electricity, heat and water through oxidoreduction reaction. PEMFC power production and overpotentials are related to the operating conditions and physical properties of cell components. Increasing cell efficiency can be achieved by reducing the overpotential losses, such as the Ohmic losses. This requires a better understanding of the relationship between the physical properties of the materials, their variation with regards to the operating conditions, and the influence of this variation on the Ohmic losses.

A PEMFC is made of an electrolyte membrane covered with two catalyst layers, that are hold between two gas diffusion layers - GDLs and compressed by two Bipolar plates - BPPs. Ohmic overpotential losses are due to the protonic resistance of the membrane, to the electronic bulk resistance of the other components and to the contact resistance of interfaces between components. These resistances are function of the material nature and structure, the operating conditions such as humidity, temperature, and especially mechanical compression. This study contributes in understanding the origin of the electronic Ohmic losses, particularly those due to the GDL and its interfaces.

The GDL plays several transport roles in the PEMFC by providing/evacuating reactant gases from/to BPP, conducting electrons and heat. It also contributes to water management and mechanically support (the catalyst coated membrane) so that it remains functional. The most common structure used to allow these various functions is a composite porous carbon fibres structure that can be paper or cloth. This porous structure is very sensitive to mechanical excitation which comes from variable external and internal sources generating unsteady state of stresses stresses. In addition, the structure of the GDL exhibits a nonlinear compression stress-strain curve, with a strain hysteresis along the loading-unloading cycles. The physical properties of the GDL are affected by this behavior and need to be studied under cyclic compression in order to better approach the use conditions inside the FC, and to get a clearer idea about the contribution of the GDL to the global Ohmic losses. The optimal levels of mechanical compression must in particular be selected in order to make a trade-off between low Ohmic losses and high reactant diffusion rates.

In this thesis, experimental investigations and analyses of electrical properties have been conducted on several types of commercial carbon paper GDLs:

- Ex-situ characterization techniques have been used to measure the in-plane resistance according to two perpendicular directions. The impact of cyclic mechanical compression, the effects of temperature and humidity were investigated on the GDL through-plane resistance as well.
- The electrical contact resistance between GDL and BPP was measured using the Transmission Line Method.

It has been observed that all resistances decreased non-linearly with compression, meaning that optimal levels of compression can be obtained for PEMFC operation regarding the GDL porosity and diffusion properties. These resistances are more or less sensitive to the cycles of compression, according to the structure of the GDLs (the felt structure being the least sensitive towards cycles). The hysteresis of electrical resistance decreases with the rise of compression levels and with the number of compression cycles. Despite the GDL anisotropy observed for the in-plane resistance, some properties were unchanged with the measurement direction, such as the rate of resistance decrease with compression and the behaviour towards the cycles of compression. Finally, in most cases, humidity was found to decrease the through-plane resistance of GDLs.

Maison du doctorat de l'Université Paris-Saclay
2ème étage aile ouest, Ecole normale supérieure Paris-Saclay
4 avenue des Sciences,
91190 Gif sur Yvette, France